A Multi-layer Thermo-mechanical Coupling Restoring Force Model for Isolation Bearings with High Damping Rubber and Lead Cores under Low-temperature Environment

SHEN JIE

2024

A Multi-layer Thermo-mechanical Coupling Restoring Force Model for Isolation Bearings with High Damping Rubber and Lead Cores under Low-temperature Environment

SHEN JIE
Department of Urban Management
Graduate School of Engineering
Kyoto University, Japan

This dissertation is submitted for the degree of
Doctor of Engineering

2024

ABSTRACT

The high damping rubber (HDR) bearing and lead high damping rubber (LHDR) bearing are efficient rubber bearings with excellent energy dissipation capacity. However, the temperature sensitivity of the rubber materials, including the non-negligible temperature dependence and heating effect, affects the behavior of the isolators. These factors complicate the time evolution of the stiffness of HDR bearing or LHDR bearing, causing difficulties in precisely predicting its hysteretic behavior and posing challenges for the application in low-temperature earthquake-prone regions.

This research aims to investigate the hysteretic behavior of HDR and LHDR bearings considering the low temperature effect. The multi-layer thermal-coupled hysteretic models of HDR and LHDR bearings are proposed to explain the hysteretic behavior coupled with the thermo-mechanism of bearings at low temperatures. An isolated bridge model with HDR and LHDR bearings is set up to further validate the efficiency of the proposed model and assess the effect of temperature on the seismic behavior of the isolated bridge.

Specifically, the research includes three parts:

(1) Investigate the temperature effects on the hysteretic behavior of bearings.

(2) Explain the thermal mechanism within the bearings and establish a thermal-coupled hysteretic model.

(3) Evaluation of the seismic performance of the isolated bridge with HDR and LHDR bearings with low-temperature effect.

In part one, two common types of bearings, HDR and LHDR bearings with the same size, were selected in the experiment. The quasi-static cyclic loading test and the pseudo-dynamic and real-time hybrid simulation tests were carried out respectively to assess the cyclic behavior and seismic performance of bearings and structures. Three ambient temperatures, 23℃, 0℃, and −20℃, were set to investigate the temperature effect on the bearings. Numerous thermocouples were settled into the bearing with different positions and layers of HDR and lead core. The factors of initial loading effect and loading interval were considered in the series experiment. The shear stress-strain relationship, equivalent shear modulus and damping ratio, and the temperature history were discussed in cyclic loading. A two-degree-of-freedom isolated bridge model was set up in the hybrid simulation. The hysteresis behavior, temperature history, and energy dissipation of bearing, and the response of structure were analyzed under the realistic ground motion.

Part two proposes a multi-layer thermo-mechanical coupling model for HDR bearing to elucidate the thermal mechanism within a bearing and its influence on the complex hysteretic restoring force behavior. To represent the thermal mechanism in the HDR bearing with sufficient accuracy, the rubber bearing is divided into multiple layers along the vertical

direction, assuming one-dimensional heat conduction and considering heat outflow around the side. The thermal mechanism is illustrated by considering the heat transfer and heating effect in the multi-layer thermal-coupled model. This model considers the non-uniform internal temperature distribution, which causes the variations in shear deformation, different from the assumption of uniformly distributed shear deformation. The restoring force and temperature history of the HDR bearing for cyclic loading condition are computed and compared with the quasi-static tests under cyclic loading at three ambient temperatures of −20℃, 0℃, and 23℃. Finally, the model is validated by experimental data obtained by real-time hybrid simulation under the assumption of application to an isolated bridge model as a presentation of a realistic seismic loading condition.

Moreover, a hysteretic model coupled with thermal mechanism and rate dependence was constructed to simulate the mechanical behavior of bearings. A thermo-mechanical model was proposed to elaborate the interactional heat transfer behavior among HDR laminates, lead cores, and steel plates. The parameters of the model were identified by an optimization algorithm in the cyclic loading. The hysteretic behavior of the bearings was validated in the pseudo-dynamic and real-time hybrid simulations. The predicted hysteresis curves and temperature history of the model were compared with the experimental data and the previous model at −20℃, 0℃, and 23℃.

In part three, a full-scaled isolated bridge model based on the highway bridge design is established to evaluate the effect of low ambient temperature on the isolated bridges with HDR or LHDR bearings. The designed HDR bearing with the bilinear model is replaced by the HDR and LHDR bearings with multi-layer temperature-dependent Bouc-Wen (MTBW). The time history dynamic analysis is conducted with four level 2 earthquake ground motions to evaluate the seismic performance of the isolated bridge. The hysteretic behavior and the energy dissipation of the bearing, and the response of the bridge, including the relative displacement of the pier top, the bending moment of the pier base, and the acceleration of the superstructure, are discussed at −20℃, 0℃, and 23℃.

ACKNOWLEDGEMENTS

First and foremost, I want to express my deepest gratitude to my advisor, Prof. Akira Igarashi, for his unwavering support, guidance, and encouragement throughout my PhD studies. His insightful advice, constructive feedback, and patience have been invaluable to the completion of this dissertation.

I am also deeply thankful to Prof. Ji Dang (Saitama University) for his guidance in the research, Prof. Di Su (The University of Tokyo) for his discussion of program application, Prof. Zhen Huang (Southeast University) for his suggestions in career, members of my dissertation committee, Prof. Yoshikazu Takahashi, and Prof. Hiroyuki Goto for their time, valuable suggestions, and constructive criticism, which have significantly improved the quality of my research.

My sincere thanks go to Prof. Nozomu Yoneyama and Secretary Miho Mori and all the members of my laboratory for their support and assistance during various stages of my research.

I am also grateful to my friends Yanyan Liu, Xinhao He, Kai Xue, Yuqing Tan, Jian Zhou, Haodong Bai and Siyi He in my laboratory, as well as Ji Chen, Rui Zhang, Ting Yan, Xinyu Chen in my daily life. My heartfelt thanks also go to all the members in the basketball team KyodaiHuaren. Thank you for your support, encouragement, and companionship. While I cannot name everyone here, please know that your contributions have been invaluable, and I am deeply grateful to each and every one of you.

Last but not least, I would like to express my deepest appreciation to all of my family members and my soulmate Ji Wo for their unconditional love, encouragement, constant support in my life.

Shen Jie
Kyoto University
August 2024

TABLE OF CONTENTS

ABSTRACT ..... **I**

ACKNOWLEDGEMENTS ..... **III**

TABLE OF CONTENTS ..... **V**

LIST OF FIGURES ..... **IX**

LIST OF TABLES ..... **XV**

CHAPTER 1 INTRODUCTION **1**

1.1 Background 1

1.2 Research Objectives 4

1.3 Organization 5

CHAPTER 2 LITERATURE REVIEW **7**

2.1 Hysteretic Model of High Damping Rubber Bearings 7

2.2 Temperature Dependence 12

2.3 Heating Effect 15

2.4 Rate dependence 20

2.5 Low Temperature Effect on Isolated Structures 22

CHAPTER 3 EXPERIMENTAL INVESTIGATION ON SEISMIC PERFORMANCE OF ELASTOMERIC BEARINGS AT LOW TEMPERATURE **25**

3.1 General 25

3.2 Specimens and Test Program 26

3.2.1 Test specimens 26

3.2.2 Test setup 28

3.2.3 Test arrangement 30

3.3 Quasi-static Cyclic Loading Test 31

3.3.1 Loading pattern 31

3.3.2 Cyclic behavior of elastomeric bearings 32

3.3.3 Temperature distribution 35

3.4 Hybrid Simulation Test 39

3.4.1 Framework of hybrid simulation test 39

3.4.2 Input ground motion 42
3.4.3 Hysteretic behavior of elastomeric bearings 43
3.4.4 Temperature history of elastomeric bearings 45
3.4.5 Energy dissipation elastomeric bearings 49
3.4.6 Structural response 49
3.5 Discussion 51
CHAPTER 4 A MULTI-LAYER THERMO-MECHANICAL COUPLING HYSTERETIC MODEL FOR HDR BEARINGS AT LOW TEMPERATURE 53
4.1 General 53
4.2 Thermal Mechanism within HDR bearings 55
4.2.1 Physical model 55
4.2.2 Basic assumptions 56
4.2.3 Numerical model of heat transfer mechanism 57
4.2.4 Heat equation of each layer in the numerical model 62
4.3 A Thermal-coupled Restoring Force Model of HDR bearings 64
4.3.1 Basic assumptions 64
4.3.2 Restoring force model 64
4.4 Model Validation 65
4.4.1 Validation of cyclic loading 65
4.4.2 Validation of hybrid simulation 69
4.5 Discussion 72
CHAPTER 5 A MULTI-LAYER THERMO-MECHANICAL COUPLING HYSTERETIC MODEL FOR LHDR BEARINGS AT LOW TEMPERATURE 75
5.1 General 75
5.2 Thermal Mechanism within LHDR bearings 77
5.2.1 Physical model 77
5.2.2 Basic assumptions 79
5.2.3 Numerical model of heat transfer mechanism 79
5.2.4 Heat equation of each layer in numerical model 82
5.3 Restoring Force Model 85
5.3.1 Basic assumptions 85
5.3.2 Restoring force model 85

5.4 Model Validation 86
5.4.1 Validation of cyclic loading 86
5.4.2 Validation of hybrid simulation 89
5.5 Discussion 94
CHAPTER 6 EFFECT OF LOW TEMPERATURE ON SEISMIC RESPONSE OF ISOLATED BRIDGES WITH HDR/LHDR BEARINGS 97
6.1 General 97
6.2 Isolated Bridge Model 98
6.2.1 Prototype of isolated bridge 98
6.2.2 Design of isolated bearing 100
6.2.3 Modeling of isolated bridge 102
6.2.4 Selection of ground motions 105
6.3 Low-Temperature Effect on Response of Bridge 106
6.3.1 Hysteretic behavior of isolated bearings 106
6.3.2 Energy dissipation capacity 110
6.3.3 Relative displacement and ductility factor of pier top 111
6.3.4 Bending moment of pier base 113
6.3.5 Acceleration of superstructure 114
6.4 Discussion 116
CHAPTER 7 CONCLUSIONS AND FUTURE WORK 119
7.1 Conclusions 119
7.2 Future Work 122
REFERENCE 123
APPENDIX A DESIGN PARAMETER OF HDR BEARING 129
A.1 Design Parameter of HDR Bearing 129
LIST OF PUBLICATIONS 131

LIST OF FIGURES

Figure 1.1 Mechanism of seismic isolation. 1

Figure 1.2 High damping rubber bearing. 2

Figure 1.3 Lead high damping rubber bearing. 2

Figure 1.4 Temperature dependence property of HDR bearings in research of Tan et al. (2023a). 3

Figure 1.5 Organization of dissertation. 6

Figure 2.1 Classic hysteretic models: (a) Bilinear model; (b) Bouc-Wen model. 7

Figure 2.2 An analytical model proposed by Abe et al. (2004). 8

Figure 2.3 An analytical model for elastomeric bearings proposed by Yamamoto et al. (2009). 9

Figure 2.4 A three-dimensional multi-spring mechanical model proposed by Kikuchi et al. (2010). 10

Figure 2.5 An analytical model proposed by Yamamoto et al. (2012). 10

Figure 2.6 A modified Park-Wen model for bi-directionally loaded elastomeric isolation bearings proposed by Dang et al. (2016). 11

Figure 2.7 Dynamic loading tests of rubber bearing specimen by Takaoka et al. (2008). 13

Figure 2.8 Experimental test of cyclic behavior of small-size elastomers by Cardone et al. (2011). 14

Figure 2.9 Model for the analysis of heat conduction in lead-rubber bearings proposed by Kalpakidis and Constantinou (2009a). 17

Figure 2.10 Analytical modeling of the bridge bent in transverse direction in research of Ozdemir et al. (2011). 18

Figure 2.11 Nonlinear restoring force model of HDR bearing with thermal mechanism proposed by Tan et al. (2023a). 19

Figure 2.12 a rheology model for HDR bearings proposed by Bhuiyan et al. (2009). 21

Figure 2.13 A rate-dependent rheology model proposed by Nguyen et al. (2015). 21

Figure 2.14 finite element model of bridge in research of Billah and Todorov (2019). 23

Figure 2.15 Elevation view and numerical model of the seismically isolated bridge in research of Wang et al. (2019). 24

Figure 3.1 Dimensions of HDR bearing specimen (mm). 27

Figure 3.2 Dimensions of LHDR bearing specimen (mm). 27

Figure 3.3 Layout of thermocouples: (a) HDR bearing; (b) LHDR bearing. 28

Figure 3.4 Test setup of specimens. 29

Figure 3.5 Horizontal loading pattern of cyclic loading for HDR bearing specimen (CL-2nd). 32

Figure 3.6 Horizontal loading pattern of cyclic loading for LHDR bearing specimen (CL-2nd). 32

Figure 3.7 Shear stress-strain relationship of HDR bearing specimen (CL-2nd). 33

Figure 3.8 Equivalent shear modulus and damping ratio of HDR bearing specimen (CL-2nd). 34

Figure 3.9 Shear stress-strain relationship of LHDR bearing specimen (CL-2nd).....34

Figure 3.10 Equivalent shear modulus and damping ratio of LHDR bearing specimen (CL-2nd). 35

Figure 3.11 Measured temperature of HDR bearing specimen (CL-2nd).....37

Figure 3.12 Measured temperature of LHDR bearing specimen (CL-2nd). 39

Figure 3.13 Framework of hybrid simulation test.....40

Figure 3.14 Input ground motion. 43

Figure 3.15 Rate of (A) pseudo-dynamic and (B) real-time hybrid simulations. 43

Figure 3.16 Hysteresis curves comparison of pseudo-dynamic and real-time hybrid simulation tests of HDR bearing specimen.....44

Figure 3.17 Shear strain comparison of pseudo-dynamic and real-time hybrid simulation tests of HDR bearing specimen.....44

Figure 3.18 Hysteresis curves comparison of pseudo-dynamic and real-time hybrid simulation tests of LHDR bearing specimen. 44

Figure 3.19 Shear strain comparison of pseudo-dynamic and real-time hybrid simulation tests of HDR bearing specimen.....45

Figure 3.20 Measured temperature of HDR bearing specimen in 2nd pseudo-dynamic hybrid simulation test (HS-PD-2nd).....45

Figure 3.21 Measured temperature of HDR bearing specimen in real-time hybrid simulation test (HS-RT). 46

Figure 3.22 Measured temperature of LHDR bearing specimen in pseudo-dynamic hybrid simulation test (HS-PD).....47

Figure 3.23 Measured temperature of HDR bearing specimen in 2nd real-time hybrid simulation test (HS-RT-2nd). 47

Figure 3.24 Temperature distribution of LHDR bearing under real-time hybrid simulation (HS-

RT-2nd) at −20℃. 49

Figure 3.25 Energy dissipation of bearing specimens in real-time and pseudo-dynamic hybrid simulation tests: (a) HDR bearing; (b) LHDR bearing. 49

Figure 3.26 Pier top displacement comparison of bridge model with HDR bearing under pseudo-dynamic and real-time hybrid simulation tests. 50

Figure 3.27 Pier acceleration comparison of bridge model with HDR bearing under pseudo-dynamic and real-time hybrid simulation tests. 50

Figure 3.28 Pier top displacement comparison of pseudo-dynamic and real-time hybrid simulation tests of LHDR bearing specimen. 50

Figure 3.29 Pier top acceleration comparison of pseudo-dynamic and real-time hybrid simulation tests of LHDR bearing specimen. 51

Figure 4.1 Non-uniform shear deformation due to the temperature effect. 54

Figure 4.2 A multi-layer heat transfer model for HDR bearing: (a) HDR bearing, (b) multi-layer heat transfer model, (c) enlarged part for Bd.1, (d) enlarged part for If.1. 56

Figure 4.3 Heat transfer mechanism within the internal layer of single medium. 58

Figure 4.4 Heat transfer mechanism of the boundary layer of single medium. 59

Figure 4.5 Heat transfer mechanism within layers of multiple media. 60

Figure 4.6 Calculation of heat generation rate by numerical method. 61

Figure 4.7 Hysteresis curve of MTBW model compared with experimental results under cyclic loading at −20℃, 0℃, and 23℃. 66

Figure 4.8 Validation of MTBW model compared with experimental results under cyclic loading at −20℃, 0℃, and 23℃: (a) equivalent shear modulus and (b) equivalent damping ratio. 67

Figure 4.9 Temperature history of rubber layers computed by MTBW model and test results under cyclic loading at −20℃, 0℃, and 23℃. 68

Figure 4.10 Temperature distribution of MTBW model along vertical direction of the bearing under cyclic loading at −20℃, 0℃, and 23℃. 69

Figure 4.11 Hysteresis curve of MTBW model compared with experimental results and previous TMC MPW model under real-time hybrid simulation at −20℃, 0℃, and 23℃. 69

Figure 4.12 Validation of MTBW model compared with experimental results and previous TMC MPW model under real-time hybrid simulation at −20℃, 0℃, and 23℃: equivalent shear modulus and damping ratio of maximum cycle. 70

Figure 4.13 Temperature history of MTBW model compared with experimental results and previous TMC MPW model under real-time hybrid simulation at −20℃, 0℃, and 23℃. 70

Figure 4.14 Temperature distribution of MTBW model along vertical direction of the bearing under real-time hybrid simulation at −20℃, 0℃, and 23℃. 71

Figure 4.15 Pier top acceleration of MTBW model compared with experimental results under real-time hybrid simulation at −20℃, 0℃, and 23℃.....71

Figure 4.16 Pier top displacement of MTBW model compared with experimental results under real-time hybrid simulation at −20℃, 0℃, and 23℃.....72

Figure 5.1 A thermo-mechanical coupling hysteretic model for LHDR bearings. 76

Figure 5.2 A multi-layer thermo-mechanical model for LHDR bearings. 78

Figure 5.3 Heat transfer mechanism between lead core and steel plate.....81

Figure 5.4 Heat transfer mechanism between steel plate and HDR laminate. 82

Figure 5.5 Rheology model of LHDR bearing. 85

Figure 5.6 Hysteresis curve of the model of LHDR bearing compared with experimental results under cyclic loading at −20℃, 0℃, and 23℃.....87

Figure 5.7 Validation of the model of LHDR bearing compared with experimental results under cyclic loading at −20℃, 0℃, and 23℃: (a) equivalent shear modulus and (b) equivalent damping ratio. 87

Figure 5.8 Temperature history of rubber layers computed by the model of LHDR and test results under cyclic loading at −20℃, 0℃, and 23℃. 89

Figure 5.9 Hysteresis curve of the model of LHDR compared with experimental results and previous TMC MPW model under real-time hybrid simulation at −20℃, 0℃, and 23℃. 89

Figure 5.10 Strain time history of the model of LHDR compared with experimental results and previous TMC MPW model under real-time hybrid simulation at −20℃, 0℃, and 23℃. 90

Figure 5.11 Validation of real-time hybrid simulation: F+(−): maximum (minimum) force; D+(−): maximum (minimum) displacement; MaxE: energy dissipation of maximum loop; R2: coefficient of determination. 90

Figure 5.12 Strain time history of the model of LHDR compared with experimental results and previous TMC MPW model under pseudo-dynamic hybrid simulation at −20℃, 0℃, and 23℃. 90

Figure 5.13 Strain time history of the model of LHDR compared with experimental results and previous TMC MPW model under pseudo-dynamic hybrid simulation at −20℃, 0℃, and 23℃. 90

Figure 5.14 Validation of pseudo-dynamic hybrid simulation: F+(−): maximum (minimum) force; D+(−): maximum (minimum) displacement; MaxE: energy dissipation of maximum loop; R2: coefficient of determination.....91

Figure 5.15 Contributions of force of lead core (fl), HDR laminate (fr), and rate dependence

(fv) under real-time and pseudo-dynamic hybrid simulations. 92

Figure 5.16 Temperature history of the model of LHDR bearing compared with experimental results and previous TMC MPW model under real-time hybrid simulation at −20℃, 0℃, and 23℃. 92

Figure 5.17 Temperature distribution of the model of LHDR bearing along vertical direction of the bearing under real-time hybrid simulation at −20℃, 0℃, and 23℃. 93

Figure 5.18 Pier top acceleration of the model of LHDR bearing compared with experimental results under real-time hybrid simulation at −20℃, 0℃, and 23℃. 93

Figure 5.19 Pier top displacement of the model of LHDR bearing compared with experimental results under real-time hybrid simulation at −20℃, 0℃, and 23℃. 94

Figure 5.20 Pier top acceleration of the model of LHDR bearing compared with experimental results under pseudo-dynamic hybrid simulation at −20℃, 0℃, and 23℃. 94

Figure 5.21 Pier top displacement of the model of LHDR bearing compared with experimental results under pseudo-dynamic hybrid simulation at −20℃, 0℃, and 23℃. 94

Figure 6.1 Overview of design bridge. 99

Figure 6.2 Dimension of the design pier 1 (P1): (a) Front view (transverse direction); (b) Side view (longitudinal direction) 99

Figure 6.3 Hysteretic characteristics of HDR bearing design in bilinear model. 100

Figure 6.4 Seismic performance design process of the bridge with isolated devices. 101

Figure 6.5 M-DOF model in dynamic analysis for Pier 1 (P1). 102

Figure 6.6 Validation of MTBW model for HDR and LHDR bearings for the maximum loop at 23℃ 104

Figure 6.7 Stiffness degradation bilinear model for RC pier. 105

Figure 6.8 Selected Level 2 earthquake ground motions. 105

Figure 6.9 Hysteresis curve of HDR bearing under level 2 earthquakes. 107

Figure 6.10 Shear strain-time history of HDR bearing under level 2 earthquakes. 107

Figure 6.11 Shear strain comparison of HDR bearing under level 2 earthquake. 108

Figure 6.12 Hysteresis curve of LHDR bearing under level 2 earthquakes. 109

Figure 6.13 Shear strain-time history of LHDR bearing under level 2 earthquakes. 109

Figure 6.14 Shear strain comparison of LHDR bearing under level 2 earthquake. 109

Figure 6.15 Dissipated energy comparison of HDR bearing under level 2 earthquake. 110

Figure 6.16 Dissipated energy comparison of LHDR bearing under level 2 earthquake. 110

Figure 6.17 Pier top displacement-time history of bridge with HDR bearing under level 2 earthquakes. 111

Figure 6.18 Maximum pier top displacement and ductility factor comparison of bridge with HDR bearing under level 2 earthquakes. 112

Figure 6.19 Pier top displacement-time history of bridge with LHDR bearing under level 2 earthquakes. 112

Figure 6.20 Maximum pier top displacement and ductility factor comparison of bridge with LHDR bearing under level 2 earthquakes. 113

Figure 6.21 Pier base bending moment-rotation curve of bridge with HDR bearing under level 2 earthquakes. 113

Figure 6.22 Pier base bending moment-rotation curve of bridge with LHDR bearing under level 2 earthquakes. 114

Figure 6.23 Superstructure acceleration-time history of bridge with HDR bearing under level 2 earthquakes. 115

Figure 6.24 Superstructure acceleration comparison of bridge with HDR bearing under level 2 earthquakes. 115

Figure 6.25 Superstructure acceleration-time history of bridge with LHDR bearing under level 2 earthquakes. 115

Figure 6.26 Superstructure acceleration comparison of bridge with LHDR bearing under level 2 earthquakes. 116

LIST OF TABLES

Table 3.1 Dimensions of HDR and LHDR bearing specimens (mm). 28
Table 3.2 Loading capacity of test setup. 30
Table 3.3 Test arrangement of HDR and LHDR bearing specimens. 31
Table 3.4 Condition of cyclic loading tests (CL-2nd) of HDR and LHDR bearing specimens. 32
Table 4.1 Thermal and basic properties of steel and HDR materials. 62
Table 4.2 Identified parameters and contribution rates of MTBW model. 65
Table 5.1 Thermal and basic properties of lead, steel, and HDR materials. 82
Table 5.2 Identified parameters of the model of LHDR. 87
Table 6.1 Design parameter of isolated bearing. 102
Table 6.2 Specifications of dynamic model. 103
Table 6.3 Parameters of bilinear model used in design of HDR bearing. 104
Table 6.4 Parameters of MTBW model used in design of HDR and LHDR bearings. 104
Table A.1 Parameter of design equivalent shear modulus for HDR bearing. 129
Table A.2 Parameter of design equivalent damping ratio for HDR bearing. 129

CHAPTER 1

INTRODUCTION

Chapter 1 introduces the background of the seismic isolated bearings. The critical issues in high damping rubber bearings considering temperature effect are analyzed. The corresponding solutions and research objectives are provided in this research. Finally, the organization of the dissertation is outlined.

1.1 Background

Seismic isolation is a technique used in structural engineering to protect buildings and infrastructure from the damage of earthquakes (Buckle and Mayes 1990; Kunde and Jangid 2003). By isolating the structure from the ground motion during an earthquake, seismic isolation extends the natural period, as shown in Fig. 1.1. Common seismic isolation devices include laminated rubber bearing, lead rubber bearing, friction pendulum, tuned mass damper, etc. The isolation device is usually placed between the structure and the ground to dissipate the seismic energy and reduce the forces and vibrations transferred to the structure, thereby minimizing damage and improving overall safety (Housner et al. 1997). This technique is particularly effective for critical facilities like hospitals, bridges, and nuclear power plants, where uninterrupted functionality during and after an earthquake is crucial (Anastasios and George 2017).

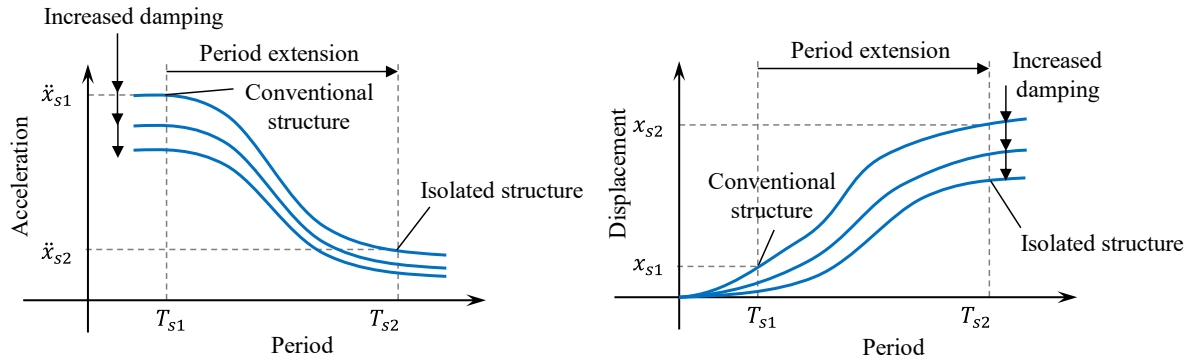

Figure 1.1 Mechanism of seismic isolation.

Rubber bearings, recognized as highly effective isolation devices, have been widely used around the world. High damping rubber (HDR) bearing, as shown in Fig. 1.2, is regarded as a promising cost-effective device for application due to its effective and stable isolation properties. The bearing consists of laminated layers of HDR and steel plate. The steel plates are installed to prevent rubber bulging and provide high vertical stiffness, while horizontal stiffness is controlled by the low elastic shear modulus of the rubber. The high damping performance of HDR bearing allows it to function as both a bearing and a damper, dissipating energy through internal friction and deformation. This eliminates the requirement for additional dissipation devices in the structure.

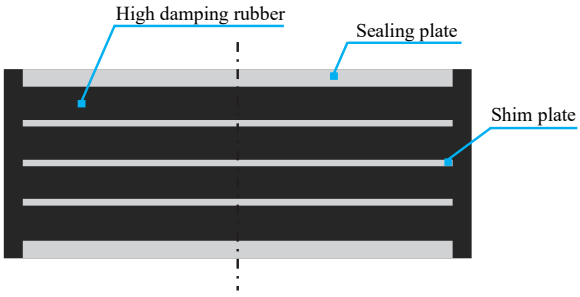

Figure 1.2 High damping rubber bearing.

To address the heightened seismic requirements, another improved type of isolated bearings, lead high damping rubber (LHDR) bearing (Gimenez and Himeno 2021), has been developed and applied, as shown in Fig. 1.3. LHDR bearings integrate the HDR with lead cores, where one or several lead cores traverse through the HDR bearing and are confined by springs, leading to the enhanced energy dissipation capacity. Compared to conventional rubber bearings, the damping performance of LHDR bearings is significantly increased. Therefore, the dimension of such bearing can be reduced to achieve the cost reduction.

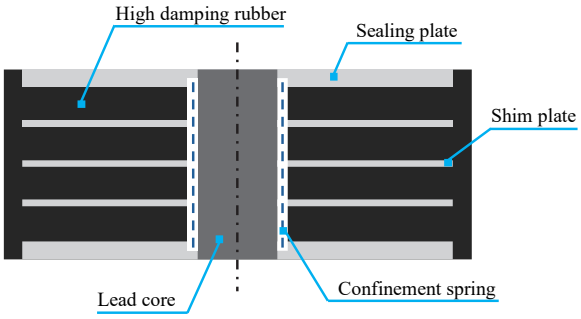

Figure 1.3 Lead high damping rubber bearing.

However, the temperature sensitivity of HDR material is a non-ignorable property, which exhibits not only the temperature dependence leading to higher stiffness at low ambient temperature but also the heating effect due to energy dissipation (Cardone et al. 2011). Fig. 1.4 illustrates the typical temperature dependence property of bearings with HDR. The bearings typically show higher initial stiffness and the equivalent damping ratio at low ambient

temperatures, which can affect the seismic response of the structure during the earthquake (Tan et al. 2023a; Yakut and Yura 2002). The heating effect, which refers to the generated heat within the bearing due to the energy dissipation of HDR and lead cores during loading, is another key point that needs to be considered in the research of HDR bearing. The heating effect coupled with the seismic response of the structure contributes to the complexity of the hysteretic behavior of bearings with HDR. These factors complicate the time evolution of the stiffness of HDR bearing or LHDR bearing, causing difficulties in precisely predicting its hysteretic behavior and posing challenges for the application in low-temperature earthquake-prone regions.

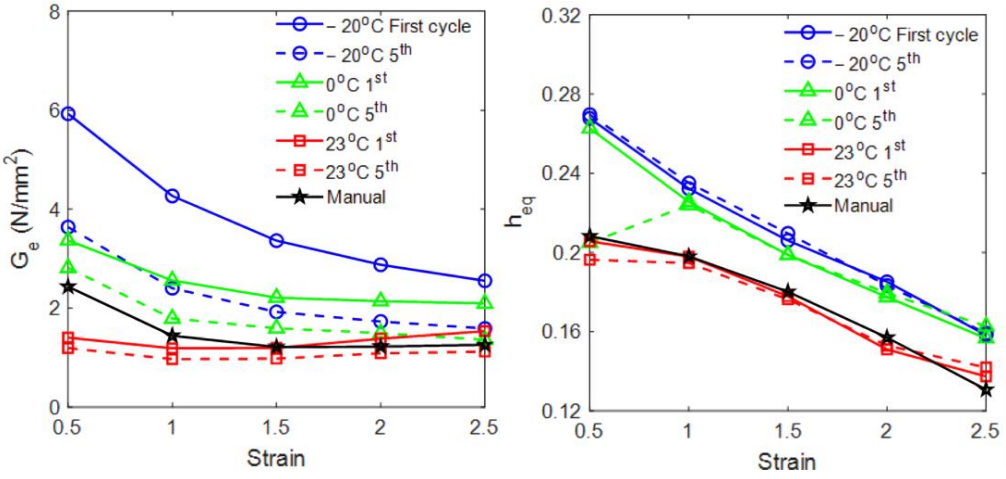

Figure 1.4 Temperature dependence property of HDR bearings in research of Tan et al. (2023a).

Although the investigation of temperature dependence and heating effect of HDR bearing and lead rubber (LR) bearing has been conducted in recent years, the thermal mechanism within the bearing is rarely considered. The bearing tends to be assumed as a uniform object, where the temperature distribution within the bearing is ignored during the earthquake. However, it may result in a deviation from the estimation of the hysteretic behavior of bearings with HDR. Moreover, the thermal mechanism of the LHDR bearing cannot be represented as a simple superposition of the HDR bearing and LR bearing. The heating effect should be considered both in the HDR and lead cores.

This research proposes multi-layer thermo-mechanical hysteretic models for HDR and LHDR bearings to elucidate the detailed thermal mechanism within the bearing and its influence on the complex hysteretic behavior of bearings. The proposed models provide predictions with improved accuracy, in terms of hysteretic behavior, temperature history, and structural response. A reliable reference can be offered by this research for the seismic design of HDR bearings in low-temperature earthquake-prone areas.

1.2 Research Objectives

This research aims to investigate the hysteretic behavior of HDR and LHDR bearings considering the low temperature effect. The multi-layer thermal-coupled hysteretic model of HDR and LHDR bearings is proposed to explain the hysteretic behavior coupled with the thermo-mechanism of bearings at low temperatures. An isolated bridge model with HDR and LHDR bearings is set up to further validate the efficiency of the proposed model and assess the effect of temperature on the seismic behavior of the isolated bridge.

(1) Investigate the temperature effects on the hysteretic behavior of bearings.

Research on temperature effect on rubber bearing has been conducted, but most focused on the cyclic loading or low-rate seismic loading, lack of real time realistic seismic loading. The real-time hybrid simulation test is necessary. The experimental tests of cyclic loading and hybrid simulation were conducted to investigate the hysteretic behavior of bearings at ambient temperature of −20℃, 0℃, and 23℃. The hysteresis curve, equivalent shear modulus, equivalent damping ratio, and temperature history were compared to analyze the effect of temperature dependence on the hysteretic behavior of the HDR and LHDR bearings.

(2) Explain the thermal mechanism within the bearings and establish a thermal-coupled hysteretic model.

The initial numerical models of thermal mechanism have been proposed. However, the temperature distribution within the bearing was non-uniform, which may result in the non-uniform deformation and local failure in rubber layers. The thermal conduction in the HDR bearing and the interacted heating effect of rubber and lead core in LHDR bearing have not been explained. To accurately represent the hysteresis behavior of the bearings at different ambient temperatures, the thermal mechanism within the bearings was modeled by a multi-layer thermos-mechanical model considering the heat transfer and heating effect. The thermal mechanism was then coupled with the hysteretic model of HDR and LHDR bearings.

(3) Evaluate the seismic performance of isolated bridges with HDR and LHDR bearings at low-temperature environment.

The bilinear model with temperature effect were used in the previous research to represent the behavior of HDR bearing or LR bearing. However, the bilinear model cannot accurately capture the behavior of the HDR bearing and LHDR bearing. To validate the accuracy of the proposed thermal-coupled hysteretic model of HDR and LHDR bearings, an isolated bridge model was set up with the application of the bearings. The seismic performance of the bridge was evaluated to validate the proposed model and investigate the temperature effect on the isolated bridge with HDR and LHDR bearings.

1.3 Organization

This dissertation is divided into seven chapters. Fig. 1.5 outlines the organization of the dissertation.

Chapter 1 introduces the background of the seismic isolated rubber bearings. The critical issues of the temperature dependence and heating effect of HDR bearing and LHDR bearing are analyzed to present the research topic and its necessity. The corresponding solutions and research objectives are then proposed.

Chapter 2 provides the literature review of the relevant research. The hysteretic models of laminated rubber bearings are introduced to summarize the existing research progress of the general hysteretic model. Factors of temperature dependence, heating effect, and rate dependence are included as the important factors that affect the hysteretic behavior of the bearings.

Chapter 3 presents the experimental investigation of the HDR and LHDR bearings at different ambient temperatures of −20°C, 0°C, and 23°C. The specimen dimensions and test program are introduced. The quasi-static cyclic loading and hybrid simulation tests are conducted to investigate the temperature effect on the hysteretic behavior of the bearings. The hysteresis curve, equivalent shear modulus, equivalent damping ratio, and temperature history are compared.

Chapter 4 investigates the thermal coupled hysteretic behavior of the HDR bearing. A multi-lay thermo-mechanical coupling hysteretic model is proposed to elaborate the thermal mechanism within the HDR bearing in detail, which cannot be explained in the previous model. The proposed model is validated by comparing the numerical and experimental results in Chapter 2.

Chapter 5 investigates the thermal coupled hysteretic behavior of the LHDR bearing. The factor of rate dependence is considered in this model. The interaction of the heating effect between the HDR laminate and lead core is illustrated in the thermos-mechanical model. A hysteretic model of LHDR considering the thermal mechanism and rate dependence is proposed and validated by the experimental test in this chapter.

Chapter 6 focuses on the effect of low ambient temperature on the isolated bridges with HDR or LHDR bearings. The full isolated bridge model based on the highway bridge design is established. The designed HDR bearing with the bilinear model is replaced by the HDR and LHDR bearings with the proposed model. The hysteretic behavior of the bearings and the response of the bridge are evaluated under selected level 2 earthquake ground motions.

Chapter 7 lists the main conclusions and future prospects of this research.

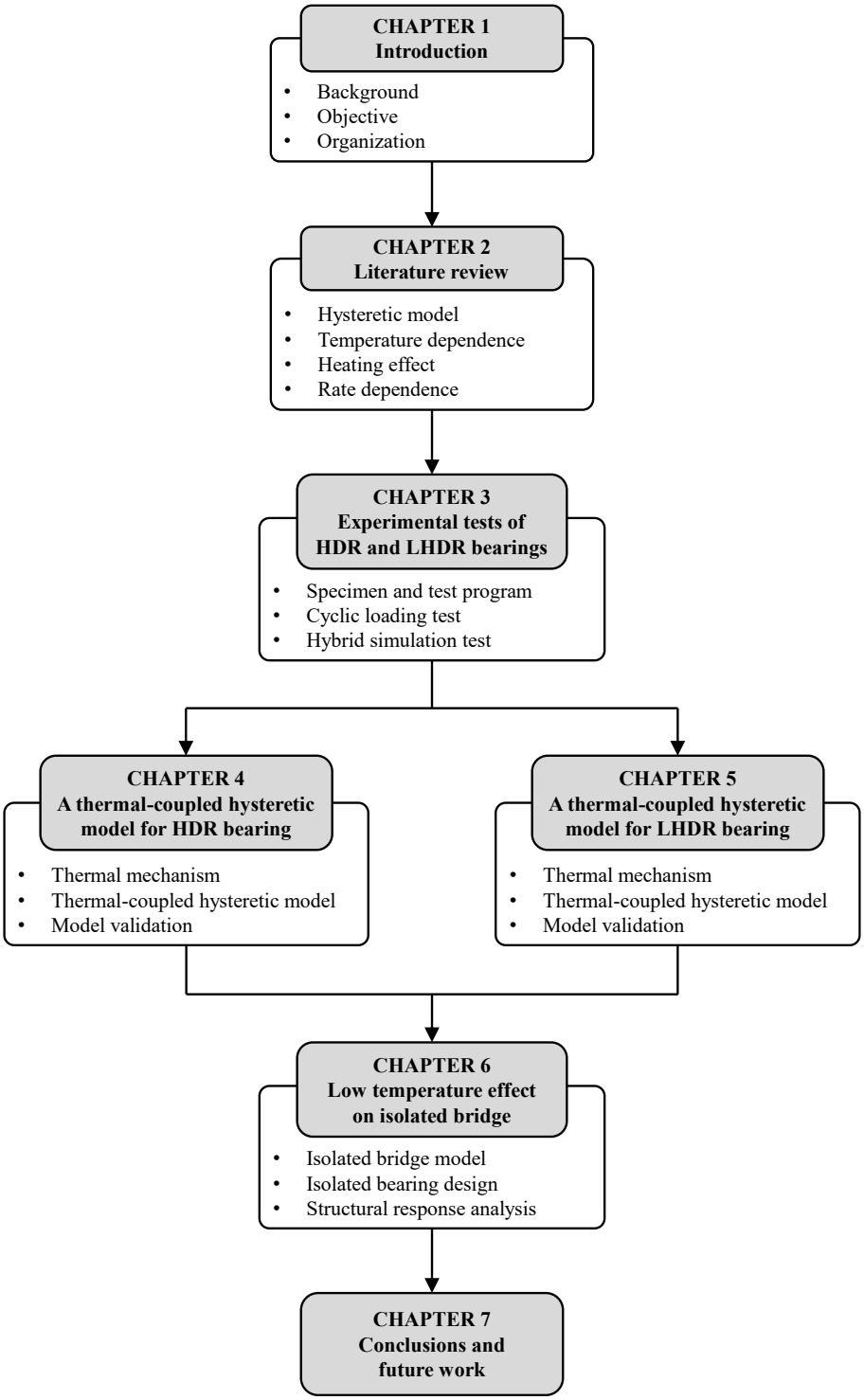

Figure 1.5 Organization of dissertation.

CHAPTER 2

LITERATURE REVIEW

Chapter 2 presents the literature review of the elastomeric bearings. Research on the existing hysteretic model of HDR bearings is listed. The important factors such as temperature dependence, heating effect, rate dependence, and low-temperature effect on structures that are related to this research are reviewed. The current research status and existing problems are analyzed to provide the basis and necessity for the research in the following chapters.

2.1 Hysteretic Model of High Damping Rubber Bearings

The most common hysteretic model for high damping rubber (HDR) bearing is the bilinear model (Skinner et al. 1993), which has been used in design codes and specifications such as the JRA (2019) and AASHTO (2010), as shown in Fig. 2.1a. It consists of a linear spring connected in parallel with a plastic element, including another linear spring connected in series with a plastic slider. Some researchers modified the bilinear model by using a linear spring connected in series with the parallel system (Sivaselvan and Reinhorn 2006).

The smooth hysteretic models such as the Bouc-Wen model (1967), as shown in Fig. 2.1b, the Park-Wen model (1976), and the Ozdemir model (1976) were proposed. In these models, the shape of the hysteresis curves was controlled by the constant parameters determined at the beginning.

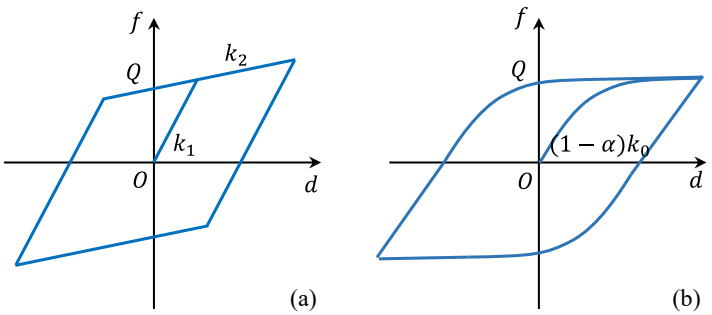

Figure 2.1 Classic hysteretic models: (a) Bilinear model; (b) Bouc-Wen model.

Ahmadi et al. (1996) developed a nonlinear hysteretic model for HDR bearings derived from

the stress-strain loop observed in high damping natural rubber compounds subjected to shear tests at a frequency of 0.5 Hz and a strain amplitude of 300%. This model accurately predicts the stress-strain response for strain amplitudes ranging from 50% to 300%. However, it falls short in estimating the energy dissipation at smaller strain amplitudes, indicating the influence of a rate-dependent dissipation mechanism.

Kikuchi and Aiken (1997) revised an analytical model to incorporate the stiffening behavior of bearings under high shear strain and the stiffness degradation observed between the initial cycle and following cycles at the same displacement amplitude. They formulated hysteresis rules applicable to both steady-state motion and randomly fluctuating displacement conditions, as commonly encountered during earthquake events. Nonetheless, the model does not consider the impact of strain rate and variations in axial load on the bearings' response.

Grant et al. (2004) proposed a strain-independent phenomenological model to characterize the bidirectional shear force-deformation behavior of HDR bearings. The restoring force vector was divided into two components: one aligned with the displacement vector and the other with the velocity vector. The displacement-aligned component was a nonlinear elastic force represented by an odd, fifth-order polynomial in shear displacement, inspired by the generalized Mooney-Rivlin energy density function. The velocity-aligned component followed a hysteretic response, modeled similarly to bounding surface plasticity. Additionally, two damage parameters were incorporated to account for long-term scragging degradation and the short-term Mullins effect (Mullins 1969).

Abe et al. (2004) enhanced the rate-independent elastoplastic model, as shown in Fig. 2.2, created by Ozdemir (1976), which initially lacked degradation, by introducing a displacement-dependent hardening rule to accurately represent behavior at shear strains exceeding 150%. Additionally, a nonlinear elastic spring was set to capture the response at strains up to 50%. This one-dimensional model was subsequently adapted to account for biaxial shear deformation through the application of a three-dimensional elastoplastic constitutive framework based on the Ozdemir model.

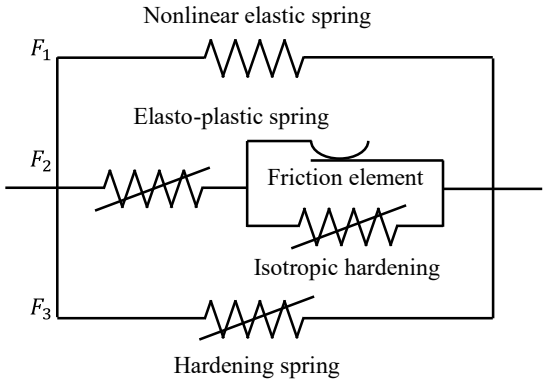

Figure 2.2 An analytical model proposed by Abe et al. (2004).

Yamamoto et al. (2009) introduced an analytical model for elastomeric bearings, as shown in

Fig. 2.3, that incorporated the interaction between shear and axial forces, nonlinear hysteretic behavior at large shear strains, and dependence on the vertical load. This model enhanced the one by Kikuchi and Aiken (1997) by adding a discrete distribution of nonlinear axial springs at the bearing top and bottom boundaries. Its effectiveness was demonstrated through comparisons with cyclic experiment results on lead rubber (LR) bearings subjected to shear strains up to 400% and various vertical load conditions ranging from zero to 30 MPa. In certain instances, the outcomes differed from those predicted by other existing models.

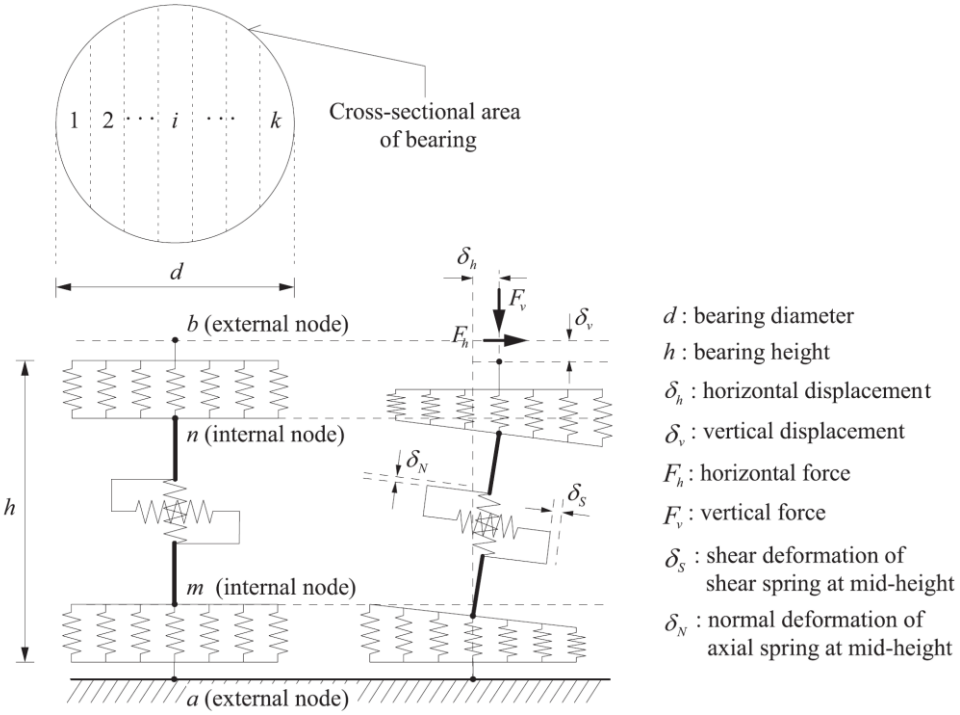

Figure 2.3 An analytical model for elastomeric bearings proposed by Yamamoto et al. (2009).

Kikuchi et al. (2010) expanded upon the previously mentioned model proposed by Yamamoto et al. (2009) to three dimensions and employed it to predict the substantial shear deformation response of square elastomeric isolation bearings. This enhanced model included multiple shear springs at mid-height and a series of axial springs at the top and bottom boundaries. Its accuracy was verified through cycling loading tests conducted on LRBs subjected to various vertical loads and horizontal loading directions. An element known as the Kikuchi Bearing Element, based on this model, has been integrated into OpenSees.

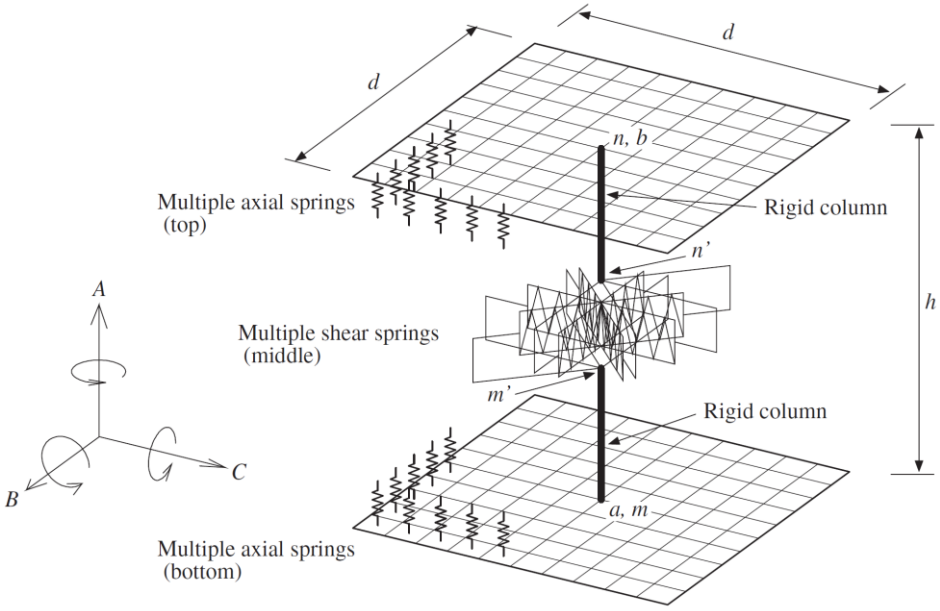

Figure 2.4 A three-dimensional multi-spring mechanical model proposed by Kikuchi et al. (2010).

Yamamoto et al. (2012) conducted the horizontal bidirectional loading tests for the full-scale HDR bearing. The analytical model, as shown in Fig. 2.5 was proposed based on the findings that the bidirectional loading induced twist deformation in the HDR bearings, increasing local shear strains. This model was also similar to the model proposed by Abe et al. (2004), but the novel identification process in this model simplifies the restoring force characteristics and results in a simple and accurate modeling.

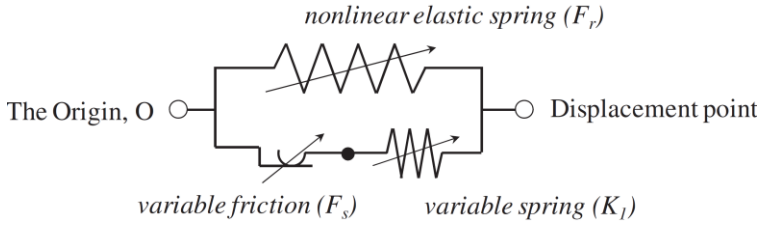

Figure 2.5 An analytical model proposed by Yamamoto et al. (2012).

Gjorgjiev and Garevski (2013) developed a 1D analytical model for simulating the nonlinear force-displacement relationship of low and HDR bearings. It expressed the restoring force as a polynomial function of bearing deformation and presented the bearing behavior through the polynomial coefficients and an additional eight parameters derived from bi-axial tests. While the model effectively captured the hardening of rubber at significant deformations, it did not incorporate the Mullins effect, strain-rate sensitivity, or dependence on axial load. The authors proposed the use of property modification factors to address aging, temperature variations, and scragging effects. The analytical model's validity was confirmed through biaxial tests conducted on square and circular bearings made from different rubber compounds. However,

it exhibited limitations in accurately predicting bearing behavior at low deformations since its calibration was focused on large strains.

Dang et al. (2016) modified the Park-Wen model for bi-directionally loaded elastomeric isolation bearings. The nonlinear part of the model was multiplied by the hyperbola and then added to the linear part, as shown in Fig 2.6. Two assumptions, the critical force depending on strain level and the critical force as bi-directional identical, are proposed to explain the bi-directional behavior of high damping bearing. The modified Park-Wen model can well fit the behavior of HDR bearing.

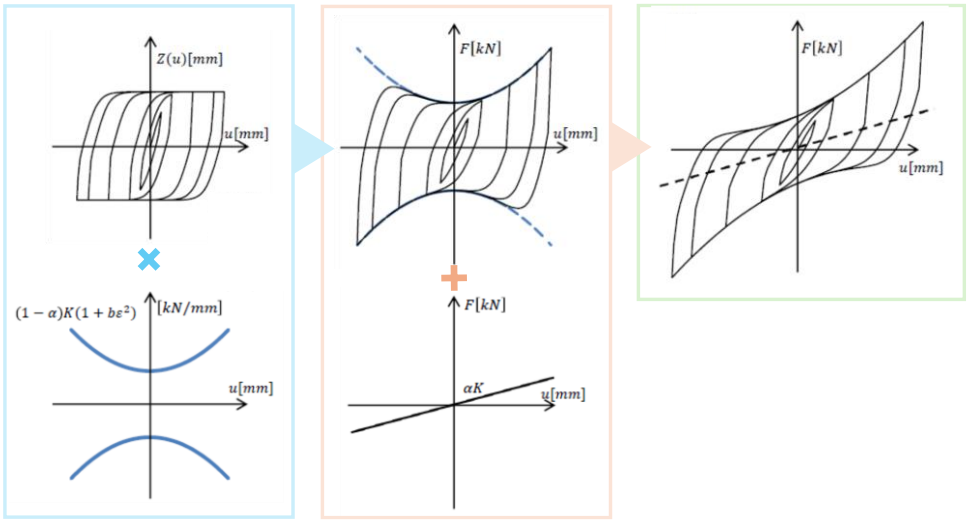

Figure 2.6 A modified Park-Wen model for bi-directionally loaded elastomeric isolation bearings proposed by Dang et al. (2016).

Gallardo et al. (2023) developed a simple but sufficiently accurate mathematical model to simulate the nonlinear shear behavior of HDR bearings under large deformations, along with a parameter estimation procedure using the geometrical features and mechanical characteristics. A novel model was also introduced to account for stiffness degradation, incorporating scragging and Mullins effects, developed based on experimental data from 924 tested devices. The proposed model demonstrated good agreement with experimental test results obtained from HDR bearings with varying geometric features and material properties.

Tan et al. (2024) proposed a random polymer (RP) model to account for the coupled temperature and Mullins effects in HDR bearings operating at low temperatures. The parameters of the RP model were determined by analyzing the hysteresis loops observed in HDR bearings during cyclic loading and hybrid simulation tests conducted with a temperature-controlled loading system at low temperatures. The accuracy of the RP model was validated by comparing the numerical seismic responses of a bridge isolated with HDR bearings, using the proposed model, with the results obtained from hybrid simulation tests.

2.2 Temperature Dependence

The property of temperature dependence of the HDR bearing poses challenges for its application in low-temperature regions. The HDR bearing typically exhibits higher initial stiffness and the equivalent damping ratio at low ambient temperatures, which can affect the seismic response of the structure during the earthquake. Extensive experimental and numerical investigations have been conducted on the temperature dependence of HDR bearing for a long time.

Roeder Charles et al. (1990) conducted an experimental program to measure the stiffness of elastomeric bearings at low temperatures. The experiments demonstrated that substantial increases in stiffness could occur, though the extent of this increase depended on the specific elastomer compound used. A design procedure was proposed to ensure the appropriate selection of elastomer compounds for bridge bearings in low-temperature environments. This research aimed to enhance the understanding of the low-temperature behavior of elastomeric bearings and offer practical design guidance to mitigate issues arising from excessive bearing stiffness.

Hwang and Hsu (2001) extended a previous application of the fractional derivative Kelvin model to predict the seismic response of (HDR) bearings. The formulation of the model was enhanced to incorporate the effect of ambient temperature, as variations in ambient temperature can significantly impact the mechanical characteristics of the bearings. Shaking table tests were conducted on a test structure comprising a steel deck isolated by four HDR bearings, with the bearings tested at temperatures ranging from 0 to 28℃. The effective shear modulus, identified from sinusoidal tests, was expressed in terms of maximum shear strain and bearing temperature. The numerical constants in the fractional derivative Kelvin model were adjusted as functions of ambient temperature.

Yakut and Yura (2002) carried out experimental research on the performance of elastomeric bridge bearings at low temperatures and identified critical parameters that influenced their performance. Full-size natural rubber and neoprene bearings were tested using specially designed setups inside a walk-in environmental chamber. Tests were carried out at temperatures of 23℃, −10℃, −20℃, and −30℃ over 21 days. The study examined the impact of cyclic compression, cyclic shear, loading rate, elastomer compound type, temperature history, creep, and slip coefficient on bearing performance. The results indicated the shear stiffness increased at low temperatures, and the temperature history is one of the important parameters influencing the performance of bearings.

Fuller et al. (2004) evaluated the effect of low-temperature crystallization on the mechanical stiffening of natural rubber. The relationship between shear modulus and crystallization was measured by simultaneously monitoring dimensional changes and stiffness. The relationship was found to be approximately independent of both crosslink density and crystallization temperature. Mechanisms for suppressing crystallization in rubber were discussed, and the low-

temperature stiffening of specially formulated rubber compounds for seismic isolation was presented. The results indicated that carefully formulated high damping natural rubber compounds could perform adequately at low temperatures.

Takaoka et al. (2008) conducted the dynamic loading tests, as shown in Fig. 2.7, on both full-scale and reduced-scale rubber bearing specimens under large deformation conditions, simulating long-period ground motion, to determine the effects of increased temperatures on the mechanical behavior of rubber bearings. The test results indicated that the temperature of the lead plug increased rapidly. Additionally, the hysteretic curve in the force-deformation relationship became smaller, and the yield load decreased with cyclic loading.

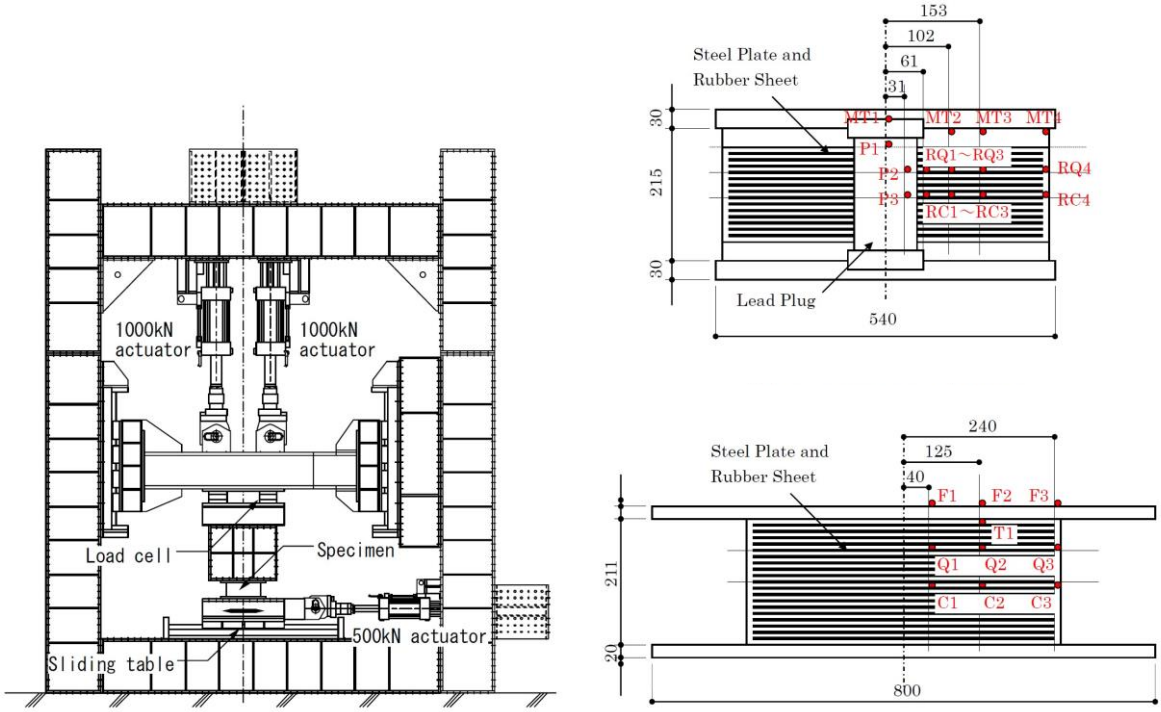

Figure 2.7 Dynamic loading tests of rubber bearing specimen by Takaoka et al. (2008).

Cardone et al. (2011) examined the temperature effects on the cyclic behavior of small-size elastomers through experiments under temperature levels ranging from 40℃ to −20℃, as shown in Fig. 2.8. The sensitivity of cyclic behavior in elastomeric isolators to air temperature variations was investigated based on extensive experimental results from a test program involving six different elastomeric compounds for seismic isolators. These compounds were characterized by a shear modulus ranging from 0.5 to 1.2 MPa at 100% shear strain and 20℃. The stress levels and the shear stiffness of elastomeric materials considerably increased while decreasing air temperature.

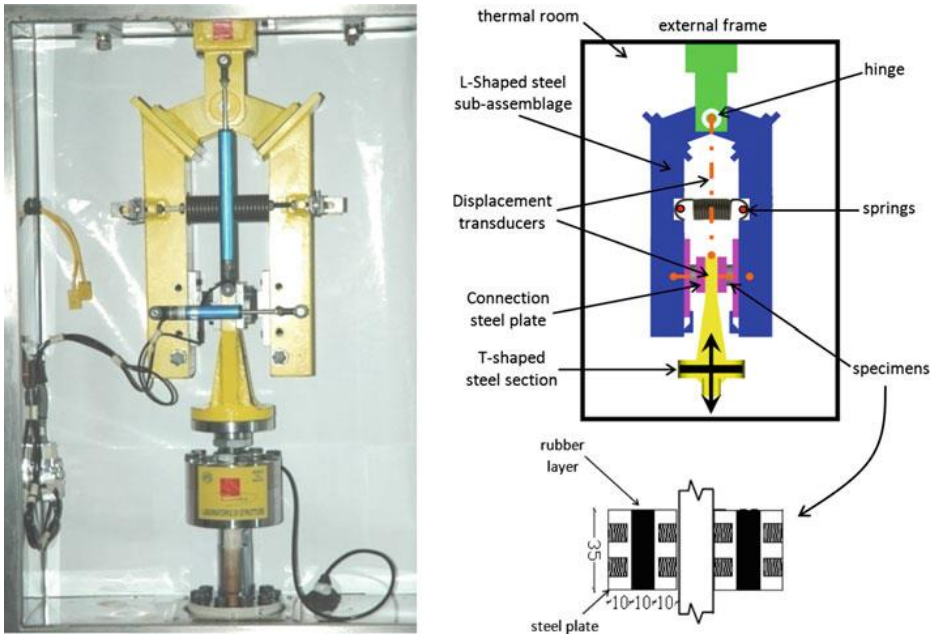

Figure 2.8 Experimental test of cyclic behavior of small-size elastomers by Cardone et al. (2011).

Saito et al. (2018) examined the mechanical properties of HDR bearings using dynamic loading tests performed in a low-temperature setting. Various temperatures were applied during fundamental cyclic loading tests using two types of HDR bearings along with a natural rubber (NR) bearing. The testing apparatus in a cold room induced 175% shear strain in the rubber thickness. The equivalent stiffness of all specimens rose in low-temperature conditions, with the extent of increase varying depending on the rubber type. The internal temperatures of the rubber bearings exhibited a linear correlation with energy loss, with the gradients of these linear relationships being influenced by the rubber type and ambient temperature.

Zhang and Li (2020) conducted a series of compression shear tests on three scaled rubber bearings, with test temperatures ranging from 30℃ to −20℃ and various levels of shear strains considered. The experimental results revealed a minimal variation in performance parameters due to changes in shear strain, while the characteristics of the bearings, such as equivalent stiffness, yield force, and post-yield stiffness, were significantly impacted by temperature. The influence coefficient functions were formulated to account for temperature effects, and the analysis values at different temperatures demonstrated good agreement with corresponding experimental values. The temperature influence coefficient function was useful for predicting the mechanical properties of rubber bearings at different temperatures.

Tan et al. (2023b) introduced a simplified thermo-mechanical coupled hysteretic restoring force model for HDR bearings. The model parameters were identified from the shear strain-stress curves of HDR bearings obtained through quasi-static cyclic loading tests at three different ambient temperatures. The accuracy of the enhanced model was verified by comparing the numerical results of a seismic response analysis of a bridge model, utilizing the proposed restoring force model, with the outcomes from hybrid simulations of the same bridge model,

which included HDR bearing loading tests under low-temperature conditions.

Yaşar et al. (2023) examined the change in hysteretic properties of a LR bearing when exposed to low temperatures. A full-scale LR bearing was conditioned at temperatures of −20°C, −10°C, 0°C, and 20°C for 24 hours and subsequently subjected to displacement-controlled cyclic motions corresponding to various levels of shear strains. The tests were conducted at loading frequencies of 0.1 Hz and 0.5 Hz. The recorded force-displacement curves were analyzed to quantify variations in isolator properties, specifically post-yield stiffness and characteristic strength (force intercept at zero displacement). The results indicated that both post-yield stiffness and characteristic strength increased as temperature decreased, with the increment becoming more pronounced at lower shear strains. It was found that characteristic strength was more sensitive to temperature changes compared to post-yield stiffness.

2.3 Heating Effect

The heating effect, which refers to the generated heat within the bearing due to the energy dissipation during loading, is another key point that needs to be considered in the research of HDR bearing. The heating effect coupled with the seismic response of the structure contributes to the complexity of the hysteretic behavior of HDR bearing.

Constantinou et al. (2007) proposed the heating model of elastomeric bearings to involve the heating effect. It provided a pioneering temperature estimation with reasonable assumption to neglect the heat radiation and heat conduction through the end plate of the bearings, which simplified the temperature independent of the space. When heat is generated in the solid, the equations of heat conduction are

$$\frac{\partial^2 T}{\partial x}+\frac{\partial^2 T}{\partial y}+\frac{\partial^2 T}{\partial z}-\frac{1}{D}\frac{\partial T}{\partial t}=-\frac{A}{k} \tag{2.1}$$

where T is the temperature rise; k is the thermal conductivity; D is the thermal diffusivity of rubber and A is the rate of heat production per unit volume per unit time.

The generated heat is independent of the space variables since it is primarily dependent on the shear strain. Another assumption is to neglect the heat radiation and heat conduction through the end plates of the bearings. Thus, the temperature is independent of the space variables. The rate of heat production per unit volume per unit time can be expressed as

$$A=\tau\frac{d\gamma}{dt} \tag{2.2}$$

where τ is the shear stress and γ is the shear strain in the rubber. Eq. (2.3) can be written as

$$\frac{\partial T}{\partial t}=\frac{D}{k}\tau\frac{d\gamma}{dt} \tag{2.3}$$

or

$$\rho c \frac{\partial T}{\partial t} = \tau \frac{d\gamma}{dt} \tag{2.4}$$

where D/k is replaced by ρc, where ρ is the density and c is the specific heat of the rubber. The temperature of the bearing can be integrated as

$$T(t) = \frac{1}{\rho c} \int_0^t \tau d\gamma \tag{2.5}$$

or

$$T(t) = \frac{1}{\rho c V} \int_0^t F du \tag{2.6}$$

where V is the volume of the rubber; F is the lateral shear force and u is the shear displacement of the rubber.

Kalpakidis and Constantinou (2009a) introduced a closed-form solution to predict the temperature of the LR bearings and establish a relationship between temperature and characteristic strength. This model explained the internal heat transfer mechanism of lead-core rubber bearings. Due to the continuous lead core in the LR bearing, most of the heat was conducted through the lead and steel plate, while the heat conducted through rubber layers can be ignored. The thermal equation for the lead core is

$$\rho_L \times c_L \times V_L \times \frac{dT_L}{dt} = \ddot{q}(t) \times V_L - 2 \times q_1(t) - q_2(t) \tag{2.7}$$

where ρ_L is the density of the lead core; c_L is the specific heat of the lead core; V_L is the volume of the lead core; T_L is the increase in the temperature of lead core; $\ddot{q}(t)$ is the heat production rate of the lead; $q_1(t)$ is the amount of heat flowing per unit time through the interface of one of the end plates and the lead core; $q_2(t)$ is the amount of heat flowing per unit time through the interface of the shim plates and the lead core, as shown in Fig. 2.9.

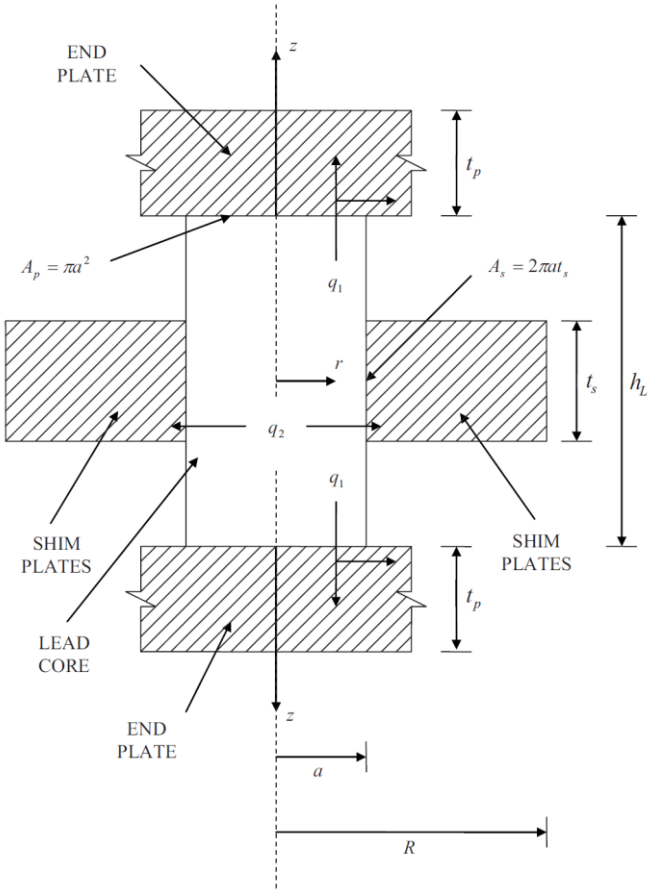

Figure 2.9 Model for the analysis of heat conduction in lead-rubber bearings proposed by Kalpakidis and Constantinou (2009a).

According to the analytical solutions of the (1) constant flux through a circular area into a semi-infinite half-space (q_1) (Beck 1979), and (2) constant flux into an infinite hollow cylinder (q_2) (Carslaw and Jaeger 1959), the heat equation of lead can be resulted in

$$\frac{dT_L}{dt} = \frac{\sigma_{YL}(T_L) \times v(t)}{\rho_L c_L h_L} - \frac{k_S \times T_L}{a \times \rho_L c_L h_L} \times \left(\frac{1}{F} + 1.274 \times \left(\frac{t_s}{a}\right) \times (t^+)^{-1/3}\right) \tag{2.8}$$

where

$$F = \begin{cases} 2 \times \left(\frac{t^+}{\pi}\right)^{\frac{1}{2}} - \frac{t^+}{\pi} \times \left[2 - \left(\frac{t^+}{4}\right) - \left(\frac{t^+}{4}\right)^2 - \frac{15}{4}\left(\frac{t^+}{4}\right)^3\right], & t^+ < 0.6 \\ \frac{8}{3\pi} - \frac{1}{2(\pi \times t^+)^{\frac{1}{2}}}\left[1 - \frac{1}{3 \times (4t^+)} + \frac{1}{6 \times (4t^+)^2} - \frac{1}{12 \times (4t^+)^3}\right], & t^+ \geq 0.6 \end{cases} \tag{2.9}$$

where σ_{YL} is the effective yield stress of lead; $v(t)$ is the velocity magnitude history; h_L is the lead core height; k_S is the thermal conductivity of steel; a lead core radius; t_s is the total shim plate thickness; t^+ is the dimensionless time.

Kalpakidis and Constantinou (2009b) conducted a comparison between theoretical predictions

and experimental results obtained from testing six lead-rubber bearings. The analytical predictions were found to be sufficiently accurate. Additionally, finite-element analysis results were presented, providing insight into the temperature distribution within the lead core, as well as the end and shim plates of the bearings. These distributions confirmed the assumptions made during the development of the theoretical solution.

Ozdemir et al. (2011) evaluated the response of seismically isolated bridges under near-field ground motions characterized by distinct pulse-type behavior, focusing on maximum isolator displacements (MIDs) and maximum isolator forces (MIFs) transmitted to the substructure. The isolation systems used LR bearings with bilinear force-deformation relationships, accounting for the yield strength deterioration due to the heating of the lead core. Nonlinear response history analyses were performed using two sets of ground motion records from different soil conditions to explore the effects of ground motion characteristics. The results showed that MIDs were overestimated by lower bound analyses when seismically isolated bridges faced near-field motions with high-velocity pulses.

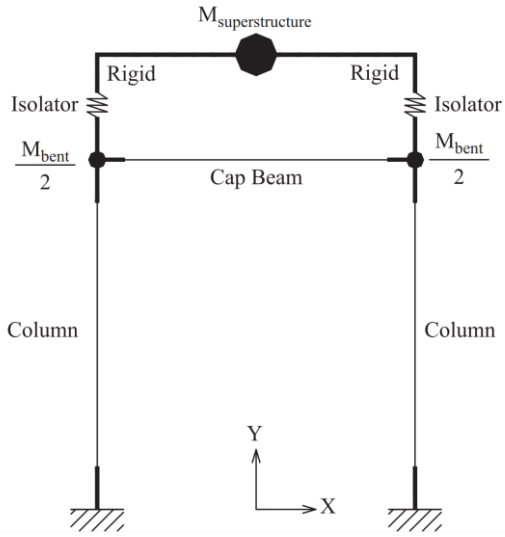

Figure 2.10 Analytical modeling of the bridge bent in transverse direction in research of Ozdemir et al. (2011).

Ozdemir and Dicleli (2012) considered the effect of lead core heating and associated strength deterioration on the seismic response of bridges isolated with LR bearing using the model of Kalpakidis and Constantinou (2009a). It is observed that the temperature rise in the lead core generally increases with the magnitude and number of near-fault ground motion velocity pulses but decreases with greater distances from the fault.

Okui et al. (2019) investigated the temperature dependence and heating effect of HDR bearings through cyclic loading tests. It found that the performance of HDR bearing is governed by the internal temperature and the heating effect needs to be considered when discussing the temperature dependence. A simple method for estimating the internal temperature was proposed. Previous cyclic loading test results at various ambient temperatures were re-

examined using the internal temperatures obtained from this proposed estimation method. The temperature dependence of HDR bearings was summarized in terms of these internal temperatures. Moreover, the boundary condition was considered and expressed as

$$\lambda_i \frac{\partial T}{\partial n} = h(T - T_a) \tag{2.10}$$

where λ_i is the thermal conductivity; n is the outer normal direction on the surface; h is the heat transfer coefficient; T_a is the ambient temperature.

The simple equation for internal temperature estimation can be derived as

$$\Delta T = \frac{\delta V_r}{m_r C_{pr} + m_s C_{ps}} \tag{2.11}$$

where δ is the dissipated energy density per cycle; V_r is the volume of HDR in a bearing; m_r and m_s are the mass of HDR and steel plates inside the bearing; C_{pr} and C_{ps} are the specific heat capacity of HDR and steel.

Miyamura et al. (2021) established finite element (FE) models to investigate the heating effect as well as the heat transfer within the HDR bearing. The bearing was modeled using hexahedral solid elements. The high damping rubber was represented by an overlaid viscohyperelastic and elastic-plastic constitutive model. Material parameters were identified based on results from one-directional loading tests, and temperature dependencies of these parameters were incorporated using a simple method based on empirical formulas for the bearing.

Tan et al. (2023a) improved the thermo-mechanical model based on Okui et al. (2019). The Eq. (2.11) was extended by including the energy loss caused by the heat radiation and conduction from the bearing contact surfaces for higher precision, as expressed by

$$\dot{T} = \left(\dot{E} - \dot{Q}\right)\lambda \tag{2.12}$$

where E is the dissipated energy; Q is the energy loss. The nonlinear restoring force model of HDR bearing with thermal mechanism can be shown as

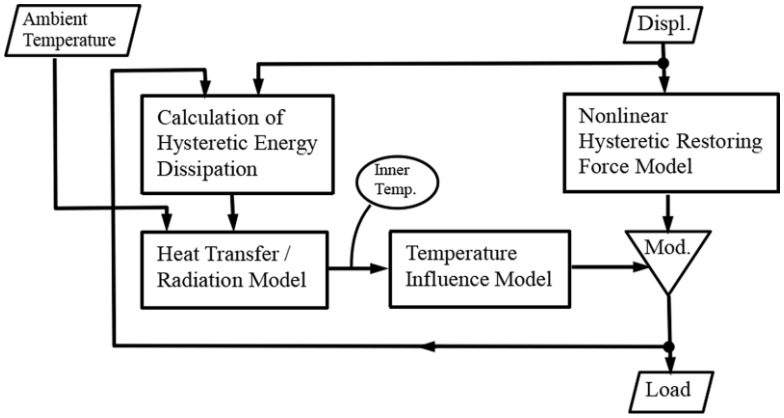

Figure 2.11 Nonlinear restoring force model of HDR bearing with thermal mechanism proposed by Tan et al. (2023a).

2.4 Rate dependence

Nagarajaiah et al. (1991) proposed a modified viscoplastic model according to the Bouc-Wen model. The novelty of the analytical model and algorithm lies in their ability to capture the highly nonlinear frictional behavior of sliding isolation systems in plane motion. Nonlinear behavior was restricted to the base, while the superstructure was assumed to remain elastic. Biaxial and uniaxial models, capable of representing both elastomeric and sliding isolation bearings, were introduced. The solution algorithm, incorporating the pseudo force method with iteration, was described. The computed results were compared with experimental data for verification.

Hwang and Ku (1997) introduced two analysis models for high damping rubber bearings based on the results of shaking table tests conducted on a seismically isolated bridge deck. These models were developed using the modified Gauss-Newton system identification method and the fractional derivative Kelvin model based on sinusoidal test results. The tests indicated a maximum shear strain in the bearing of approximately 100%. Additionally, two existing equivalent linear models, as specified by AASHTO and JPWRI, were characterized using sinusoidal test results. A comparison was made between the predicted seismic responses of the test structure using the proposed models and the two equivalent linear models with the measured responses. It was concluded that the proposed models provided better predictions of the seismic responses of the bearing compared to the two equivalent linear models. For practical application, the fractional derivative Kelvin model was integrated into an iteration procedure adopted in current design practices.

Hwang and Wang (1998) conducted an equivalent linear analysis to predict the seismic response of the test structure. A fractional derivative Maxwell model of the supports was developed, and an explicit integration scheme was implemented to solve the equations of motion of the test structure subjected to ground motions. Two sets of numerical parameters involved in the fractional derivative Maxwell model were determined based on the best-fit values of the dynamic amplification function and phase angle obtained from the sinusoidal tests.

Hwang et al. (2002) then developed an analytical model for HDR bearings to describe mathematically the damping force and restoring force of the rubber material and bearing. Ten parameters including the rubber compound, Mullins effect, scragging effect, frequency, temperature, and axial load were identified from cyclic loading tests. A sensitivity analysis is presented to show how the behavior is affected by changes in the parameters.

Dall'Asta and Ragni (2006) introduced a nonlinear viscoelastic damage model to characterize the behavior of HDR under cyclic loading. This model interpreted the transient (Mullins softening effect) and stable responses of rubber across the range of strain rates and amplitudes relevant to seismic applications. Internal variables and their evolution laws were incorporated to describe the inelastic phenomena during both the transient and stable phases of the response. The analytical results showed a good agreement with the experimental data.

Bhuiyan et al. (2009) developed a rheology model for HDR bearings, as shown in Fig. 2.11, that could accurately capture their behavior under seismic loading conditions. Experimental tests, including multi-step relaxation tests, cyclic shear tests, and simple relaxation tests, were conducted to identify the constitutive parameters of the rheology model. The developed model incorporated rate-independent and rate-dependent responses, addressing the complex behavior of HDR bearings under different loading conditions. The research emphasized the importance of understanding and modeling the nonlinear viscosity behavior of HDR materials for effective seismic analysis and design of structures using these bearings.

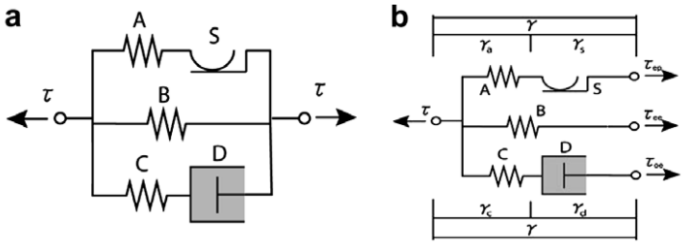

Figure 2.12 a rheology model for HDR bearings proposed by Bhuiyan et al. (2009).

Nguyen et al. (2015) proposed a rheology model, as shown in Fig. 2.12, to describe the rate-dependent cyclic behavior at low and room temperatures. In this model, three sets of parameters of stress and strain were identified for three ambient temperatures. An expanded Maxwell model is used to describe the rate-dependent behavior of the bearings, that is the linear elastic spring of the Maxwell model is replaced by a bilinear system. The model was reasonably successful in reproducing the typical rate-dependent cyclic behavior of HDR bearings under various testing conditions.

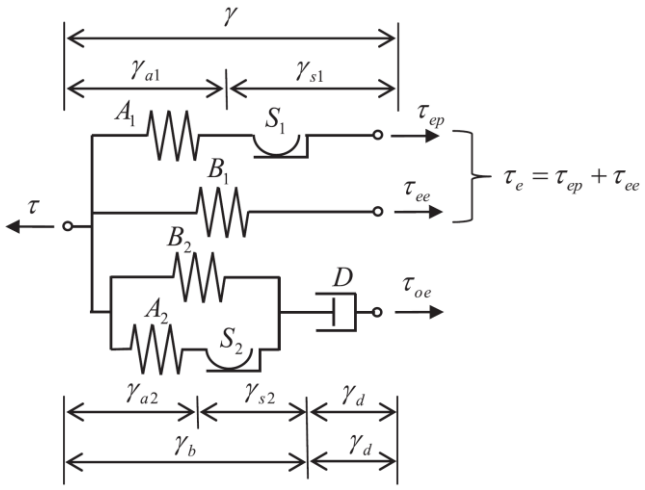

Figure 2.13 A rate-dependent rheology model proposed by Nguyen et al. (2015).

Yuan et al. (2016) A constitutive model for HDR bearings was introduced to accurately represent the force-displacement relationship, including rate-dependent shear deformation. The proposed constitutive model consisted of two hyperelastic springs and a nonlinear damping

element, expressing the finite deformation viscoelastic law based on the classical Zener model. The Fletcher-Gent effect was manifested as high horizontal stiffness at small strains, caused by carbon fillers in HDR bearings, accurately expressed through an additional stiffness correction factor in a novel strain energy function. Several material parameters were used to simulate the response of high damping rubber at different strain levels, and a nonlinear viscosity coefficient was introduced to characterize rate dependency. The parameter identification scheme was applied to the results of multi-step relaxation tests and cyclic shear tests, obtaining a three-dimensional function of the nonlinear viscosity coefficient concerning strain and strain rate.

Aghaeidoost and Billah (2024) developed a comprehensive analytical model to accurately predict the behavior of LR bearings at low to high strain levels. The proposed model considered the nonlinearity, hysteresis, stiffness, damping, and rate-dependent behavior of the LR bearing. It also accounted for the effects of rubber and lead components under temperature variations. The developed model was validated through experimental results, demonstrating its ability to accurately predict the response of the LR bearing at different strain levels.

2.5 Low Temperature Effect on Isolated Structures

The effect of low temperature on the isolated bearings has attracted significant attention due to the temperature sensitivity of the rubber material. Numerous studies have shown that the mechanical properties of the bearing will change at low temperatures. Accordingly, the seismic response of the isolated bridge will be also changed, including the maximum displacement and shear force of the pier. It indicates that the low-temperature effect may have a notable impact on the response of the structures.

The most current specifications, such as JRA Specifications for Highway Bridges. Part V: Seismic Design (2019); AASHTO Guide Specification for Seismic Isolation Design (2010); EN 15,129: Anti-Seismic Devices (2018) do not consider the temperature effect and require the low-temperature testing of isolated bearings. However, the newest version of the Canadian Highway Bridge Design Code (2014) adds the requirement of testing for isolated bearings at low temperatures.

Guay and Bouaanani (2016) presented key data and relevant analyses assessing low-temperature exposure for the design and evaluation of elastomeric bridge bearings and isolators in Canada. A comprehensive database of temperature records was analyzed to explore the potential for immediate thermal stiffening and crystallization. The proposed methodology and resulting data served as effective tools for identifying site-specific temperature conditions, thereby improving performance-based design and evaluation of bridges in Canada.

Billah and Todorov (2019) conducted a FE bridge model into dynamic analysis according to a realistic bridge located in Montreal, Quebec, Canada, where a temperature variation between +35℃ to −35℃ is expected. The performance of the isolated bridge was evaluated at summer and winter service temperatures. Analysis results showed that freezing conditions may have a notable effect on the component fragility as well as the bridge system fragility.

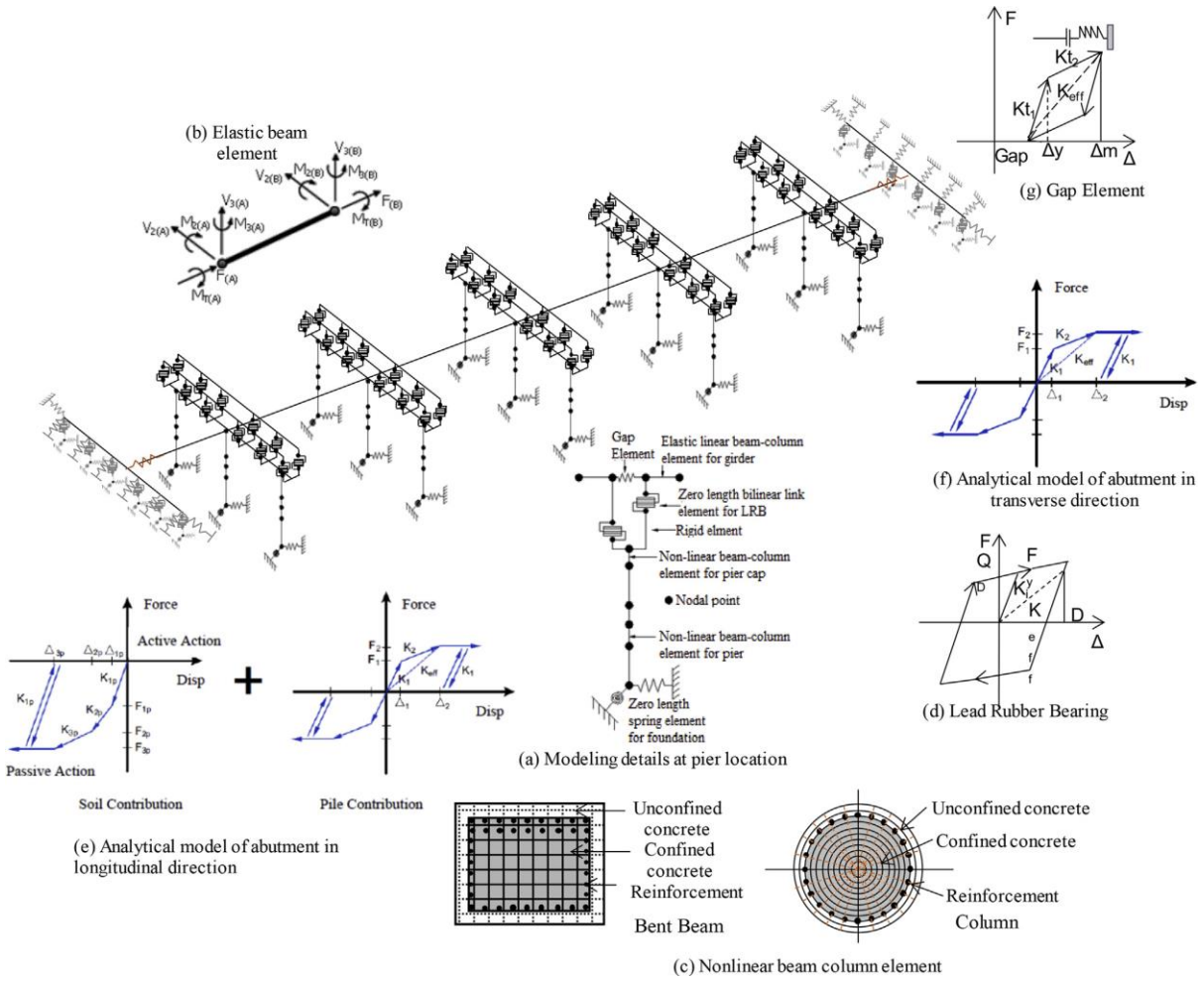

Figure 2.14 finite element model of bridge in research of Billah and Todorov (2019).

Wang et al. (2019) presented the seismic responses of bridges isolated by lead rubber bearings with a bilinear force-deformation model under near-fault excitations. The joint effects of ambient temperature, initial displacement, and lead core heating on the responses of seismically isolated bridges were considered. The results showed that ambient temperature, initial displacement, and lead core heating had significant joint effects on the responses of seismically isolated bridges. When such joint effects were ignored at low temperatures, the maximum isolator displacements could be overestimated, whereas the maximum isolator forces and the base forces could be underestimated.

Deng et al. (2020) established a FE model to investigate the detrimental effects of low temperatures on the seismic responses of a highway viaduct equipped with LR bearings. A dynamic bearing property definition was introduced to address the temperature changes resulting from absorbed earthquake energy and the corresponding property variations of LR bearings. At low temperatures, the base isolation effectiveness of LR bearings, which were optimized for room temperature, was significantly reduced. This reduction was evident through shorter fundamental natural periods of the structure and increased damage and forces experienced by structural members.

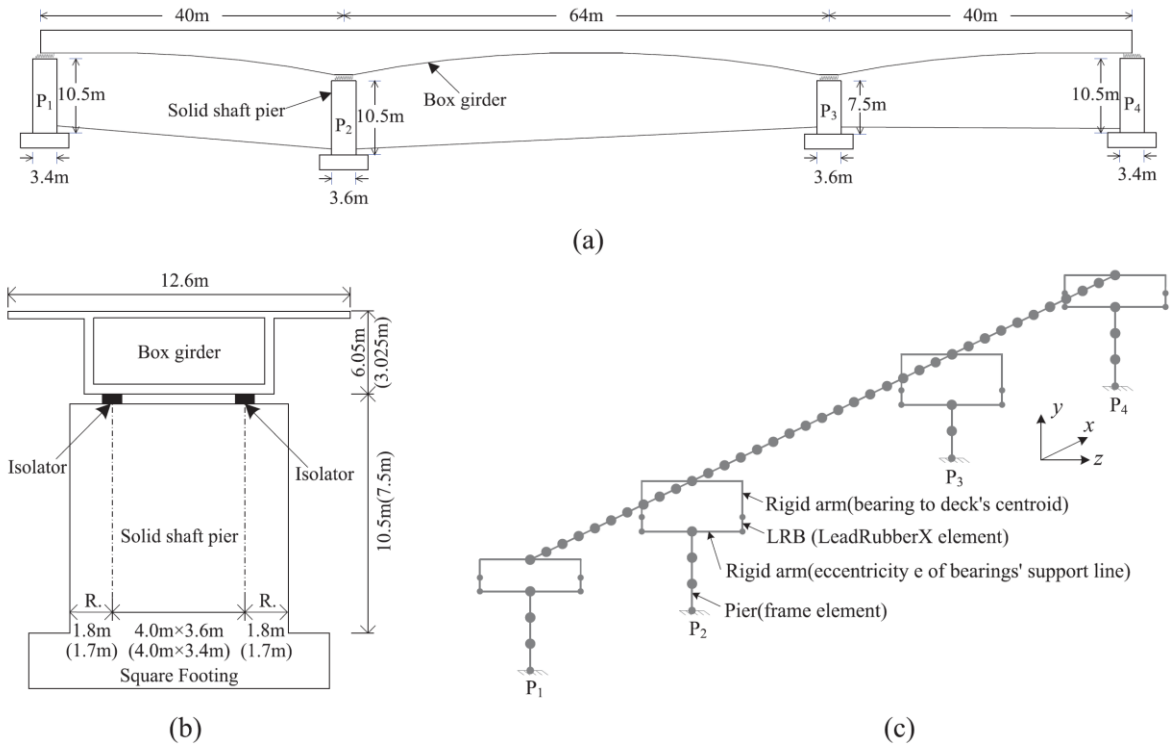

Figure 2.15 Elevation view and numerical model of the seismically isolated bridge in research of Wang et al. (2019).

CHAPTER 3

EXPERIMENTAL INVESTIGATION ON SEISMIC PERFORMANCE OF ELASTOMERIC BEARINGS AT LOW TEMPERATURE

Chapter 3 focuses on the experimental investigation of elastomeric bearings at low temperature. After analyzing the previous research findings, it is necessary to conduct specimen tests to investigate the seismic performance of HDR and LHDR bearings considering the temperature effect. The quasi-static cyclic loading hybrid simulation tests are carried out and discussed in this chapter. The experimental results in this chapter will also provide validation data for the numerical models in chapters 4 and 5.

3.1 General

High damping rubber (HDR) bearings and lead high damping rubber (LHDR) bearings are two types of effective elastomeric bearings in seismic isolation technology. The high damping property of the HDR bearing makes it become a bearing and a damper, which eliminates the requirement for additional dissipation devices in the structure. Moreover, with the addition of the spring-confined lead cores, the LHDR bearing presents significantly improved seismic performance compared with the conventional rubber bearings. Thus, these two bearings are regarded as promising cost-effective devices for application due to their effective and stable isolation properties.

However, HDR material shows significant temperature sensitivity, exhibiting not only the temperature dependence leading to higher stiffness at low ambient temperature but also the heating effect due to the energy dissipation. The heating effect of the lead core in the LHDR bearing is also non-ignorable. The HDR bearings typically exhibit higher initial stiffness and equivalent damping ratio at low ambient temperatures, which can affect the seismic response of the structure during the earthquake. These factors complicate the time evolution of the device's stiffness, causing difficulties in precisely predicting its hysteretic behavior. The properties of temperature dependence and heating effect of the HDR and LHDR bearing pose

challenges for their application in low-temperature earthquake-prone regions. Although numerous studies have proposed restoring force models for rubber bearings, few have focused on the effect of temperature on the mechanical properties of bearings. Moreover, most research on temperature effect was concentrated on the cyclic behavior of the bearing. However, the realistic earthquake ground motion is quite different from the cyclic loading. The response of the structure should also be considered. Conducting cyclic loading and seismic hybrid simulations at different ambient temperatures is of necessity to investigate the hysteretic behavior of HDR and LHDR bearings considering temperature effect and provide validation for numerical models.

This chapter aims to experimentally investigate the seismic behavior of HDR and LHDR bearings at different ambient temperatures. Two common types of bearings, HDR and LHDR bearings with the same size, were selected in the experiment. The quasi-static cyclic loading test and the pseudo-dynamic and real-time hybrid simulation tests were carried out respectively to assess the cyclic behavior and seismic performance of bearings and structures. Three ambient temperatures, 23℃, 0℃, and −20℃, were set to investigate the temperature effect on the bearings. Numerous thermocouples were settled into the bearing with different positions and layers of HDR and lead core. The factors of initial loading effect and loading interval were considered in the series experiment. The shear stress-strain relationship, equivalent shear modulus and damping ratio, and the temperature history were discussed in cyclic loading. A two-degree-of-freedom isolated bridge model was set up in the hybrid simulation. The hysteresis behavior, temperature history, energy dissipation of bearing, and the response of structure were analyzed under realistic ground motion.

3.2 Specimens and Test Program

3.2.1 Test specimens

The dimensions of the HDR and LHDR bearings and the placement of thermocouples are shown in Figs. 3.1 and 3.2. Table 3.1 lists the dimensions and material properties of HDR bearings. The 1/6-scale square cross-sectional HDR and LHDR bearing specimens manufactured by Kawakin Co., Ltd. were tested in the experiment. The specimen had a cross-section of 240 mm × 240 mm and was composed of six rubber layers with a thickness of 5 mm (30 mm in total) and five steel plates with a thickness of 3.2 mm (16 mm in total). Steel ending plates with a thickness of 25 mm were attached on two outer sides for connection. The bearing was covered by rubber with a thickness of 5 mm during fabrication. As for the LHDR bearing specimen, four lead cores with a diameter of 34.5 mm were embedded in the bearing.

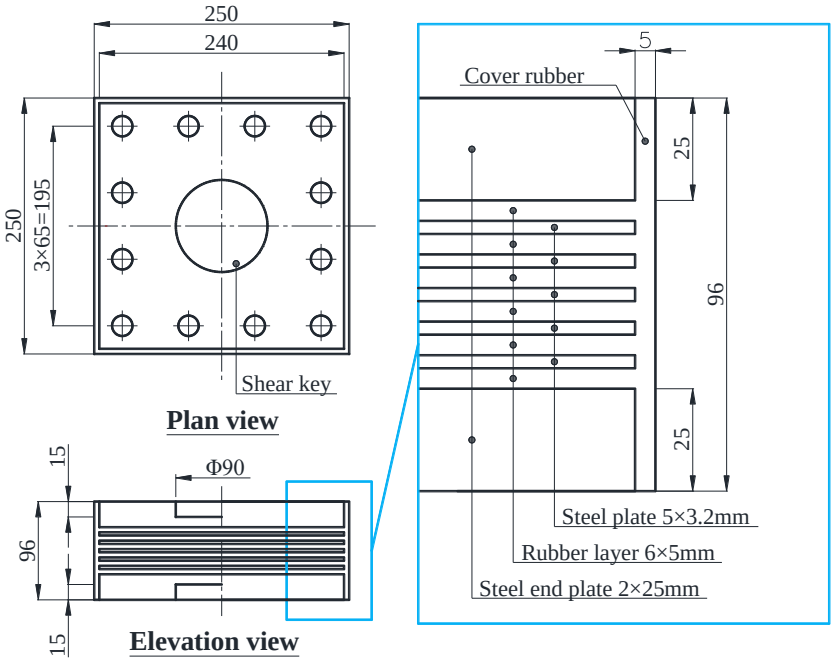

Figure 3.1 Dimensions of HDR bearing specimen (mm).

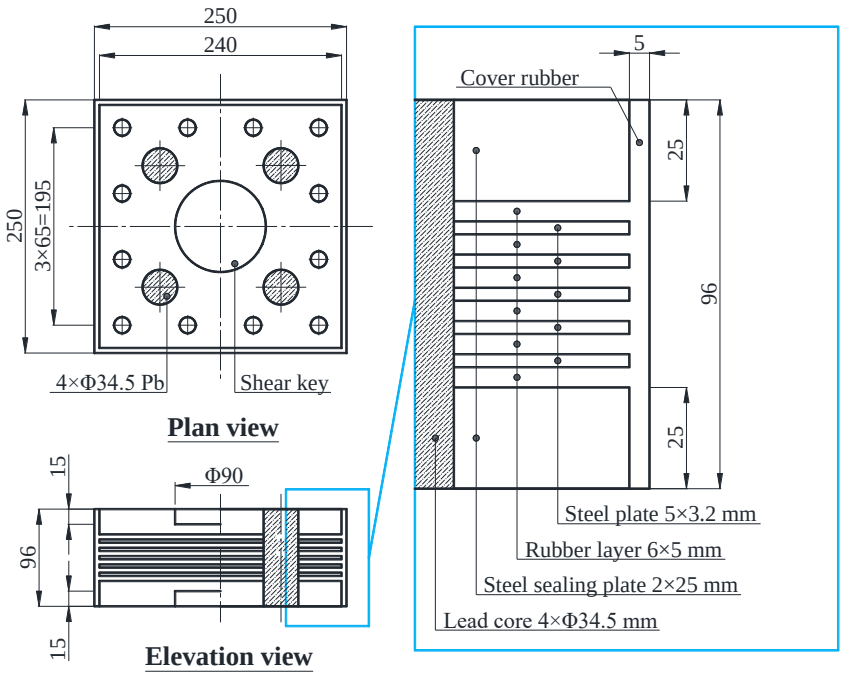

Figure 3.2 Dimensions of LHDR bearing specimen (mm).

Table 3.1 Dimensions of HDR and LHDR bearing specimens (mm).

Parameter	HDR	LHDR
A, Cross section (mm^2)	240×240	240×240
d_l, Diameter of lead core (mm)	-	34.5
n_l, Number of lead core	-	4
n_r, Number of HDR laminate	6	6
t_r, Thickness of single HDR laminate (mm)	5	5
n_s, Number of steel plate	5	5
t_s, Thickness of single steel plate (mm)	3.2	3.2
G, Shear modulus (MPa)	1.2	1.2
S_1, First shape factor	12	12
S_2, Second shape factor	8	8

The layout of the thermocouples is shown in Fig. 3.3. The thermocouples were placed in the first and third HDR layers, as well as in the lead core to record the inner temperature and temperature difference. Eight thermocouples were used in the HDR bearing specimen, at the center, middle of side, and corner of the HDR layer. Twelve thermocouples were used in the LHDR bearing specimen. Two of them were embedded in the lead cores, while others were placed in the HDR layers.

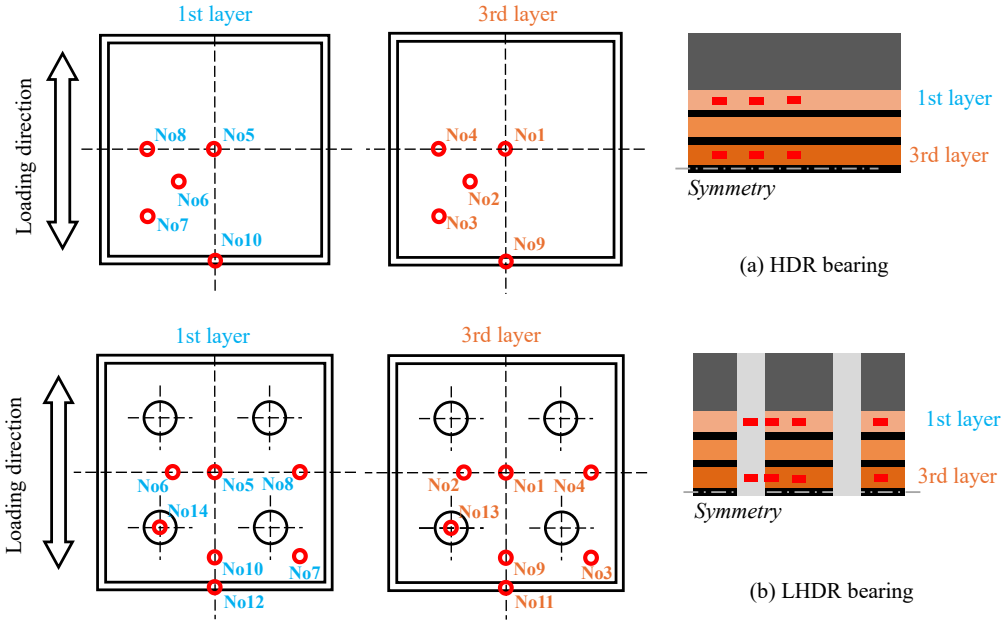

Figure 3.3 Layout of thermocouples: (a) HDR bearing; (b) LHDR bearing.

3.2.2 Test setup

The test setup is illustrated in Fig. 3.4. An axial stress corresponding to 6 MPa was applied to the bearing specimen by a vertical actuator in a loading test machine. A horizontal actuator in the test machine was used for shear loading to the bearing specimen. The specimen was fixed on the platform capable of one-axis horizontal movement along the linear guide. Table 3.2 lists the loading capacity of the test setup. The maximum loading force, displacement, and speed of

the vertical actuator in two directions were +1000/−2000 kN, ±150 mm, and 7 mm/s, respectively, while those of the horizontal actuator were ±400 kN, ±200 mm, and 630 mm/s, respectively. A shear key was set to transfer the shear force between the loading system and the top of the bearing (as shown in Fig. 3.1).

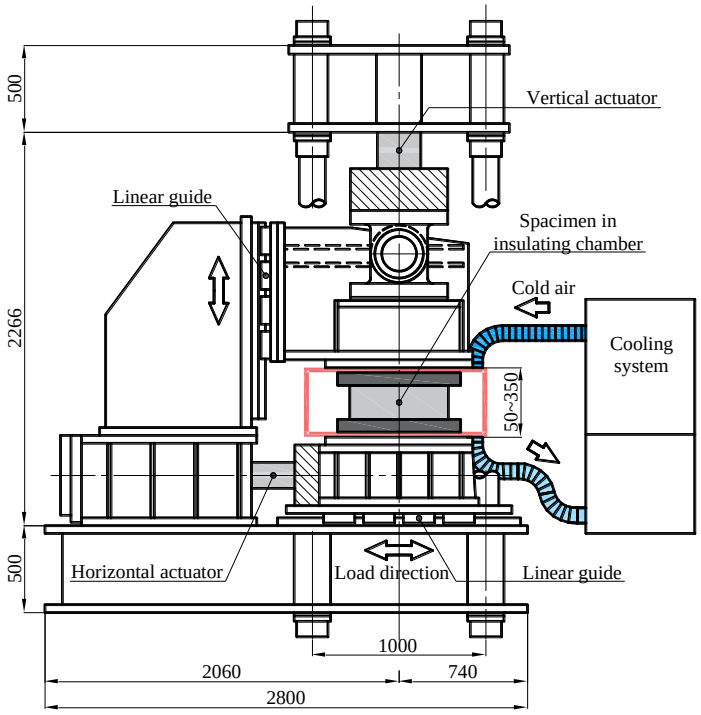

(a) Schematic diagram of test setup (unit: mm).

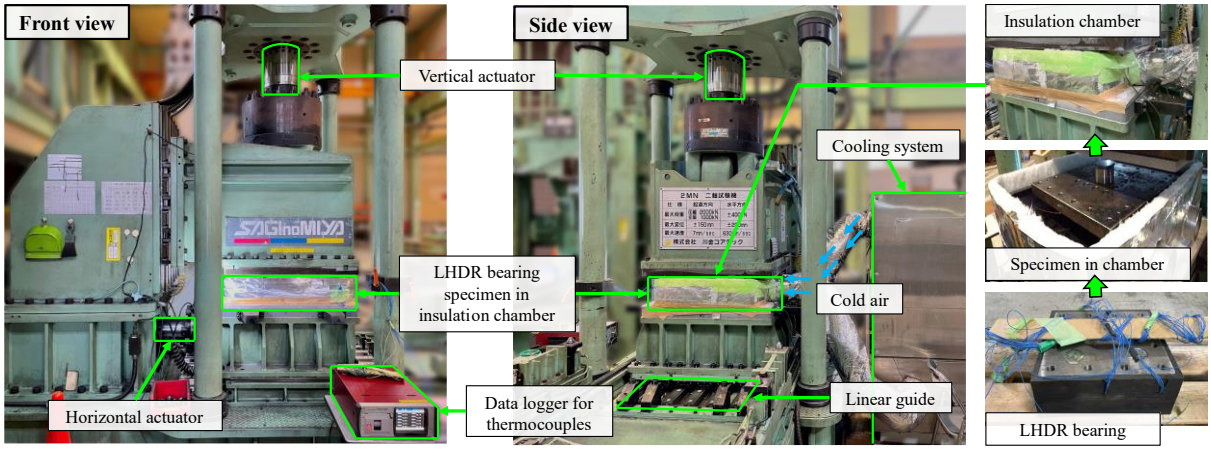

(b) Photos of test setup.

Figure 3.4 Test setup of specimens.

Table 3.2 Loading capacity of test setup.

	Vertical direction	Horizontal direction
Maximum force	+1000/−2000 kN	±400 kN
Maximum displacement	±150 mm	±200 mm
Maximum speed	7 mm/s	630 mm/s

The tests were conducted under three different ambient temperature conditions: 23℃ (room temperature), 0℃ (cold temperature), and −20℃ (extremely cold temperature). In order to investigate the temperature dependence of the HDR bearing, a cooling system was applied to maintain the constant ambient temperature during the test. The specimen was wrapped in an insulating chamber that was connected to the cooling system via pipes. The insulating chamber was horizontally moved along the loading apparatus, with sufficient space maintained between the chamber and the specimen to facilitate the specimen's movement during the test. The specimen was placed in the cooling system for a sufficient time to ensure that the internal temperature of the specimen was consistent with the ambient temperature. The inner temperature of the specimen was measured by thermocouples and recorded in the data logger.

3.2.3 Test arrangement

The test arrangement of HDR and LHDR bearing specimens is listed in Table 3.3. The cyclic loading (CL) test was conducted to identify the parameters of the restoring force model of bearings, while the hybrid simulation (HS) test was set to evaluate the hysteretic behavior of the bearing under the realistic seismic loading condition. The hybrid simulation test can be divided into pseudo-dynamic (PD) and real-time (RT) patterns, which will be introduced in section 3.4. Two batches of tests were conducted for both HDR and LHDR bearing specimens. For the HDR bearing specimen, the hybrid simulation test was the pseudo-dynamic type in Test No. 1 to prevent the maximum force of the bearing from exceeding the maximum loading capacity of the test setup. During the cyclic loading in Test No. 1, no interval was set between levels of strain amplitude. In Test No. 2, the real-time hybrid simulation was selected for loading. The loading interval was set in the cyclic loading test. The loading arrangement for the LHDR bearing specimen is similar. Moreover, the initial loading effect was also considered in every batch of tests.

Table 3.3 Test arrangement of HDR and LHDR bearing specimens.

Test No.	Bearing type	Loading pattern	Specimen No.			Initial loading	Loading interval
			23℃	0℃	−20℃		
1	HDR bearing	HS-PD-1st	No. 4	No. 3	No. 2	Yes	-
		CL-1st	No. 1	No. 3	No. 2	No	No
		HS-PD-2nd	No. 1	No. 3	No. 2	No	-
2	HDR bearing	CL-2nd	No. 5	No. 6	No. 7	Yes	Yes
		HS-RT	No. 5	No. 6	No. 7	No	-
3	LHDR bearing	CL-1st	No. 8	No. 9	No. 10	Yes	No
		HS-PD	No. 8	No. 9	No. 10	No	-
4	LHDR bearing	HS-RT-1st	No. 11	No. 12	No. 13	Yes	-
		CL-2nd	No. 11	No. 12	No. 13	No	Yes
		HS-RT-2nd	No. 11	No. 12	No. 13	No	-

Notes: HS means the hybrid simulation test; CL means the cyclic loading test; PD means the pseudo-dynamic test; RT the means real-time test.

3.3 Quasi-static Cyclic Loading Test

3.3.1 Loading pattern

The quasi-static cyclic loading test was conducted for parameter identification of the numerical model. In this research, only the cyclic loading tests of Test No. 2 and 4 (CL-2nd, considering loading interval) were used. The detailed loading condition and results of Test No. 1 and 3 (CL-1st, without loading inter) can be found in (Tan 2022). Figs. 3.5 and 3.6 show the horizontal loading patterns of cyclic loading tests for HDR and LHDR bearing specimens in Test No. 2 and 4 (CL-2nd), respectively. Table 3.4 lists the condition of cyclic loading tests of HDR and LHDR bearing specimens. The triangular wave was used for HDR bearing specimen, while the sinusoidal wave was used for LHDR bearing specimen. The specimens underwent cyclic shear tests with a constant loading rate of 30 mm/s under the three ambient temperatures. Shear strain amplitudes of 50%, 100%, 150%, 200%, and 250% were applied with five cycles for each amplitude. Note that the sixth cycle with a small strain amplitude was set after the five cycles to smoothly stop the loading. Intervals were set between loading cycles of different strain amplitudes to make sure the internal temperature of the bearing returned to the ambient temperature. Note that the exact time was not given in Figs. 3.5 and 3.6 as the loading time and interval time (about 1-1.5 hours) varied at each stain amplitude.

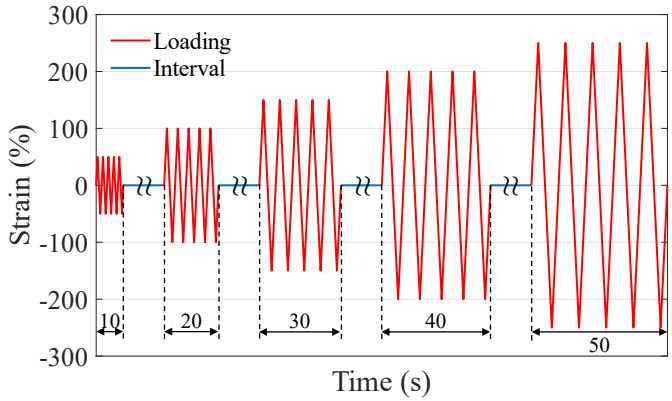

Figure 3.5 Horizontal loading pattern of cyclic loading for HDR bearing specimen (CL-2nd).

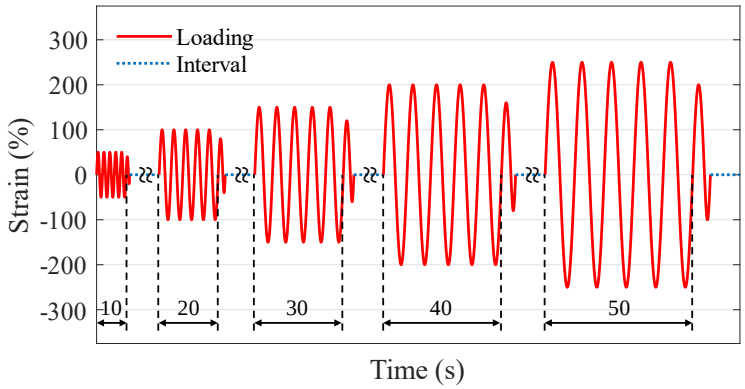

Figure 3.6 Horizontal loading pattern of cyclic loading for LHDR bearing specimen (CL-2nd).

Table 3.4 Condition of cyclic loading tests (CL-2nd) of HDR and LHDR bearing specimens.

Strain amplitude (%)	50	100	150	200	250
Horizontal displacement (mm)	15	30	45	60	75
Loading rate (mm/s)	30	30	30	30	30
Period (s)	2	4	6	8	10
Frequency (Hz)	0.50	0.25	0.17	0.13	0.10
Axial stress (MPa)			6		
Number of cycles			5		
Loading waveform			Triangular/sinusoidal wave*		
Ambient temperature (°C)			23, 0, −20		

Note: For the HDR bearing specimen, the triangular wave was used, while for the LHDR bearing specimen, the sinusoidal wave was used.

3.3.2 Cyclic behavior of elastomeric bearings

The shear stress-strain relationship of HDR bearing specimen under cyclic loading (CL-2nd, the loading pattern is shown in Fig. 3.5) at ambient temperatures of −20°C, 0°C, and 23°C is shown in Fig. 3.7. The reason to choose the CL-2nd into analysis is that the loading interval

between two strain amplitudes is considered in this loading. The cyclic loading data is used for parameter identification for the numerical model, which is also considered the cooling period. It can be found that the stress and the covered area increased as the decrease of the temperature. Moreover, due to the effect of initial loading, the stiffness of the first cycle of each strain amplitude is high, which is larger than that of the next strain level. The obvious decrease between the stiffness of the first cycle and other cycles of each strain amplitude can also be found due to the scragging and Mullins effect.

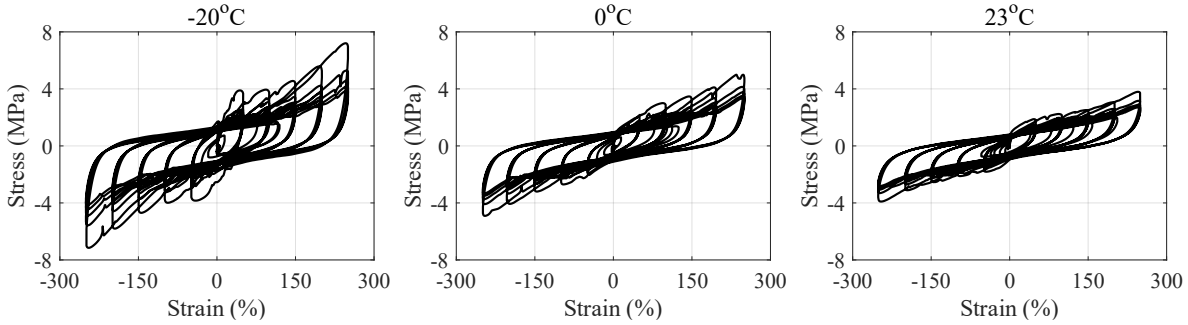

Figure 3.7 Shear stress-strain relationship of HDR bearing specimen (CL-2nd).

The equivalent shear modulus and damping ratio of the HDR bearing specimen are shown in Fig. 3.8. The equivalent shear modulus is defined as

$$G_e = \frac{t_r}{A_r} \cdot \frac{|f_{max}| + |f_{min}|}{|d_{max}| + |d_{min}|} \tag{3.1}$$

where t_r is the total thickness of the HDR lay; A_r is the cross-sectional area of the bearing; f_{max} and f_{min} are the maximum and minimum forces of the loading; d_{max} and d_{min} are the maximum and minimum displacements of the loading.

The equivalent damping ratio is defined as

$$h_{eq} = \frac{E}{4\pi W} \tag{3.2}$$

where E is the dissipated energy per cycle, calculated by the area of the force-displacement loop; W is the elastic strain energy, shown in Fig 3.8b.

The values of the first and fifth cycles at three ambient temperatures were compared. The equivalent shear modulus and damping ratio in the first cycle of each strain amplitude were usually higher than those in the fifth cycle. Additionally, the equivalent shear modulus and damping ratio tended to decrease as the strain amplitude increased.

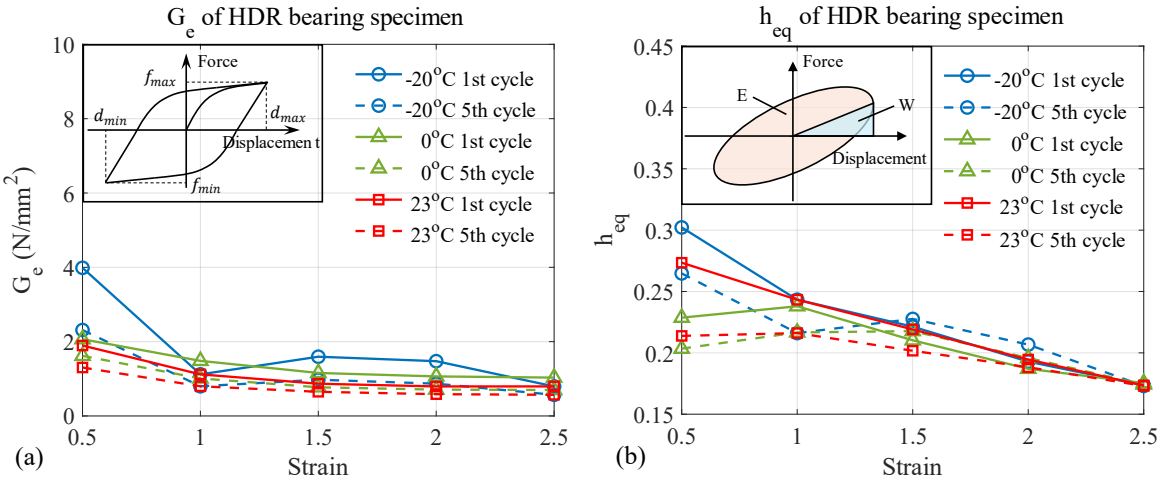

Figure 3.8 Equivalent shear modulus and damping ratio of HDR bearing specimen (CL-2nd).

The shear stress-strain relationship of the LHDR bearing specimen under cyclic loading (CL-2nd, with the loading pattern shown in Fig. 3.6) at three ambient temperatures is shown in Fig. 3.9. Similar results are observed in LHDR bearing specimens compared to HDR bearing specimens. The stress and the covered area of the loop increase as the temperature decreases. Obvious stiffness degradation is present at each strain amplitude. However, the initial loading effect is eliminated in this loading.

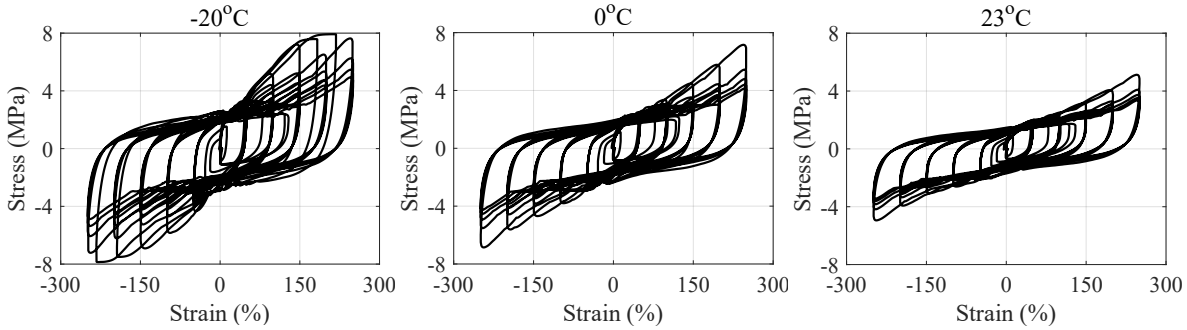

Figure 3.9 Shear stress-strain relationship of LHDR bearing specimen (CL-2nd).

The equivalent shear modulus and damping ratio of the LHDR bearing specimen are shown in Fig. 3.10. Similar to the HDR bearing specimen, the equivalent shear modulus decreases with increasing temperature and loading cycles at each strain amplitude. However, the pattern in the equivalent damping ratio is not as obvious.

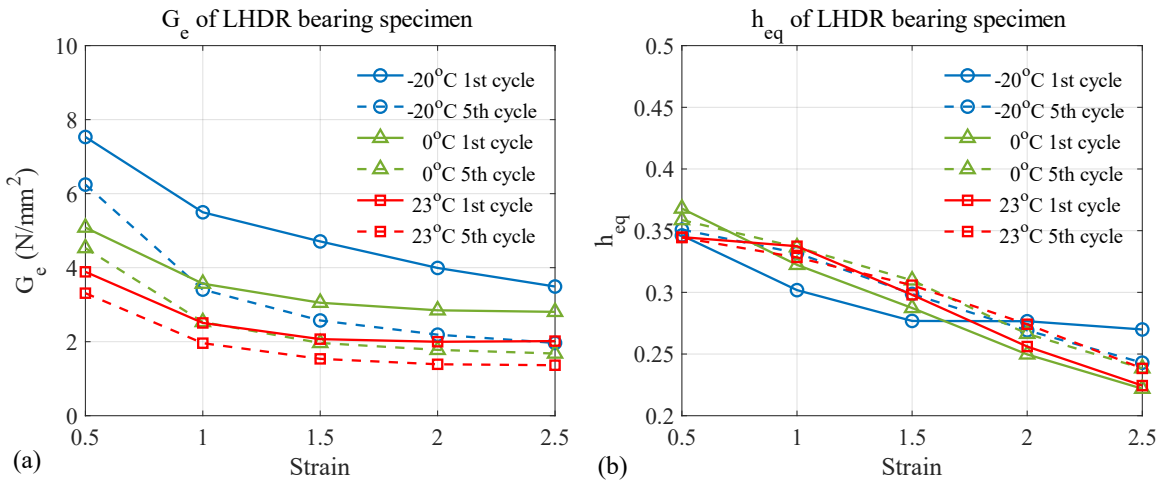

Figure 3.10 Equivalent shear modulus and damping ratio of LHDR bearing specimen (CL-2nd).

3.3.3 Temperature distribution

The layout of thermocouples and the temperature history of the HDR bearing specimen are shown in Fig. 3.11. The temperature history of the thermocouples in the first and third HDR layers at the same position is compared. A temperature difference between the first and third HDR layers is observed, with the temperature in the third layer usually being higher than that of the first layer due to heat accumulation. Additionally, as the ambient temperature decreases, the temperature increment for each strain amplitude rises.

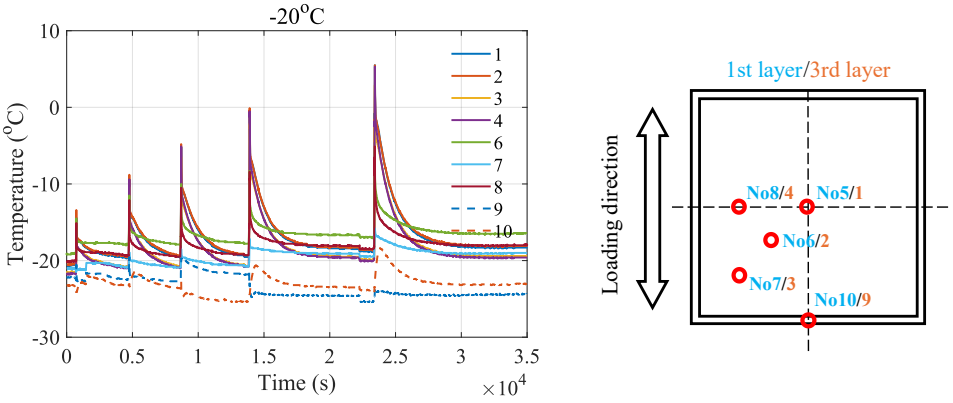

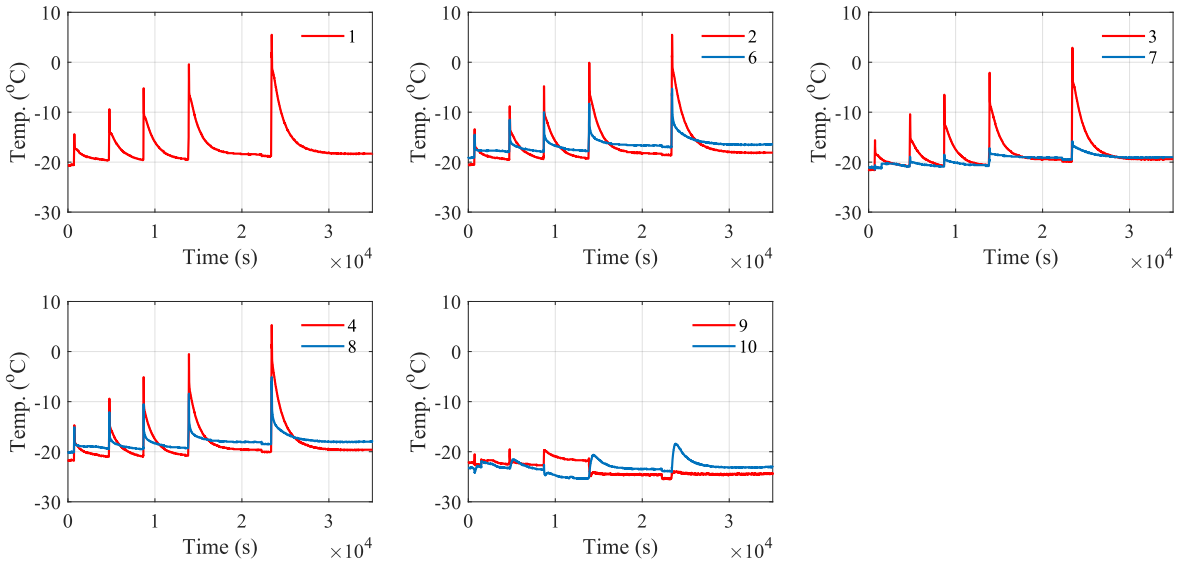
Temp. (°C)
Time (s)
×10^4
1
2
6
3
7
4
8
9
10

(a) −20°C

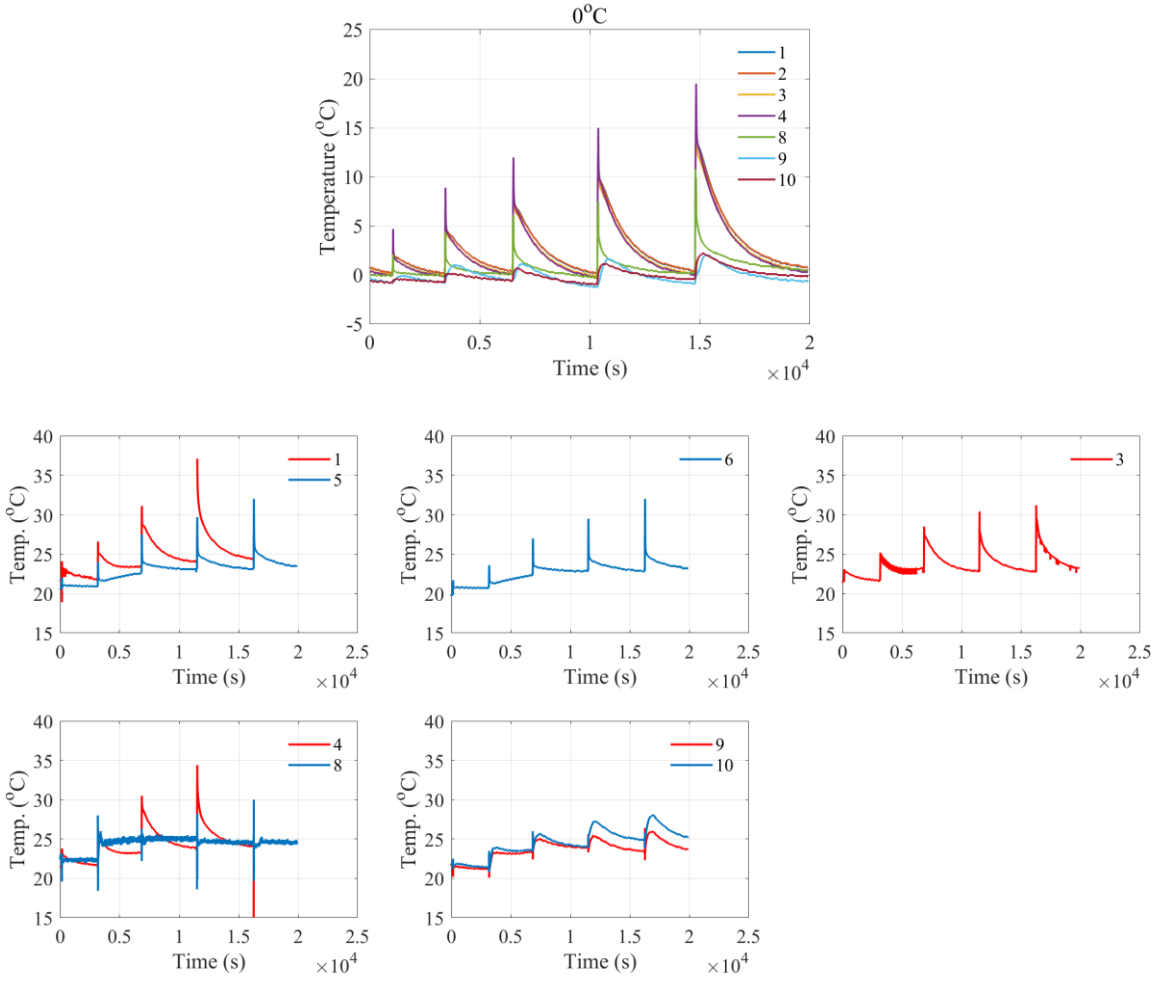
0°C
Temperature (°C)
Temp. (°C)
Time (s)
×10^4
1
2
3
4
8
9
10
5
6

(b) 0°C

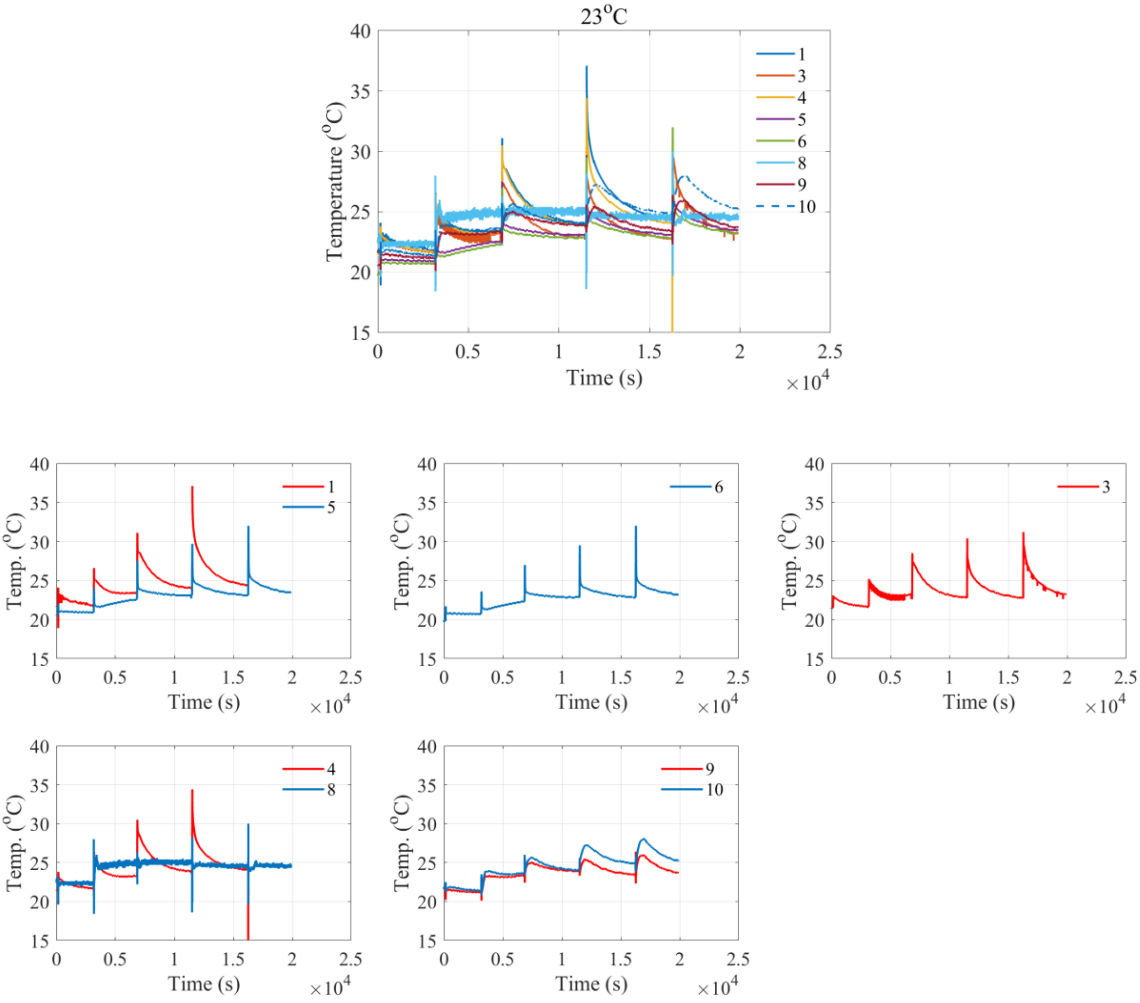

(c) 23℃

Figure 3.11 Measured temperature of HDR bearing specimen (CL-2nd).

The layout of thermocouples and the temperature history of the LHDR bearing specimen are shown in Fig. 3.12. The significant difference between HDR bearings and LHDR bearings is the temperature of the lead cores. In LHDR bearings, the temperature of the lead core exhibits a rapid increase during loading and then a decrease during cooling due to larger thermal conductivity. The temperature increment of the lead core is much higher than that of the HDR bearing because of the smaller specific heat. Other aspects are similar to the HDR bearings.

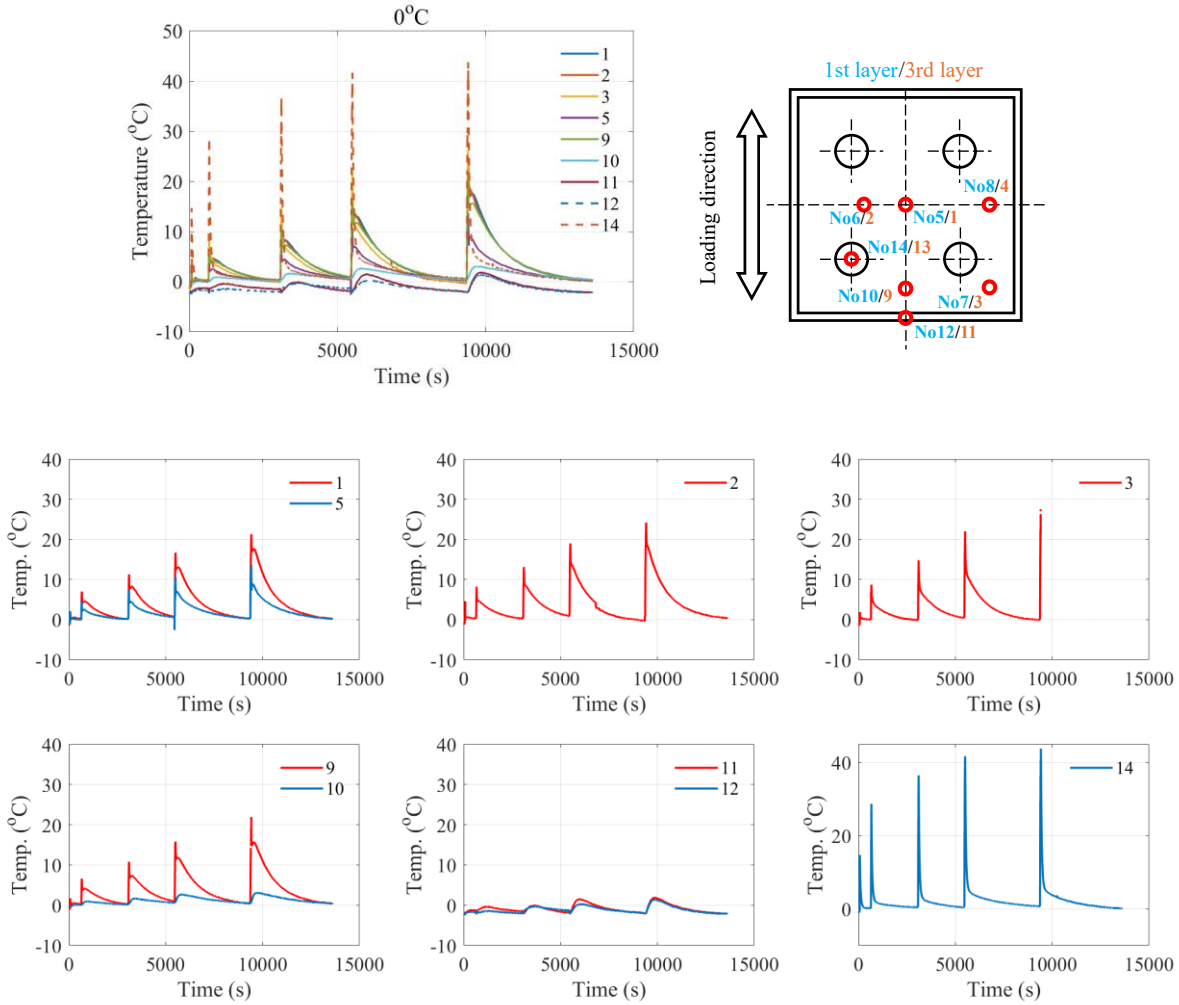
0°C
Temperature (°C)
Time (s)
1
2
3
5
9
10
11
12
14
1st layer/3rd layer
Loading direction
No8/4
No6/2
No5/1
No14/13
No10/9
No7/3
No12/11
Temp. (°C)
Time (s)

(a) 0°C

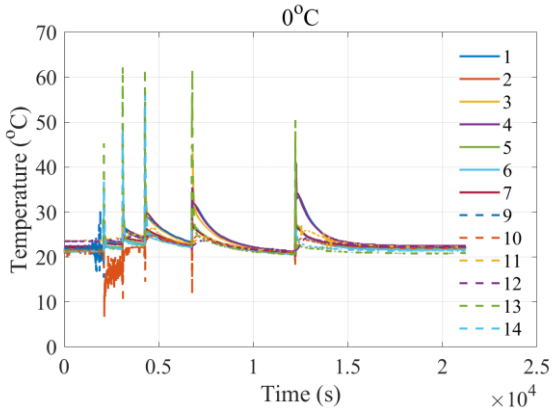
0°C
Temperature (°C)
Time (s)
×10^4
1
2
3
4
5
6
7
9
10
11
12
13
14

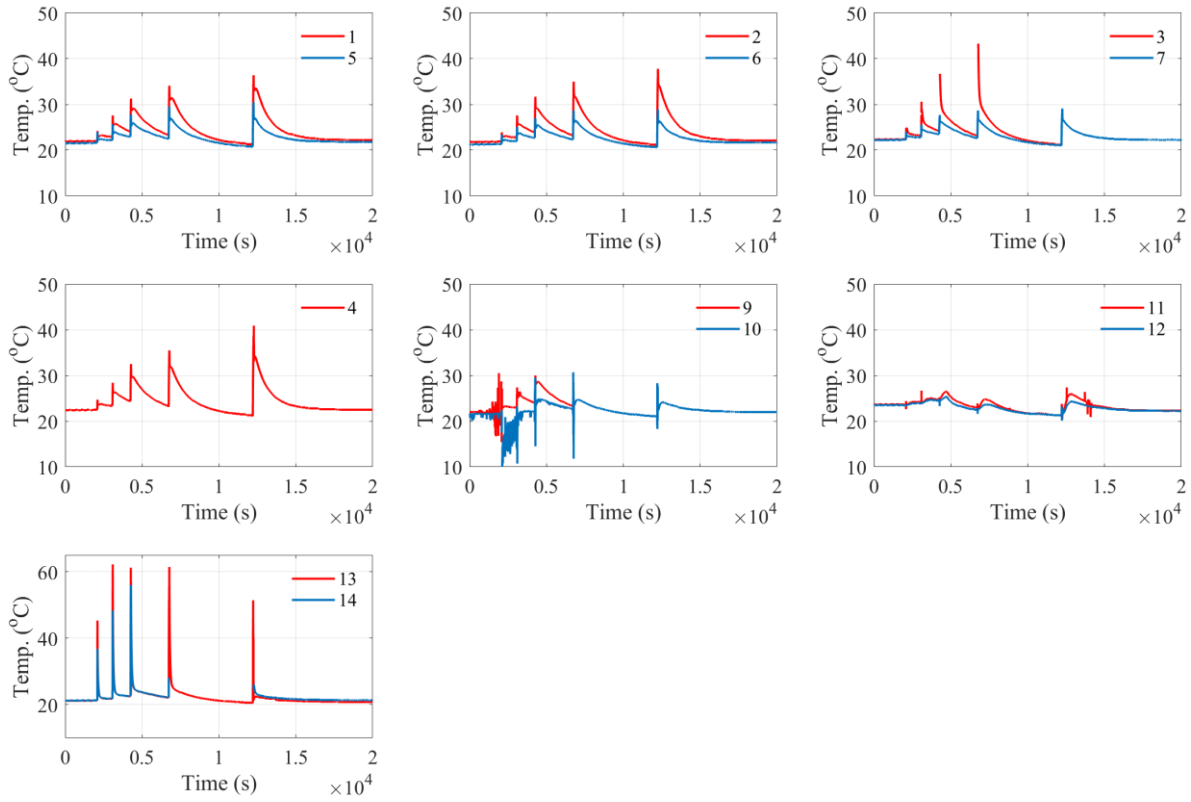

(b) 23℃

Figure 3.12 Measured temperature of LHDR bearing specimen (CL-2nd).

3.4 Hybrid Simulation Test

3.4.1 Framework of hybrid simulation test

Hybrid simulation provides a cost-effective way to conduct irregular loading tests for model validation. Fig. 3.13 shows the framework of the hybrid simulation test. A hypothetical 3-span continuous girder bridge model (as shown in Fig. 3.13a) with eight LHDR bearings was simplified to a 2-DOF pier model (as shown in Fig. 3.13b) with two bearings. Table 3.5 lists the main parameters of the model. The hybrid simulation system was a combination of the experimental test and numerical model simulation, as shown in as shown in Fig. 3.13c. The experimental part involved the scaled HDR or LHDR bearing and the superstructure of the bridge. Note that the prototype of the bearing had a cross-section of 1440 mm × 1440 mm and a total rubber thickness of 180 mm. In the numerical part, the ground motion was input into the numerical model. The structural response analysis of the model was conducted in digital signal processing (DSP). The signal was collected by the load control computer and converted into the loading instructions of the actuators through the control panel. The restoring force and displacement were measured by another computer. The temperature inside the bearing was measured by the thermocouples and recorded by the temperature logger.

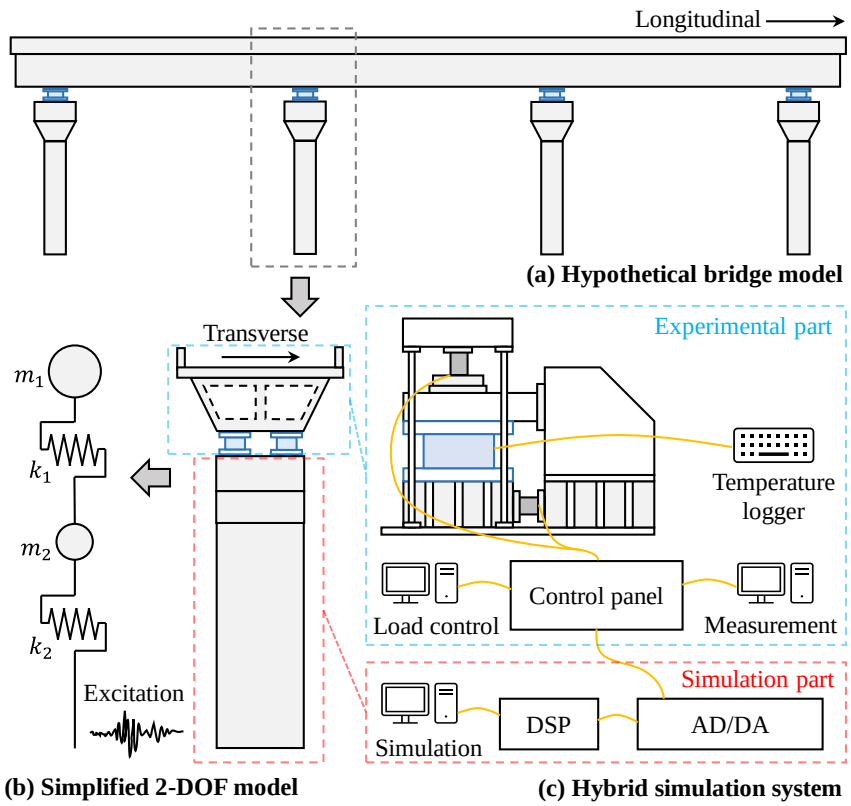

Figure 3.13 Framework of hybrid simulation test.

Table 3.5 Parameters of the 2-DOF bridge model.

Parameter	Specification
m_1, mass of superstructure (t)	10156
m_2, mass of pier (t)	3385
k_1, initial stiffness of bearing (kN/mm)	376
k_2, stiffness of pier (kN/mm)	400
ξ, damping ratio	0.05
T, natural period (s)	1.30

The motion equation of the structural model can be expressed as

$$[M]\{a\} + [C]\{v\} + [K]\{d\} = [M]\{a_g\} \tag{3.3}$$

where $[M]$, $[C]$ and $[K]$ were the matrices of the structural mass, damping, and stiffness; $\{a\}$, $\{v\}$ and $\{d\}$ were the acceleration, velocity and displacement vectors of structure; $\{a_g\}$ was the acceleration of ground.

The motion equation of the system in increment form at time step $n+1$ can be expressed as

$$[M]\{\Delta a_{n+1}\} + [C]\{\Delta v_{n+1}\} + [K]\{\Delta d_{n+1}\} = [M]\{\Delta a_{g,n+1}\} \tag{3.4}$$

where

$$\{\Delta a_{n+1}\} = \{a_{n+1}\} - \{a_n\} \tag{3.5}$$

$$\{\Delta v_{n+1}\} = \{v_{n+1}\} - \{v_n\} = \{a_n\}\Delta t + \frac{1}{2}\{\Delta a_{n+1}\}\Delta t \tag{3.6}$$

$$\{\Delta d_{n+1}\} = \{d_{n+1}\} - \{d_n\} = \{v_n\}\Delta t + \frac{1}{2}\{\Delta a_n\}\Delta t^2 + \beta\{\Delta a_{n+1}\}\Delta t^2 \tag{3.7}$$

Take Eqs. (3.5)–(3.7) into Eq. (3.4), it can be written as

$$[\widehat{M}]\{\Delta a_{n+1}\} = [M]\{\Delta a_{g,n+1}\} - [A_a]\{a_n\} - [A_v]\{v_n\} = [\Delta \widehat{F}] \tag{3.8}$$

where

$$[\widehat{M}] = [M] + \frac{1}{2}[C]\Delta t + \beta[K]\Delta t^2 \tag{3.9}$$

$$[A_a] = [C]\Delta t + \frac{1}{2}[K]\Delta t^2 \tag{3.10}$$

$$[A_v] = [K]\Delta t \tag{3.11}$$

The predicted acceleration increment of the structure was

$$\{\Delta a_{p,n+1}\} = [\widehat{M}]^{-1}[\Delta \widehat{F_p}] \tag{3.12}$$

The predicted vertical and displacement increments $\{\Delta v_{p,n+1}\}$ and $\{\Delta d_{p,n+1}\}$ can be determined according to the Eqs. (3.6) and (3.7). However, the predicted values were still the linear approximations and needed to be corrected for the following step analysis. Thus, the $[K]\{\Delta d_{n+1}\}$ in Eq. (3.4) was replaced by the actual $\{\Delta f_{n+1}\}$. The motion equation can be expressed as

$$[M]\{\Delta a_{n+1}\} + [C]\{\Delta v_{n+1}\} + [K]\{\Delta d_{n+1}\} + (\{\Delta f_{n+1}\} - [K]\{\Delta d_{n+1}\}) = [M]\{\Delta a_{g,n+1}\} \tag{3.13}$$

The corrected force $\{\Delta f_c\} = \{\Delta f_{n+1}\} - [K]\{\Delta d_{p,n+1}\}$, the corrected acceleration increment $\{\Delta a_{c,n+1}\} = [\widehat{M}]^{-1}\{\Delta f_c\}$. The actual acceleration can be calculated as

$$\{\Delta a_{n+1}\} = [\widehat{M}]^{-1}[\Delta \widehat{F_p}] - [\widehat{M}]^{-1}\{\Delta f_c\} = \{\Delta a_{p,n+1}\} - \{\Delta a_{c,n+1}\} \tag{3.14}$$

The vectors of velocity and displacement $\{\Delta v_{n+1}\}$ and $\{\Delta d_{n+1}\}$ can be calculated as

$$\{\Delta v_{n+1}\} = \{\Delta v_{p,n+1}\} + \frac{1}{2}\{\Delta v_{c,n+1}\}\Delta t \tag{3.15}$$

$$\{\Delta d_{n+1}\} = \{\Delta d_{p,n+1}\} + \beta\{\Delta d_{c,n+1}\}\Delta t^2 \tag{3.16}$$

After the correction, the computational accuracy of hybrid simulation can be ensured.

Considering the similitude requirement for the scaled bearing model, the measured restoring forces and displacements of the HDR bearing in the experimental part were used as input for the analytical part. Table 3.6 lists the similitude law for the hybrid simulation, which is based on the scale factor, s, and the same strain rate between the scaled-size and the full-size bearings. It was important to note that, in order to consider the sensitivity of HDR bearing to the strain rate, the scale of time was taken as 1 in the real-time hybrid simulation, and the corresponding strain rate was also 1.

Table 3.6 Similitude law for hybrid simulation.

Physical quantity	Dimension	Scale factor
		Pseudo dynamic loading
Length	L	s
Time	T	s
Mass	M	s^3
Strain rate	T^{-1}	s^{-1}
Displacement	L	s
Velocity	LT^{-1}	1
Acceleration	LT^{-2}	s^{-1}
Force	MLT^{-2}	s^2

Generally, due to the time delay of the hydraulic loading, control, and calculation systems, it would be necessary to conduct compensation to the control algorithm. However, based on the following reasons, the real-time hybrid simulation in this paper ignored the error caused by the time delay.

1. The HDR specimens were used as the physical loading part of the structure model which was accompanied by high hysteresis damping during the loading. Thus, the effect of delay as negative damping was not easy to occur during this experimental setting[35].
2. The target structure was an isolated structure with a relatively longer period (depending on amplitude but generally over one second), thus high-frequency components were trended to be filtered by the structure response to the earthquake input.
3. Due to the effectiveness of the isolation system in the structure, the response velocity was relatively low. Thus, the loading speed was also scaled to a lower speed due to the similarity rule used in this test.

In this kind of experiment conditions, the effect of time delay was considerably small. The seismic response measured after the real-time hybrid simulation was also compared with pseudo-dynamic loading within the reasonable response range and without unstable effects.

3.4.2 Input ground motion

The input ground motion, as shown in Fig. 3.14, was the Level-2, Type II, Ground-type II, Accelerogram 1 (II-II-1), specified in the Design Specification of Highway Bridges (JRA 2019). The Newmark-beta integration scheme ($\beta = 1/6$) was adopted to obtain the displacement response of the superstructure under the ground motion. The experiment involved two different loading rates: a constant rate of 10 mm/s and a real-time rate, as shown in Fig. 3.15. A constant

rate, or pseudo-dynamic (PD) hybrid simulation, was performed to prevent the maximum force of the bearing from exceeding the loading capacity of the testing device, caused by stiffness hardening. A real-time (RT) hybrid simulation was conducted to investigate the actual seismic response of the bearing.

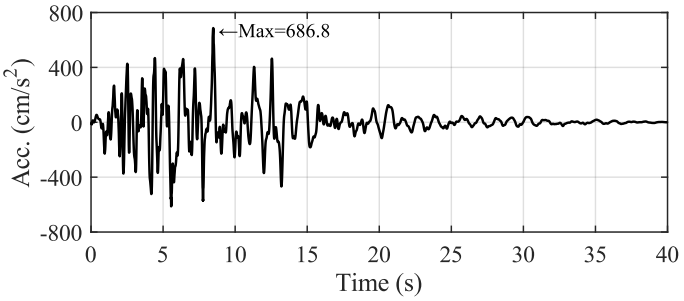

Figure 3.14 Input ground motion.

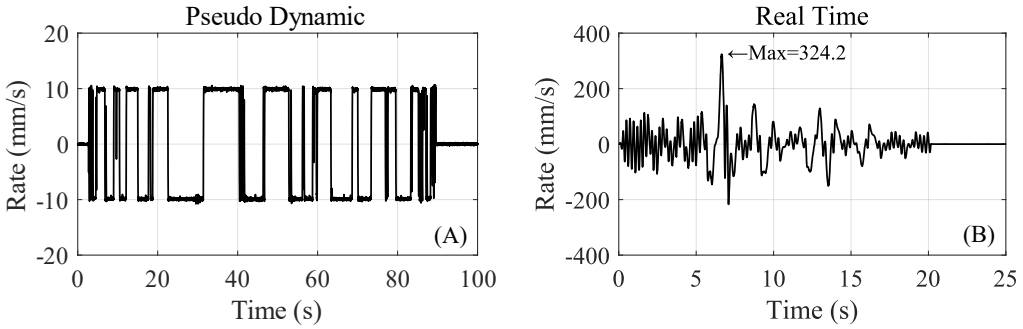

Figure 3.15 Rate of (A) pseudo-dynamic and (B) real-time hybrid simulations.

3.4.3 Hysteretic behavior of elastomeric bearings

The hysteresis curves of HDR bearing specimens under the first and second pseudo-dynamic and real-time hybrid simulations are compared in Fig. 3.16. The corresponding shear strain comparison is shown in Fig. 3.17. The stress and the covered area of the loop increase as the ambient temperature decreases, similar to the behavior observed in cyclic loading. At −20°C and 0°C, the stress of the pseudo-dynamic hybrid simulation presents higher stress than that of the real-time hybrid simulation. At 0°C, the stress of 2nd pseudo-dynamic hybrid simulation is reduced compared to the 1st test, while this reduction is not noticeable at the other two temperatures.

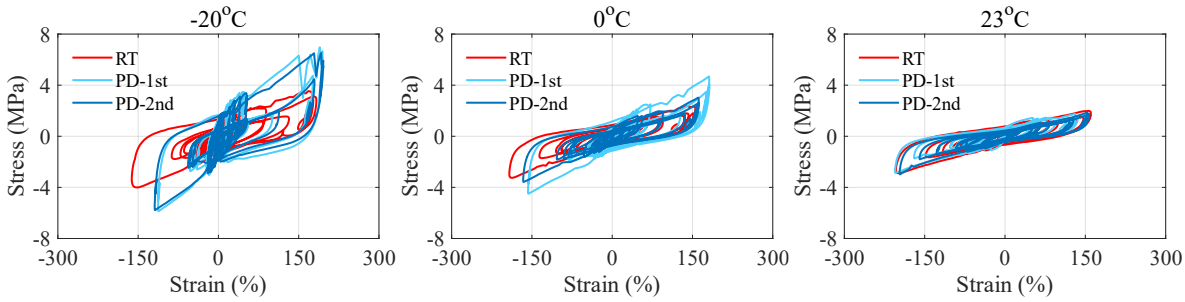

Figure 3.16 Hysteresis curves comparison of pseudo-dynamic and real-time hybrid simulation tests of HDR bearing specimen.

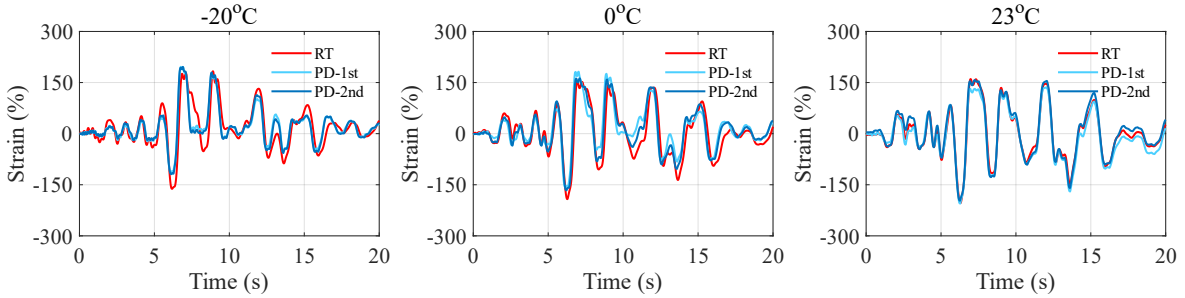

Figure 3.17 Shear strain comparison of pseudo-dynamic and real-time hybrid simulation tests of HDR bearing specimen.

The hysteresis curves of HDR bearing specimens under pseudo-dynamic and 1st and 2nd real-time hybrid simulation tests are compared in Fig. 3.18. The corresponding shear strain comparison is shown in Fig. 3.19. The significant difference between LHDR bearing and HDR bearing is that the stress of LHDR in real-time hybrid simulation is larger than that of the pseudo-dynamic hybrid simulation. The stress decrement between 1st and 2nd real-time hybrid simulation tests is also obvious.

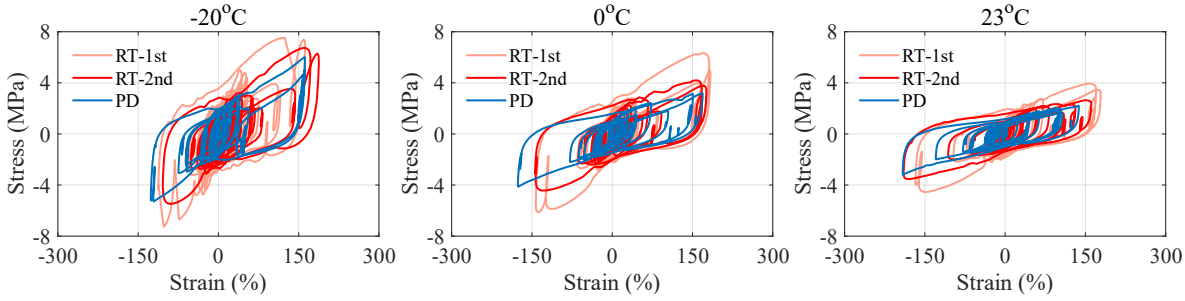

Figure 3.18 Hysteresis curves comparison of pseudo-dynamic and real-time hybrid simulation tests of LHDR bearing specimen.

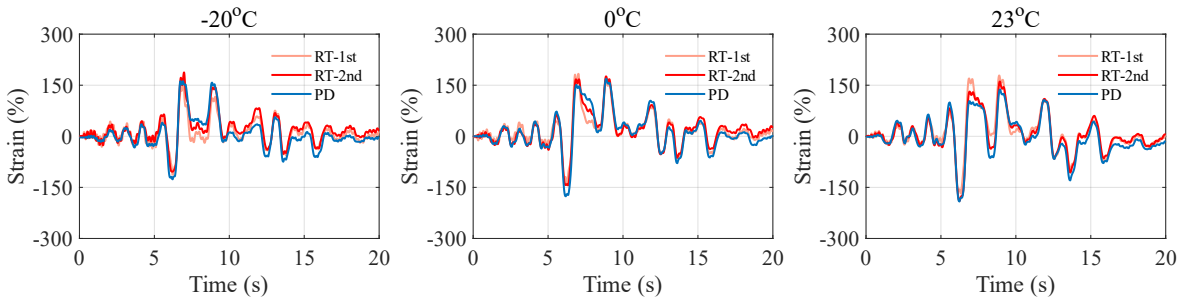

Figure 3.19 Shear strain comparison of pseudo-dynamic and real-time hybrid simulation tests of HDR bearing specimen.

3.4.4 Temperature history of elastomeric bearings

The temperature history of HDR bearing specimens under pseudo-dynamic and real-time hybrid simulation tests are shown in Figs. 3.20 and 3.21. The temperature increment of the HDR layer in real-time hybrid simulations is a little bit higher than that of the pseudo-dynamic hybrid simulations, owing to the different times of heat dissipation.

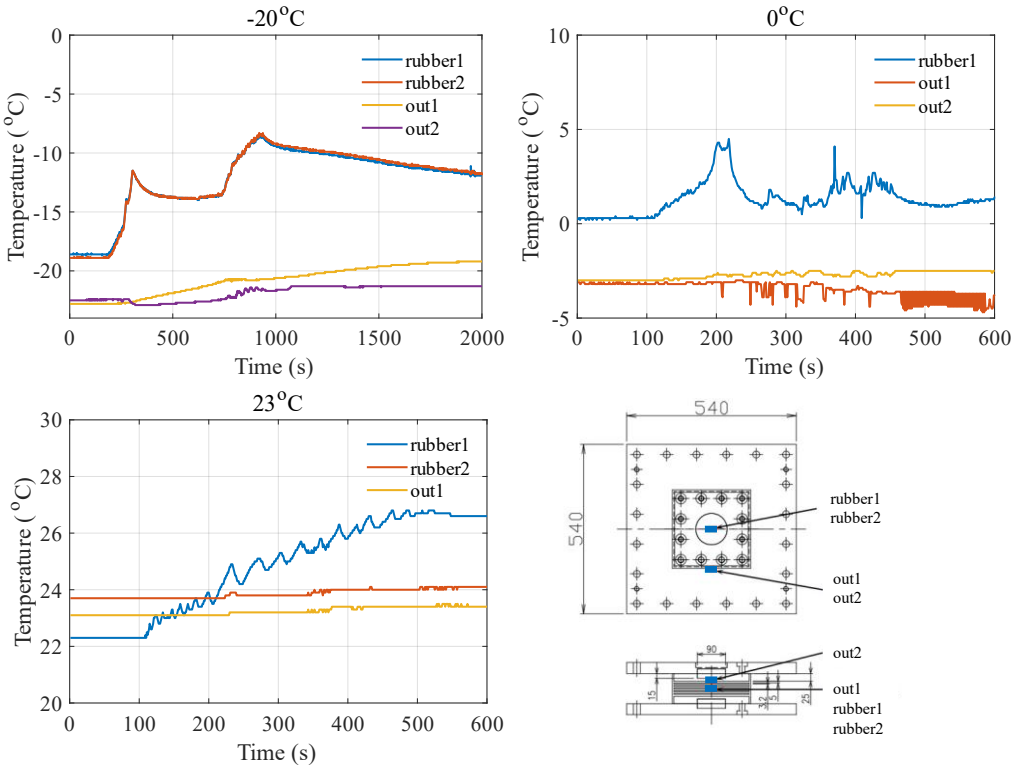

Figure 3.20 Measured temperature of HDR bearing specimen in 2nd pseudo-dynamic hybrid simulation test (HS-PD-2nd).

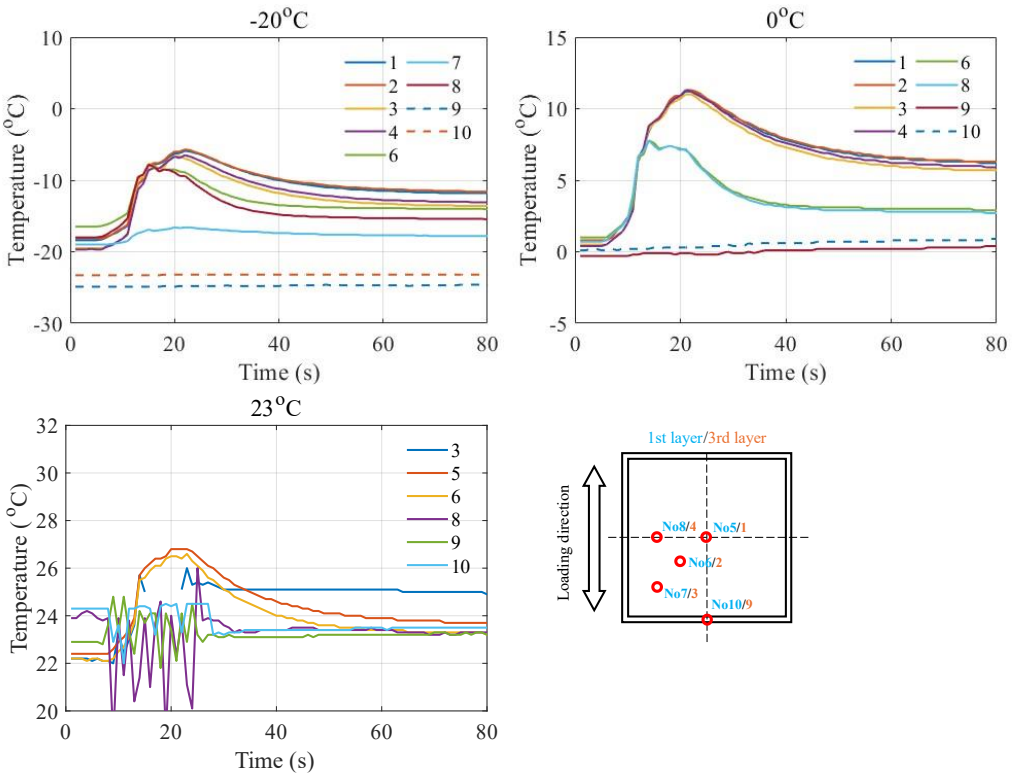

Figure 3.21 Measured temperature of HDR bearing specimen in real-time hybrid simulation test (HS-RT).

The temperature history of LHDR bearing specimens under pseudo-dynamic and real-time hybrid simulation tests are shown in Figs. 3.22 and 3.23. The temperature increment of the HDR layer is similar to the HDR bearing specimen. Moreover, the difference in temperature increment of lead cores is significant between real-time and pseudo-dynamic hybrid simulation tests.

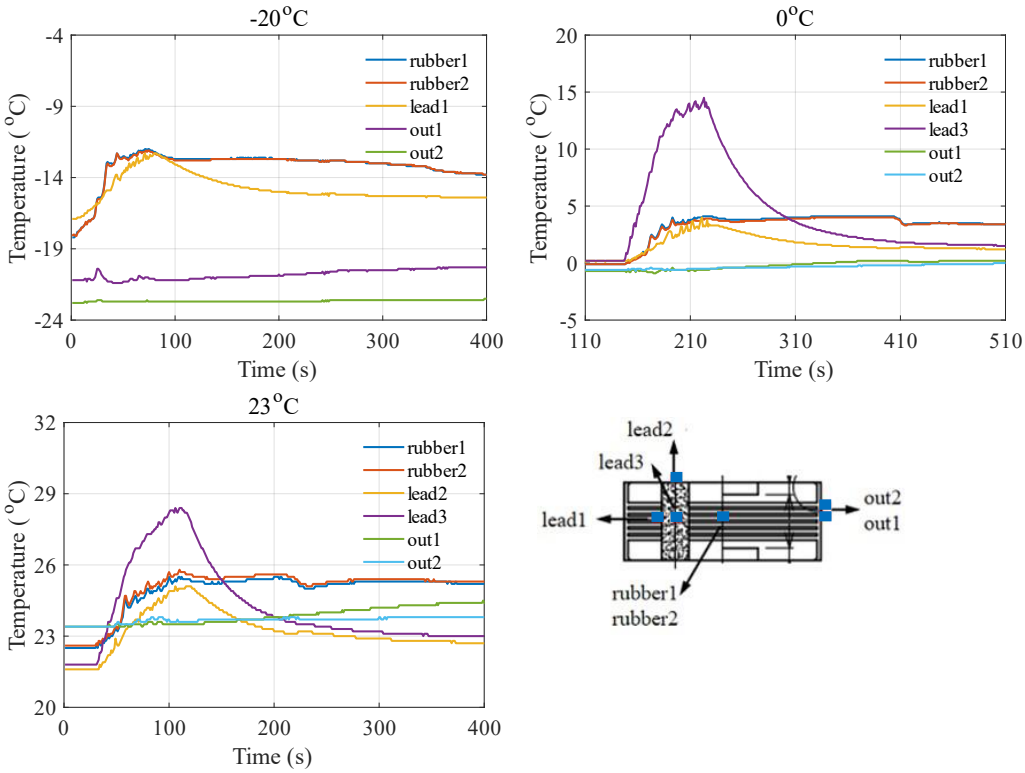

Figure 3.22 Measured temperature of LHDR bearing specimen in pseudo-dynamic hybrid simulation test (HS-PD).

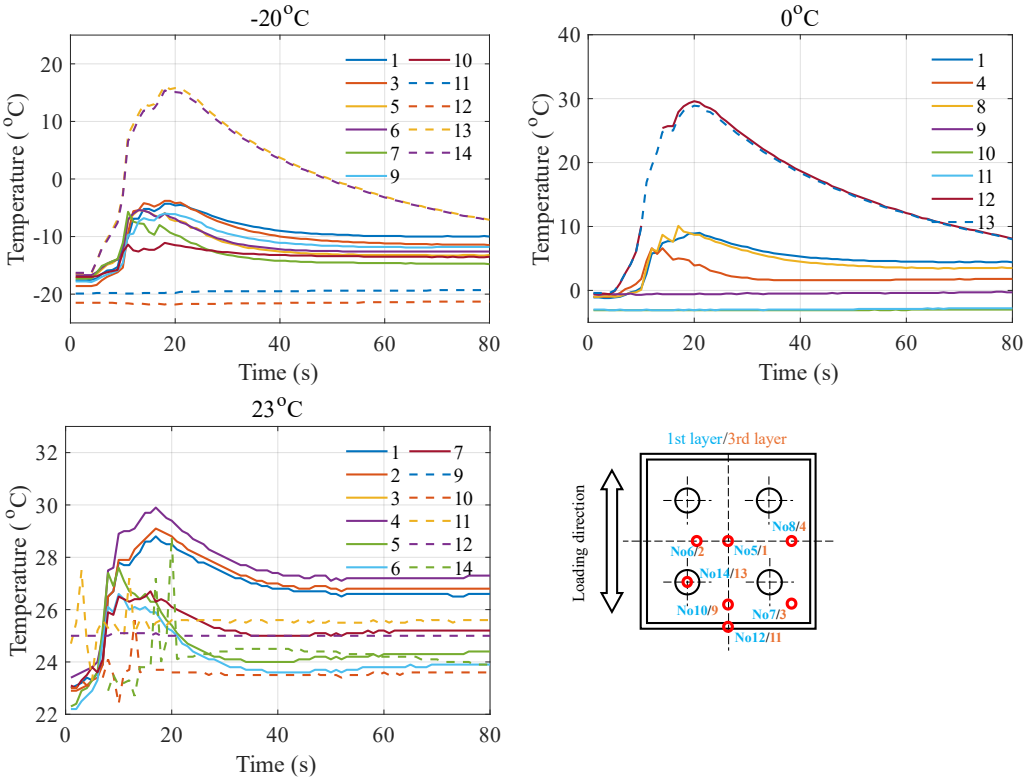

Figure 3.23 Measured temperature of HDR bearing specimen in 2nd real-time hybrid

simulation test (HS-RT-2nd).

Fig. 3.24 shows a three-dimensional temperature distribution of LHDR bearing under real-time hybrid simulation (HS-RT-2nd) at −20℃. In Fig. 3.24a, the temperature difference between 1st and 3rd rubber layers can be observed during the hybrid simulation. It was interesting to note that the initial stiffness of the bearing increased with decreasing ambient temperature, while the stiffness decreased with the rise of internal temperature during loading. The decreased stiffness owing to the heating effect seemed to be beneficial to the effectiveness of the isolation system. However, for pulse-like ground motions, the internal temperature of the bearing did not show a significant rise when the seismic acceleration reached the peak. In fact, even when the ground motion ended, the internal temperature may still not reach room temperature. The low-temperature effect still dominated, resulting in a relatively high stiffness of the bearing. For instance, Fig. 3.24b depicts the temperature distribution of 1st rubber layer of the specimen under real-time loading at −20℃ according to the recorded temperature data. The maximum acceleration of ground motion was at the 8-second. The temperature of the rubber was near −15℃ and −5℃ at the 5-second and 10-second, while it was still below 0℃ after 20 seconds, which is far below the room temperature. Additionally, the scale effect also affected the heat conduction within the bearing. In general, the low temperature had a significant impact on the hysteretic behavior of the bearing, even the heating effect was considered.

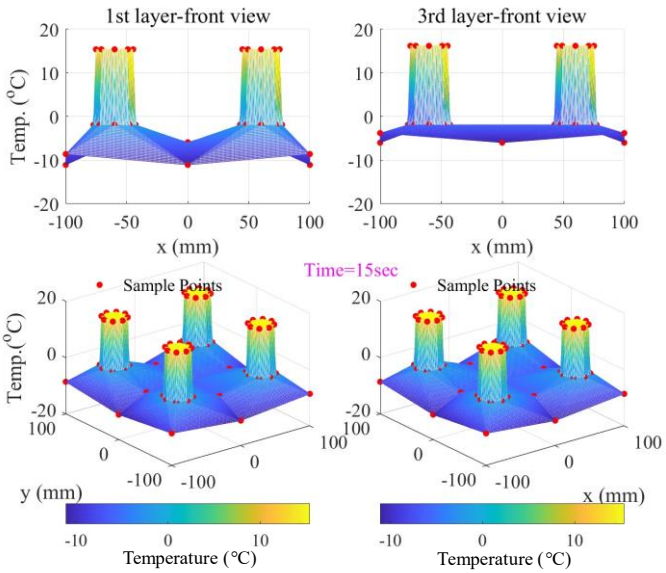

(a) Temperature distribution of 1st and 3rd rubber layers at the 15th second.

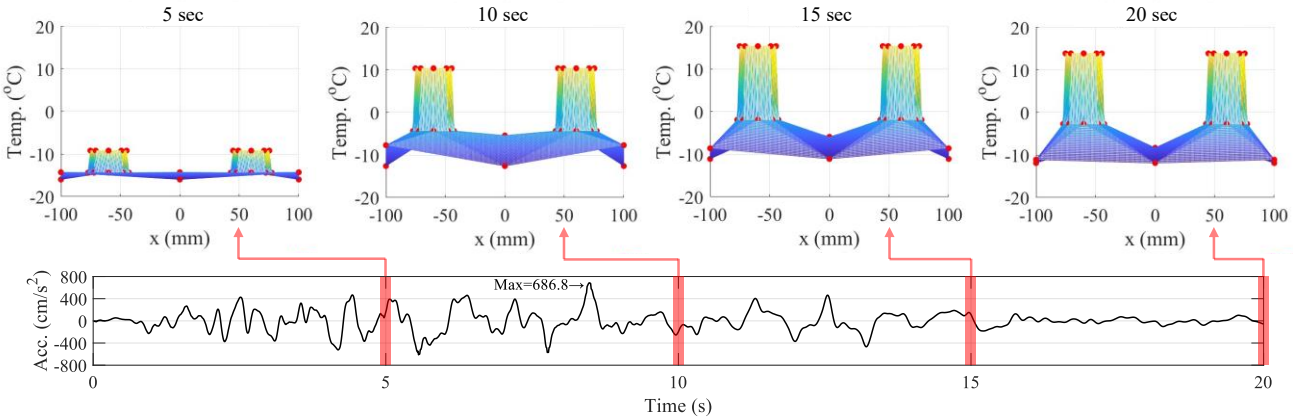

(b) Temperature distribution of 1st rubber layer at 5th, 10th,15th, and 20th seconds.

Figure 3.24 Temperature distribution of LHDR bearing under real-time hybrid simulation (HS-RT-2nd) at −20°C.

3.4.5 Energy dissipation elastomeric bearings

The energy dissipation of HDR bearing and LHDR bearing specimens is shown in Fig. 3.24. Note that the effect of initial loading is eliminated. As the ambient temperature decreases, the dissipated energy increases due to higher stress. The energy dissipation capacity of the LHDR bearing is approximately twice that of the HDR bearing because of the addition of the lead cores. This indicates that the LHDR bearing has better energy dissipation capacity with the same size. The accumulated dissipated energy in pseudo-dynamic hybrid simulation is usually lower than in the corresponding real-time hybrid simulation test. However, the test of the HDR bearing at −20°C is different.

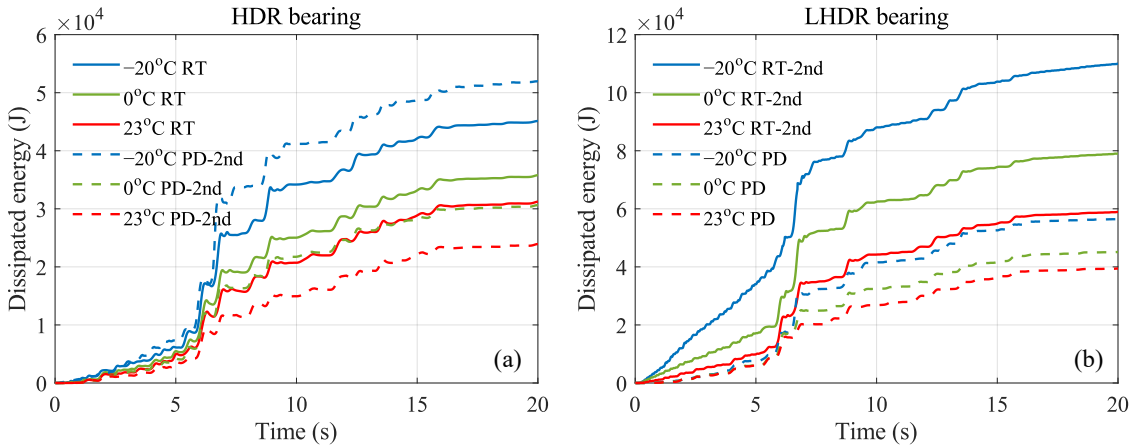

Figure 3.25 Energy dissipation of bearing specimens in real-time and pseudo-dynamic hybrid simulation tests: (a) HDR bearing; (b) LHDR bearing.

3.4.6 Structural response

The pier top displacement and acceleration of the bridge model with HDR bearings under

pseudo-dynamic and real-time hybrid simulation tests are shown in Figs. 3.25 and 3.26. The displacement and acceleration responses tend to be higher with the decrease in ambient temperature. No significant difference in response is found between pseudo-dynamic and real-time hybrid simulation tests.

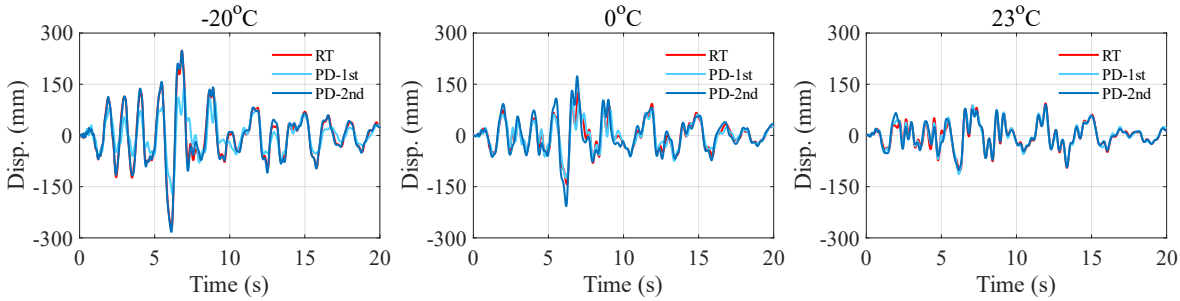

Figure 3.26 Pier top displacement comparison of bridge model with HDR bearing under pseudo-dynamic and real-time hybrid simulation tests.

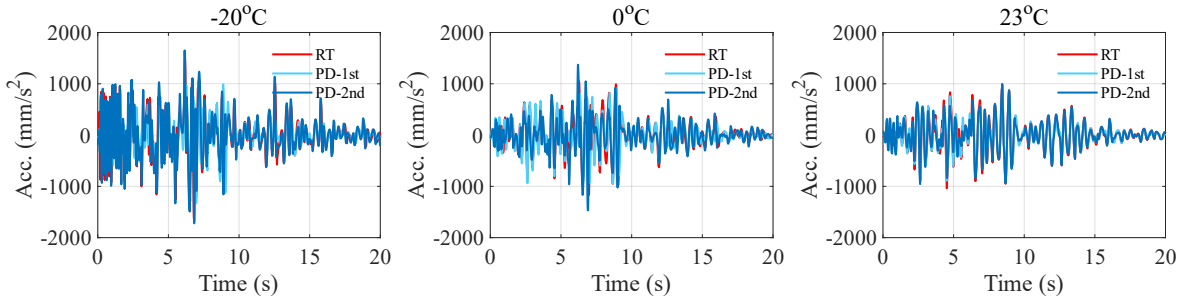

Figure 3.27 Pier acceleration comparison of bridge model with HDR bearing under pseudo-dynamic and real-time hybrid simulation tests.

The pier top displacement and acceleration under pseudo-dynamic and real-time hybrid simulation tests are shown in Figs. 3.27 and 3.28. Similarly, the response of displacement and acceleration increases as the decrease of ambient temperature. Moreover, the response of real-time hybrid simulation is more intense compared with the pseudo-dynamic hybrid simulation test.

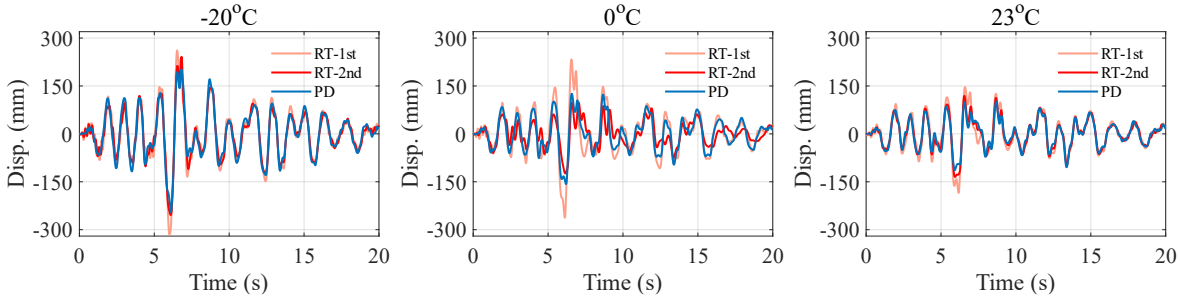

Figure 3.28 Pier top displacement comparison of pseudo-dynamic and real-time hybrid simulation tests of LHDR bearing specimen.

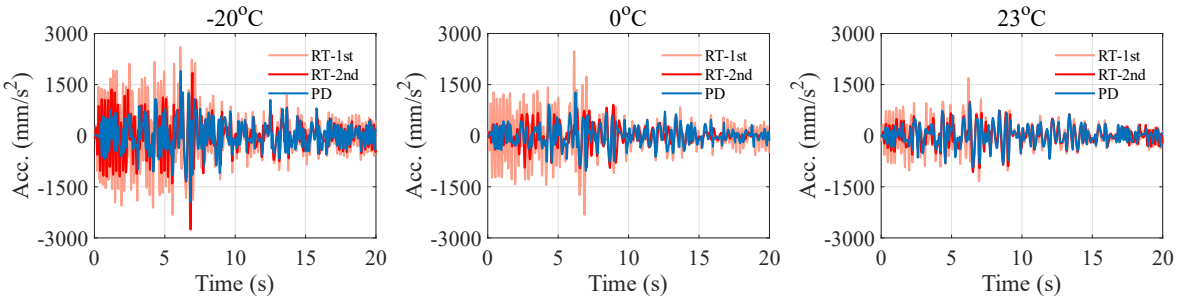

Figure 3.29 Pier top acceleration comparison of pseudo-dynamic and real-time hybrid simulation tests of LHDR bearing specimen.

3.5 Discussion

In this chapter, the experimental investigations of quasi-static cyclic loading and hybrid simulation tests are conducted to assess the seismic performance of HDR and LHDR bearings at different ambient temperatures. The factors of the initial loading effect and loading interval are considered in the experiment. The shear stress-strain relationship, equivalent shear modulus and damping ratio, and the temperature history are analyzed in cyclic loading. In the hybrid simulation, the hysteresis behavior, temperature history, energy dissipation of bearing, and the response of structure are analyzed under realistic ground motion. Here are the main points to be discussed:

(1) Factors of initial loading effect and loading interval are considered in the test arrangement. In cyclic loading, the loadings with intervals between each strain amplitude are selected for analysis because the thermal mechanism of both the heating and cooling of bearings will be modeled in the next chapters. In the hybrid simulation, the hysteretic behavior of bearings with the elimination of the initial loading effect is analyzed and provided as the validating data for the numerical model in the next chapters.

(2) In cyclic loading, the cyclic behavior of HDR and LHDR bearings shows significant temperature dependence. The shear stress and covered area of the cyclic loading hysteresis curve increase as the ambient temperature decreases. The equivalent shear modulus and damping ratio decrease with the increase of the loading cycle and the decrease of the strain amplitude. They also show a negative correlation with the ambient temperature. The maximum shear stress of the LHDR bearing is higher than that of the HDR bearing at three ambient temperatures due to the addition of the lead cores, indicating an improved energy dissipation capacity.

(3) The numerous thermocouples are settled into the different positions and layers of the HDR and lead cores. In both HDR and LHDR bearings, the temperature in the third HDR layer is higher than that in the first layer due to heat accumulation, which means the temperature difference exists within the bearings. In LHDR bearings, the temperature of the lead core exhibits a rapid increase during the loading and then a decrease during the cooling owing to the larger thermal conductivity. The temperature increment of the lead core is much

higher than that of the HDR owing to the smaller specific. The temperature increment of HDR in the HDR bearing is lower than that of the LHDR bearing, possibly because the heating effect of the lead core influences the heat conduction of the HDR. It indicates the thermal mechanism of the LHDR bearing is different from the HDR bearing.

(4) In hybrid simulation, the loading patterns of pseudo-dynamic and real-time tests are carried out for HDR and LHDR bearings. Similar to the cyclic loading, the hysteresis curves of hybrid simulation show significant temperature dependence. However, the hysteretic behavior of pseudo-dynamic and real-time hybrid simulation is different in HDR and LHDR bearings, especially for the maximum shear stress. In LHDR bearings, the maximum shear stresses of the real-time test at −20℃ and 0℃ are larger than those of the pseudo-dynamic test, while in HDR bearings, the results are opposite. In general, the maximum shear stress increases as the loading rate increases, which is called rate dependence. The cause of stress abnormality in HDR bearings in hybrid simulation remains to be further analyzed by more experimental tests.

(5) The temperature history of HDR and LHDR bearings in hybrid simulation is similar to that in the cyclic loading test. A temperature difference can be observed between the first and third HDR layers. The lead core exhibits a rapid temperature increase during loading and a decrease during cooling. In terms of energy dissipation, specimens in real-time hybrid simulation typically show higher dissipated energy than those in pseudo-dynamic tests, except for the HDR bearing specimen at −20℃. This is because of the larger shear strain in the pseudo-dynamic test mentioned before. LHDR bearings have a better energy dissipation capacity compared to HDR bearings of the same size.

CHAPTER 4

A MULTI-LAYER THERMO-MECHANICAL COUPLING HYSTERETIC MODEL FOR HDR BEARINGS AT LOW TEMPERATURE

Chapter 4 proposes a multi-layer thermo-mechanical coupling hysteretic model for HDR bearings. Based on the experimental investigation of the hysteretic behavior and temperature history of HDR bearing in Chapter 3, the mechanism of thermal conduction and heating effect are modeled and coupled in the hysteretic model of HDR bearing. The hysteretic behavior and temperature history of HDR bearing predicted from the model are validated by the cyclic loading and real-time hybrid simulation test results. Moreover, this model will be used in Chapter 6 to analyze the temperature effect on the seismic performance of isolated bridges.

4.1 General

High damping rubber (HDR) bearing has been proven as an effective device in seismic isolation technology. The high damping property and excellent energy dissipation make it widely applied. However, the temperature sensitivity including temperature dependence and heating effect influences the behavior of HDR bearing, especially in the low-temperature region.

Numerous experimental investigations have shown that the effect of temperature on the seismic performance of HDR bearing cannot be ignored (Cardone et al. 2011; Nguyen et al. 2015; Okui et al. 2019; Yakut and Yura 2002). The experimental research in Chapter 3 confirmed that the behavior of HDR bearing at low temperatures showed a larger restoring force due to the increase of the initial stiffness, which would affect the safety of the structure under earthquake. Moreover, the experiment found that the temperature distribution within the bearing was non-uniform leading to variations in stiffness for each rubber layer and further the ununiform shear deformation profile, as shown in Fig. 4.1. Therefore, the temperature difference in the bearing cannot be ignored.

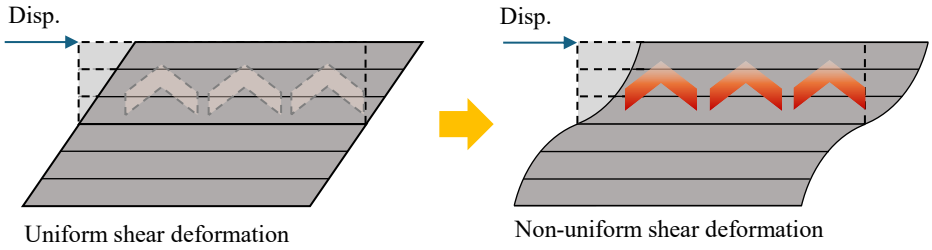

Figure 4.1 Non-uniform shear deformation due to the temperature effect.

Although some current restoring force models have considered the effect of temperature on HDR bearing, the temperature difference within the bearing was not considered. Constantinou et al. (2007) proposed the heating model of elastomeric bearings to involve the heating effect. It provided a pioneering temperature estimation with reasonable assumption to neglect the heat radiation and heat conduction through the end plate of the bearings, which simplified the temperature independent of the space. Tan et al. (2023a) developed a simplified thermo-mechanical coupled hysteretic model including the effect of ambient temperature. This model illustrated the thermal mechanism that influenced the behavior of HDR bearings including the heating effect. However, internal heat transfer is not considered in the model, and it has a limitation in the use of a single temperature value assigned to the entire bearing, even though the internal temperature distribution is non-uniform in reality. Okui et al. (2019) and Miyamura et al. (2021) established finite element (FE) models to investigate the heating effect as well as the heat transfer within the HDR bearing. Although the model can provide highly accurate results, it might be time-consuming. Kalpakidis and Constantinou (2009a) introduced a closed-form solution to predict the temperature of the lead rubber (LR) bearings and establish a relationship between temperature and characteristic strength. This model explained the internal heat transfer mechanism of lead-core rubber bearings. Due to the continuous lead core in the LR bearing, most of the heat was conducted through the lead and steel plate, while the heat conducted through rubber layers can be ignored. However, the heat transfer mechanism of HDR bearing differed from that of LR bearing.

To precisely predict the hysteretic behavior of HDR bearing considering the heating effect, a more applicable model for HDR bearing with a multi-layer thermal mechanism to illustrate the heating effect and heat transfer needs to be introduced (Shen et al. 2024). As generated heat transfers outward, the temperature distribution will be ununiform within the bearing, which leads to variations in stiffness for each rubber layer and further the ununiform shear deformation profile. This condition is different from the general assumption that the shear deformation is linear along the vertical direction of the bearing. The restoring force behavior will be affected due to the irregular shear deformation.

This chapter presents a multi-layer thermo-mechanical coupling model for HDR bearing. The model aims to elucidate the thermal mechanism within a bearing and its influence on the complex hysteretic restoring force behavior. To represent the thermal mechanism in the HDR

bearing with sufficient accuracy, the rubber bearing is divided into multiple layers along the vertical direction, assuming one-dimensional heat conduction and considering heat outflow around the side. The thermal mechanism is illustrated by considering the heat transfer and heating effect in the multi-layer thermal-coupled model. This model considers the non-uniform internal temperature distribution, which causes the variations in shear deformation, different from the assumption of uniformly distributed shear deformation. The restoring force and temperature history of the HDR bearing for cyclic loading condition are computed and compared with the quasi-static tests under cyclic loading at three ambient temperatures of −20℃, 0℃, and 23℃. Finally, the model is validated by experimental data obtained by real-time hybrid simulation under the assumption of application to an isolated bridge model as a presentation of a realistic seismic loading condition.

4.2 Thermal Mechanism within HDR bearings

4.2.1 Physical model

The physical model is shown in Fig. 4.2a. The heat transfer mechanism within the HDR bearing can be treated as the problem of heat conduction through different materials. The variation in temperature within the bearing is related to the increment of thermal energy, including the heat conduction through the bearing, the heat generated in rubber layers, and the heat outflow to the side of the bearing. At boundary 1 (Bd.1) on the top of the steel ending plate, the boundary condition can be the adiabatic state or the constant ambient temperature based on the experimental condition. At boundary 2 (Bd.2) on the surface of symmetry, the boundary condition is the adiabatic state, where the gradient of temperature is zero.

Considering the heat conduction, heat generation, and heat outflow within the HDR bearing, the heat equation can be expressed as

$$\frac{\partial T(x,t)}{\partial t} = \alpha \frac{\partial^2 T(x,t)}{\partial x^2} + \frac{\dot{w}(t)}{c\rho} - \frac{\dot{u}(t)}{c\rho} \tag{4.1}$$

$$\alpha = \frac{k}{c\rho} \tag{4.2}$$

$$w(t) = \int_0^t \sigma(\tau)\dot{\varepsilon}(\tau)d\tau \tag{4.3}$$

$$\dot{u}(t) = \lambda[T(x,t) - T_{\mathrm{A}}] \tag{4.4}$$

where $T(x,t)$ is the temperature of the bearing; α is the thermal diffusivity; k is the thermal conductivity; c is the specific heat; ρ is the density; $\dot{w}(t)$ is the volumetric heat generation rate (heat generation per unit volume per unit time); $\sigma(\tau)$ and $\varepsilon(\tau)$ are shear stress and strain; $\dot{u}(t)$ is the heat loss per unit volume per unit time caused by heat outflow; $\lambda = Ah/V$, where A is the lateral area where heat outflow takes place; h is the convective heat transfer coefficient; T_A is the ambient temperature; V is the volume of the heat outflow part.

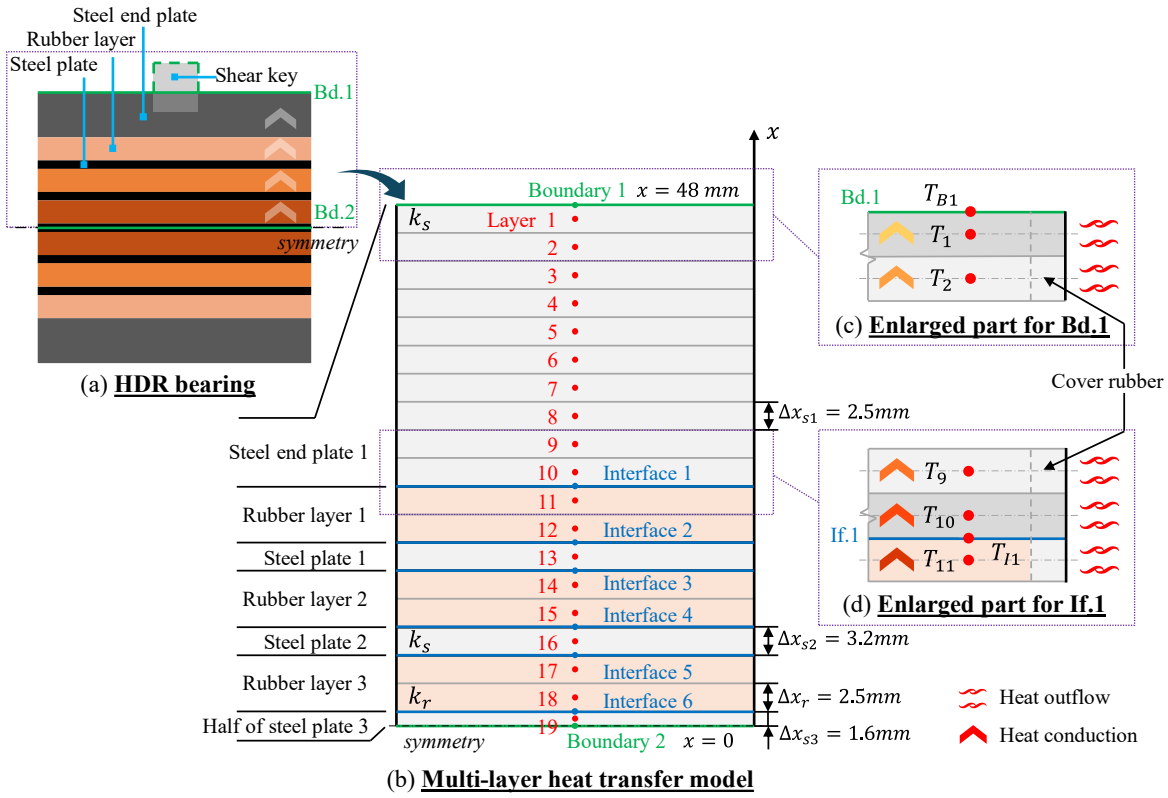

Figure 4.2 A multi-layer heat transfer model for HDR bearing: (a) HDR bearing, (b) multi-layer heat transfer model, (c) enlarged part for Bd.1, (d) enlarged part for If.1.

The boundary condition (see Fig. 4.2b) is given by

$$\begin{cases} \dfrac{\partial T(x,t)}{\partial x} = 0 & x = 0 \\ \dfrac{\partial T(x,t)}{\partial x} = 0 \text{ or } T = T_A & x = 48\ mm \end{cases} \tag{4.5}$$

4.2.2 Basic assumptions

A multi-layer heat transfer model is proposed to illustrate the internal heat transfer mechanism and the heating effect of the HDR bearing. To simplify the model with accuracy and efficiency, the following assumptions are made:

(1) The heat flux is only conducted along the vertical direction of the bearing, while that along the horizontal direction is neglected. This implies that the temperature is uniformly distributed on the horizontal plane.

(2) The heat outflow on the side of the bearing is considered because the high damping rubber and steel are covered by side rubber which is directly in contact with the ambient environment.

(3) The thermal properties (such as thermal conductivity and specific heat) of the materials are assumed to be constant and independent of temperature for the model simplification.

(4) A perfect contact between the rubber and steel layers is assumed, implying that no thermal resistance exists between materials. The temperature on the interface between two materials is assumed to be equal.

(5) The distribution of shear deformation for each rubber layer is uniform. It implies that the generated heat caused by the loading is uniformly distributed for each rubber layer.

(6) Due to the structural symmetry, an identical half of the bearing is chosen in the analysis along the vertical direction. The boundary condition on the symmetry plane can be assumed as the adiabatic state. On the other hand, the boundary condition on the surface outside the steel ending plate can be changed depending on the specific circumstances. For instance, if the bearing is tested under a large testing machine or fixed beneath a steel girder, the boundary condition can be regarded as the constant temperature (equal to the ambient temperature, T_A); if the bearing is fixed with concrete, it can be treated as a heat insulation condition.

4.2.3 Numerical model of heat transfer mechanism

The Crank-Nicolson scheme (1947) is employed to numerically solve the heat equation Eq. (4.1) due to its numerical stability. The detailed conditions of the thermal transfer in the HDR bearing involve (1) internal layers of a single medium, (2) boundary layers of a single medium, and (3) layers within multiple media.

4.2.3.1 Heat transfer within internal layer of single medium

Fig. 4.3 shows the heat transfer mechanism within the internal layer of single medium (e.g. layers 2-9 in Fig. 4.2b). The spatial domain of the heat equation Eq. (4.1) (first term of the right side) can be approximated as

$$\frac{\partial^2 T(x,t)}{\partial x^2} \approx \frac{1}{2(\Delta x)^2}\left(T_{j+1}^{i+1} - 2T_j^{i+1} + T_{j-1}^{i+1} + T_{j+1}^{i} - 2T_j^{i} + T_{j-1}^{i}\right) \tag{4.6}$$

where Δx is the thickness of the layer; T_j^i is the central temperature of layer j at the time i (T_{j-1}^i, T_{j+1}^i, T_{j-1}^{i+1}, T_j^{i+1}, T_{j+1}^{i+1} have similar definitions).

The time domain of the heat equation (the left side) can be approximated as

$$\frac{\partial T}{\partial t} \approx \frac{T_j^{i+1} - T_j^i}{\Delta t} \tag{4.7}$$

where Δt is the time step for the heat transfer.

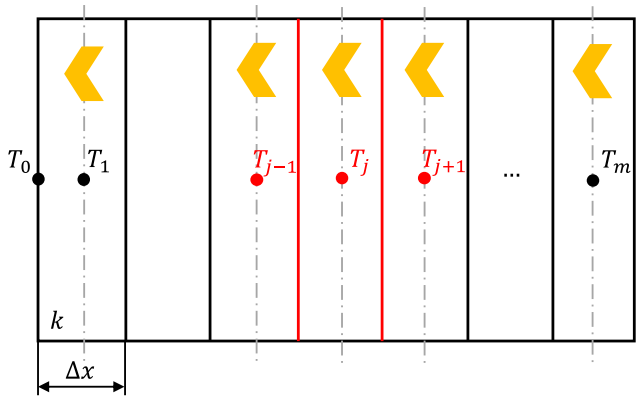

Figure 4.3 Heat transfer mechanism within the internal layer of single medium.

The heat equation Eq. (4.1) can be expressed as

$$\frac{T_j^{i+1}-T_j^i}{\Delta t}=\frac{\alpha}{2(\Delta x)^2}\left(T_{j+1}^{i+1}-2T_j^{i+1}+T_{j-1}^{i+1}+T_{j+1}^{i}-2T_j^{i}+T_{j-1}^{i}\right)+\frac{\dot{w}_j^i}{c\rho}-\frac{\dot{u}_j^i}{c\rho} \tag{4.8}$$

where $\dot{w}_j^i$ is the increment of the heat generation within time step i for layer j, which is the representation of $\dot{w}$ in numerical calculation; $\dot{u}_j^i$ is increment of the heat loss per unit volume per unit time caused by heat outflow within time step i for layer j, which can be expressed as

$$\dot{u}_j^i=\frac{4h\left(T_j^i-T_A\right)}{a} \tag{4.9}$$

where a is the length of the bearing.

Then Eq. (4.8) can be transferred into

$$-\beta T_{j-1}^{i+1}+(2\beta+1)T_j^{i+1}-\beta T_{j+1}^{i+1}=\beta T_{j-1}^{i}-(2\beta+\theta-1)T_j^{i}+\beta T_{j+1}^{i}+\frac{\dot{w}_j^i\Delta t}{c\rho}+\theta T_A \tag{4.10}$$

where $\beta=\frac{\alpha\Delta t}{2`(\Delta x)^2}$; $\theta=\frac{4h\Delta t}{ac\rho}$.

4.2.3.2 Heat transfer of boundary layer of single medium

Fig. 4.4 shows the heat transfer mechanism of the boundary layer of single medium (e.g. layer 1 or Bd.1 in Fig. 4.2c). The spatial domain of the heat equation Eq. (4.1) (first term of the right side) can be approximated as

$$\frac{\partial^2 T}{\partial x^2}=\frac{\frac{T_2-T_1}{\Delta x}-\frac{T_1-T_{B1}}{\Delta x/2}}{\Delta x}=\frac{T_2-3T_1+2T_0}{(\Delta x)^2} \tag{4.11}$$

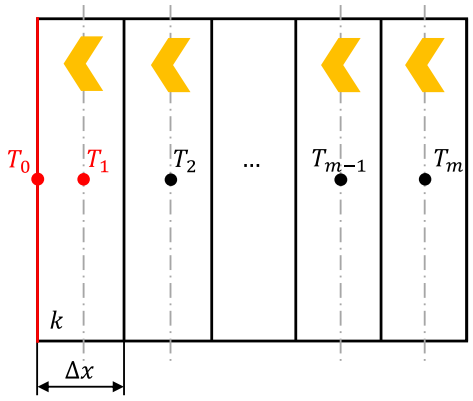

Figure 4.4 Heat transfer mechanism of the boundary layer of single medium.

The heat equation Eq. (4.1) can be expressed as

$$-2\beta T_0^{i+1} + (3\beta + 1)T_1^{i+1} - \beta T_2^{i+1} = 2\beta T_0^i - (3\beta + \theta - 1)T_1^i + \beta T_2^i + \frac{\dot{w}_1^i \Delta t}{c\rho} + \theta T_A \quad (4.12)$$

The boundary conditions can be adjusted according to actual conditions. In general, it can be divided into two situations: adiabatic state and constant boundary temperature.

(1) Adiabatic state

In the adiabatic state, the temperature gradient is zero, which means the temperature at the boundary is equal to the temperature of the adjacent layer, that is, $T_0 = T_1$. Eq. (4.12) can be written as

$$(\beta + 1)T_1^{i+1} - \beta T_2^{i+1} = -(\beta + \theta - 1)T_1^i + \beta T_2^i + \frac{\dot{w}_1^i \Delta t}{c\rho} + \theta T_A \quad (4.13)$$

(2) Constant ambient temperature state

In the state of constant ambient temperature, the temperature at the boundary equals to the ambient temperature, that is, $T_0 = T_A$. Eq. (4.12) can be written as

$$(3\beta + 1)T_1^{i+1} - \beta T_2^{i+1} = -(3\beta + \theta - 1)T_1^i + \beta T_2^i + \frac{\dot{w}_1^i \Delta t}{c\rho} + (4\beta + \theta)T_A \quad (4.14)$$

Actually, the boundary condition may be between the adiabatic state and constant ambient temperature. This is because a shear key (as shown in Fig. 4.2a) connects the loading system and the top of the bearing. Heat will transfer to the outside through the shear key. However, its cross-section is smaller than that of the bearing, limiting the amount of heat transfer. A middle boundary condition is assumed to simplify the analysis.

Use Eq (4.15) to combine the Eqs (4.13) and (4.14) to represent the heat equation of layer 1,

$$(\eta_B\beta + 1)T_1^{i+1} - \beta T_2^{i+1} = -(\eta_B\beta + \theta - 1)T_1^i + \beta T_2^i + \frac{\Delta w_1^i \Delta t}{c\rho} + [2(\eta_B - 1)\beta + \theta]T_A \quad (4.15)$$

where η_B is the coefficient of middle boundary condition ($1 \leq \eta_B \leq 3$), when $\eta_B = 1$, it represents the adiabatic state; when $\eta_B = 3$, it represents the state of constant ambient temperature.

4.2.3.3 Heat transfer within layers of multiple media

Fig. 4.5 shows the heat transfer mechanism within layers of multiple media (e.g. layers 10 and 11 or If.1 in Fig. 4.2d). The heat equation of layer m can be written as

$$-\beta T_{m-1}^{i+1} + (3\beta + 1)T_m^{i+1} - 2\beta T_0^{i+1} = \beta T_{m-1}^{i} - (3\beta - 1)T_m^{i} + 2\beta T_0^{i} + \frac{\Delta w_m^i \Delta t}{c\rho} + \theta T_A \quad (4.16)$$

The heat equation of layer 1 in Fig. 4.5 can be written as

$$-2\beta T_0^{i+1} + (3\beta + 1)T_1^{i+1} - \beta T_2^{i+1} = 2\beta T_0^{i} - (3\beta + \theta - 1)T_1^{i} + \beta T_2^{i} + \frac{\Delta w_1^i \Delta t}{c\rho} + \theta T_A \quad (4.17)$$

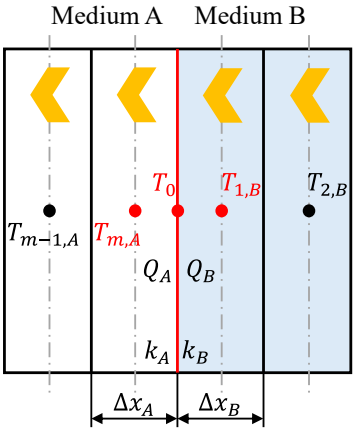

Figure 4.5 Heat transfer mechanism within layers of multiple media.

Based on the assumption (4), the heat transfer between two adjacent layers with different media should be equal. The temperature of the contact surface of the two media should be the same. According to the equal heat transferred within two layers,

$$k_A \frac{T_0 - T_{m,A}}{\Delta x_A/2} = k_B \frac{T_{1,B} - T_0}{\Delta x_B/2} \quad (4.18)$$

where k_A and k_B are the thermal conductivity of media A and B; Δx_A and Δx_B are the thickness of layers m and 1.

Thus, T_0 can be expressed as

$$T_0 = \frac{k_A \Delta x_B T_{m,A} + k_B \Delta x_A T_{1,B}}{k_A \Delta x_B + k_B \Delta x_A} = \gamma_{AB} T_{m,A} + \gamma_{BA} T_{1,B} \quad (4.19)$$

where $\gamma_{AB} = \frac{k_A \Delta x_B}{k_A \Delta x_B + k_B \Delta x_A}$, and $\gamma_{BA} = \frac{k_B \Delta x_A}{k_A \Delta x_B + k_B \Delta x_A}$.

Submit Eq. (4.19) into Eqs. (4.16) and (4.17), it obtains

$$\begin{aligned} &-\beta_A T_{m-1,A}^{i+1} + [\beta_A(3-2\gamma_{AB})+1]T_{m,A}^{i+1} - 2\beta_A\gamma_{BA}T_{1,B}^{i+1} \\ &= \beta_A T_{m-1,A}^{i} - [2\beta_A(3-2\gamma_{AB})-1]T_{m,A}^{i} + 2\beta_A\gamma_{BA}T_{1,B}^{i} + \frac{\Delta w_m^i \Delta t}{c\rho} + \theta T_A \end{aligned} \tag{4.20}$$

and

$$\begin{aligned} &-2\beta_B\gamma_{AB}T_{m,A}^{i+1} + [\beta_B(3-2\gamma_{BA})+1]T_{1,B}^{i+1} - \beta_B T_{2,B}^{i+1} \\ &= 2\beta_B\gamma_{AB}T_{m,A}^{i} - [\beta_B(3-2\gamma_{BA})-1]T_{1,B}^{i} + \beta_B T_{2,B}^{i} + \frac{\Delta w_1^i \Delta t}{c\rho} + \theta T_A \end{aligned} \tag{4.21}$$

When the HDR bearing is subjected to external loading, such as cyclic loading or seismic action, a significant amount of heat accumulates within the bearing and transfers to the surroundings due to the high energy dissipation of the HDR, referred to as the heating effect. In heat Equation Eq. (4.1), the second term of the right side, $\dot{w}/c\rho$ considers the heat generation within the rubbers. The volumetric heat generation rate, $\dot{w}$ can be represented as the increment of heat generation within one time step, $\Delta\dot{w}^i$, in numerical calculation. It can be calculated by the area of the hysteresis curve per unit volume per unit time, as shown in Fig. 4.6, which can be expressed as

$$\dot{w}^i = \frac{\Delta w^i}{\Delta t} = \frac{\left(d_r^{i+1} - d_r^i\right)\left(f_r^{i+1} + f_r^i\right)}{2V_r\Delta t} = \frac{\left(\varepsilon_r^{i+1} - \varepsilon_r^i\right)\left(\sigma_r^{i+1} + \sigma_r^i\right)}{2\Delta t} \tag{4.22}$$

where V_r is the volume of each rubber layer; d_r^{i+1}, f_r^{i+1}, d_r^i and f_r^i are the input horizontal displacements and corresponding restoring forces of each rubber layer at time $i+1$ and i; ε_r^{i+1}, σ_r^{i+1}, ε_r^i, and σ_r^i are the shear strains and stresses of each rubber layer at time $i+1$ and i.

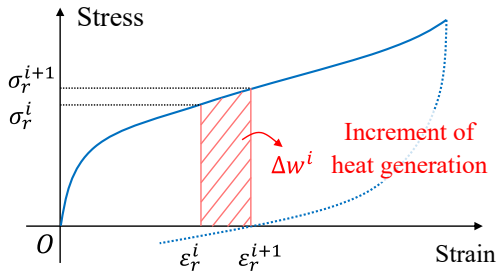

Figure 4.6 Calculation of heat generation rate by numerical method.

The analyzed bearing is composed of six layers of rubber and five layers of steel plate. Based on the assumption of heat transfer, the rubber and steel plates are discretized into numerical layers to represent the bearing. Fig. 4.2b illustrates the multi-layer heat transfer model for HDR bearings where a symmetric half of the bearing is discretized into 19 layers. The steel ending plate with a thickness of 25 mm is divided into ten layers, each with a thickness of 2.5 mm. The rubber with a thickness of 5 mm is divided into two layers, each with a thickness of 2.5 mm. The steel plate between the rubbers is set as a single layer with a thickness of 3.2 mm.

Note that half of steel plate 3, with a thickness of 1.6 mm, is selected in the analysis due to the symmetry. It is reasonable to keep the similar thickness of each layer to ensure sufficient accuracy in the calculation of thermal conduction. The thermal and basic properties of steel and rubber materials are listed in Table 4.1.

Table 4.1 Thermal and basic properties of steel and HDR materials.

Material	Steel	HDR
k, thermal conductivity [W/(m·K)]	38.76	0.31
h, convective heat transfer coefficient [W/(m^2·K)]	11.6	11.6
c, specific heat [J/(kg·K)]	432	1732
ρ, density (kg/m^3)	7740	1146

4.2.4 Heat equation of each layer in the numerical model

The heat equation of each layer (shown in Fig. 4.2b) can be expressed as follows:

For layer 1,

$$(\eta_B\beta_{s1}+1)T_1^{i+1}-\beta_{s1}T_2^{i+1}=-(\eta_B\beta_{s1}+\theta-1)T_1^{i}+\beta_{s1}T_2^{i}+[2(\eta_B-1)\beta_{s1}+\theta]T_A \quad (4.23)$$

where $\beta_{s1}=\frac{\alpha_s\Delta t}{2(\Delta x_{s1})^2}$; $\theta=\frac{4h_r\Delta t}{ac_r\rho_r}$; α_s is the thermal diffusivity of steel; Δx_{s1} is the thickness of the layer of steel ending plate; h_r is the convective heat transfer coefficient; c_r is the specific heat of HDR; ρ_r is the density of HDR.

For layers 2-9 ($j=2-9$),

$$\begin{aligned}&-\beta_{s1}T_{j-1}^{i+1}+(2\beta_{s1}+1)T_j^{i+1}-\beta_{s1}T_{j+1}^{i+1}\\&=\beta_{s1}T_{j-1}^{i}-(2\beta_{s1}+\theta-1)T_j^{i}+\beta_{s1}T_{j+1}^{i}+\theta T_A\end{aligned} \quad (4.24)$$

For layer 10,

$$\begin{aligned}&-\beta_{s1}T_9^{i+1}+[\beta_{s1}(3-2\gamma_{s1r})+1]T_{10}^{i+1}-2\beta_{s1}\gamma_{rs1}T_{11}^{i+1}\\&=\beta_{s1}T_9^{i}-[\beta_{s1}(3-2\gamma_{s1r})+\theta-1]T_{10}^{i}+2\beta_{s1}\gamma_{rs1}T_{11}^{i}+\theta T_A\end{aligned} \quad (4.25)$$

where $\gamma_{s1r}=\frac{k_s\Delta x_r}{k_s\Delta x_r+k_r\Delta x_{s1}}$; $\gamma_{rs1}=\frac{k_r\Delta x_{s1}}{k_s\Delta x_r+k_r\Delta x_{s1}}$; k_s and k_r are the thermal conductivity of steel and HDR; Δx_r is the thickness of the HDR layer.

For layer 11,

$$\begin{aligned}&-2\beta_r\gamma_{s1r}T_{10}^{i+1}+[\beta_r(3-2\gamma_{rs1})+1]T_{11}^{i+1}-\beta_rT_{12}^{i+1}\\&=2\beta_r\gamma_{s1r}T_{10}^{i}-[\beta_r(3-2\gamma_{rs1})+\theta-1]T_{11}^{i}+\beta_rT_{12}^{i}+\frac{\dot{w}_{11}^{i}\Delta t}{c_r\rho_r}+\theta T_A\end{aligned} \quad (4.26)$$

where $\beta_r=\frac{\alpha_r\Delta t}{2(\Delta x_r)^2}$.

For layers 12 and 15 ($j=12,15$),

$$-\beta_r T_{j-1}^{i+1} + [\beta_r(3-2\gamma_{rs2})+1]T_j^{i+1} - 2\beta_r\gamma_{s2r}T_{j+1}^{i+1}$$
$$= \beta_r T_{j-1}^{i} - [\beta_r(3-2\gamma_{rs2})+\theta-1]T_j^{i} + 2\beta_r\gamma_{s2r}T_{j+1}^{i} + \frac{\dot{w}_j^i \Delta t}{c_r\rho_r} + \theta T_A \quad (4.27)$$

where $\gamma_{s2r} = \frac{k_s\Delta x_r}{k_s\Delta x_r + k_r\Delta x_{s2}}$; $\gamma_{rs2} = \frac{k_r\Delta x_{s2}}{k_s\Delta x_r + k_r\Delta x_{s2}}$.

For layers 13 and 16 ($j = 13, 16$),

$$-4\beta_{s2}\gamma_{rs2}T_{j-1}^{i+1} + [8\beta_{s2}(1-\gamma_{s2r})+1]T_j^{i+1} - 4\beta_{s2}\gamma_{rs2}T_{j+1}^{i+1}$$
$$= 4\beta_{s2}\gamma_{rs2}T_{j-1}^{i} - [8\beta_{s2}(1-\gamma_{s2r})+\theta-1]T_j^{i} + 4\beta_{s2}\gamma_{rs2}T_{j+1}^{i} + \theta T_A \quad (4.28)$$

where $\beta_{s2} = \frac{\alpha_s\Delta t}{2(\Delta x_{s2})^2}$.

For layers 14 and 17 ($j = 14, 17$),

$$-2\beta_r\gamma_{s2r}T_{j-1}^{i+1} + [\beta_r(3-2\gamma_{rs2})+1]T_j^{i+1} - \beta_r T_{j+1}^{i+1}$$
$$= 2\beta_r\gamma_{s2r}T_{j-1}^{i} - [\beta_r(3-2\gamma_{rs2})+\theta-1]T_j^{i} + \beta_r T_{j+1}^{i} + \frac{\dot{w}_j^i \Delta t}{c_r\rho_r} + \theta T_A \quad (4.29)$$

For layer 18,

$$-\beta_r T_{17}^{i+1} + [\beta_r(3-2\gamma_{rs3})+1]T_{18}^{i+1} - 2\beta_r\gamma_{s3r}T_{19}^{i+1}$$
$$= \beta_r T_{17}^{i} - [\beta_r(3-2\gamma_{rs3})+\theta-1]T_{18}^{i} + 2\beta_r\gamma_{s3r}T_{19}^{i} + \frac{\dot{w}_{18}^i \Delta t}{c_r\rho_r} + \theta T_A \quad (4.30)$$

where $\gamma_{s3r} = \frac{k_s\Delta x_r}{k_s\Delta x_r + k_r\Delta x_{s3}}$; $\gamma_{rs3} = \frac{k_r\Delta x_{s3}}{k_s\Delta x_r + k_r\Delta x_{s3}}$.

For layer 19,

$$-4\beta_{s3}\gamma_{rs3}T_{18}^{i+1} + [4\beta_{s3}(1-\gamma_{s3r})+1]T_{19}^{i+1}$$
$$= 4\beta_{s3}\gamma_{rs3}T_{18}^{i} - [4\beta_{s3}(1-\gamma_{s3r})+\theta-1]T_{19}^{i} + \theta T_A \quad (4.31)$$

where $\beta_{s3} = \frac{\alpha_s\Delta t}{2(\Delta x_{s3})^2}$.

Combining the Eqs (4.23)-(4.31), a system of linear equations is obtained, in the matrix form as

$$\begin{bmatrix} B_1^{i+1} & C_1^{i+1} & 0 & \dots & 0 \\ A_2^{i+1} & B_2^{i+1} & C_2^{i+1} & \dots & 0 \\ \vdots & \ddots & \ddots & \ddots & \vdots \\ 0 & 0 & \dots & B_{18}^{i+1} & C_{18}^{i+1} \\ 0 & 0 & \dots & A_{19}^{i+1} & B_{19}^{i+1} \end{bmatrix} \begin{Bmatrix} T_1^{i+1} \\ T_2^{i+1} \\ \vdots \\ T_{18}^{i+1} \\ T_{19}^{i+1} \end{Bmatrix} = \begin{bmatrix} B_1^{i} & C_1^{i} & 0 & \dots & 0 \\ A_2^{i} & B_2^{i} & C_2^{i} & \dots & 0 \\ \vdots & \ddots & \ddots & \ddots & \vdots \\ 0 & 0 & \dots & B_{18}^{i} & C_{18}^{i} \\ 0 & 0 & \dots & A_{19}^{i} & B_{19}^{i} \end{bmatrix} \begin{Bmatrix} T_1^{i} \\ T_2^{i} \\ \vdots \\ T_{18}^{i} \\ T_{19}^{i} \end{Bmatrix} + \boldsymbol{w^i} + \boldsymbol{\theta^i} T_A \quad (4.32)$$

where A_j^{i+1}, B_j^{i+1}, C_j^{i+1}, A_j^i, B_j^i, and C_j^i are the coefficients of T_{j-1}^{i+1}, T_j^{i+1}, T_{j+1}^{i+1}, T_{j-1}^i, T_j^i, and T_{j+1}^i in the discretized heat equation for layer j; $\boldsymbol{w^i}$ is the vector of heat generation; $\boldsymbol{\theta^i}$ is the vector of heat outflow. Equation (4.32) can be denoted by

$$\boldsymbol{K^{i+1}t^{i+1}} = \boldsymbol{K^i t^i} + \boldsymbol{w^i} + \boldsymbol{\theta^i} T_A \tag{4.33}$$

where $\boldsymbol{K^{i+1}}$ and $\boldsymbol{K^i}$ are the coefficient matrices of temperature vectors $\boldsymbol{t^{i+1}}$ and $\boldsymbol{t^i}$.

In general, the multi-layer heat transfer model illustrates the heat transfer and heating effect within the bearing by calculating temperature at each time step. The variation in temperature will affect the stiffness and the characteristic strength of HDR bearings, which is called temperature dependence. Additionally, the history of temperature can be obtained through this model, which will be discussed in the following section.

4.3 A Thermal-coupled Restoring Force Model of HDR bearings

4.3.1 Basic assumptions

The developed multi-layer temperature Bouc-Wen (MTBW) model elucidates the hysteretic restoring force-displacement relationship for a single rubber layer based on the previously proposed thermo-mechanical coupled modified Park-Wen (TMC MPW) model, and the bearing is simplified as a series of interconnected TMC MPW models that represent the rubber layers considering the internal heat transfer of the bearing.

The general assumptions are as follows:

(1) The total displacement of the bearing will be distributed among rubber layers according to their respective stiffness.
(2) The restoring force of each rubber layer should be equal, which also represents the overall restoring force of the bearing.
(3) Since heat is generated and transferred outward, the temperature will not be distributed uniformly. The temperature at the center of the rubber layer represents the temperature of that layer and is used in the calculation of the MTBW model.

4.3.2 Restoring force model

The MTBW model can be expressed as

$$f_r(t) = \alpha_0 e^{m_T \times \frac{T_r(t)-23}{100}} K_r d_r(t) + [1 + b(d_r(t)/t_r)^2](1-\alpha_0) e^{n_T \times \frac{T_r(t)-23}{100}} K_r Z_r(t) \tag{4.34}$$

where

$$\dot{Z}_r(t) = A\dot{d}_r(t) - \beta\left|\dot{d}_r(t) Z_r(t)\right| Z_r(t) - \gamma \dot{d}_r(t) Z_r(t)^2 \tag{4.35}$$

$$\beta = \frac{1}{(1+s)d_y^2} \tag{4.36}$$

$$\gamma = s \cdot \beta \tag{4.37}$$

where α_0 is the post-yielding stiffness ratio; m_T and n_T are the parameters describing temperature dependence; $T_r(t)$ is the temperature at the center of the rubber layer; K_r is the initial stiffness of each rubber layer; $d_r(t)$ is the input horizontal displacement of each rubber layer; t_r is the thickness of each rubber layer; $Z_r(t)$ is the hysteretic component of restoring force of each rubber layer; b, A, β, γ, and s are the dimensionless parameters of hysteresis curve; d_y is the yield displacement. The Euler scheme is adopted to numerically solve the restoring force-displacement equation.

4.4 Model Validation

4.4.1 Validation of cyclic loading

4.4.1.1 Optimization algorithm for parameter identification

To determine the parameters α_0, K_r, d_y, s, b, m_T and n_T in Eq. (4.37), the optimization algorithm named the KH method is adopted. It proves advantageous in situations where the derivative of the objective function is uncertain, such as the complex problems of parameter determination for simulations involving nonlinear behavior. The parameters of the hysteretic model are identified according to the cyclic loading tests and subsequently employed in seismic analysis. The accuracy of restoring force between simulation and experimental results is defined by contribution rate (or the coefficient of determination) R^2, expressed as

$$R^2 = 1 - \frac{\sum_{i=1}^{n}\left(F_{a,i} - F_{e,i}\right)^2}{\sum_{i=1}^{n}\left(\overline{F_e} - F_{e,i}\right)^2} \tag{4.38}$$

where $F_{\mathrm{a},i}$ is the restoring force of bearing calculated by the analytical MTBW model at time step i; $F_{\mathrm{e},i}$ is the restoring force of bearing in the experiment at time step i; $\overline{F_{\mathrm{e}}}$ is the average value of $F_{\mathrm{e},i}$. The parameters are adjusted to get the maximum value of R^2, which means the selected parameters make the simulation results best match the experimental data. The identified parameters obtained by the fitting of the cyclic loading test result to the MTBW model are listed in Table 4.2 The contribution rates for all three different temperatures exceed 0.95, indicating an excellent concordance of hysteresis curves between the model and experiment.

Table 4.2 Identified parameters and contribution rates of MTBW model.

α_0	K_r (kN/mm)	s	d_y (mm)	b	m_T	n_T	$R^2_{-20℃}$	$R^2_{0℃}$	$R^2_{23℃}$
0.266	30.738	-0.864	1.549	0.272	-0.914	-2.189	0.9601	0.9765	0.9484

4.4.1.2 Hysteresis curve and temperature prediction

Fig. 4.7 depicts the hysteresis curve of the MTBW model compared with the corresponding experimental results under cyclic loading at −20°C, 0°C, and 23°C. The hysteresis curves in Fig. 4.7 show a good agreement between numerical simulation and experimental results. This result demonstrates that the MTBW model accurately captures the strain amplitude dependence of the hysteresis behavior, as well as the progressively decreasing stiffness with an increased number of loading cycles due to the heating effect. Note that the maximum stress of the first cycle of each strain amplitude is underestimated in the MTBW model compared with the experimental results. This may be due to neglecting the scragging, which represents degradation during the first cycle. Moreover, since the scragging and Mullins effects are not considered in the model, the simulated hysteresis curves obtained after the parameter identification tend towards the average of each cycle, showing the deviation in the first cycle at each strain amplitude. Also, the stiffness degradation becomes more significant at the lower ambient temperature.

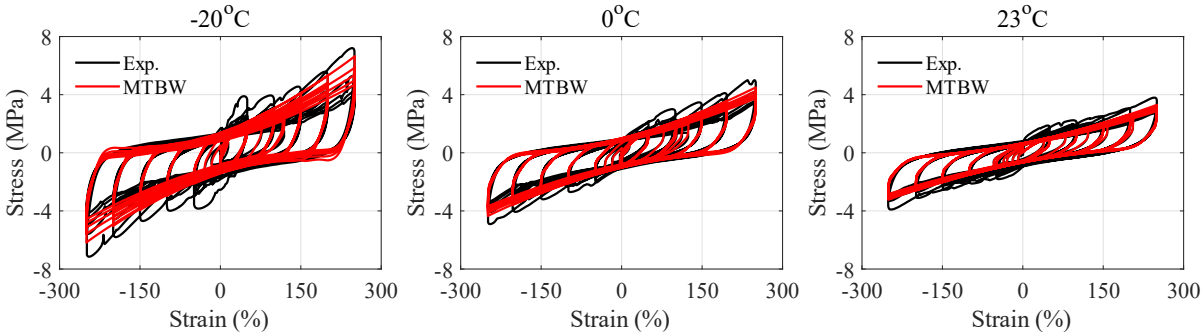

Figure 4.7 Hysteresis curve of MTBW model compared with experimental results under cyclic loading at −20°C, 0°C, and 23°C.

Figs. 8a and 8b illustrates the equivalent shear modulus and damping ratio of the bearings in simulation and test. The first, second, and fifth cycles of each strain amplitude in cyclic loading are compared. The equivalent shear modulus in the first cycle and small strain amplitude usually show a higher value and its deviation between test and simulation is larger due to the lack of consideration of scragging and Mullins effect. However, the deviation almost disappears in the subsequent loading. The equivalent damping ratio has a similar trend in that the deviation is eliminated after the first cycle and small strain amplitude, indicating the accuracy of the model.

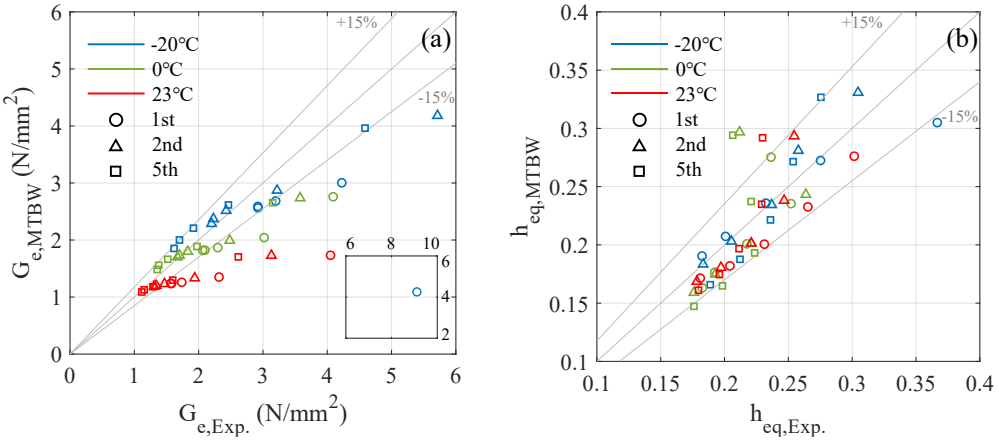

Figure 4.8 Validation of MTBW model compared with experimental results under cyclic loading at −20℃, 0℃, and 23℃: (a) equivalent shear modulus and (b) equivalent damping ratio.

Fig. 4.9 shows the temperature time history of the first and third rubber layers computed with the MTBW model and that of the test results. The computed results well capture the measured temperature change during the cyclic loading, suggesting the effectiveness of the MTBW model in depicting the heat transfer mechanism within the HDR bearing. The relative error (RE, Eq (4.39)) is calculated to validate the accuracy of the temperature prediction.

$$RE = \frac{\left|\Delta T_{\mathrm{MTBW}} - \Delta T_{\mathrm{Exp.}}\right|}{\Delta T_{\mathrm{Exp.}}} \tag{4.39}$$

where ΔT_{MTBW} is the temperature increment of MTBW model; $\Delta T_{\mathrm{Exp.}}$ is the temperature increment of the test. The RE is lower during the loading time, which represents a good capture of the heating effect. Note that during the cooling time of the tests, the temperature of rubber layers undergoes a significant decrease immediately after the loading time at each strain amplitude. After approximately 10 seconds, the rate of temperature decrease gradually slows down. The simulation results show a slower temperature decrease during the cooling period compared with the test, which may be caused by the simplification of the heat transfer mechanism.

Moreover, Fig. 4.9 provides the temperature history prediction of the second rubber layer, which is not measured in the experiment. It is observed that the temperature of the third layer is slightly higher than that of the second layer, and both are significantly higher than the temperature of the first layer. During the cooling period, the first layer experiences rapid heat conduction due to its connection with a thick steel ending plate, whereas the second and third layers exhibit slower heat transfer due to their connection with thinner steel plates. Meanwhile, an increase in the inner temperature leads to a reduction in the stiffness of the rubber, resulting in a greater distribution of displacement to the internal layer. This leads to higher energy dissipation and subsequent temperature increases. Similarly, during the cooling interval, the

rate of temperature decrease gradually drops from the external layer to the internal one.

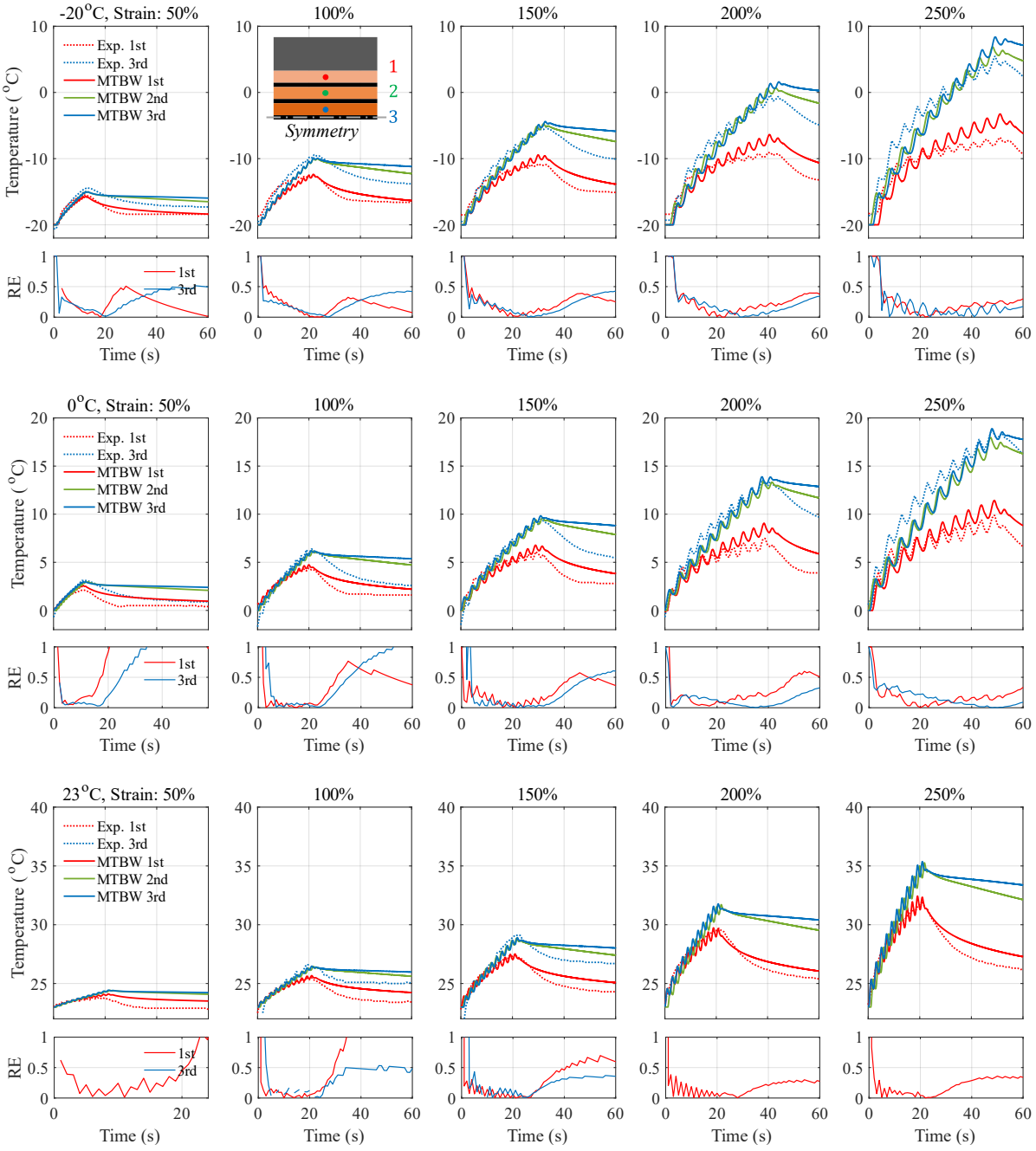

Figure 4.9 Temperature history of rubber layers computed by MTBW model and test results under cyclic loading at −20℃, 0℃, and 23℃.

Fig. 4.10 illustrates the temperature distribution along the vertical direction of the bearing. The temperatures at the end of the loading, or the maximum temperatures of each strain amplitude are shown in the plot. The corresponding experimental temperature data is marked by dots. The temperature distribution along the height exhibits a parabolic contour. It is found that the temperature of the steel plate is lower than that of the rubber layer. Since the heat generated and transferred by the rubber layer is not sufficient to raise the temperature of the steel plate to

a comparable level, a sawtooth-like temperature distribution pattern in the region of steel plate rubber and layers can be seen in the figure.

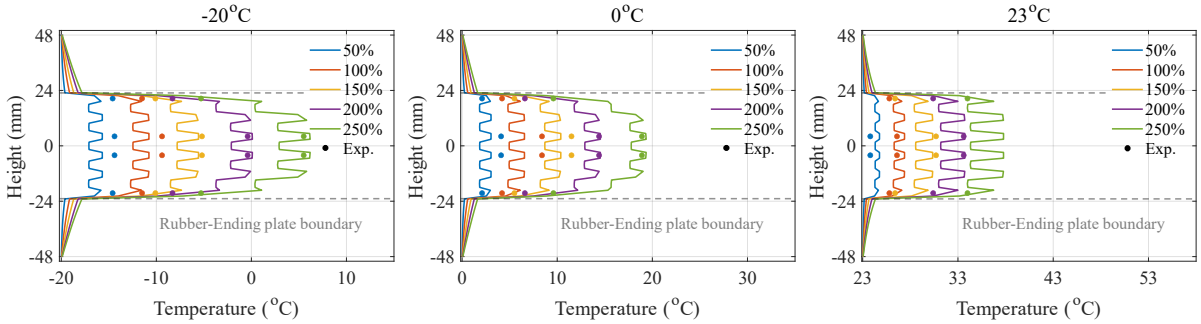

Figure 4.10 Temperature distribution of MTBW model along vertical direction of the bearing under cyclic loading at −20°C, 0°C, and 23°C.

4.4.2 Validation of hybrid simulation

4.4.2.1 Hysteresis curve of HDR bearing

To validate the effectiveness of the proposed model, one set of the identified parameters in Table 4.2 is used in the dynamic analysis of the real-time hybrid simulation. The first 20-second input ground motion in Fig. 3.14 is utilized for seismic analysis. The simulation results of the MTBW model are compared with the experimental data and the previous TMC MPW model in terms of hysteresis curve and temperature time history. Fig. 4.11 shows the comparison of the hysteresis curves between the MTBW model, the test results, and the TMC MPW model. The results show that both the MTBW model and the previous model can well simulate the stress-strain relationship obtained by the real-time hybrid seismic simulation at three ambient temperatures. The proposed MTBW model demonstrates an improvement in assessing the maximum stress and strain of bearings.

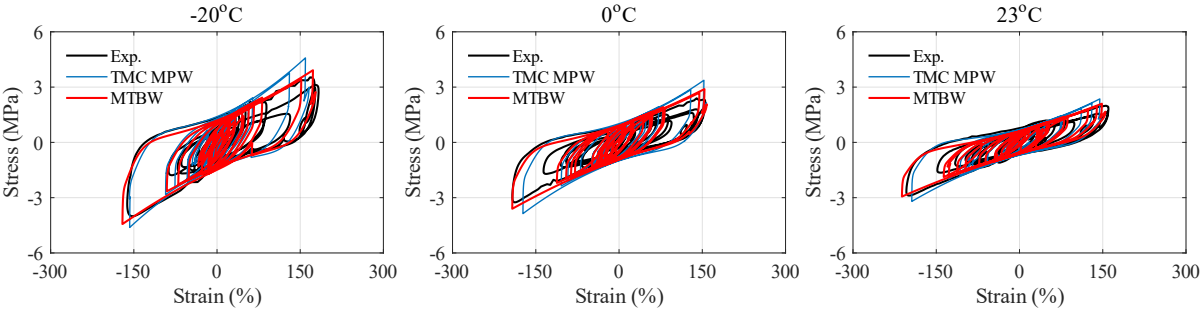

Figure 4.11 Hysteresis curve of MTBW model compared with experimental results and previous TMC MPW model under real-time hybrid simulation at −20°C, 0°C, and 23°C.

Fig. 4.12 compares the equivalent shear modulus and damping ratio of the maximum cycle for the MTBW model and the experimental results, indicating a reasonable accuracy of the predicted hysteretic behavior of the HDR bearings. Moreover, the bearing exhibits larger initial stiffness and restoring force under the same loading pattern at lower ambient temperatures.

This phenomenon should be carefully considered when implementing HDR bearings to bridges in cold regions.

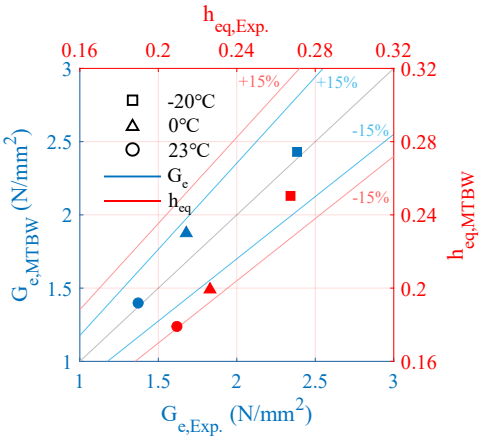

Figure 4.12 Validation of MTBW model compared with experimental results and previous TMC MPW model under real-time hybrid simulation at −20°C, 0°C, and 23°C: equivalent shear modulus and damping ratio of maximum cycle.

4.4.2.2 Temperature history prediction of HDR bearing

Fig. 4.13 shows the time history of the temperature of the first and third rubber layers in the MTBW model compared with that of the experimental results. The results of the calculation using the previous TMC MPW model are also shown in the plot. The temperature time history obtained by the MTBW model shows an acceptable agreement with the experiment in the duration of temperature rise at −20°C, 0°C, and 23°C, with the lower RE values during the seismic loading. Although the temperature data of 23°C for the third rubber layer is not available, it is reasonable to predict that the MTBW model can accurately simulate the temperature time history. It is observed that the previous TMC MPW model underestimates the temperature of the bearing in all cases, possibly because of the assumption of a uniform temperature distribution throughout the bearing.

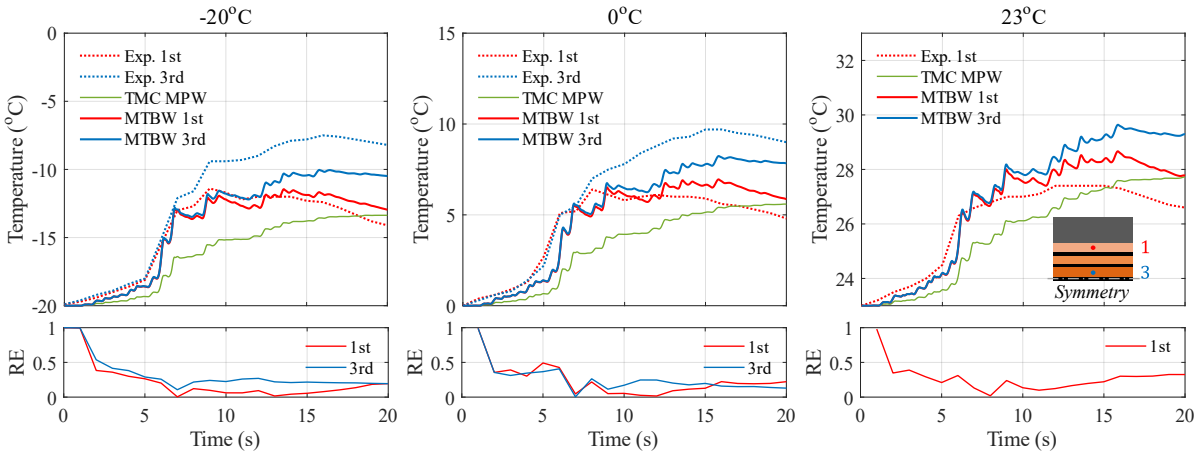

Figure 4.13 Temperature history of MTBW model compared with experimental results and

previous TMC MPW model under real-time hybrid simulation at −20℃, 0℃, and 23℃.

Fig. 4.14 demonstrates the temperature distribution along the vertical direction of the bearing at different times. The corresponding experimental temperature data is marked by dots. It exhibits a similar pattern to cyclic loading in terms of temperature increase: the lower ambient temperature results in a higher temperature increase within the bearing. A rapid temperature increase occurs during the 5-10 seconds of loading because the bearing experiences large strain during this time range. Due to the different thermal properties of the high damping rubber and steel, there exists a significant temperature difference between the adjacent rubber and steel layers, especially during the time range of large strain loading. As the intensity of the input ground motion decreases, the rise of temperature within the bearing slows down, resulting in a gradual decrease in the temperature difference between the rubber and steel layers.

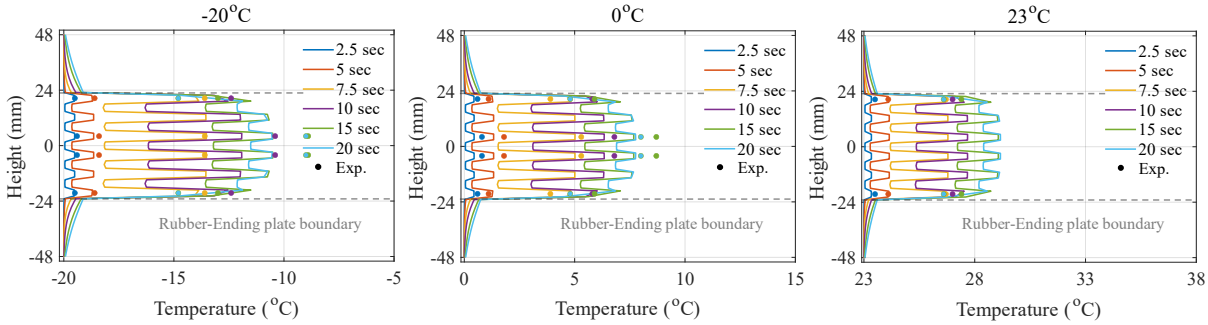

Figure 4.14 Temperature distribution of MTBW model along vertical direction of the bearing under real-time hybrid simulation at −20℃, 0℃, and 23℃.

4.4.2.3 Structural response

The pier top acceleration and displacement of the MTBW model compared with the experiment results under the real-time hybrid simulation are shown in Figs. 4.15 and 4.16. The proposed MTBW model can well capture the structure response of an isolated bridge model with HDR bearing at three ambient temperatures.

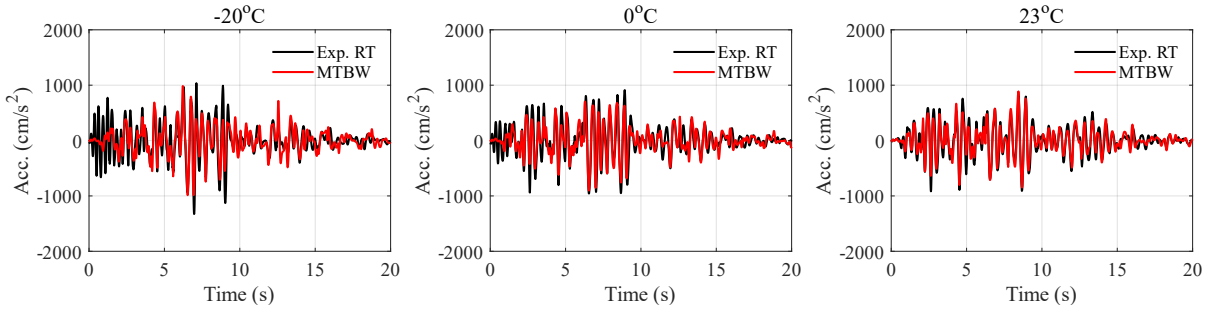

Figure 4.15 Pier top acceleration of MTBW model compared with experimental results under real-time hybrid simulation at −20℃, 0℃, and 23℃.

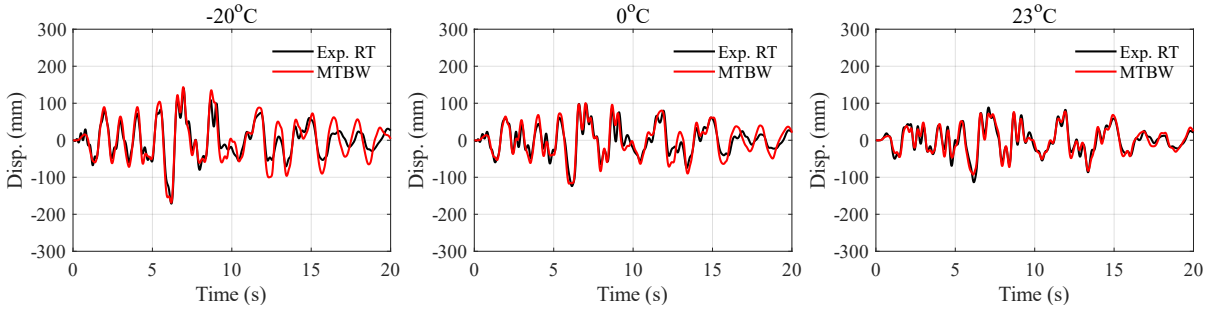

Figure 4.16 Pier top displacement of MTBW model compared with experimental results under real-time hybrid simulation at −20℃, 0℃, and 23℃.

4.5 Discussion

In this chapter, a multi-layer thermo-mechanical coupling model (MTBW model) is developed to investigate the hysteretic behavior of HDR bearings involving temperature dependence, heating effect, and heat transfer. The MTBW model can represent the time-dependent thermal mechanism within the bearing, with the non-uniform distribution of internal temperature. The consideration of the inner temperature improves the accuracy of the hysteretic behavior of HDR bearing. The simulated hysteresis curve, temperature history, and temperature distribution are compared with the previous model and the experimental results under quasi-static cyclic loading and real-time hybrid simulation tests at three ambient temperatures. Here are the main points to be discussed:

(1) A multi-layer thermo-mechanical coupling model (MTBW model) is developed for HDR bearing to simulate its hysteretic behavior. Different from the existing model, the MTBW model considers the temperature difference and illustrates the thermal mechanism within the bearing. The non-uniform internal temperature distribution causes variations in shear deformation, different from the assumption of uniformly distributed shear deformation.

(2) The MTBW model elucidates the thermal mechanism including the heating effect and heat transfer within HDR bearings and accurately predicts the history of temperature. The hysteretic restoring force behavior calculated by the MTBW model under cyclic loading and hybrid simulation achieves a decent agreement with the experiment and shows improved accuracy compared with the previous model. The heating and cooling behaviors are well simulated, and the temperature variation of each rubber layer is verified by the test results with improved accuracy compared with the existing simplified thermos-mechanical coupling model. Moreover, the temperature distribution along the vertical direction of the HDR bearing is calculated to analyze the trend of the internal temperature variation and the difference in heat transfer between the steel plate and rubber layer.

(3) The factor of rate dependence is not considered in this model. In the validation of the hybrid simulation, only the real-time hybrid simulation is used to compare with the model. As

mentioned in Chapter 3, the maximum stress of HDR bearing in pseudo-dynamic hybrid simulation is larger than that in the real-time hybrid simulation, which is contrary to common perception (the maximum stress should increase as the loading ratio increases). This phenomenon needs to be confirmed by further experimental studies.

(4) Based on the precise temperature prediction, the accuracy of the thermal coupling hysteretic model for HDR bearings is improved. The numerical results of the hysteresis curve under the quasi-static cyclic loading and real-time hybrid simulation tests show good agreement with the experimental data. The MTBW model effectively captures the temperature-dependent hysteresis behavior of HDR bearings, including the strain-stress relationship at different temperatures and the gradual decrease in stiffness due to the heating effect.

CHAPTER 5

A MULTI-LAYER THERMO-MECHANICAL COUPLING HYSTERETIC MODEL FOR LHDR BEARINGS AT LOW TEMPERATURE

Chapter 5 proposes a multi-layer thermo-mechanical coupling hysteretic model for LHDR bearings. Different from the model proposed in Chapter 4, this model considers the interaction of the heating effect between the HDR laminate and lead core, illustrating the thermal mechanism of the LHDR bearing. Moreover, the rate dependence is also included and validated by the real-time and pseudo-dynamic hybrid simulation tests in Chapter 3. The hysteretic behavior and temperature history of LHDR bearing predicted from this model are compared to the cyclic loading and hybrid simulation test results.

5.1 General

Lead high damping rubber (LHDR) bearing is one of the isolated rubber bearings developed in recent decades. LHDR bearing has two effective energy dissipation parts: high damping rubber and lead core, which performs better behavior under earthquake. Similar to high damping rubber (HDR) bearings and lead rubber (LR) bearings, the hysteretic behavior of LHDR bearings significantly changes at low temperatures due to the non-negligible temperature dependence and heating effect. The complex heat transfer mechanism in these bearings differs from that of HDR bearings or LR bearings owing to the interacted heating effect of HDRs and lead cores. Additionally, the hysteretic behavior is affected by the loading rate.

A rate-dependent thermo-mechanical coupling hysteretic model for LHDR bearings is proposed to illustrate the thermal mechanism within the bearings when the heating effect cannot be ignored. Fig. 5.1 depicts the overview of the thermal-coupled hysteretic model, which consists of the rate-dependent hysteretic model and the thermo-mechanical model.

(1) Rate-dependent hysteretic model: The hysteretic behavior of HDR is modeled using the multi-layer temperature-dependent Bouc-Wen (MTBW) model, while that of lead core is modeled using the bilinear (BL) model. A series combination of a dashpot and spring is

utilized to simulate the rate-dependent characteristics of the bearing.

(2) Thermo-mechanical model: Owing to the temperature dependence of the HDR, the initial stiffness of HDR will be affected by the ambient temperature. Moreover, the heat is generated in both the HDR and lead core as the bearing is dissipating energy. The heat conduction is considered within the bearing, leading to the internal temperature variation that subsequently impacts hysteresis behavior.

This model incorporates the mutual coupling between the hysteretic behavior and temperature dependence. The restoring force of the bearing is influenced not only by displacement but by temperature, which aligns more closely with the actual mechanical behavior of the bearing. The bearing is made of HDR laminates and steel plates. The outer HDR laminates are connected to the steel sealing plates. One or several lead cores (constricted by springs) traverse through the bearing. The lateral side of the bearing is covered by the rubber, and both two ends of the bearing are connected to the steel end plates.

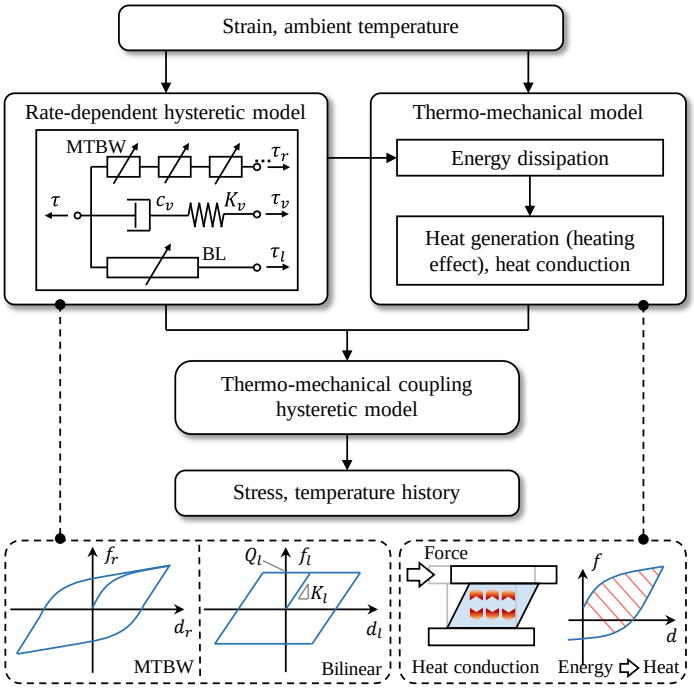

Figure 5.1 A thermo-mechanical coupling hysteretic model for LHDR bearings.

This chapter aims to investigate the hysteretic behavior of LHDR bearings considering the thermal mechanism and the rate dependence. A hysteretic model coupled with thermal mechanism and rate dependence was constructed to simulate the mechanical behavior of bearings. A thermo-mechanical model was proposed to elaborate the interactional heat transfer behavior among HDR laminates, lead cores, and steel plates. The parameters of the model were identified by an optimization algorithm in the cyclic loading. The hysteretic behavior of the bearings was validated in the pseudo-dynamic and real-time hybrid simulations. The predicted hysteresis curves and temperature history of the model were compared with the experimental data and the previous model at −20°C, 0°C, and 23°C.

5.2 Thermal Mechanism within LHDR bearings

5.2.1 Physical model

The general physical model of LHDR bearing is shown in Fig. 5.2a. Considering heat generation and transfer, separate heat equations can be formulated for each component. The heat equation for the single lead core is

$$\frac{\partial T(t)}{\partial t} = \frac{\dot{w}_l(t)}{c_l \rho_l} - \frac{2\dot{q}_{l1}(t)}{c_l \rho_l} - \frac{\dot{q}_{l2}(t)}{c_l \rho_l} \tag{5.1}$$

where

$$\dot{w}_l(t) = \int_0^t \sigma_l(\tau)\dot{\varepsilon}_l(\tau)d\tau \tag{5.2}$$

$$\dot{q}_{l1}(t) = \frac{A_{l1}}{V_l} \cdot \frac{pk_s T_L}{r_l T_p^+(t)} \tag{5.3}$$

$$\dot{q}_{l2}(t) = \frac{A_{l2}}{V_l} \cdot \frac{pk_s T_L}{0.785 r_l (t^+)^{\frac{1}{3}}} \tag{5.4}$$

$$T_p^+(\mathrm{t}^+) = \begin{cases} 2\left(\frac{t^+}{\pi}\right)^{\frac{1}{2}} - \left(\frac{t^+}{\pi}\right)\left[2 - \left(\frac{t^+}{4}\right) - \left(\frac{t^+}{4}\right)^2 - \frac{15}{4}\left(\frac{t^+}{4}\right)^3\right] & t^+ < 0.6 \\ \frac{8}{3\pi} - \frac{1}{2(\pi t^+)^{\frac{1}{2}}}\left[1 - \frac{1}{3(4t^+)} + \frac{1}{6(4t^+)^2} - \frac{1}{12(4t^+)^3}\right] & t^+ \geq 0.6 \end{cases} \tag{5.5}$$

$$t^+(\mathrm{t}) = \frac{\alpha_l t}{r_l^2} \tag{5.6}$$

$$\alpha_l = \frac{k_l}{c_l \rho_l} \tag{5.7}$$

where T is the temperature of the lead core; $\dot{w}_l(t)$ is the volumetric heat generation rate of lead core (heat generation per unit volume per unit time); $\dot{q}_{l1}(t)$ is the heat flux per unit volume per unit time through the interface of one end plate and single lead core (note that the thermal conduction calculation between the lead core and the steel plate is referenced from the research (Kalpakidis and Constantinou 2009a), see Fig. 2c); $\dot{q}_{l2}(t)$ is the heat flux per unit volume per unit time through the interface of sealing or shim plate and single lead core; c_l is the specific heat of lead core; ρ_l is the density of lead core; A_{l1} is the area of the interface of one end plate and single lead core; A_{l2} is the area of the interface of sealing or shim plate and single lead core; V_l is the volume of single lead core; p is the ratio of surface and inner temperature increase of lead core; k_s and k_l are the thermal conductivity of steel and lead, respectively; T_L is the temperature increase of lead core; r_l is the lead core radius; α_l is the thermal diffusivity of lead core; t is the time.

The heat equation for the steel plate is

$$\frac{\partial T(x,t)}{\partial t} = \alpha_s \frac{\partial^2 T(x,t)}{\partial x^2} + \frac{n_l \dot{q}_{l1}(t)}{c_l \rho_l} + \frac{n_l \dot{q}_{l2}(t)}{c_l \rho_l} \tag{5.8}$$

where α_s is the thermal diffusivity of steel; n_l is the number of the lead cores.

The heat equation for the high damping rubber is

$$\frac{\partial T(x,t)}{\partial t} = \alpha_r \frac{\partial^2 T(x,t)}{\partial x^2} + \frac{\dot{w}_r(t)}{c_r \rho_r} \tag{5.9}$$

where α_r is the thermal diffusivity of HDR; $\dot{w}_r(t)$ is the volumetric heat generation rate of HDR (heat generation per unit volume per unit time); c_r is the specific heat of HDR; ρ_r is the density of HDR.

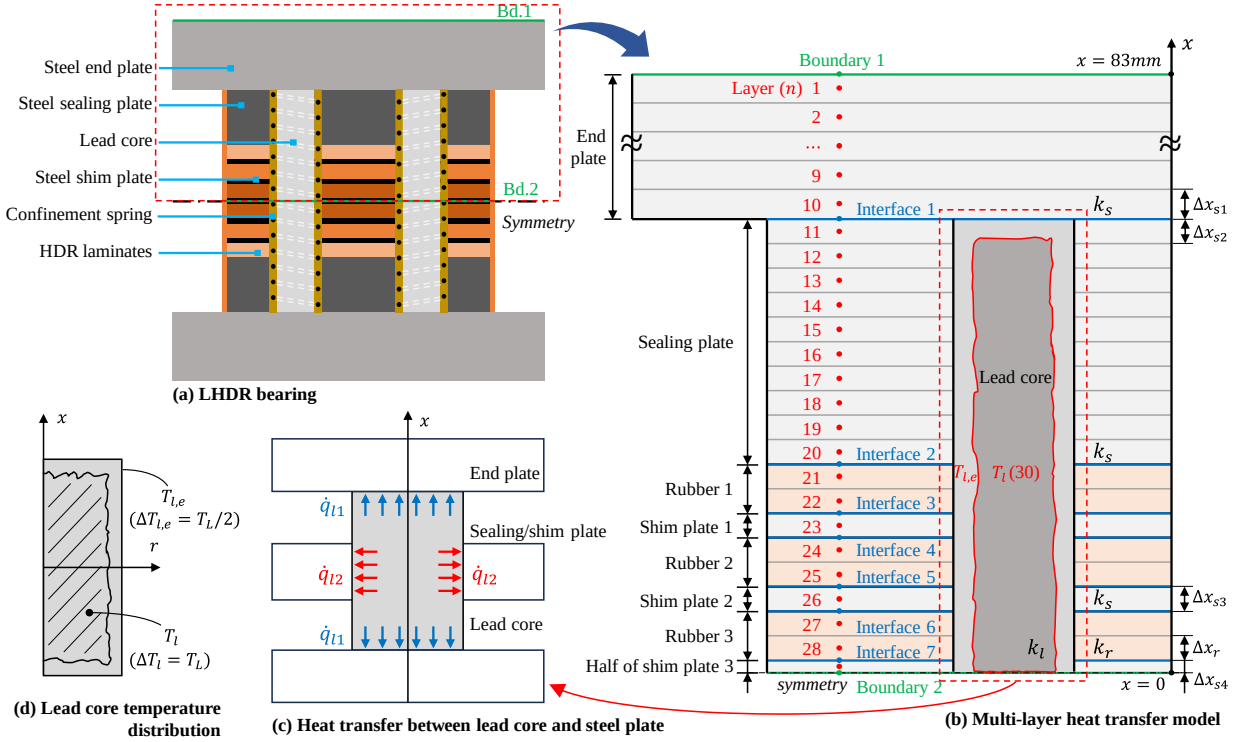

Figure 5.2 A multi-layer thermo-mechanical model for LHDR bearings.

The two boundaries of the model are shown in Fig. 2b. The boundary 1 at the top of the end plate can be treated as either an adiabatic state or a constant temperature condition, depending on actual circumstances. The boundary 2 on the symmetrical face can be regarded as an adiabatic state with a zero-gradient temperature condition. The boundary condition is

$$\begin{cases} \dfrac{\partial T}{\partial x} = 0 & x = 0 \\ \dfrac{\partial T}{\partial x} = 0 \text{ or } T = T_A & x = 83\ mm \end{cases} \tag{5.10}$$

where T_A is the ambient temperature.

5.2.2 Basic assumptions

A multi-layer thermo-mechanical model is established to incorporate the heating effect of HDR and lead core and heat conduction within the LHDR bearing. To simplify the model reasonably, the following assumptions are made:

(1) Heat conduction: The one-dimensional heat transfer is assumed between the rubber laminates and steel plates, indicating that the heat flux only conducts vertically. The heat transfer between the lead core and the steel plate is considered due to the high thermal conductivity, whereas that between the lead core and rubber laminates is neglected.

(2) Temperature of each component: The temperature distribution of the rubber laminates and steel plates is uniform across the horizontal plane. The temperature distribution of the lead core follows the assumption made in the previous research (Kalpakidis and Constantinou 2009a) as shown in Fig. 2d. The temperature increment within the lead core (T_L) is solely a function of time. The temperature in the bulk of the lead core is evenly distributed, which is a convenient approximation of the temperature rise. The increased temperature at the surface of the lead core is half ($T_L/2$) of that in the bulk of the lead core, according to the FE analysis in(Kalpakidis and Constantinou 2009b). This assumption simplifies the complex temperature distribution of the lead core and facilitates numerical calculation. Based on the experimental data on temperature variation of the lead core, this assumption is acceptable.

(3) Heat convection: The heat convection from the bearing to the air can be ignored because the heat loss according to the cover rubber to the surrounding air is much smaller than the heat conduction to the end plates.

(4) Thermal property: The thermal properties of the materials are assumed to remain constant and unaffected by temperature variations because the variation of the thermal properties of the material is small enough to be ignored and will not affect the accuracy of the results in the temperature range of interest.

(5) Heat generation: The heat is uniformly generated within each HDR laminate or lead core.

(6) Symmetry: The half of the bearing along the vertical direction is analyzed for model simplification due to the symmetry of the structure.

5.2.3 Numerical model of heat transfer mechanism

A numerical method is employed to solve the heat equation. Fig. 2b shows the multi-layer heat transfer model. The steel plates and HDR laminates are discretized into the required number of layers (n) for numerical calculations, as shown in Fig. 2b. The Crank-Nicolson scheme (1947) is utilized for numerically solving the heat equation due to its excellent stability. The heat transfer mechanism between the HDR laminate and steel plate is similar to the model of HDR bearings. However, the heat transfer mechanism between the lead core and steel plate is the

main issue discussed in this section.

5.2.3.1 Heat transfer within an internal layer of a single medium

In Chapter 4, Fig. 4.3 shows the heat transfer mechanism within the internal layer of a single medium. In this chapter, it applies to the steel plate of layers 2-9 in Fig. 5.2. Based on the approximation of spatial and time domains (Eqs. (4.6) and (4.7)), the heat equation of the single medium can be expressed as

$$-\beta T_{j-1}^{i+1} + (2\beta + 1)T_j^{i+1} - \beta T_{j+1}^{i+1} = \beta T_{j-1}^{i} - (2\beta - 1)T_j^{i} + \beta T_{j+1}^{i} \tag{5.11}$$

where $\beta = \frac{\alpha \Delta t}{2(\Delta x)^2}$; Δt is the time step for the heat transfer; Δx is the thickness of the layer; T_j^i is the central temperature of layer j at the time i (T_{j-1}^i, T_{j+1}^i, T_{j-1}^{i+1}, T_j^{i+1}, T_{j+1}^{i+1} have similar definitions).

5.2.3.2 Heat transfer of boundary layer of a single medium

Fig. 4.4 shows the heat transfer mechanism within the internal layer of a single medium. In this chapter, it applies to the steel plate of layer 1 in Fig. 5.2b. Based on the approximation of spatial and time domains (Eqs. (4.11) and (4.7)), the heat equation of the boundary layer can be expressed as

$$(\eta_B \beta + 1)T_1^{i+1} - \beta T_2^{i+1} = -(\eta_B \beta - 1)T_1^{i} + \beta T_2^{i} + [2(\eta_B - 1)\beta]T_A \tag{5.12}$$

where η_B is the coefficient of boundary condition ($1 \le \eta_B \le 3$).

5.2.3.3 Heat transfer between lead core and steel plate

Fig. 5.3 shows the heat transfer between the lead core and steel end plate (e.g., layer 10 in Fig. 5.2b), as well as the lead core and steel sealing/shim plate (e.g., layer 11 in Fig. 5.2b). For the layer m (steel end plate) upper the interface 1 in Fig. 5.3, the heat equation of steel plate, Eq. (5.8) can be expressed as

$$\begin{aligned} &-\beta_{s1} T_{m-1,s1}^{i+1} + (3\beta_{s1} + 1)T_{m,s1}^{i+1} - 2\beta_{s1} T_{I1}^{i+1} \\ &= \beta_{s1} T_{m-1,s1}^{i} - (3\beta_{s1} - 1)T_{m,s1}^{i} + 2\beta_{s1} T_{I1}^{i} + n_l \theta_{l1} T_l^i - n_l \theta_{l1} T_A \end{aligned} \tag{5.13}$$

where T_{I1} is the temperature of the interface 1; $\beta_{s1} = \frac{\alpha_s \Delta t}{2(\Delta x_{s1})^2}$; $\theta_{l1} = \frac{n_l \Delta t}{c_l \rho_l} \cdot \frac{A_{l1}}{V_l} \cdot \frac{p k_s}{r_l T_p^+}$.

According to the Eq. (4.18), the temperature of the interface 1 can be expressed as

$$T_{I1} = \gamma_{s1} T_{m,s1} + \gamma_{s2} T_{1,s2} \tag{5.14}$$

where $\gamma_{s1s2} = \frac{\Delta x_{s2}}{\Delta x_{s2} + \Delta x_{s1}}$; $\gamma_{s2s1} = \frac{\Delta x_{s1}}{\Delta x_{s2} + \Delta x_{s1}}$; Δx_{s1} and Δx_{s2} are the thickness of steel plates.

Take Eq. (5.14) into Eq. (5.13), the heat equation of layer m upper the interface 1 can be written as

$$-\beta_{s1}T_{m-1,s1}^{i+1} + [\beta_{s1}(3-2\gamma_{s1s2})+1]T_{m,s1}^{i+1} - 2\beta_{s1}\gamma_{s2s1}T_{1,s2}^{i+1}$$
$$= \beta_{s1}T_{m-1,s1}^{i} - [\beta_{s1}(3-2\gamma_{s1s2})-1]T_{m,s1}^{i} + 2\beta_{s1}\gamma_{s2s1}T_{1,s2}^{i} + n_l\theta_{l1}T_l^i - n_l\theta_{l1}T_A \quad (5.15)$$

Similarly, the heat equation of layer 1 (steel sealing plate) below the interface 1 can be written as

$$2\beta_{s2}\gamma_{s1s2}T_{m,s1}^{i+1} + [\beta_{s2}(3-2\gamma_{s2s1})+1]T_{1,s2}^{i+1} - \beta_{s2}T_{2,s2}^{i+1}$$
$$= 2\beta_{s2}\gamma_{s1s2}T_{m,s1}^{i} - [\beta_{s2}(3-2\gamma_{s2s1})-1]T_{1,s2}^{i} + \beta_{s2}T_{2,s2}^{i} + n_l\theta'_{l2}T_l^i - n_l\theta'_{l2}T_A \quad (5.16)$$

where $\beta_{s2} = \frac{\alpha_s \Delta t}{2(\Delta x_{s2})^2}$; $\theta'_{l2} = \frac{\Delta x_{s2}}{\sum \Delta x_s} \cdot \frac{n_l \Delta t}{c_l \rho_l} \cdot \frac{A_{l2}}{V_l} \cdot \frac{pk_s}{0.785 r_l (t^+)^{\frac{1}{3}}}$.

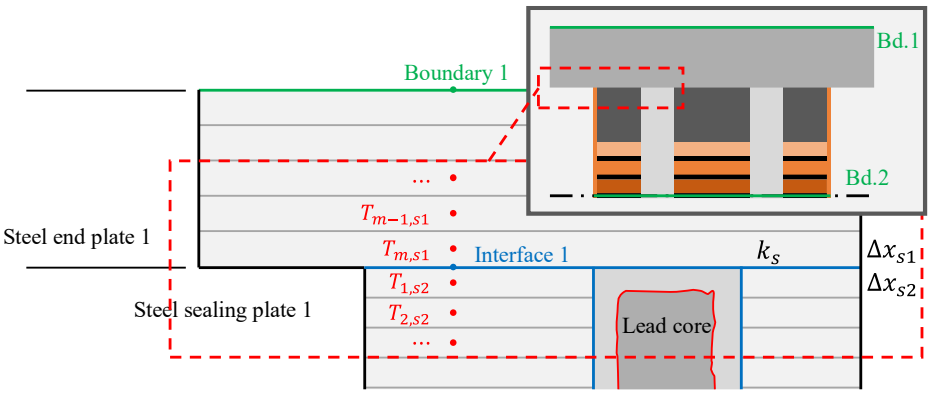

Figure 5.3 Heat transfer mechanism between lead core and steel plate.

5.2.3.4 Heat transfer between steel plate and HDR laminate

Fig. 5.4 shows the heat transfer between the steel plate and HDR laminate (e.g., layers 20 and 21 in Fig. 5.2b). At the same time, the heat transfer between the lead core and steel plate is considered due to the large thermal conductivity, while the heat transfer between the lead core and HDR laminate is ignored due to the small thermal conductivity of HDR material. For the layer m (steel end plate) upper interface 2 in Fig. 5.4, the heat equation of steel plate, Eq. (5.8), can be expressed as

$$-\beta_{s2}T_{m-1,s2}^{i+1} + [\beta_{s2}(3-2\gamma_{s2r})+1]T_{m,s2}^{i+1} - 2\beta_{s2}\gamma_{rs2}T_{1,r}^{i+1}$$
$$= \beta_{s2}T_{m-1,s2}^{i} - [\beta_{s2}(3-2\gamma_{s2r})-1]T_{m,s2}^{i} + 2\beta_{s2}\gamma_{rs2}T_{1,r}^{i} + n_l\theta'_{l2}T_l^i - n_l\theta'_{l2}T_A \quad (5.17)$$

where $\gamma_{s2r} = \frac{k_s \Delta x_r}{k_s \Delta x_r + k_r \Delta x_{s2}}$; $\gamma_{rs2} = \frac{k_r \Delta x_{s2}}{k_s \Delta x_r + k_r \Delta x_{s2}}$.

Similarly, the heat equation of layer 1 (HDR laminate) below the interface 2 can be written as

$$-2\beta_r\gamma_{s2r}T_{m,s2}^{i+1} + [\beta_r(3-2\gamma_{rs2})+1]T_{1,r}^{i+1} - \beta_r T_{2,r}^{i+1}$$
$$= 2\beta_r\gamma_{s2r}T_{m,s2}^{i} - [\beta_r(3-2\gamma_{rs2})-1]T_{1,r}^{i} + \beta_r T_{2,r}^{i} + \frac{\dot{w}_1^i \Delta t}{c_r \rho_r} \quad (5.18)$$

where $\beta_r = \frac{\alpha_r \Delta t}{2(\Delta x_r)^2}$; $\dot{w}_1^i$ is the increment of heat generation within time step i for layer 1, expressed in Eq. (4.22).

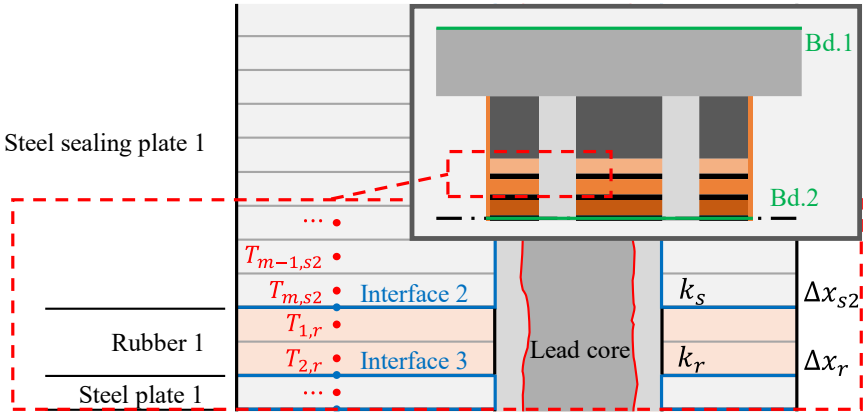

Figure 5.4 Heat transfer mechanism between steel plate and HDR laminate.

The numerical model is discretized into 29 layers, as shown in Fig. 5.2b. Specifically, the end plate and sealing plate are divided into 10 layers with single-layer thicknesses of 3.5 mm and 2.5 mm (Δx_{s1} and Δx_{s2}), respectively. The HDR laminate is divided into 2 layers with a single-layer thickness of 2.5 mm (Δx_r). The shim plate between the HDR laminates is set as a single layer with a thickness of 3.2 mm (Δx_{s3}). The lead core can be defined as a special layer for ease of subsequent calculation. The thermal and basic properties of steel and rubber materials are listed in Table 5.1.

Table 5.1 Thermal and basic properties of lead, steel, and HDR materials.

Material	Lead	Steel	HDR
k, thermal conductivity [W/(m·K)]	35.30	38.76	0.31
c, specific heat [J/(kg·K)]	129	432	1732
ρ, density (kg/m^3)	11360	7740	1146

5.2.4 Heat equation of each layer in numerical model

The heat equations for each layer (as shown in Fig. 5.2b) can be expressed as follows:

For layer 1 (steel end plate),

$$(\eta_B\beta_{s1} + 1)T_1^{i+1} - \beta_{s1}T_2^{i+1} = -(\eta_B\beta_{s1} - 1)T_1^i + \beta_{s1}T_2^i + [2(\theta_B - 1)\beta_{s1}]T_A \quad (5.19)$$

For layers 2-9 ($j = 2 - 9$, steel end plate),

$$-\beta_{s1}T_{j-1}^{i+1} + (2\beta_{s1} + 1)T_j^{i+1} - \beta_{s1}T_{j+1}^{i+1} = \beta_{s1}T_{j-1}^i - (2\beta_{s1} - 1)T_j^i + \beta_{s1}T_{j+1}^i \quad (5.20)$$

For layer 10 (steel end plate),

$$\begin{aligned} &-\beta_{s1}T_9^{i+1} + [\beta_{s1}(3 - 2\gamma_{s1s2}) + 1]T_{10}^{i+1} - 2\beta_{s1}\gamma_{s2s1}T_{11}^{i+1} \\ &= \beta_{s1}T_9^i - [\beta_{s1}(3 - 2\gamma_{s1s2}) - 1]T_{10}^i + 2\beta_{s1}\gamma_{s2s1}T_{11}^i + n_l\theta_{l1}T_l^i - n_l\theta_{l1}T_A \end{aligned} \quad (5.21)$$

For layer 11 (steel sealing plate),

$$\begin{aligned} &2\beta_{s2}\gamma_{s1s2}T_{10}^{i+1} + [\beta_{s2}(3-2\gamma_{s2s1})+1]T_{11}^{i+1} - \beta_{s2}T_{12}^{i+1} \\ &= 2\beta_{s2}\gamma_{s1s2}T_{10}^{i} - [\beta_{s2}(3-2\gamma_{s2s1})-1]T_{11}^{i} + \beta_{s2}T_{12}^{i} + n_l\theta'_{l2}T_l^i - n_l\theta'_{l2}T_A \end{aligned} \tag{5.22}$$

For layers 12-19 ($j = 12-19$, steel sealing plate),

$$\begin{aligned} &-2\beta_{s2}T_{j-1}^{i+1} + (2\beta_{s2}+1)T_j^{i+1} - \beta_{s2}T_{j+1}^{i+1} \\ &= \beta_{s2}T_{j-1}^{i} - 2(\beta_{s2}-1)T_j^i + \beta_{s2}T_{j+1}^{i} + n_l\theta'_{l2}T_l^i - n_l\theta'_{l2}T_A \end{aligned} \tag{5.23}$$

For layer 20 (steel sealing plate),

$$\begin{aligned} &-\beta_{s2}T_{19}^{i+1} + [\beta_{s2}(3-2\gamma_{s2r})+1]T_{20}^{i+1} - 2\beta_{s2}\gamma_{rs2}T_{21}^{i+1} \\ &= \beta_{s2}T_{19}^{i} - [\beta_{s2}(3-2\gamma_{s2r})-1]T_{20}^{i} + 2\beta_{s2}\gamma_{rs2}T_{21}^{i} + n_l\theta'_{l2}T_l^i - n_l\theta'_{l2}T_A \end{aligned} \tag{5.24}$$

For layer 21 (HDR laminate),

$$\begin{aligned} &-2\beta_r\gamma_{s2r}T_{20}^{i+1} + [\beta_r(3-2\gamma_{rs2})+1]T_{21}^{i+1} - \beta_r T_{22}^{i+1} \\ &= 2\beta_r\gamma_{s2r}T_{20}^{i} - [\beta_r(3-2\gamma_{rs2})-1]T_{21}^{i} + \beta_r T_{22}^{i} + \frac{\dot{w}_{22}^{i}\Delta t}{c_r\rho_r} \end{aligned} \tag{5.25}$$

For layers 22, 25 ($j = 22, 25$, HDR laminate),

$$\begin{aligned} &-\beta_r T_{j-1}^{i+1} + [\beta_r(3-2\gamma_{rs3})+1]T_j^{i+1} - 2\beta_r\gamma_{s3r}T_{j+1}^{i+1} \\ &= \beta_r T_{j-1}^{i} - [\beta_r(3-2\gamma_{rs3})-1]T_j^{i} + 2\beta_r\gamma_{s3r}T_{j+1}^{i} + \frac{\dot{w}_{j}^{i}\Delta t}{c_r\rho_r} \end{aligned} \tag{5.26}$$

where $\beta_{s3} = \frac{\alpha_s\Delta t}{2(\Delta x_{s3})^2}$; $\gamma_{s3r} = \frac{k_s\Delta x_r}{k_s\Delta x_r + k_r\Delta x_{s3}}$; $\gamma_{rs3} = \frac{k_r\Delta x_{s3}}{k_s\Delta x_r + k_r\Delta x_{s3}}$.

For layers 23, 26 ($j = 23, 26$, steel shim plate),

$$\begin{aligned} &-4\beta_{s3}\gamma_{rs3}T_{j-1}^{i+1} + [8\beta_{s3}(1-\gamma_{s3r})+1]T_j^{i+1} - 4\beta_{s3}\gamma_{rs3}T_{j+1}^{i+1} \\ &= 4\beta_{s3}\gamma_{rs3}T_{j-1}^{i} - [8\beta_{s3}(1-\gamma_{s3r})-1]T_j^{i} + 4\beta_{s3}\gamma_{rs3}T_{j+1}^{i} + n_l\theta'_{l2}T_l^i - n_l\theta'_{l2}T_A \end{aligned} \tag{5.27}$$

For layers 24, 27 ($j = 24, 27$, HDR laminate),

$$\begin{aligned} &-2\beta_r\gamma_{s3r}T_{j-1}^{i+1} + [\beta_r(3-2\gamma_{rs3})+1]T_j^{i+1} - \beta_r T_{j+1}^{i+1} \\ &= 2\beta_r\gamma_{s3r}T_{j-1}^{i} - [\beta_r(3-2\gamma_{rs3})-1]T_j^{i} + \beta_r T_{j+1}^{i} + \frac{\dot{w}_{j}^{i}\Delta t}{c_r\rho_r} \end{aligned} \tag{5.28}$$

For layer 28 (HDR laminate),

$$\begin{aligned} &-\beta_r T_{27}^{i+1} + [\beta_r(3-2\gamma_{rs4})+1]T_{28}^{i+1} - 2\beta_r\gamma_{s4r}T_{29}^{i+1} \\ &= \beta_r T_{27}^{i} - [\beta_r(3-2\gamma_{rs4})-1]T_{28}^{i} + 2\beta_r\gamma_{s4r}T_{29}^{i} + \frac{\dot{w}_{28}^{i}\Delta t}{c_r\rho_r} \end{aligned} \tag{5.29}$$

where $\beta_{s4} = \frac{\alpha_s \Delta t}{2(\Delta x_{s4})^2}$; $\gamma_{s4r} = \frac{k_s \Delta x_r}{k_s \Delta x_r + k_r \Delta x_{s4}}$; $\gamma_{rs4} = \frac{k_r \Delta x_{s4}}{k_s \Delta x_r + k_r \Delta x_{s4}}$.

For layers 29 (steel shim plate),

$$\begin{aligned} &-4\beta_{s4}\gamma_{rs4}T_{28}^{i+1} + [4\beta_{s4}(1-\gamma_{s4r})+1]T_{29}^{i+1} \\ &= 4\beta_{s4}\gamma_{rs4}T_{28}^{i} - [4\beta_{s4}(1-\gamma_{s4r})-1]T_{29}^{i} + n_l\theta'_{l2}T_l^i - n_l\theta'_{l2}T_A \end{aligned} \tag{5.30}$$

For single lead core,

$$T_l^{i+1} = (1-2\theta_{l1}-\theta_{l2})T_l^i + (2\theta_{l1}+\theta_{l2})T_A + \frac{\dot{w}_l^i \Delta t}{c_l \rho_l} \tag{5.31}$$

where $\theta_{l2} = \frac{n_l \Delta t}{c_l \rho_l} \cdot \frac{A_{l2}}{V_l} \cdot \frac{pk_s}{0.785 r_l (t^+)^{\frac{1}{3}}}$.

Combining all the heat equations for each layer and lead core, a system of linear equations of the thermo-mechanical model can be represented as

$$\begin{aligned} &\begin{bmatrix} B_1^{i+1} & C_1^{i+1} & 0 & \dots & 0 & 0 \\ A_2^{i+1} & B_2^{i+1} & C_2^{i+1} & \dots & 0 & 0 \\ \vdots & \ddots & \ddots & \ddots & \vdots & \vdots \\ 0 & 0 & \dots & B_{n-1}^{i+1} & C_{n-1}^{i+1} & 0 \\ 0 & 0 & \dots & A_n^{i+1} & B_n^{i+1} & 0 \\ 0 & 0 & \dots & 0 & 0 & 1 \end{bmatrix} \begin{Bmatrix} T_1^{i+1} \\ T_2^{i+1} \\ \vdots \\ T_{n-1}^{i+1} \\ T_n^{i+1} \\ T_l^{i+1} \end{Bmatrix} \\ &= \begin{bmatrix} B_1^i & C_1^i & 0 & \dots & 0 & D_1^i \\ A_2^i & B_2^i & C_2^i & \dots & 0 & D_2^i \\ \vdots & \ddots & \ddots & \ddots & \vdots & \vdots \\ 0 & 0 & \dots & B_{n-1}^i & C_{n-1}^i & D_{n-1}^i \\ 0 & 0 & \dots & A_n^i & B_n^i & D_n^i \\ 0 & 0 & \dots & 0 & 0 & D_l^i \end{bmatrix} \begin{Bmatrix} T_1^i \\ T_2^i \\ \vdots \\ T_{n-1}^i \\ T_n^i \\ T_l^i \end{Bmatrix} + \boldsymbol{\theta^i} T_A + \boldsymbol{w^i} \end{aligned} \tag{5.32}$$

where A_j^i, B_j^i, and C_j^i are coefficients of T_{j-1}^i, T_j^i, and T_{j+1}^i in heat equation of layer j; $\boldsymbol{\theta^i}$ is the temperature coefficient vector with $n \times 1$; $\boldsymbol{w^i}$ is the heat generation vector with $n \times 1$.

The equations can be shortened as

$$\boldsymbol{K^{i+1} t^{i+1}} = \boldsymbol{K^i t^i} + \boldsymbol{\theta^i} T_A + \boldsymbol{w^i} \tag{5.33}$$

where $\boldsymbol{K^{i+1}}$ and $\boldsymbol{K^i}$ are coefficient matrices of temperature vectors $\boldsymbol{t^{i+1}}$ and $\boldsymbol{t^i}$.

Note that the lead cores are covered by the confinement springs in this case. The heat generated from the lead core cannot be transferred to the surrounding sealing and shim plates, as shown in Fig. 5.2a. Therefore, the heat conduction coefficient between the lead core and surrounding sealing and shim plates, θ'_{l2} (or θ_{l2}) is set to 0. The numerical results will be analyzed and compared with the tests for model validation.

5.3 Restoring Force Model

5.3.1 Basic assumptions

The rate-dependent hysteretic model for LHDR bearings is composed of the HDR part and the lead core part. The rheology model is shown in Fig. 5.5. The hysteretic behavior of HDR is modeled using the multi-layer temperature-dependent Bouc-Wen (MTBW) model, while that of lead core is modeled using the bilinear (BL) model. A series combination of a dashpot and spring is utilized to simulate the rate-dependent characteristics of the bearing.

The general assumptions are as follows:

(1) The total displacement of the bearing will be distributed among rubber layers according to their respective stiffness. The displacement of the single lead core is equal to the total displacement of the bearing.
(2) The total restoring force of the bearing is the addition of the force of HDR laminates, rate dependence, and lead cord. The restoring force of each rubber layer should be equal, which also represents the overall restoring force of the bearing.
(3) Since heat is generated and transferred outward, the temperature will not be distributed uniformly. The temperature at the center of the rubber layer represents the temperature of that layer and is used in the calculation of the MTBW model.

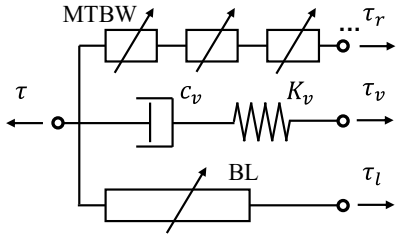

Figure 5.5 Rheology model of LHDR bearing.

5.3.2 Restoring force model

The restoring force and displacement relationship of MTBW model can be expressed as

$$f_r(t) = \alpha_1 e^{m_r \times \frac{T_r(t)-23}{100}} K_r d_r(t) + [1 + b(d_r\,(t)/t_r)^2](1-\alpha_1) e^{n_r \times \frac{T_r(t)-23}{100}} K_r Z_r(t) \quad (5.34)$$

where

$$\dot{Z}_r(\mathrm{t}) = \dot{d}_r(\mathrm{t}) - \beta\left|\dot{d}_r(\mathrm{t}) Z_r(\mathrm{t})\right| Z_r(\mathrm{t}) - \gamma \dot{d}_r(\mathrm{t}) Z_r^2(t) \quad (5.35)$$

$$\beta = \frac{1}{(1+s) d_y^2} \quad (5.36)$$

$$\gamma = s \cdot \beta \quad (5.37)$$

where α_1 is the post-yielding stiffness ratio; m_r and n_r are parameters describing temperature

dependence; $T_r(t)$ is the temperature at the center of single HDR laminate; K_r is the initial stiffness of each HDR laminate; $d_r(t)$ is the input horizontal displacement of each HDR laminate; t_r is the thickness of each HDR laminate; $Z_r(t)$ is the hysteretic component of restoring force of each HDR laminate; b, A, β, γ, and s are dimensionless parameters of hysteresis curve; d_y is the yield displacement. The Euler scheme is adopted to numerically solve the restoring force-displacement equation.

The rate dependence is represented by a dashpot and a spring in series, with the parameters of the dashpot constant (c_v) and the spring constant (K_v). The restoring force related to the rate dependence (f_v) can be expressed as

$$f_v = c_v \dot{d}_d = K_v d_s \tag{5.38}$$

where d_d is the displacement of the dashpot; d_s is the displacement of the spring. The sum of d_d and d_s should be the total displacement of the LHDR bearing (d), written as

$$d = d_d + d_s \tag{5.39}$$

The hysteretic behavior of the lead core is indicated by the BL model (as shown in Fig. 5.5), with the parameters of initial stiffness (K_l) and characteristic strength ($Q_l = 11.21$ kN). The characteristic strength can be by multiplying the yield stress ($\sigma_{Yl} = 12.0$ N/mm^2, in this case) by the cross-sectional area of the single lead core (A_l). Note that the secondary stiffness of the BL model is zero.

The total restoring force of the rubber bearing (f) can be obtained by adding the HDR laminate (f_r), rate dependence (f_v), and lead cord (f_l) parts, as

$$f = f_r + f_v + f_l \tag{5.40}$$

In general, the proposed model elaborated on the interacted heating effect of HDR laminate and lead core and the heat conduction within the LHDR bearings. The hysteretic behavior of LHDR bearings affected by the thermal mechanism and rate dependence is presented, which differs from a simple combination of the models of HDR bearing and LR bearing. This model provided an effective way to reflect the real hysteretic behavior of the LHDR bearings.

5.4 Model Validation

5.4.1 Validation of cyclic loading

5.4.1.1 Parameter identification

The parameters of the bearing hysteretic model in Eqs. (5.34)-(5.37) are identified from the cyclic loading tests according to the design manual. These parameters are used in the time history analysis to evaluate the seismic performance of isolated structures with bearings without the need for shaking table tests. The KH method mentioned in Chapter 4 is used for parameter identification. Table 5.2 presents one set of parameters of the rate-dependent thermal coupled hysteretic model for LHDR bearings, which is identified from cyclic loading tests at three ambient temperatures.

Table 5.2 Identified parameters of the model of LHDR.

α_1	K_r (kN/mm)	s	d_y (mm)	b	m_r	n_r	c_v	K_v (kN/mm)	K_l (kN/mm)
0.313	26.783	-0.800	1.208	0.457	-1.924	-3.299	0.213	1.890	22.066

5.4.1.2 Hysteresis curve and temperature prediction

The comparison of hysteresis curves between the model and experimental results under cyclic loading tests at ambient temperatures of −20°C, 0°C, and 23°C is shown in Fig. 5.6. The hysteresis curves of the numerical results show good agreement with the experimental data, indicating that the proposed model well captures the stiffness degradation and temperature dependence of LHDR bearings at three different ambient temperature cases. Note that the model underestimates the maximum stress of the first cycle in each strain amplitude. The phenomenon of the stiffness degradation between the first and second cycles is called the scragging effect in rubber laminates, which is not considered in this model. Moreover, the force contribution of rate dependence is small in cyclic loading tests due to the lower rate.

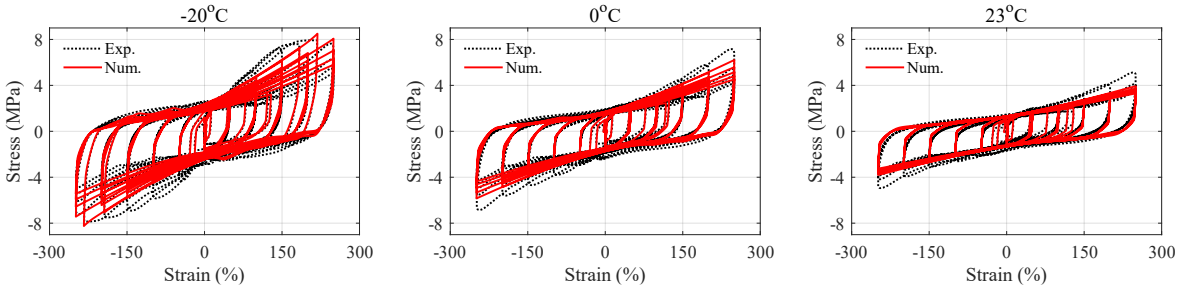

Figure 5.6 Hysteresis curve of the model of LHDR bearing compared with experimental results under cyclic loading at −20°C, 0°C, and 23°C.

The validation of the equivalent shear modulus and damping ratio for the first, second, and fifth cycles in each strain amplitude at three ambient temperature cases is shown in Fig. 5.7. The error for nearly all values remains well within 15%, demonstrating that the thermo-coupled hysteretic model effectively describes the hysteretic behavior of LHDR bearings with accuracy.

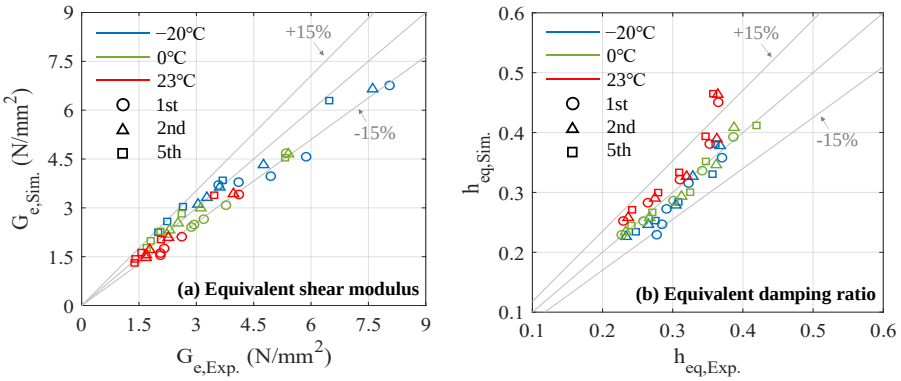

Figure 5.7 Validation of the model of LHDR bearing compared with experimental results

under cyclic loading at −20℃, 0℃, and 23℃: (a) equivalent shear modulus and (b) equivalent damping ratio.

The temperature history of the first and third rubber layers and the lead core is shown in Fig. 5.8. The numerical results are compared with the experimental data in five strain amplitudes separately at three ambient temperature cases. The temperature history of the experiment is measured by the thermocouples placed in the rubber layers and lead core, as shown in Fig. 3.3b. During loading, the internal temperature of the lead core rises significantly compared with the rubbers, while during cooling, its temperature decreases quickly. This is because the lead core has a smaller specific heat than that of the rubber, leading to the internal temperature rising rapidly during loading. Additionally, compared with the rubber material, the larger thermal conductivity of the lead core facilitates the rapid transfer of accumulated heat to the outside, resulting in a sudden temperature drop. Note that the experimental data indicates slight variations in temperature distribution across various locations of single HDR laminate as well as the lead core at different heights. However, these differences are assumed to be uniform for model simplification. The proposed model can well predict the time history of the HDR laminate and lead core during loading, while the temperature drop during cooling is slightly underestimated but deemed acceptable due to the temperature distribution assumption at ambient temperatures of 0℃ and 23℃. Despite the absence of data for −20℃, it is reasonable to infer the reliability of the temperature history based on the temperature increase of each component across five strain amplitudes.

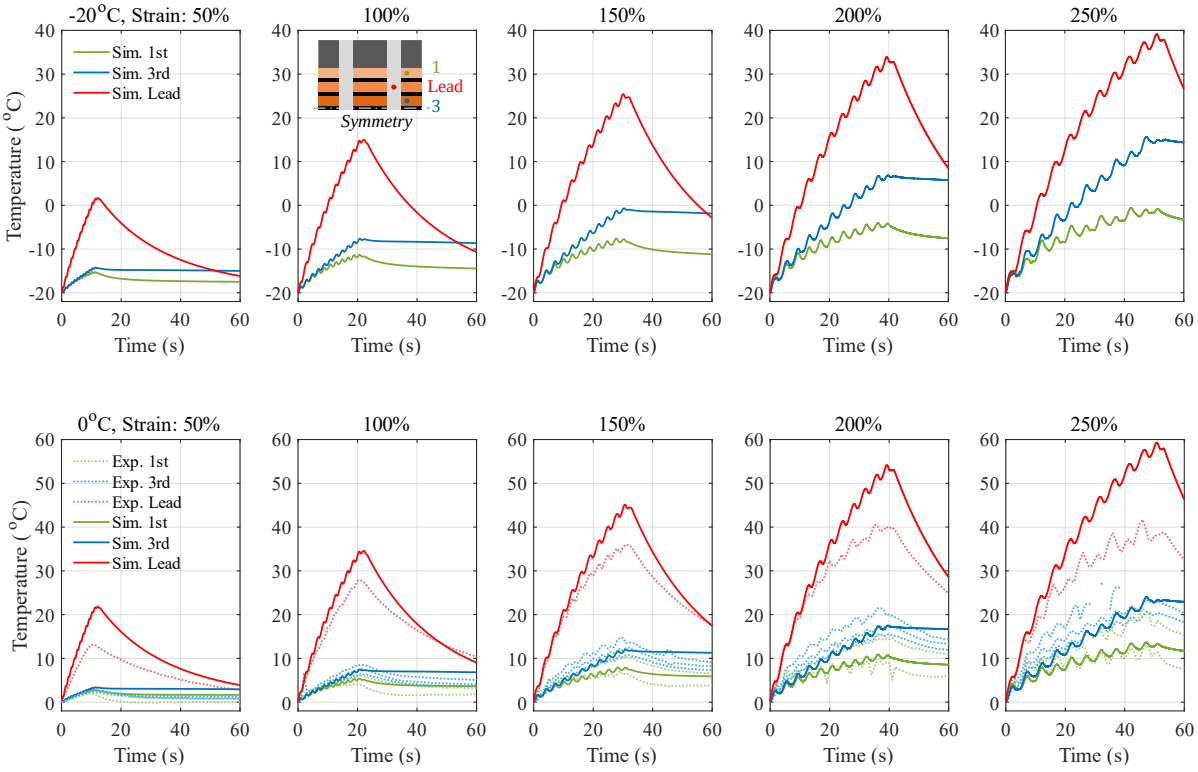

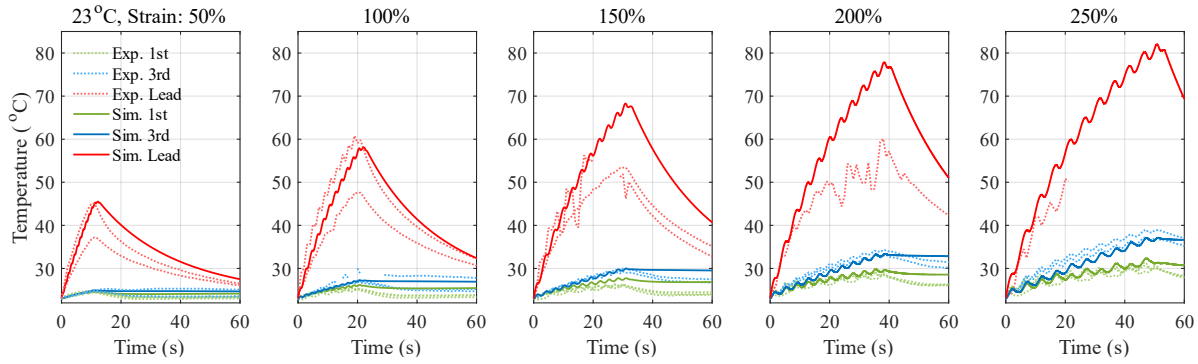

Figure 5.8 Temperature history of rubber layers computed by the model of LHDR and test results under cyclic loading at −20℃, 0℃, and 23℃.

5.4.2 Validation of hybrid simulation

5.4.2.1 Hysteresis curve of LHDR bearing

Only one set of the identified parameters in Table 5.2 is input into the time history analysis. The first 20-second response of the LHDR bearing is taken into analysis. The hysteresis curves of real-time and pseudo-dynamic loading are shown in Figs. 5.9 and 5.12, respectively. The hysteresis curves of the proposed model are compared with the experimental results and the previous TMC MPW model at ambient temperatures of −20℃, 0℃, and 23℃. The strain time history of the bearings is shown in Figs. 5.10 and 5.13. The hysteretic behavior of the LHDR, including the maximum (minimum) force (F+(−)), maximum (minimum) displacement (D+(−)), energy dissipation of the maximum loop (MaxE), and coefficient of determination (R^2) are compared in Fig. 5.11 and 5.14. The hysteretic behavior can be well simulated by the proposed model and the TMC MPW model. However, the proposed model presents improved accuracy including the prediction of the maximum or minimum force and displacement, as well as the coefficient of determination. In addition, the characteristic of rate dependence is simulated by the proposed model, represented by the smoother corner when the loading direction is changed.

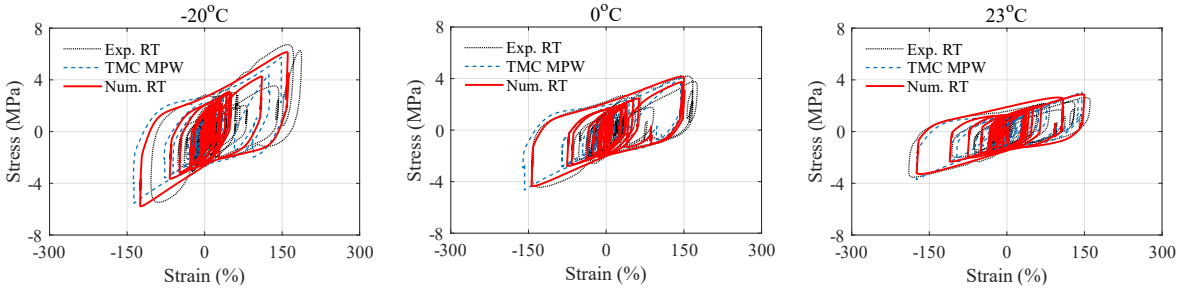

Figure 5.9 Hysteresis curve of the model of LHDR compared with experimental results and previous TMC MPW model under real-time hybrid simulation at −20℃, 0℃, and 23℃.

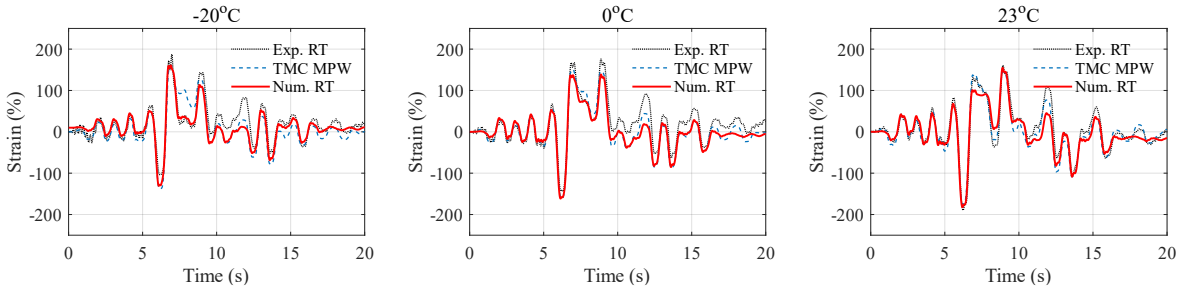

Figure 5.10 Strain time history of the model of LHDR compared with experimental results and previous TMC MPW model under real-time hybrid simulation at −20℃, 0℃, and 23℃.

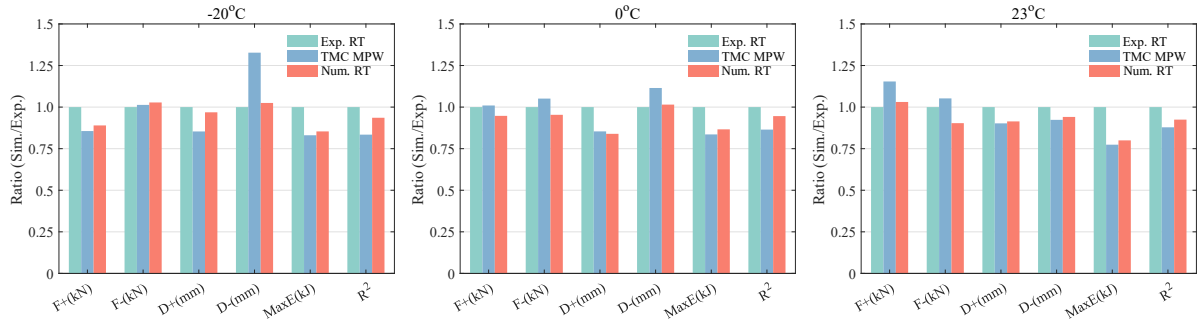

Figure 5.11 Validation of real-time hybrid simulation: F+(−): maximum (minimum) force; D+(−): maximum (minimum) displacement; MaxE: energy dissipation of maximum loop; R2: coefficient of determination.

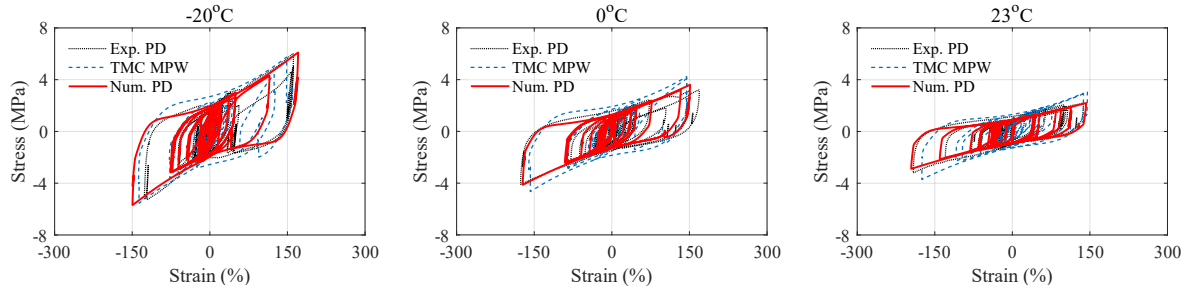

Figure 5.12 Strain time history of the model of LHDR compared with experimental results and previous TMC MPW model under pseudo-dynamic hybrid simulation at −20℃, 0℃, and 23℃.

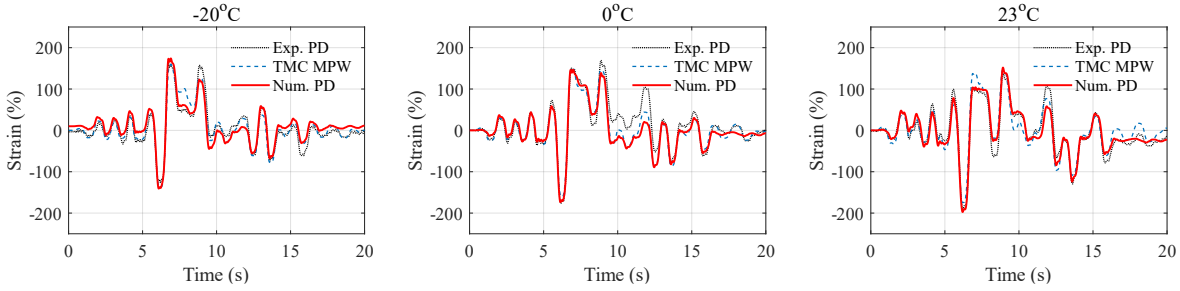

Figure 5.13 Strain time history of the model of LHDR compared with experimental results

and previous TMC MPW model under pseudo-dynamic hybrid simulation at −20℃, 0℃, and 23℃.

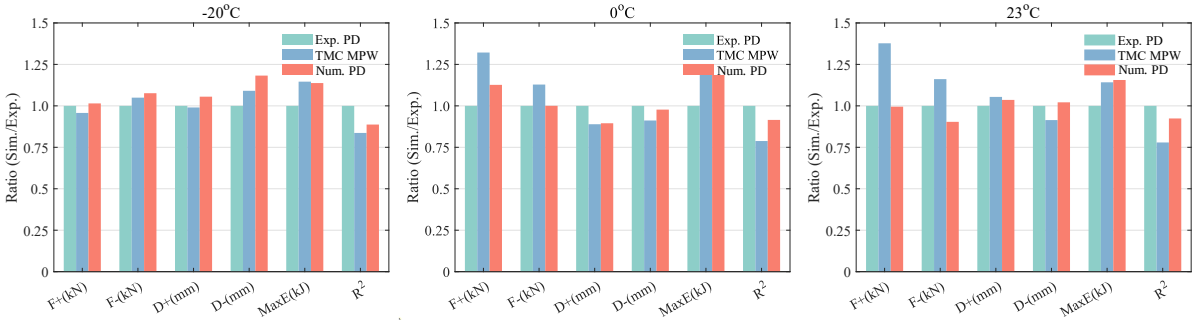

Figure 5.14 Validation of pseudo-dynamic hybrid simulation: F+(−): maximum (minimum) force; D+(−): maximum (minimum) displacement; MaxE: energy dissipation of maximum loop; R2: coefficient of determination.

The contributions of the force of the lead core (f_l), the HDR laminate (f_r), and the rate dependence (f_v) under real-time and pseudo-dynamic hybrid simulations are shown in Fig. 5.15. In the numerical simulation of the force-time history curve, the peak force of the real-time loading in each cycle was slightly larger than that of the pseudo-dynamic loading due to the higher loading rate. The force proportion of the loading rate in real-time loading was larger than that in pseudo-dynamic loading as expected. The force proportion of the loading rate decreased with the drop in the ambient temperature, which was because the increase in the stiffness of the rubber at low ambient temperature enlarged the force proportion of the rubber. Moreover, the force proportion of the loading rate at the beginning of pseudo-dynamic loading accounted for over 75% because the constant loading rate of 10 mm/s was relatively larger than that in real-time loading at the beginning, resulting in a larger force.

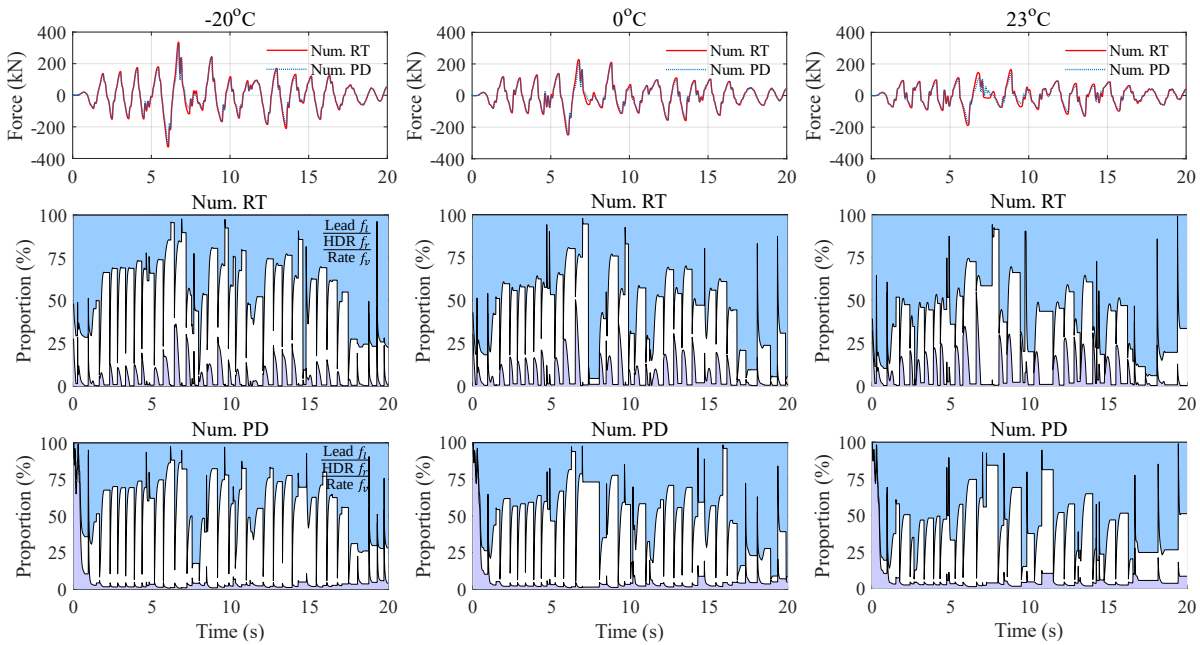

Figure 5.15 Contributions of force of lead core (f_l), HDR laminate (f_r), and rate dependence (f_v) under real-time and pseudo-dynamic hybrid simulations.

5.4.2.2 Temperature history prediction of LHDR bearing

The temperature history of the real-time hybrid simulation tests at three temperature cases is shown in Fig. 5.16. The multi-layer thermal-coupled model shows advantages in predicting the temperature history of each layer, while the TMC MPW model only simulates a single-point temperature history representing the entire bearing. The temperature history predicted by the proposed model closely matches the trend observed in the experimental data. Despite the lack of data on the lead core at 23°C due to the failure of the thermocouples in the lead core, it can be reasonably inferred that the results predicted by the model are reliable.

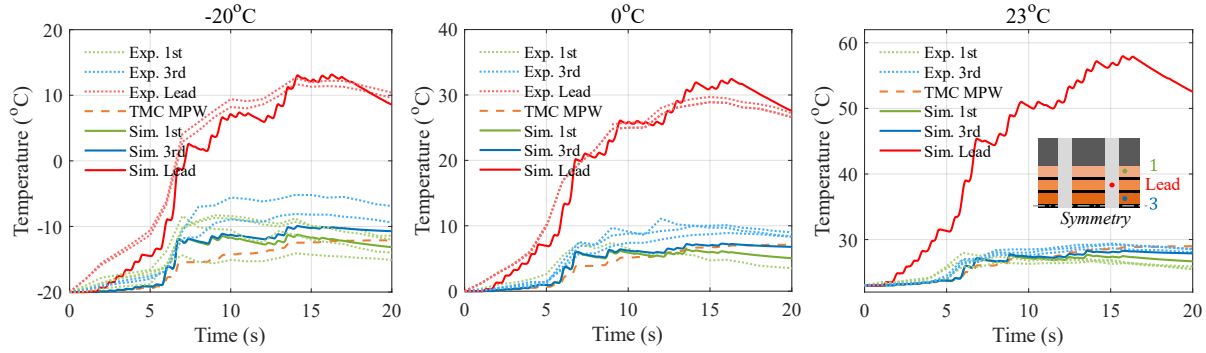

Figure 5.16 Temperature history of the model of LHDR bearing compared with experimental results and previous TMC MPW model under real-time hybrid simulation at −20°C, 0°C, and 23°C.

The temperature profile along the vertical direction of the LHDR bearings at different times is

shown in Fig. 5.17. The solid line represents the temperature distribution of the HDR and steel plates, while the dotted line represents that of the lead core. The temperature profile of the HDR and steel plates exhibits a sawtooth-like distribution due to the limited transfer of heat from the HDR laminate to the steel plate within a short timeframe. The temperature difference becomes significant as the intensity of the input ground motion increases. The temperature of the lead core shows rapid change during loading. Note that the peak points of temperature are found at the height of 48 mm, corresponding to the interface between the sealing and end plates, shown as layers 10 and 11 in Fig. 5.2b. Based on the assumption that the heat generated within the lead core is transferred solely along its upper and lower interfaces, the heat would accumulate in these interfaces before transferring to adjacent layers.

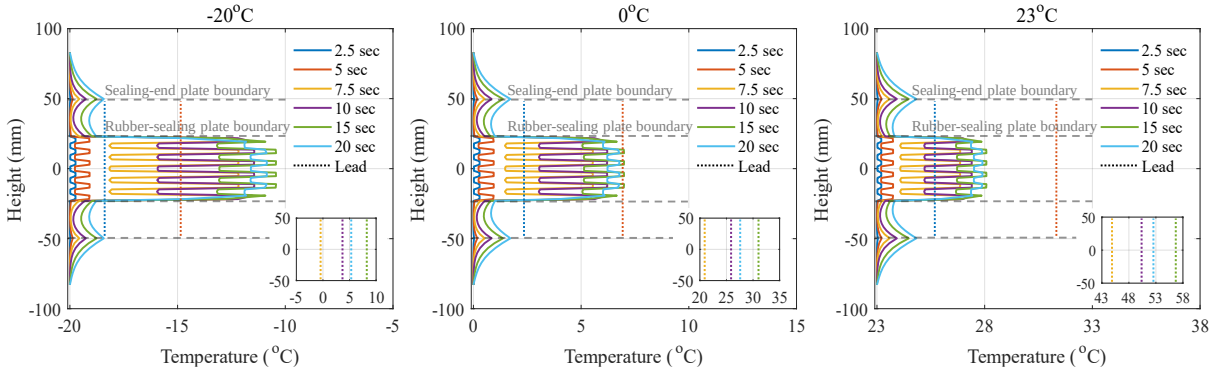

Figure 5.17 Temperature distribution of the model of LHDR bearing along vertical direction of the bearing under real-time hybrid simulation at −20℃, 0℃, and 23℃.

5.4.2.3 Structural response

The pier top acceleration and displacement of the MTBW model compared with the experiment results under the real-time hybrid simulation are shown in Figs. 5.18 and 5.19. The proposed model of LHDR bearing exhibits underestimation of the pier top acceleration at −20℃ and 0℃. But it can well capture the pier top displacement of isolated bridge model with HDR bearing at three ambient temperatures.

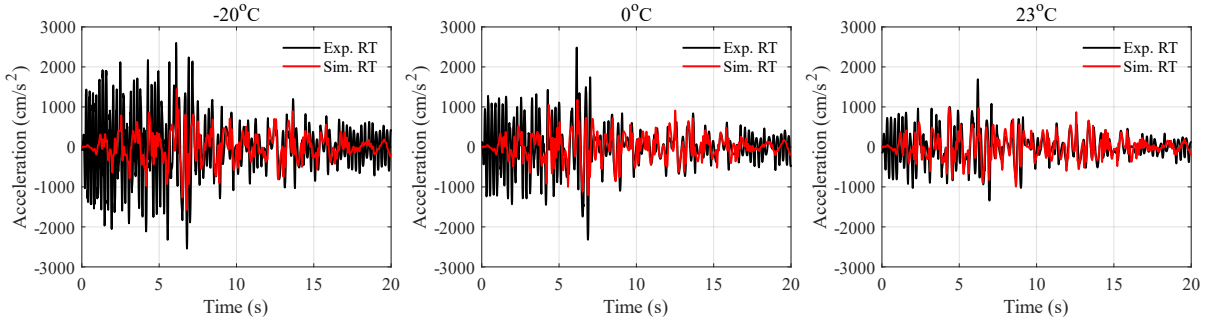

Figure 5.18 Pier top acceleration of the model of LHDR bearing compared with experimental results under real-time hybrid simulation at −20℃, 0℃, and 23℃.

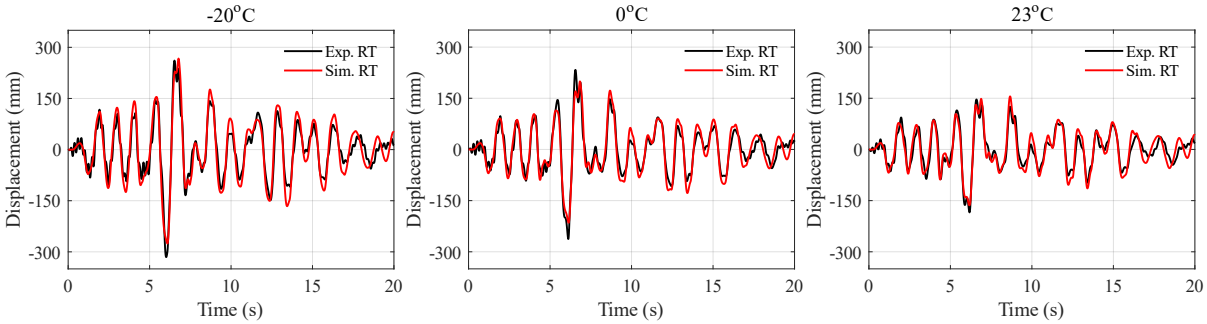

Figure 5.19 Pier top displacement of the model of LHDR bearing compared with experimental results under real-time hybrid simulation at −20℃, 0℃, and 23℃.

The pier top acceleration and displacement of the MTBW model compared with the experiment results under the pseudo-dynamic hybrid simulation are shown in Figs. 5.20 and 5.21. The proposed model can well capture the structure response of an isolated bridge model with HDR bearing at three ambient temperatures.

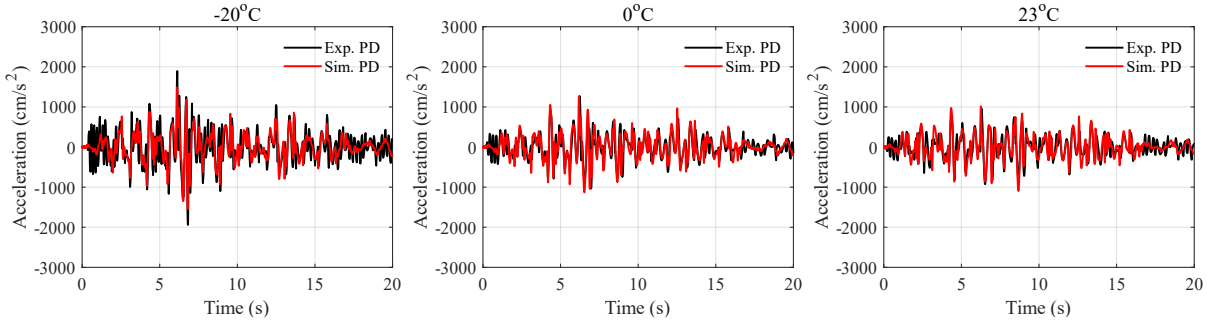

Figure 5.20 Pier top acceleration of the model of LHDR bearing compared with experimental results under pseudo-dynamic hybrid simulation at −20℃, 0℃, and 23℃.

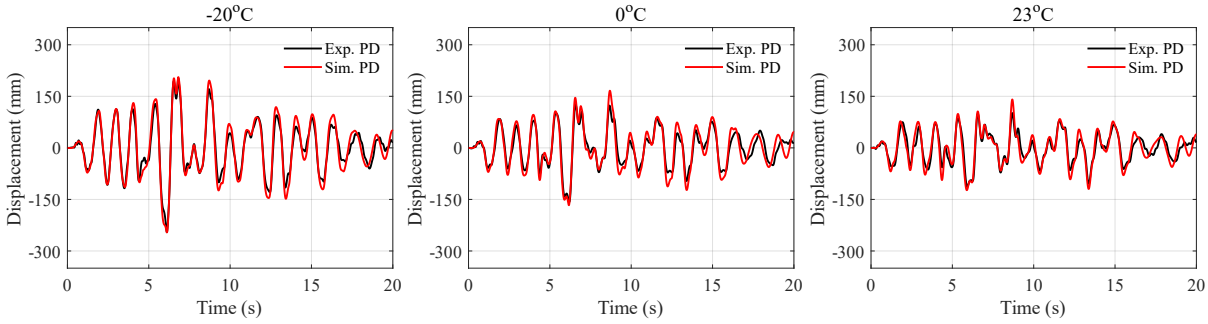

Figure 5.21 Pier top displacement of the model of LHDR bearing compared with experimental results under pseudo-dynamic hybrid simulation at −20℃, 0℃, and 23℃.

5.5 Discussion

In this chapter, a rate-dependent thermo-mechanical coupling hysteretic model was proposed

for LHDR bearings to illustrate the hysteretic behavior considering thermal mechanism and rate dependence. The heat transfer and heating effect of the LHDR bearings was illustrated by the proposed thermo-mechanical model. The temperature history was predicted and validated by the cyclic loading with inner temperature control and hybrid simulation at different ambient temperatures. The rate-dependent property of LHDR bearings was reflected in the proposed hysteretic model and verified by the real-time and pseudo-dynamic hybrid simulations. Here are the main points to be discussed:

(1) A rate-dependent thermo-mechanical coupling hysteretic model was proposed for LHDR bearings to illustrate the hysteretic behavior. Different from the model proposed in Chapter 4, this model considers the interaction of the heating effect between the HDR laminate and lead core, illustrating the thermal mechanism of the LHDR bearing. Moreover, the factor of rate dependence is also included in this model.

(2) The heat conduction and heating effect in HDR laminates, lead cores, and steel plates were modeled by the thermo-mechanical model. The temperature history was accurately predicted and validated by the cyclic loading and hybrid simulation at −20℃, 0℃, and 23℃. The nonlinearly distributed temperature profile of the LHDR bearing was presented to illustrate the direct distribution of temperature as the loading time varied.

(3) The thermal-coupled hysteretic model accurately captured the hysteretic behavior of LHDR bearings, including the stiffness degradation and temperature dependence, under cyclic loading and hybrid simulation. One set of parameters of the model was identified by the optimization algorithm to represent the behavior of the bearings at different ambient temperatures. The rate dependence property of the LHDR bearing was incorporated into the proposed model and validated by real-time and pseudo-dynamic hybrid simulations. The proposed model demonstrated the improved accuracy of the hysteretic behavior compared to the existing model.

(4) Future research endeavors will primarily concentrate on verifying the significant effect of temperature on the seismic response of bridges using this model. Although the 2-DOF model of the pier is set up in the hybrid simulation, a full model of the bridge needs to be established to evaluate the structural response considering the variation of the temperature, which will be discussed in Chapter 6.

CHAPTER 6

EFFECT OF LOW TEMPERATURE ON SEISMIC RESPONSE OF ISOLATED BRIDGES WITH HDR/LHDR BEARINGS

Chapter 6 develops an isolated bridge model with HDR and LHDR bearings to investigate the effects of low temperature on the seismic response of isolated structures. A 6-span continuous bridge with a spread foundation is selected as the numerical model for time history analysis. The proposed multi-layer thermo-mechanical models of elastomeric bearings in chapters 4 and 5 are included in the analysis. The hysteretic behavior of bearings and the response of the structure are discussed to evaluate the effect of low temperature on the seismic behavior of the isolated bridges.

6.1 General

Seismic isolation is a well-established technology for structures of bridges, buildings, and other infrastructure in earthquake-prone regions. By isolating the structure from the ground motion during an earthquake, seismic isolation extends the natural period of bridges to avoid resonance which may lead to major damage or even collapse. The adequate flexibility of bridges can be ensured by applying effective seismic isolation technology, reducing the acceleration of the bridge deck and the shear force transmitted to the substructure.

The effect of low temperature on the isolated bearings has attracted significant attention due to the temperature sensitivity of the rubber material. Numerous studies have shown that the mechanical properties of the bearing will change at low temperatures. The equivalent shear modulus and damping ratio will increase as the temperature decreases, which is also proven by this research. Accordingly, the seismic response of the isolated bridge will be also changed. Specifically, the maximum displacement of the bearing would be overestimated, and the maximum shear force of the bearing and displacement of the pier top would be underestimated under low temperatures. It indicates that the low-temperature effect may have a notable effect on the response of the structures.

However, the most current specifications, such as JRA Specifications for Highway Bridges. Part V: Seismic Design (2019); AASHTO Guide Specification for Seismic Isolation Design (2010); EN 15,129: Anti-Seismic Devices (2018) do not consider the temperature effect and require the low-temperature testing of isolated bearings. Only the newest version of the Canadian Highway Bridge Design Code (2014) adds the requirement of testing for isolated bearings at low temperatures. The ignorance of the low-temperature effect on the structures may result in the unsafety estimation of the seismic performance of the structures.

Moreover, although the multi-layer thermo-mechanical models for high damping rubber (HDR) and lead high damping rubber (LHDR) bearings in chapters 4 and 5 have been validated in the hybrid simulation with realistic earthquake and numerical pier model, a full bridge model needs to be established to evaluate the hysteretic behavior of bearing and seismic response of structure considering the yielding of the pier and the foundation under low temperature.

This chapter aims to capture the effect of low ambient temperature on isolated bridges with HDR or LHDR bearings. The full isolated bridge model based on the highway bridge design is established to conduct time history analysis and further validate the multi-layer thermo-mechanical models for HDR and LHDR bearings. The designed HDR bearing with the bilinear model is replaced by the HDR and LHDR bearings with multi-layer temperature-dependent Bouc-Wen (MTBW). The hysteretic behavior and the energy dissipation of the bearing, and the response of the bridge, including the relative displacement of the pier top, the bending moment of the pier base, and the acceleration of the superstructure, are evaluated at −20℃, 0℃, and 23℃.

6.2 Isolated Bridge Model

6.2.1 Prototype of isolated bridge

A five-span continuous highway bridge with HDR bearings is selected for analysis from Materials for Seismic Design of Road Bridges (1997). The bridge is designed according to the JRA Specifications for Highway Bridges. Part V: Seismic Design (2019). The HDR bearing is designed according to the Manual on Seismic Isolation and Vibration Control Design Methods for Highway Bridges (2011). The bridge is classified as a class B bridge in Specifications for Highway Bridges. Part V: Seismic Design (2019), which means the bridge is of particularly high importance in seismic design. The ground type of seismic design is type I. The type of the site is the sand below the support layer. Fig. 6.1a shows the elevation of the bridge and Fig. 6.1b shows the cross-section of the superstructure. The superstructure consists of a five-span continuous steel girder, with 40 m for each span. The superstructure is isolated by five HDR bearings at the bottom of each pier or abutment (G1-G5) to facilitate the longitudinal and transverse vibration of the deck resulting from the ground motion. The substructure consists of four piers with a height of 12 m. Fig. 6.2 illustrates the dimension of the design pier (P1). The pier is T-shaped with a spread foundation at the bottom. The inertial force acting position of the superstructure in the transverse direction is 2.5 m above the pier top, while that in the

longitudinal direction is on the pier top.

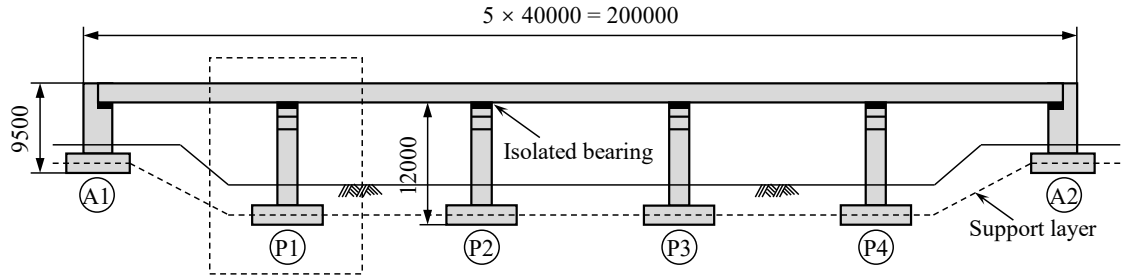

(a) Elevation of the bridge

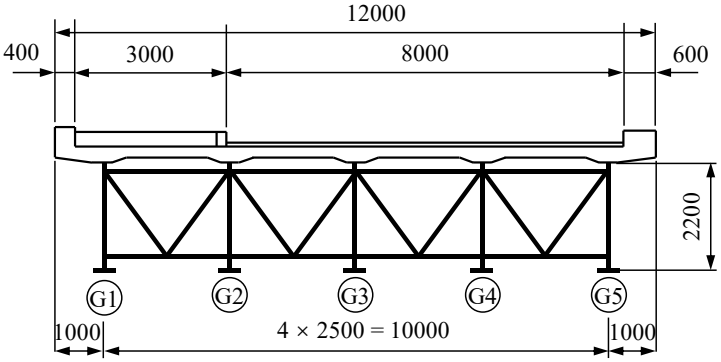

(b) Cross-section of the superstructure

Figure 6.1 Overview of design bridge.

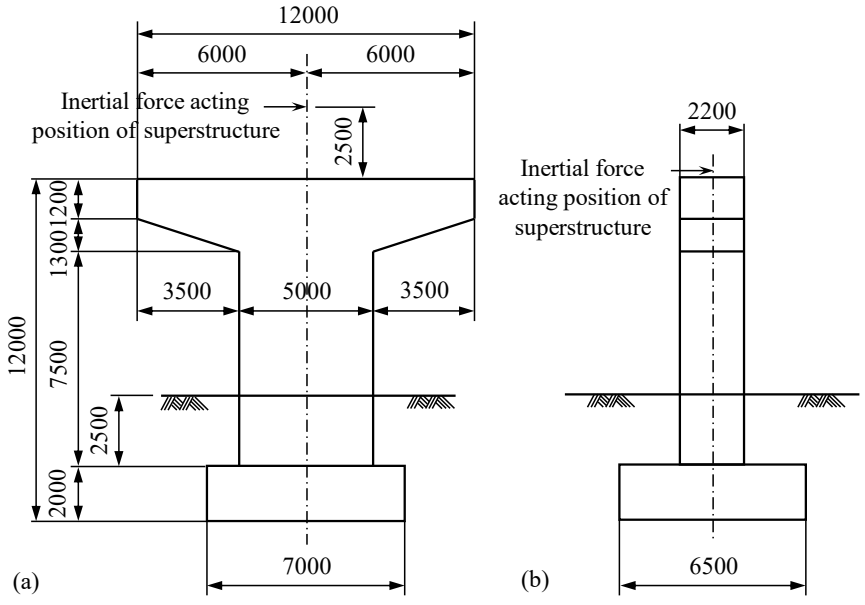

Figure 6.2 Dimension of the design pier 1 (P1): (a) Front view (transverse direction); (b) Side view (longitudinal direction).

6.2.2 Design of isolated bearing

According to the Manual on Seismic Isolation and Vibration Control Design Methods for Highway Bridges (2011), the bilinear model is used to represent the hysteretic behavior of HDR bearings. Fig. 6.3 shows the typical bilinear model for rubber bearings. The nonlinear hysteretic characteristics are shown in the bilinear model, including the first stiffness K_1, second stiffness K_2, characteristic strength Q_d. Based on the equivalent linearization method in the design model, the design equivalent stiffness K_B can be calculated by

$$K_B = \frac{G_e(\gamma_{uB}) \cdot A_e}{\sum t_e} \tag{6.1}$$

where G_e is the design equivalent shear modulus; γ_{uB} is the design shear strain corresponding to the design displacement u_B; A_e is the effective compression area of HDR bearing excluding the covered rubber on the side; $\sum t_e$ is the total thickness of the HDR.

The design equivalent shear modulus G_e can be calculated by

$$G_e(\gamma_{uB}) = c_0 + c_1\gamma_{uB} + c_2\gamma_{uB}^2 + \cdots + c_i\gamma_{uB}^i \tag{6.2}$$

where c_i is the parameters of the design equivalent shear modulus calculation (for HDR bearing, $i = 4$; for HDR-Super bearing, $i = 5$), which can be found in Table A.1 in Appendix A.

The design equivalent damping ratio h_B can be calculated by

$$h_B(\gamma_{uB}) = d_0 + d_1\gamma_{uB} + d_2\gamma_{uB}^2 + \cdots + d_i\gamma_{uB}^i \tag{6.3}$$

where d_i is the parameters of the design equivalent damping ratio calculation (for HDR bearing, $i = 3$; for HDR-Super bearing, $i = 4$), which can be found in Table A.2 in Appendix A.

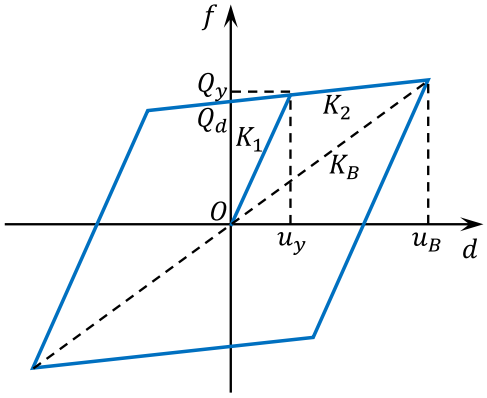

Figure 6.3 Hysteretic characteristics of HDR bearing design in bilinear model.

The design process of seismic performance of the bridge with isolated devices can be followed by Fig. 6.4. The design displacement of the HDR bearing is assumed after the design parameters, such as the thickness of rubber, and compression area of the bearing, are determined. The equivalent shear modulus and damping ratio are then calculated for the bilinear hysteretic model. If the above-mentioned characteristics of the bearing are in accordance with the required values, a nonlinear dynamic analysis will be conducted. The

maximum lateral displacement of the bearing in the dynamic analysis will be compared with the design displacement. If the difference between the maximum displacement and design displacement is no more than 10%, the design of the bearing is reasonable, and the seismic performance of the isolated bridge will be checked. If the difference is larger than 10%, the maximum displacement will replace the design one and the dynamic analysis will be repeated.

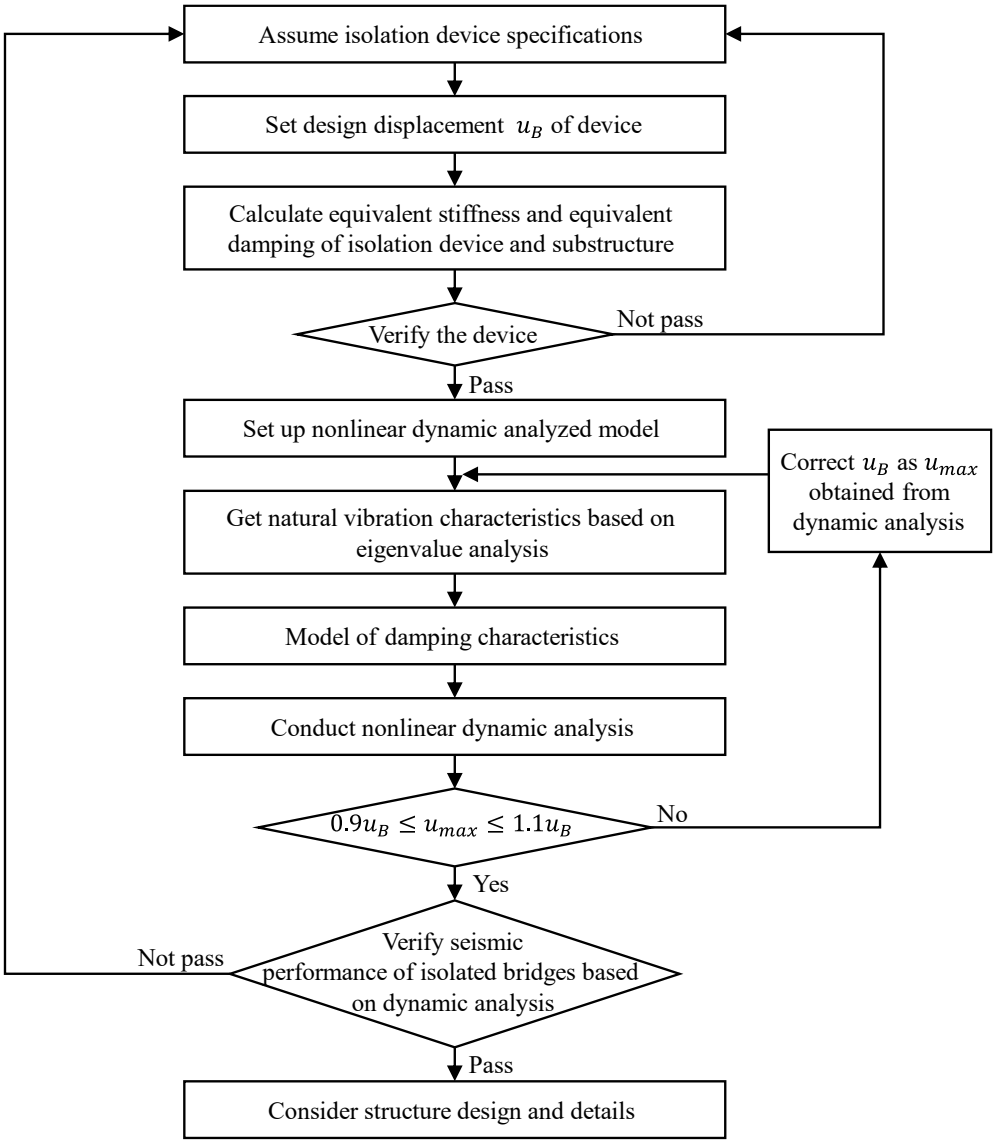

Figure 6.4 Seismic performance design process of the bridge with isolated devices.

Based on the design process of the bridge with isolated devices, the dimension of the HDR bearing is determined. The HDR bearing (use the bilinear model in design) with a shear modulus of 0.8 N/mm^2 (G8) has an effective sectional area of 600 mm × 600 mm and 8 HDR layers with 14 mm for each layer, listed in Table 6.1. The design parameters of HDR and LHDR bearings using the MTBW model are provided in Table 6.1 and will be discussed in the following sections.

Table 6.1 Design parameter of isolated bearing.

Design parameter	HDR bearing (bilinear model)	HDR bearing (MTBW model)	LHDR bearing (MTBW model)
Sectional area A_e (mm^2)	600×600	480×480	480×480
Thickness of HDR $\sum t_e$ (mm)	14×8	17×6	17×6
Compressive stress σ (MPa)	2.18	3.40	3.40
Shear modulus G (N/mm)	0.8	1.2	1.2
Equivalent stiffness K_B (N/mm)	2615.3	2633.1	2543.4
Number of lead core n_l	-	-	4
Diameter of lead core d_l (mm)	-	-	50

6.2.3 Modeling of isolated bridge

For bridges using seismic isolation design, it is necessary to consider the nonlinear behavior of both piers and isolated bearings through dynamic analysis. Fig 6.5 shows the multiple degrees of freedom (M-DOF) model of Pier 1 (P1), consisting of the superstructure, seismic isolation bearings, pier, footing, and ground spring. Moreover, when the pier heights differ or the vibration characteristics between piers vary, the model of the entire bridge system should be set up for dynamic analysis. Table 6.2 lists the specifications of the model.

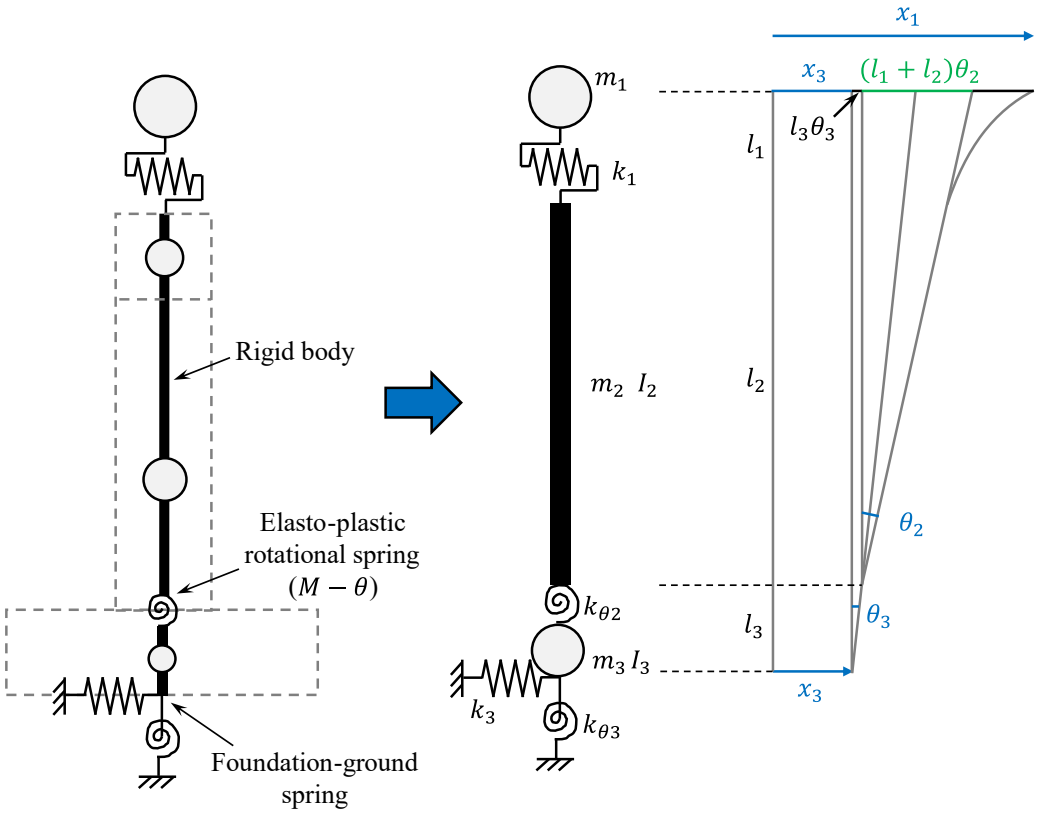

Figure 6.5 M-DOF model in dynamic analysis for Pier 1 (P1).

Table 6.2 Specifications of dynamic model.

Node	Height (m)	Mass		Base pier rotational spring	
		Horizontal (ton)	Rotational (ton·m)	Bending moment (kN·m)	34839
				Rotation angle (rad)	0.309×10^{-2}
1	10.00	400.0	-	Ground spring	
2	10.00	-	-	Horizontal spring (kN/m)	1.397×10^{6}
3	8.90	140.0	-	Rotational spring (kN/rad)	1.725×10^{6}
4	3.75	206.3	-	Damping ratio	
5	0.00	-	-	Isolated bearing (%)	0
6	−1.00	227.5	876.8	Pier (%)	2
7	−2.00	-	-	Foundation-ground (%)	10

The dynamic model can be simplified into a four DOF numerical model, with the horizontal displacement of the bearing (x_1), rotation of the base pier (θ_2), and horizontal displacement and rotation of the foundation (x_3 and θ_3). The equation of motion can be expressed as:

For horizontal displacement of the bearing x_1,

$$\begin{aligned} &m_1\ddot{x}_1 + c_1\left[\dot{x}_1 - \dot{x}_3 - \dot{\theta}_3 l_3 - \dot{\theta}_2(l_1+l_2)\right] \\ &+k_1[x_1 - x_3 - \theta_3 l_3 - \theta_2(l_1+l_2)] = -m_1\ddot{z} \end{aligned} \tag{6.4}$$

For rotation of the base pier θ_2,

$$\begin{aligned} &I_2\ddot{\theta}_2 + c_1(l_1+l_2)\left[\dot{x}_1 - \dot{x}_3 - \dot{\theta}_3 l_3 - \dot{\theta}_2(l_1+l_2)\right] + c_2\left(\dot{\theta}_2 - \dot{\theta}_3\right) \\ &-k_1(l_1+l_2)[x_1 - x_3 - \theta_3 l_3 - \theta_2(l_1+l_2)] + k_{\theta 2}(\theta_2 - \theta_3) = 0 \end{aligned} \tag{6.5}$$

For horizontal displacement of the foundation x_3,

$$\begin{aligned} &m_3\ddot{x}_3 + c_1\left[\dot{x}_1 - \dot{x}_3 - \dot{\theta}_3 l_3 - \dot{\theta}_2(l_1+l_2)\right] + c_3\dot{x}_3 \\ &-k_1[x_1 - x_3 - \theta_3 l_3 - \theta_2(l_1+l_2)] + k_3 x_3 = -m_3\ddot{z} \end{aligned} \tag{6.6}$$

For rotation of the foundation θ_3,

$$\begin{aligned} &I_3\ddot{\theta}_3 + c_1 l_3\left[\dot{x}_1 - \dot{x}_3 - \dot{\theta}_3 l_3 - \dot{\theta}_2(l_1+l_2)\right] - c_2\left(\dot{\theta}_2 - \dot{\theta}_3\right) \\ &+c_3\dot{\theta}_3 - k_1 l_3[x_1 - x_3 - \theta_3 l_3 - \theta_2(l_1+l_2)] - k_{\theta 2}(\theta_2 - \theta_3) + k_{\theta 3}\theta_3 = 0 \end{aligned} \tag{6.7}$$

The bilinear of the HDR bearing in the design is shown in Fig. 6.6. The parameter of the design HDR bearing is listed in Table 6.3. However, to consider the temperature effect on the seismic response of isolated bridges, the MTBW model is to be used in the dynamic analysis. Although this model cannot be directly used in the seismic design, a comparison of the hysteretic behavior between the bilinear model and the proposed model in the dynamic analysis is conducted to ensure the effectiveness of the parameters of the isolated bearings. The validation is also shown in Fig. 6.6. The maximum and minimum shear force (F+(−)) and displacement (D+(−)) and equivalent stiffness are compared. The design parameters of the proposed model in Chapters 4 and 5 are listed in Table 6.4.

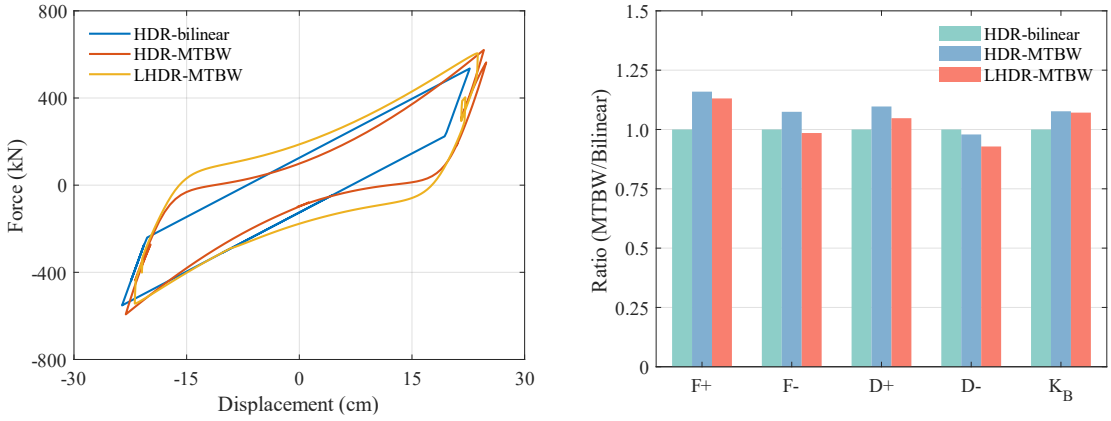

Figure 6.6 Validation of MTBW model for HDR and LHDR bearings for the maximum loop at 23℃.

Table 6.3 Parameters of bilinear model used in design of HDR bearing.

K_1 (kN/mm)	K_2 (kN/mm)	α	Q_d (kN)	Q_y (kN)	u_y (mm)	u_B (mm)	K_B (kN/mm)
9.51	1.81	0.19	125.4	154.8	16	178	2.62

Table 6.4 Parameters of MTBW model used in design of HDR and LHDR bearings.

HDR bearing									
α_0	K_r (kN/mm)	s	d_y (mm)	b	m_T	n_T			
0.32	25	-0.95	6.0	0.40	-1.87	-1.44			
LHDR bearing									
α_1	K_r (kN/mm)	s	d_y (mm)	b	m_r	n_r	c_v	K_v (kN/mm)	K_l (kN/mm)
0.25	20	-0.95	6.0	0.40	-1.92	-3.30	0.21	0.50	22

Since the reinforced concrete (RC) piers are judged to be a flexural failure, a nonlinear model, the Takeda model, that represents nonlinear flexural behavior is used. The bending moment-rotation angle relationship of the model is shown in Fig. 6.7. Note the second stiffness of the model is zero.

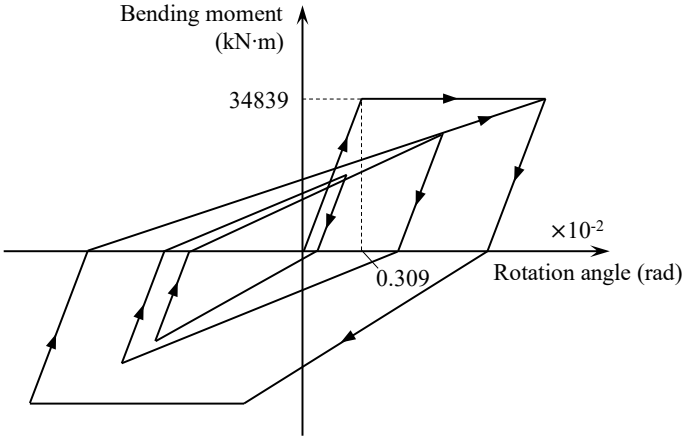

Figure 6.7 Stiffness degradation bilinear model for RC pier.

Moreover, the equivalent linear springs are used as ground springs. The viscous damping coefficients were 0% for the seismic isolation bearings, 2% for the RC piers, and 10% for the foundation-ground system considering dissipation damping. For the damping matrix used in nonlinear dynamic analysis, a Rayleigh-type damping matrix is adopted to achieve the damping coefficients for the first and second modes.

6.2.4 Selection of ground motions

Four pieces of level 2 earthquake ground motions, as shown in Fig 6.8, are selected in the time history analysis according to the JRA Specifications for Highway Bridges. Part V: Seismic Design (2019). Only the level 2 earthquakes are considered as the substructure is expected to yield under this situation. The nonlinear behavior needs to be included in such intensive ground motion. However, in the level 1 earthquake, the pier is in elasticity, indicating no obvious damage. The type I earthquake belongs to the interpolate earthquake, while the type II earthquake belongs to the inland intraplate earthquake.

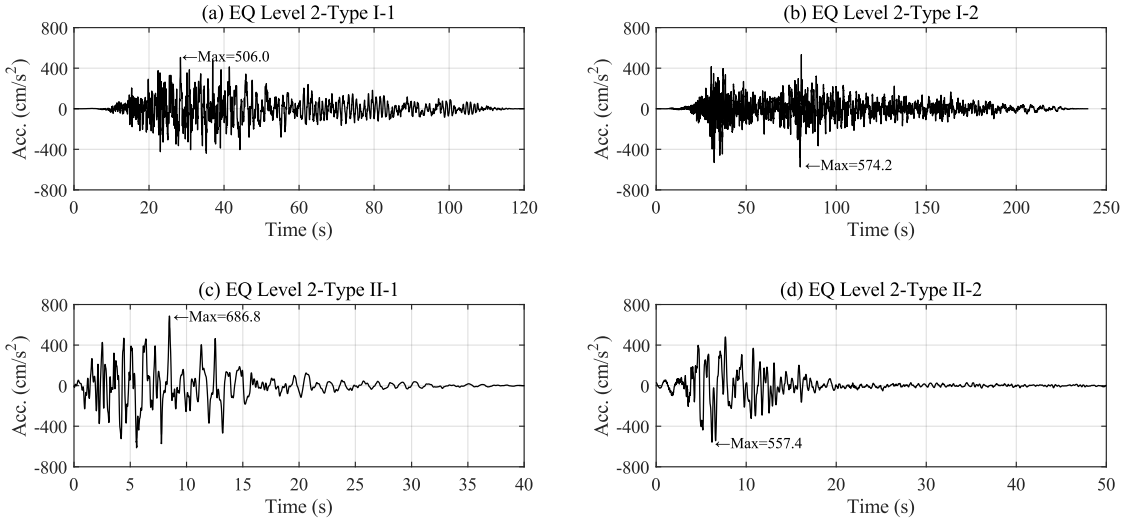

Figure 6.8 Selected Level 2 earthquake ground motions.

6.3 Low-Temperature Effect on Response of Bridge

The time history analysis is conducted to investigate the low-temperature effect on the response of the isolated bridge. The HDR bearing designed by the bilinear model in the design plan is replaced by HDR and LHDR bearings with the MTBW model. The hysteretic behavior is validated at 23°C, and then the seismic performance of the isolated bridge with HDR and LHDR bearings using the MTBW model is carried out at −20°C and 0°C. The Newmark-beta integration scheme (β=1/6) is applied to the dynamic analysis. From the eigenvalue analysis, the first dominant period of the bridge is 1.70 s. In order to evaluate the seismic performance of the isolated bridge with HDR and LHDR bearings using the MTBW model at different ambient temperatures, the hysteretic behavior and energy dissipation capacity of bearings, the relative displacement of the pier top, the bending moment of pier base, and the acceleration of superstructure are compared and discussed.

6.3.1 Hysteretic behavior of isolated bearings

The hysteresis curve of HDR bearing under level 2 earthquakes is shown in Fig. 6.9. The MTBW model is compared with the bilinear model at 23°C. It can be found that the hysteresis curves of HDR bearing using the MTBW model and bilinear model have obvious differences at 23°C. As the temperature decreases, the shape of the hysteresis loop tends to be bilinear. Moreover, the shear force of the HDR bearing becomes larger, and the displacement becomes smaller when the ambient temperature decreases, which is consistent with the experiment of hybrid simulation in Chapter 3 (Figs. 3.16 and 3.18). This is owing to the increase in the stiffness of the bearing at low temperatures.

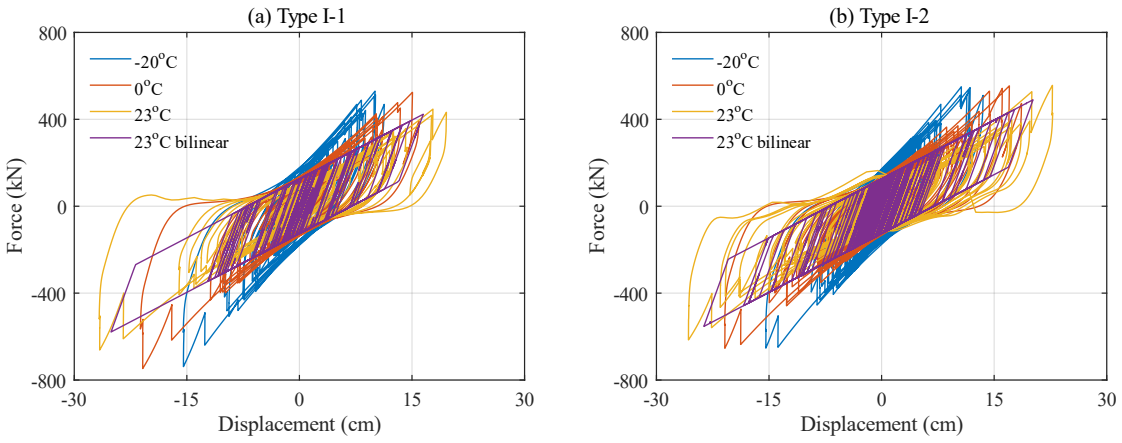

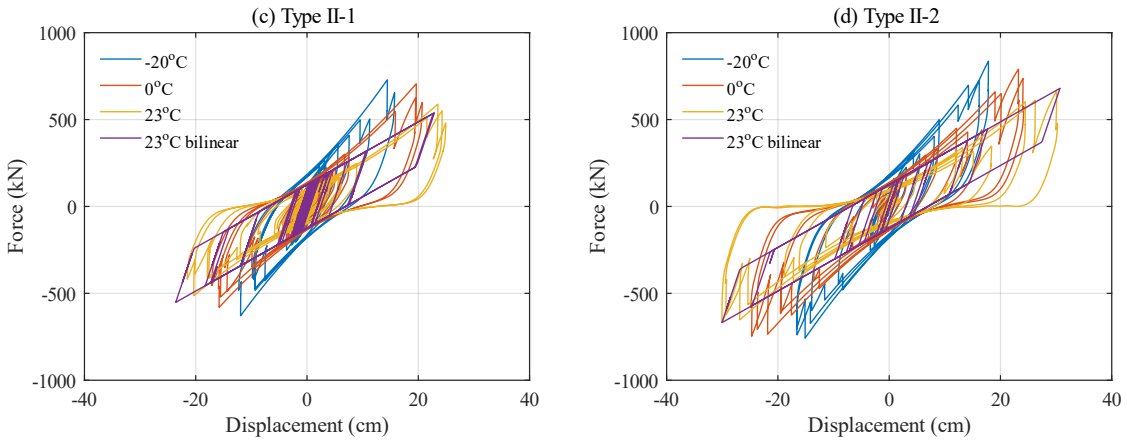

Figure 6.9 Hysteresis curve of HDR bearing under level 2 earthquakes.

The displacement of the HDR bearing is normalized into the shear strain and its time history curve is shown in Fig. 6.10. The maximum shear strains of each ground motion at three ambient temperatures are compared in Fig. 6.11. Under four ground motions, the maximum shear strain shows the same trend that the maximum strain decreases as temperature decreases. It indicates that the low-temperature effect has no adverse effect on the design of the bearing. However, the effectiveness of the isolation system is weakened by low temperatures. The displacement of the pier top and superstructure will be affected at low temperatures, which will discussed in the following section.

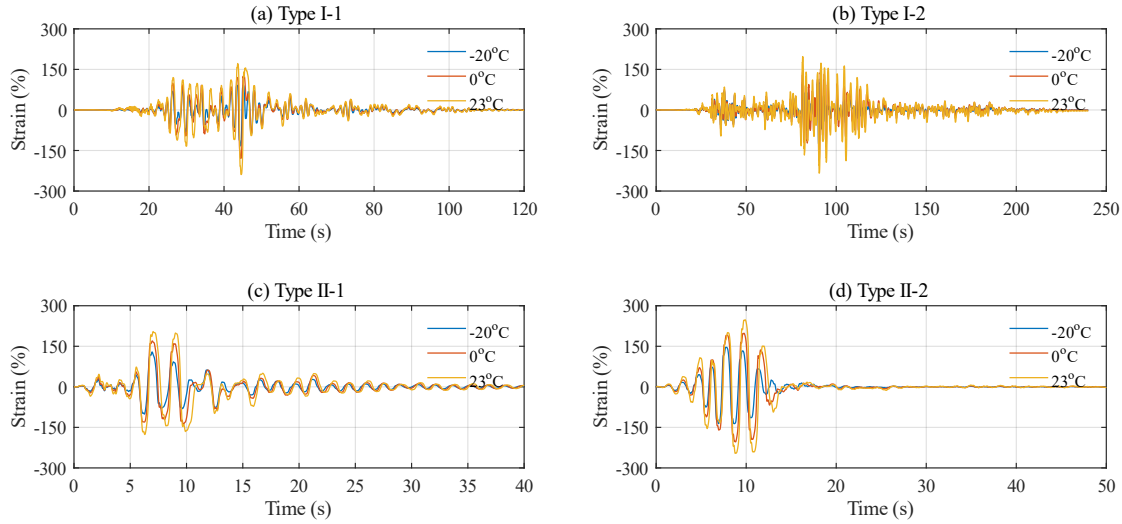

Figure 6.10 Shear strain-time history of HDR bearing under level 2 earthquakes.

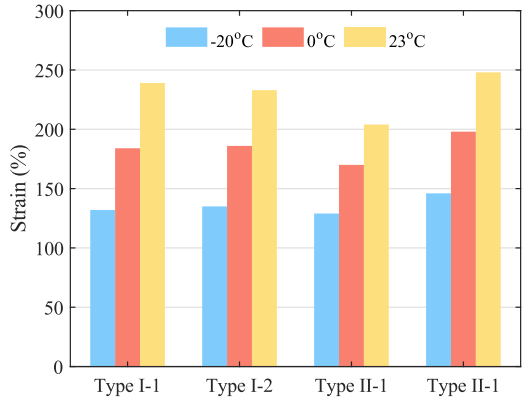

Figure 6.11 Shear strain comparison of HDR bearing under level 2 earthquake.

The hysteresis curve of LHDR bearing under four level 2 ground motions is shown in Fig. 6.12. The shear strain-time history of the bearing is shown in Fig. 6.13. The maximum strains at different ambient temperatures are compared in Fig. 6.14. The hysteretic behavior of the LHDR bearing is similar to that of the HDR bearing. Owing to considering the rate dependence in the hysteretic model of LHDR bearing, it can well capture the behavior of LHDR bearing compared with the bilinear model. Moreover, due to the addition of the lead core, the LHDR bearing shows better isolation performance with lower maximum strain.

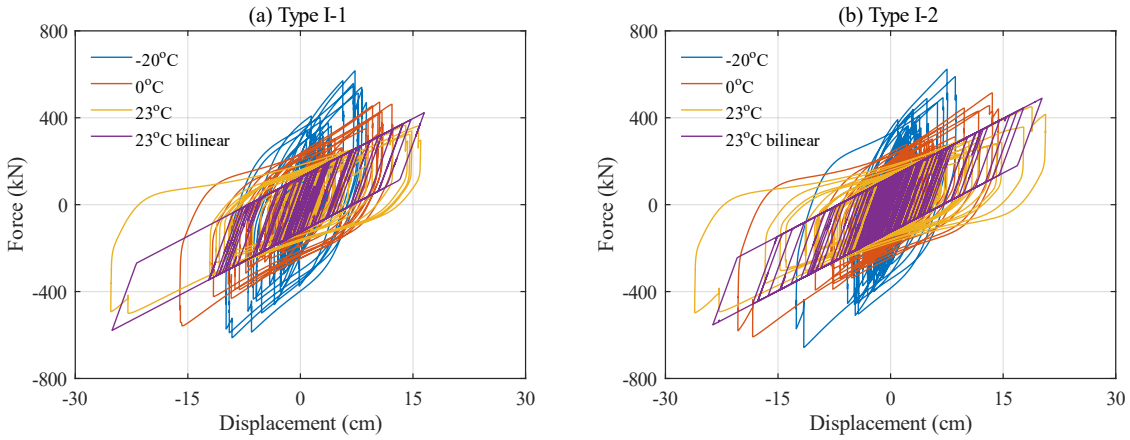

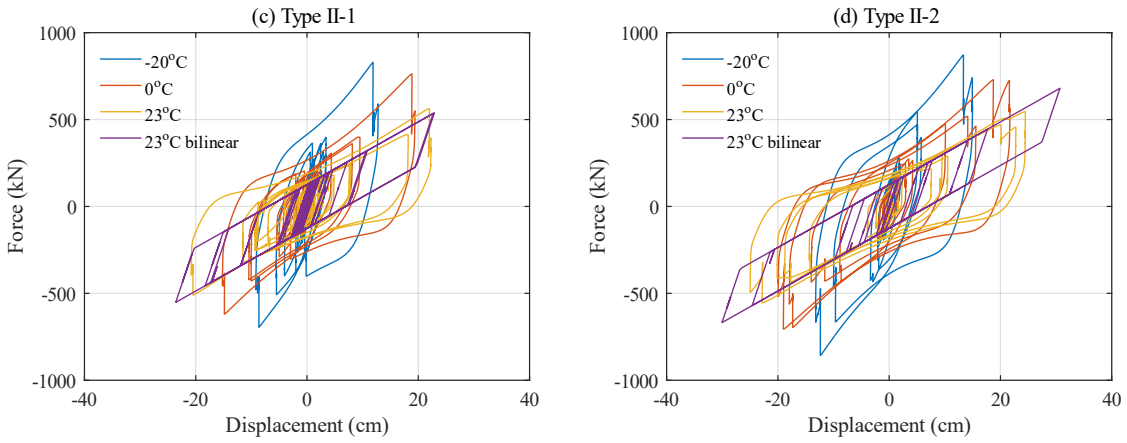

Figure 6.12 Hysteresis curve of LHDR bearing under level 2 earthquakes.

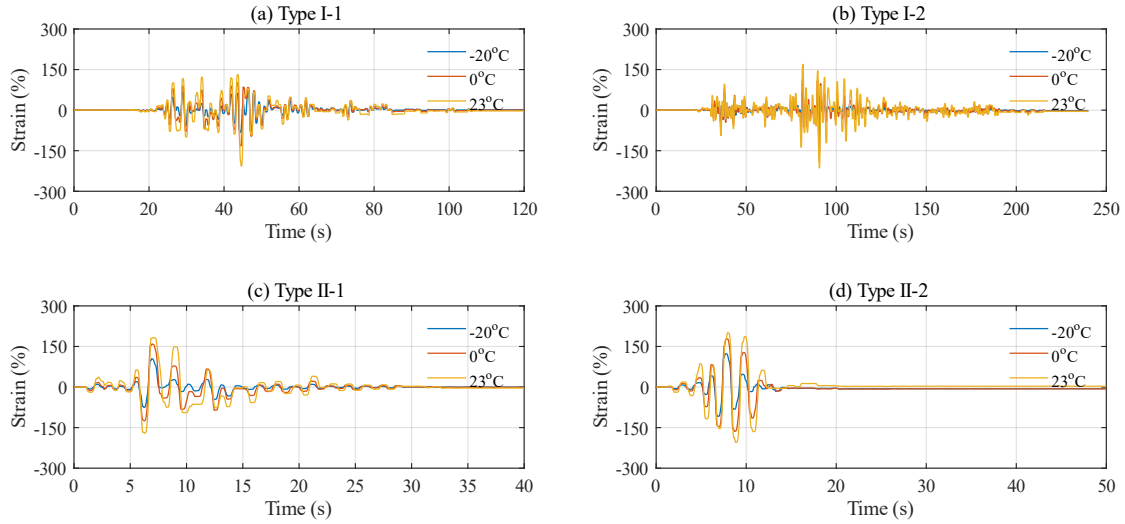

Figure 6.13 Shear strain-time history of LHDR bearing under level 2 earthquakes.

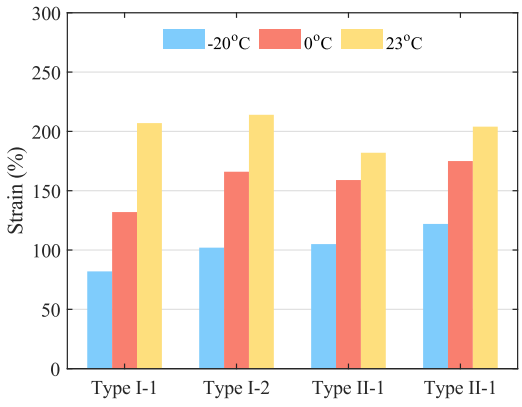

Figure 6.14 Shear strain comparison of LHDR bearing under level 2 earthquake.

6.3.2 Energy dissipation capacity

The energy dissipation capacity of HDR and LHDR bearings at three ambient temperatures is compared in Figs. 6.15 and 6.16. The energy dissipation of HDR and LHDR bearings in the isolated bridge model decreases as the ambient temperature decreases, which is in accordance with the research of Billah and Todorov (2019). For instance, the dissipated energy of LHDR bearing is reduced by 9.3% and 56.1% at 0℃ and −20℃ respectively, compared with that at 23℃ under type II-1 ground motion. However, it is contrary to the experiment of hybrid simulation in Chapter 3 (Fig .3.24). One of the possible reasons is that the yielding of the pier is considered in this bridge model while that is not considered in the model of hybrid simulation. The larger displacement of the post-yielding pier reduces the displacement of the bearing. The decreased energy dissipation capacity of bearing at low ambient temperature indicates the effectiveness of the isolation system is weakened, which is detrimental to the seismic performance of the bridge.

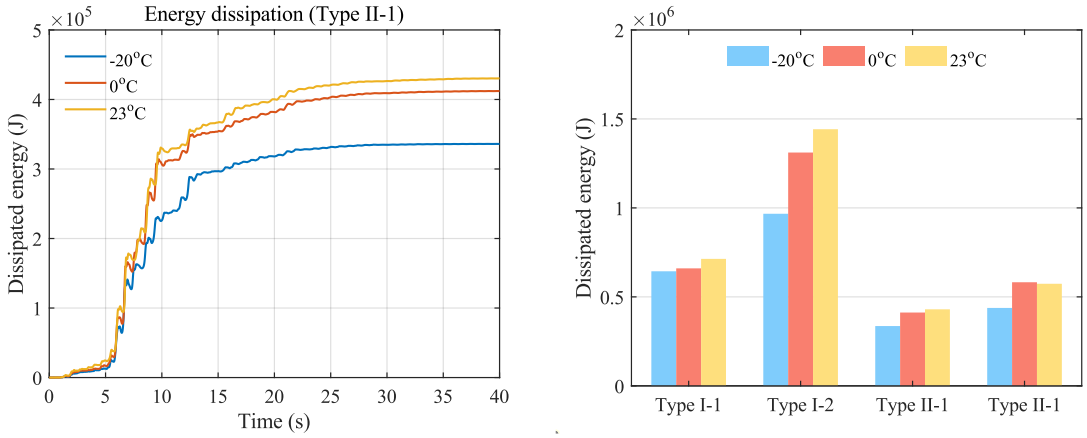

Figure 6.15 Dissipated energy comparison of HDR bearing under level 2 earthquake.

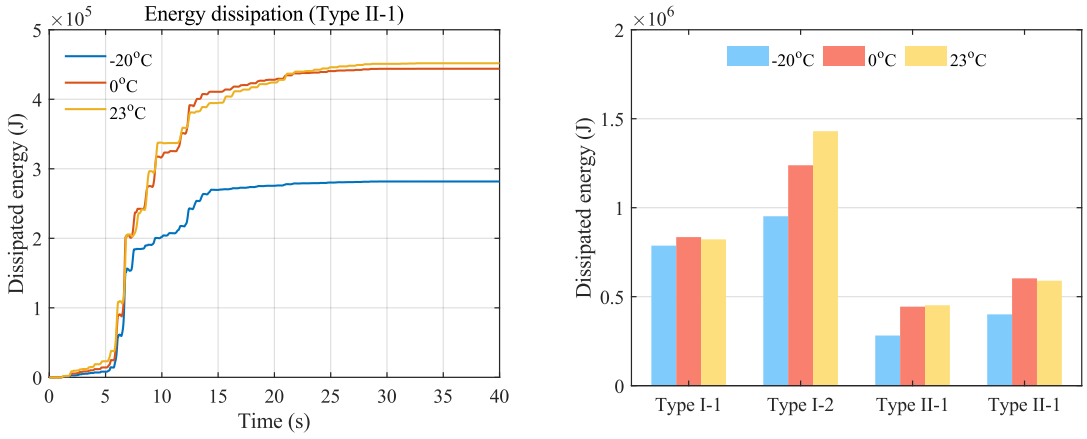

Figure 6.16 Dissipated energy comparison of LHDR bearing under level 2 earthquake.

6.3.3 Relative displacement and ductility factor of pier top

The relative pier top displacement of HDR and LHDR bearings under level 2 earthquake is compared in Figs. 6.17 and 6.19. The maximum pier top displacement and ductility factor of HDR and LHDR bearings are compared in Figs. 6.18 and 6.20. The ductility factor can be calculated as

$$\mu = \frac{\delta_u}{\delta_y} \tag{6.8}$$

where δ_u is the maximum displacement of the pier top; δ_y is the yield displacement of the pier top.

Owing to the weakened effectiveness of the isolation system at low ambient temperatures, the displacement of the pier top increases. The maximum pier top displacement is smaller in type I ground but larger in type II ground motion possibly due to the location of the earthquake. The difference in the maximum pier top displacement at different ambient temperatures also becomes obvious in type II ground motion. During the seismic design for isolated bridges, the pier is expected to yield or near the yielding state. The ductility of the pier in Figs. 6.18 and 6.20 are around 1.0 at 23℃. However, it rises as the ambient temperature decreases. Especially in type-II ground motion at −20℃, the ductility factor of the pier even reaches around 3.0, which is a large value for a pier in the isolated bridge. This proves once again that the effectiveness of seismic isolation is weakened at low temperatures.

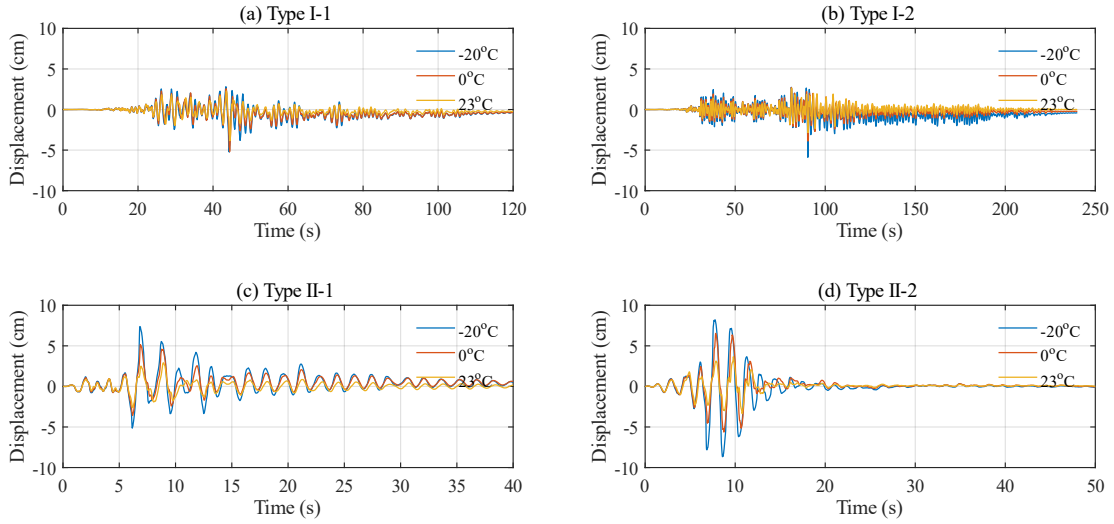

Figure 6.17 Pier top displacement-time history of bridge with HDR bearing under level 2 earthquakes.

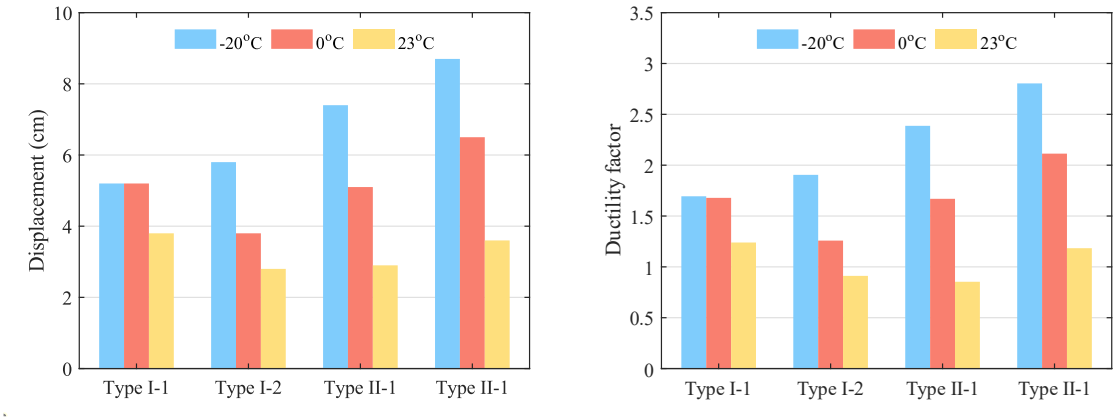

Figure 6.18 Maximum pier top displacement and ductility factor comparison of bridge with HDR bearing under level 2 earthquakes.

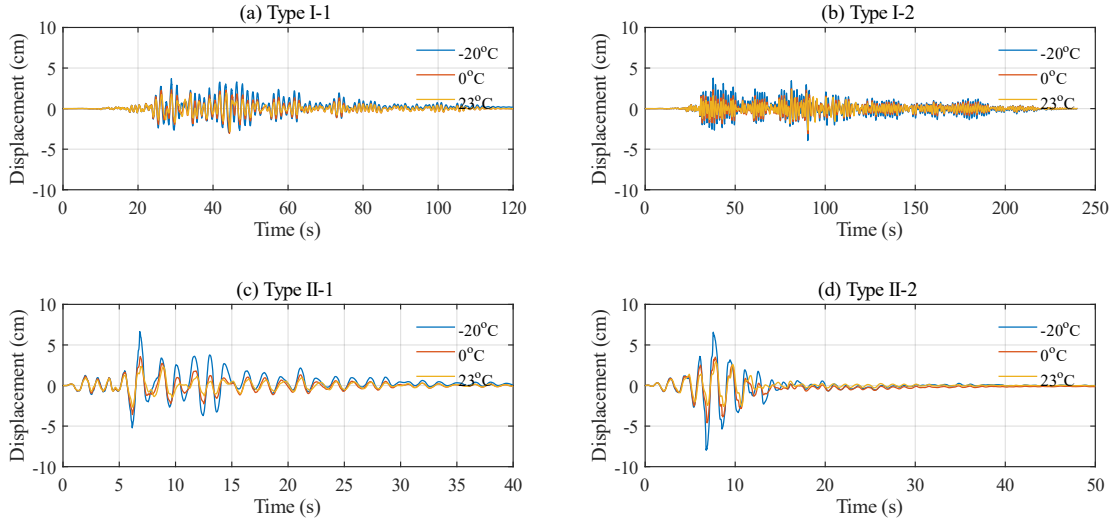

Figure 6.19 Pier top displacement-time history of bridge with LHDR bearing under level 2 earthquakes.

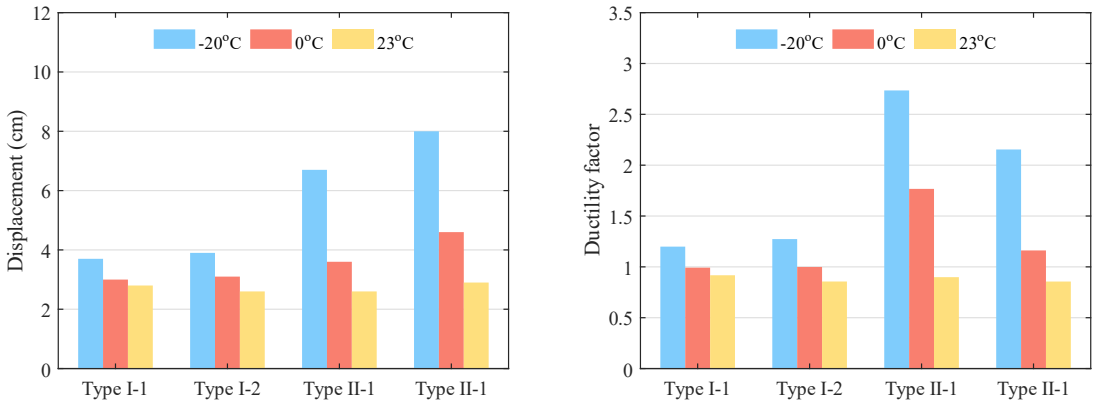

Figure 6.20 Maximum pier top displacement and ductility factor comparison of bridge with LHDR bearing under level 2 earthquakes.

6.3.4 Bending moment of pier base

The bending moment-rotation curve of the pier base of HDR and LHDR bearings is compared under four level 2 ground motions in Figs. 6.21 and 6.22. According to JRA Specifications for Highway Bridges. Part V: Seismic Design (2019), the pier is required to yield under level 2 earthquake ground motion.

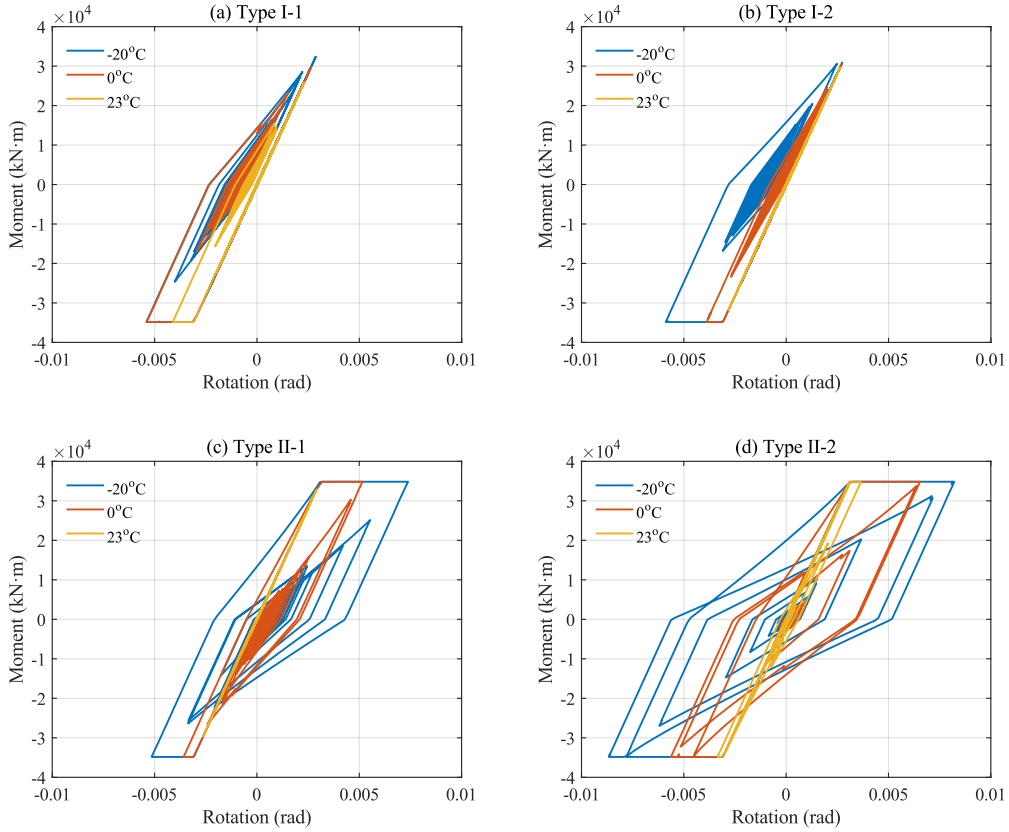

Figure 6.21 Pier base bending moment-rotation curve of bridge with HDR bearing under level 2 earthquakes.

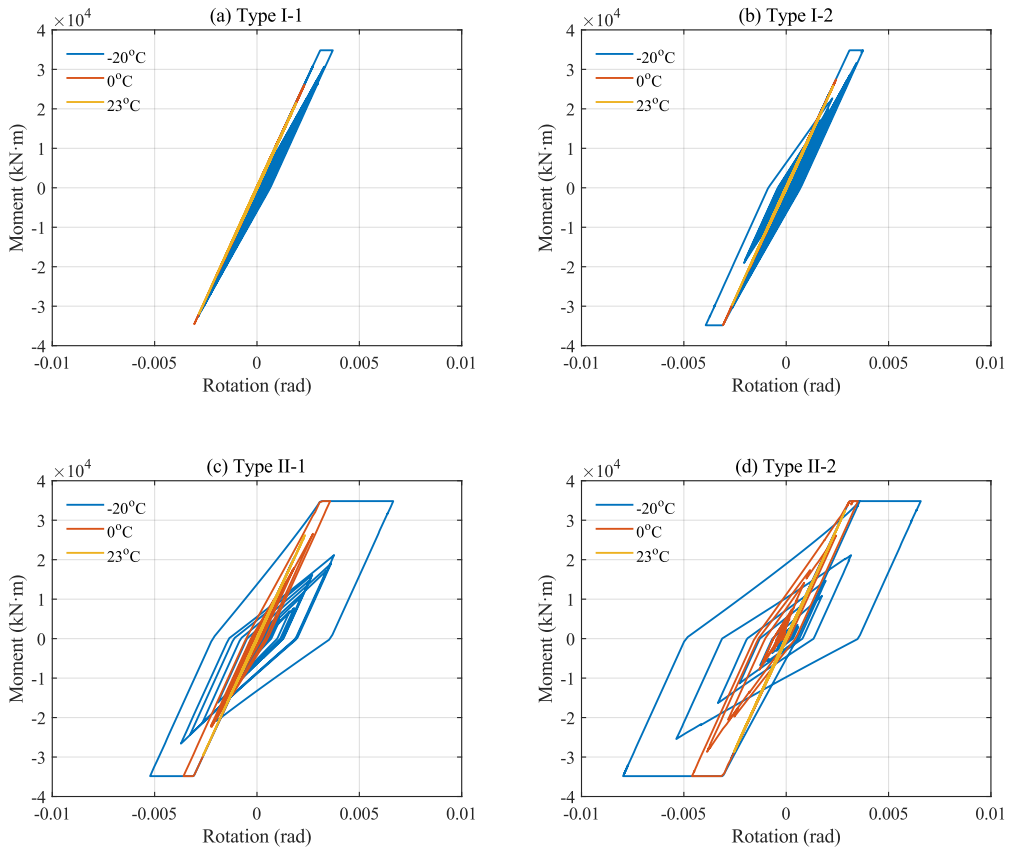

Figure 6.22 Pier base bending moment-rotation curve of bridge with LHDR bearing under level 2 earthquakes.

6.3.5 Acceleration of superstructure

The superstructure acceleration of HDR and LHDR bearings under level 2 earthquake is compared in Figs. 6.23 and 6.25. The maximum superstructure acceleration of HDR and LHDR bearings is compared in Figs. 6.24 and 6.26. The maximum acceleration of the superstructure tends to become larger under the low ambient temperature. However, the difference is not significant.

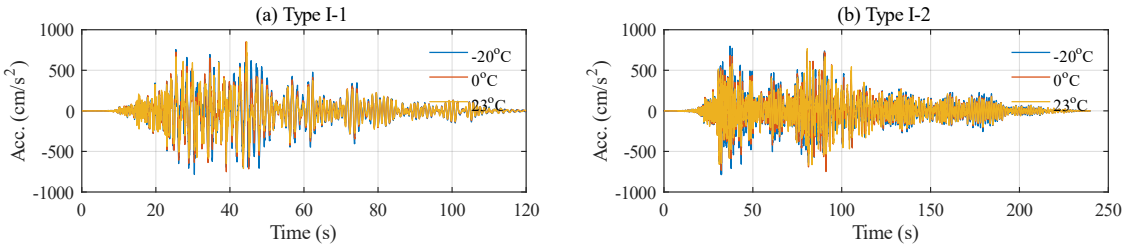

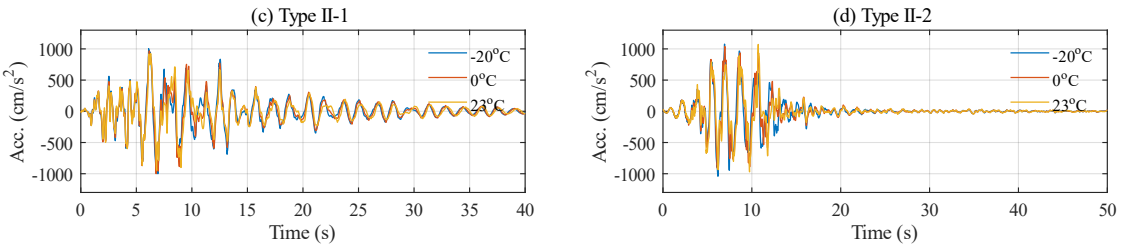

Figure 6.23 Superstructure acceleration-time history of bridge with HDR bearing under level 2 earthquakes.

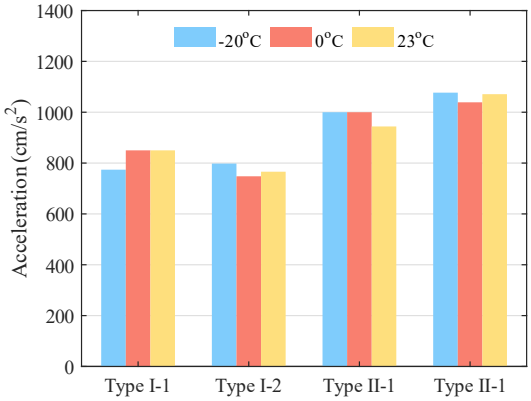

Figure 6.24 Superstructure acceleration comparison of bridge with HDR bearing under level 2 earthquakes.

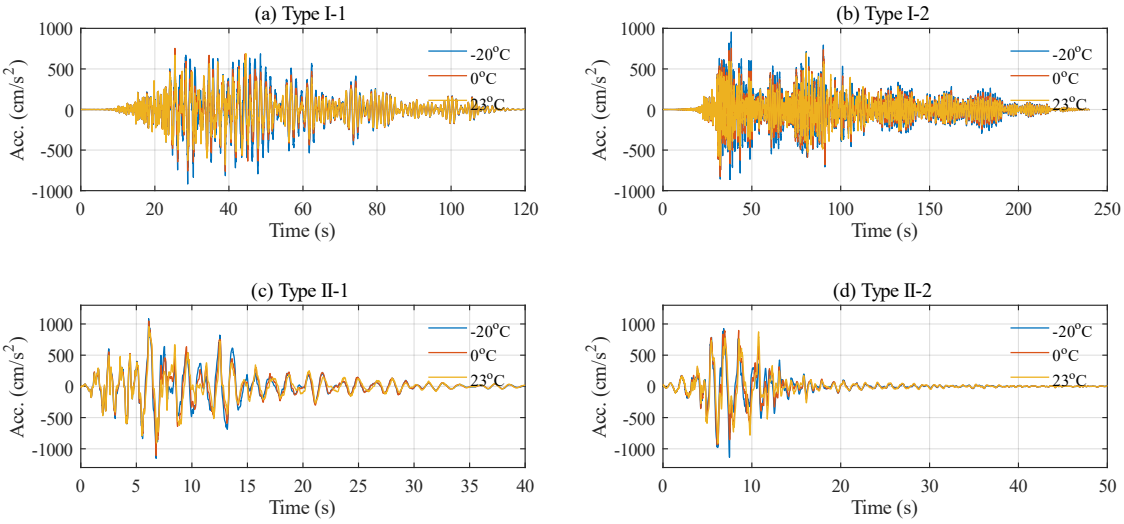

Figure 6.25 Superstructure acceleration-time history of bridge with LHDR bearing under level 2 earthquakes.

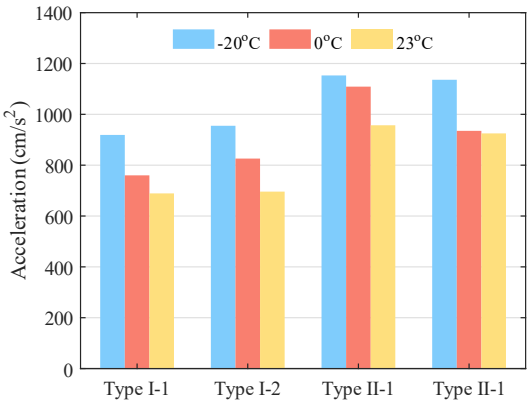

Figure 6.26 Superstructure acceleration comparison of bridge with LHDR bearing under level 2 earthquakes.

6.4 Discussion

In this chapter, a full-scaled isolated bridge model is established to conduct time history dynamic analysis and evaluate the effect of low ambient temperature on the isolated bridges with HDR or LHDR bearings. The MTBW model is validated by the bilinear model at 23℃ and then analyzed at −20℃ and 0℃. Four pieces of level 2 earthquake ground motions are selected for dynamic analysis. The hysteretic behavior and the energy dissipation of the bearing, the relative displacement of the pier top, the bending moment of the pier base, and the acceleration of the superstructure are evaluated at −20℃, 0℃, and 23℃. Here are the main points to be discussed:

(1) A five-span continuous highway bridge with HDR bearings using the bilinear model is selected for analysis. Two types of isolated bearings, HDR and LHDR bearings using the MTBW model, are designed to evaluate the effectiveness of the isolation system at low ambient temperatures. The bridge including the superstructure, isolation system, pier, and foundation, is modeled as a four-degree of freedom system conducted dynamic analysis. The first dominant period of the bridge is 1.70 s.

(2) For the hysteretic behavior of bearings, the shear force of isolated bearings using the MTBW model becomes larger, and the displacement becomes smaller when the ambient temperature decreases, owing to the increase of the stiffness of the bearing at low temperatures. The maximum shear strain shows the same trend that the maximum strain decreases as temperature decreases. The strain demand of bearings at low ambient temperatures is reduced significantly.

(3) The energy dissipation of isolated bearings using the MTBW model in the isolated bridge model decreases as the ambient temperature decreases. However, it is contrary to the

experiment of hybrid simulation possibly because the yielding of the pier is considered in this bridge model while that is not considered in the model of hybrid simulation. The decreased energy dissipation capacity of bearing at low ambient temperature indicates the effectiveness of the isolation system is weakened.

(4) For response of the structure, the displacement of the pier top increases as the temperature decreases. The difference in the maximum pier top displacement at different ambient temperatures also becomes obvious in type II ground motion. The ductility factor of the pier even reaches around 3.0 at −20℃, proving that the effectiveness of seismic isolation is weakened at low temperatures. The maximum acceleration of the superstructure tends to become larger under the low ambient temperature. However, the difference is not significant.

CHAPTER 7

CONCLUSIONS AND FUTURE WORK

7.1 Conclusions

This research aims to investigate the hysteretic behavior of HDR and LHDR bearings considering the low temperature effect. The multi-layer thermal-coupled hysteretic model of HDR and LHDR bearings is proposed to explain the hysteretic behavior coupled with the thermo-mechanism of bearings at low temperatures. An isolated bridge model with HDR and LHDR bearings is set up to further validate the efficiency of the proposed model and assess the effect of temperature on the seismic behavior of the isolated bridge. Specifically, it includes:

(1) Investigate the temperature effects on the hysteretic behavior of bearings.

(2) Explain the thermal mechanism within the bearings and establish a thermal-coupled hysteretic model.

(3) Evaluation of the seismic performance of isolated bridges with HDR and LHDR bearings at low-temperature environment.

In Chapter 1, The background of the seismic isolated bearings. The critical issues in high damping rubber bearings considering temperature effect are analyzed. The corresponding solutions and research objectives are provided in this research. Finally, the organization of the dissertation is outlined.

In Chapter 2, the literature review of the elastomeric bearings is introduced. Research on the existing hysteretic model of HDR bearings is listed. The important factors such as temperature dependence, heating effect, rate dependence, and low-temperature effect on structures that are related to this research are reviewed. The current research status and existing problems are analyzed to provide the basis and necessity for the research in the following chapters.

In Chapter 3, the experimental investigations of quasi-static cyclic loading and hybrid simulation tests were conducted to assess the seismic performance of HDR and LHDR bearings at different ambient temperatures. The factors of initial loading effect and loading interval were considered in the experiment. The hysteresis behavior and the temperature history of the bearing, and the response of the structure are analyzed to evaluate the seismic behavior of the isolated structures. The main findings are:

(1) In cyclic loading, the cyclic behavior of HDR and LHDR bearings shows significant temperature dependence. The shear stress and covered area of the cyclic loading hysteresis curve increase as the ambient temperature decreases. The equivalent shear modulus and

damping ratio decrease with the increase of the loading cycle and the decrease of the strain amplitude. They also show a negative correlation with the ambient temperature. The maximum shear stress of the LHDR bearing is higher than that of the HDR bearing at three ambient temperatures due to the addition of the lead cores, indicating an improved energy dissipation capacity.

(2) The numerous thermocouples are settled into the different positions and layers of the HDR and lead cores. In both HDR and LHDR bearings, the temperature in the third HDR layer is higher than that in the first layer due to heat accumulation, which means the temperature difference exists within the bearings. In LHDR bearings, the temperature of the lead core exhibits a rapid increase during the loading and then a decrease during the cooling owing to the larger thermal conductivity. The temperature increment of the lead core is much higher than that of the HDR owing to the smaller specific. The temperature increment of HDR in the HDR bearing is lower than that of the LHDR bearing, possibly because the heating effect of the lead core influences the heat conduction of the HDR. It indicates the thermal mechanism of the LHDR bearing is different from the HDR bearing.

(3) In hybrid simulation, the loading patterns of pseudo-dynamic and real-time tests are carried out for HDR and LHDR bearings. Similar to the cyclic loading, the hysteresis curves of hybrid simulation show significant temperature dependence. However, the hysteretic behavior of pseudo-dynamic and real-time hybrid simulation is different in HDR and LHDR bearings, especially for the maximum shear stress. In LHDR bearings, the maximum shear stresses of the real-time test at −20℃ and 0℃ are larger than those of the pseudo-dynamic test, while in HDR bearings, the results are opposite.

(4) The temperature history of HDR and LHDR bearings in hybrid simulation is similar to that in the cyclic loading test. A temperature difference can be observed between the first and third HDR layers. The lead core exhibits a rapid temperature increase during loading and a decrease during cooling. In terms of energy dissipation, specimens in real-time hybrid simulation typically show higher dissipated energy than those in pseudo-dynamic tests, except for the HDR bearing specimen at −20℃.

In Chapter 4, a multi-layer thermo-mechanical coupling model (MTBW model) is developed to investigate the hysteretic behavior of HDR bearings involving temperature dependence, heating effect, and heat transfer. The MTBW model can represent the time-dependent thermal mechanism within the bearing, with the non-uniform distribution of internal temperature. The consideration of the inner temperature improves the accuracy of the hysteretic behavior of HDR bearing. The simulated hysteresis curve, temperature history, and temperature distribution are compared with the previous model and the experimental results under quasi-static cyclic loading and real-time hybrid simulation tests at three ambient temperatures. The main findings are:

(1) The MTBW model elucidates the thermal mechanism including the heating effect and heat transfer within HDR bearings and accurately predicts the history of temperature. The hysteretic restoring force behavior calculated by the MTBW model under cyclic loading

and hybrid simulation achieves a decent agreement with the experiment and shows improved accuracy compared with the previous model. The heating and cooling behaviors are well simulated, and the temperature variation of each rubber layer is verified by the test results with improved accuracy compared with the existing simplified thermo-mechanical coupling model.

(2) Based on the precise temperature prediction, the accuracy of the thermal coupling hysteretic model for HDR bearings is improved. The numerical results of the hysteresis curve under the quasi-static cyclic loading and real-time hybrid simulation tests show good agreement with the experimental data. The MTBW model effectively captures the temperature-dependent hysteresis behavior of HDR bearings, including the strain-stress relationship at different temperatures and the gradual decrease in stiffness due to the heating effect.

In chapter 5, a rate-dependent thermo-mechanical coupling hysteretic model was proposed for LHDR bearings to illustrate the hysteretic behavior considering thermal mechanism and rate dependence. The heat transfer and heating effect of the LHDR bearings was illustrated by the proposed thermo-mechanical model. The temperature history was predicted and validated by the cyclic loading with inner temperature control and hybrid simulation at different ambient temperatures. The rate-dependent property of LHDR bearings was reflected in the proposed hysteretic model and verified by the real-time and pseudo-dynamic hybrid simulations. The main findings are:

(1) The heat conduction and heating effect in HDR laminates, lead cores, and steel plates were modeled by the thermo-mechanical model. The temperature history was accurately predicted and validated by the cyclic loading and hybrid simulation at −20℃, 0℃, and 23℃. The nonlinearly distributed temperature profile of the LHDR bearing was validated by the proposed model.

(2) The thermal-coupled hysteretic model accurately captured the hysteretic behavior of LHDR bearings, including the stiffness degradation and temperature dependence, under cyclic loading and hybrid simulation. One set of parameters of the model was identified by the optimization algorithm to represent the behavior of the bearings at different ambient temperatures. The rate dependence property of the LHDR bearing was incorporated into the proposed model and validated by real-time and pseudo-dynamic hybrid simulations. The proposed model demonstrated the improved accuracy of the hysteretic behavior compared to the existing model.

In Chapter 6, a fully isolated bridge model is established to conduct the time history dynamic analysis and evaluate the effect of low ambient temperature on the isolated bridges with HDR or LHDR bearings. The MTBW model is validated by the bilinear model at 23℃ and then analyzed at −20℃ and 0℃. Four pieces of level 2 earthquake ground motions are selected for dynamic analysis. The hysteretic behavior and the energy dissipation of the bearing, the relative displacement of the pier top, the bending moment of the pier base, and the acceleration of the superstructure are evaluated at −20℃, 0℃, and 23℃. The main findings are:

(1) For the hysteretic behavior of bearings, the shear force of isolated bearings using the MTBW model becomes larger, and the displacement becomes smaller when the ambient temperature decreases, owing to the increase of the stiffness of the bearing at low temperatures. The strain demand of bearings at low ambient temperatures is reduced significantly.

(2) The energy dissipation of isolated bearings using the MTBW model in the isolated bridge model decreases as the ambient temperature decreases. The decreased energy dissipation capacity of bearing at low ambient temperature indicates the effectiveness of the isolation system is weakened.

(3) For response of the structure, the displacement of the pier top increases as the temperature decreases. The difference in the maximum pier top displacement at different ambient temperatures also becomes obvious in type II ground motion. It proves that the effectiveness of seismic isolation is weakened at low temperatures. The maximum acceleration of the superstructure tends to become larger under the low ambient temperature.

7.2 Future Work

As for the future prospects of this research, several suggestions and recommendations are proposed for potential areas of further exploration and development.

1. Experimental investigation on performance of isolation bearings with HDR and lead cores

More real-time hybrid simulation tests are suggested to conducted under ground motions with different ground motions to fully understand the seismic performance of these bearings.

The scale factor is an important factor that affects the thermal mechanism within the bearings. Full-size or large-size specimen testing is expected to conduct to investigate the validation of the thermo-mechanical model.

2. Numerical restoring force model of isolation bearings coupled with thermal mechanism

A more effective parameter identification method is expected to propose to obtain the key parameters of restoring model considering the temperature effect.

3. Seismic design for isolated bridges

It is suggested to consider the low-temperature effect on the seismic design of the isolated bridges according to the investigation. The effectiveness of seismic isolation is weakened at low ambient temperatures. Also, the high-performance isolation system or energy dissipation device is suggested to use in low-temperature earthquake-prone areas.

REFERENCE

AASHTO. 2010. *Guide specification for seismic isolation design (3rd ed)*. Washington DC.

Abe, M., Yoshida, J., and Fujino, Y. 2004. "Multiaxial behaviors of laminated rubber bearings and their modeling. II: modeling." *Journal of Structural Engineering*, 130(8), 1133-1144.

Aghaeidoost, V., and Billah, A. H. M. M. 2024. "An advanced rate-dependent analytical model of lead rubber bearing." *Earthquake Engineering and Structural Dynamics*.

Ahmadi, H., Fuller, K., and Muhr, A. 1996. "Predicting response of non-linear high damping rubber isolation systems." In *Proc., 11th World Conference on Earthquake Engineering*.

Anastasios, G. S., and George, D. M. 2017. *Dynamic response of infrastructure to environmentally induced loads: Analysis, measurements, testing, and design*. Springer.

Beck, J. V. 1979. "Average transient temperature within a body heated by a disk heat source." In *Proc., AIAA 17th Aerospace Sciences Meeting*. American Institute of Aeronautics and Astronautics.

Bhuiyan, A. R., Okui, Y., Mitamura, H., and Imai, T. 2009. "A rheology model of high damping rubber bearings for seismic analysis: Identification of nonlinear viscosity." *International Journal of Solids and Structures*, 46(7), 1778-1792.

Billah, A. H. M. M., and Todorov, B. 2019. "Effects of subfreezing temperature on the seismic response of lead rubber bearing isolated bridge." *Soil Dynamics and Earthquake Engineering*, 126, 105814.

Bouc, R. 1967. "Forced vibrations of a mechanical system with hysteresis." In *Proc., 4th Conference on Non-linear Oscillations*, 315.

Buckle, I. G., and Mayes, R. L. 1990. "Seismic Isolation: History, Application, and Performance - A World View." *Journal of Earthquake Spectra*, 6, 161-201.

Cardone, D., Gesualdi, G., and Nigro, D. 2011. "Effects of air temperature on the cyclic behavior of elastomeric seismic isolators." *Bulletin of Earthquake Engineering*, 9(4), 1227-1255.

Carslaw, H. S., and Jaeger, J. C. 1959. *Conduction of heat in solids*. Oxford, U.K.: Oxford University, 2nd Ed.

CEN. 2018. *EN 15129 Anti-seismic devices*. Brussels: Comité Européen de Normalisation (CEN).

Constantinou, M., Whittaker, A., Kalpakidis, I., Fenz, D., and Warn, G. 2007. "Performance of seismic isolation hardware under service and seismic loading." In *Technical Rep*.

Crank, J., and Nicolson, P. 1947. "A practical method for numerical evaluation of solutions of partial differential equations of the heat-conduction type." *Mathematical Proceedings of the Cambridge Philosophical Society*, 43(1), 50-67.

CSA. 2014. *CAN/CSA-S6-14: Canadian highway bridge design code*. Toronto: Canadian

Standard Association.

Dall'Asta, A., and Ragni, L. 2006. "Experimental tests and analytical model of high damping rubber dissipating devices." *Engineering Structures*, 28(13), 1874-1884.

Dang, J., Igarashi, A., and Murakoshi, Y. 2016. "Development of hysteretic model for high-damping rubber bearings under bi-directional and large strain domain loading." *Journal of Japan Society of Civil Engineers, Ser. A1 (Structural Engineering & Earthquake Engineering (SE/EE))*, 72(1), 250-262.

Deng, P., Gan, Z., Hayashikawa, T., and Matsumoto, T. 2020. "Seismic response of highway viaducts equipped with lead-rubber bearings under low temperature." *Engineering Structures*, 209, 110008.

Fuller, K. N. G., Gough, J., and Thomas, A. G. 2004. "The effect of low-temperature crystallization on the mechanical behavior of rubber." *Journal of Polymer Science Part B: Polymer Physics*, 42(11), 2181-2190.

Gallardo, J. A., de la Llera, J. C., Restrepo, J. I., and Chen, M. 2023. "A numerical model for non-linear shear behavior of high damping rubber bearings." *Engineering Structures*, 289, 116234.

Gimenez, J. L., and Himeno, T. 2021. "Seismic isolation of bridges using rubber bearings with high energy dissipation capacity." In *Proc., 20th ASEP Int. Convention: "Structural Engineering: Getting Smarter to New and Future Challenges"*Manila, Philippines.

Gjorgjiev, I., and Garevski, M. 2013. "A polynomial analytical model of rubber bearings based on series of tests." *Engineering Structures*, 56, 600-609.

Grant, D. N., Fenves, G. L., and Whittaker, A. S. 2004. "Bidirectional modelling of high-damping rubber bearings." *Journal of Earthquake Engineering*, 8(sup001), 161-185.

Guay, L.-P., and Bouaanani, N. 2016. "Assessment of low temperature exposure for design and evaluation of elastomeric bridge bearings and seismic isolators in Canada." *Canadian Journal of Civil Engineering*, 43(9), 851-863.

Housner, G. W., Bergman, L. A., Caughey, T. K., Chassiakos, A. G., Claus, R. O., Masri, S. F., Skelton, R. E., Soong, T. T., Spencer, B. F., and Yao, J. T. P. 1997. "Structural Control: Past, Present, and Future." *Journal of Engineering Mechanics*, 123(9), 897-971.

Hwang, J. S., and Hsu, T. Y. 2001. "A fractional derivative model to include effect of ambient temperature on HDR bearings." *Engineering Structures*, 23(5), 484-490.

Hwang, J. S., and Ku, S. W. 1997. "Analytical modeling of high damping rubber Bearings." *Journal of Structural Engineering*, 123(8), 1029-1036.

Hwang, J. S., and Wang, J. C. 1998. "Seismic response prediction of HDR bearings using fractional derivative Maxwell model." *Engineering Structures*, 20(9), 849-856.

Hwang, J. S., Wu, J. D., Pan, T. C., and Yang, G. 2002. "A mathematical hysteretic model for elastomeric isolation bearings." *Earthquake Engineering and Structural Dynamics*, 31(4), 771-789.

JRA 1997. *Japan Road Association: Materials for seismic design of road bridges*. Japan: Maruzen.

JRA. 2019. *Japan Road Association: Specifications for highway bridges. Part V: Seismic*

design. Tokyo: Maruzen.

Kalpakidis, I. V., and Constantinou, M. C. 2009a. “Effects of heating on the behavior of lead-rubber bearings. I: Theory.” *Journal of Structural Engineering*, 135(12), 1440-1449.

Kalpakidis, I. V., and Constantinou, M. C. 2009b. “Effects of heating on the behavior of lead-rubber bearings. II: Verification of theory.” *Journal of Structural Engineering*, 135(12), 1450-1461.

Kikuchi, M., and Aiken, I. D. 1997. “An analytical hysteresis model for elastomeric seismic isolation bearings.” *Earthquake Engineering and Structural Dynamics*, 26(2), 215-231.

Kikuchi, M., Nakamura, T., and Aiken, I. D. 2010. “Three-dimensional analysis for square seismic isolation bearings under large shear deformations and high axial loads.” *Earthquake Engineering and Structural Dynamics*, 39(13), 1513-1531.

Kunde, M. C., and Jangid, R. S. 2003. “Seismic behavior of isolated bridges: A-state-of-the-art review.” *Electronic Journal of Structural Engineering*, 3, 140-170.

Miyamura, T., Ohsaki, M., Fujiwara, J., and Yamamoto, M. 2021. “Coupled structural and heat conduction FE analysis of laminated high damping rubber bearing.” *Earthquake Engineering and Structural Dynamics*, 50(9), 2462-2487.

Mullins, L. 1969. “Softening of rubber by deformation.” *Rubber Chemistry and Technology*, 42(1), 339-362.

Nagarajaiah, S., Reinhorn Andrei, M., and Constantinou Michalakis, C. 1991. "Nonlinear dynamic analysis of 3-D-base-isolated structures." *Journal of Structural Engineering*, 117(7), 2035-2054.

Nguyen, D. A., Dang, J., Okui, Y., Amin, A. F. M. S., Okada, S., and Imai, T. 2015. “An improved rheology model for the description of the rate-dependent cyclic behavior of high damping rubber bearings.” *Soil Dynamics and Earthquake Engineering*, 77, 416-431.

Okui, Y., Nakamura, K., Sato, T., and Imai, T. 2019. “Seismic response of isolated bridge with high damping rubber bearings.” *Steel Construction*, 12(1), 2-9.

Ozdemir, G., Avsar, O., and Bayhan, B. 2011. “Change in response of bridges isolated with LRBs due to lead core heating.” *Soil Dynamics and Earthquake Engineering*, 31(7), 921-929.

Ozdemir, G., and Dicleli, M. 2012. “Effect of lead core heating on the seismic performance of bridges isolated with LRB in near-fault zones.” *Earthquake Engineering & Structural Dynamics*, 41(14), 1989-2007.

Ozdemir, H. 1976. *Nonlinear transient dynamic analysis of yielding structures*. University of California, Berkeley.

Research Committee on Seismic Isolation Structure of Highway Bridges. 2011. *Manual on seismic isolation and vibration control design methods for highway bridges*. Japan: Civil Engineering Research Center.

Roeder Charles, W., Stanton John, F., and Feller, T. 1990. "Low-temperature performance of elastomeric bearings." *Journal of Cold Regions Engineering*, 4(3), 113-132.

Saito, T., Irie, S., Nakamura, Y., Takenouchi, K., Miyamori, Y., and Yamazaki, T. 2018.

"Mechanical characteristics of high damping rubber bearings by dynamic loading tests under the low temperature environment." *Journal of Japan Society of Civil Engineers, Ser. A1 (Structural Engineering & Earthquake Engineering (SE/EE))*, 37, 765-776.

Shen, J., Akira, I., Dang, J., Hamada, Y., and Himeno, T. 2024. "A multi-layer thermo-mechanical coupling hysteretic model for high damping rubber bearings at low temperature." *Earthquake Engineering and Structural Dynamics*, 53(3), 1028-1047.

Sivaselvan, M. V., and Reinhorn, A. M. 2006. "Lagrangian approach to structural collapse simulation." *Journal of Engineering Mechanics*, 132(8), 795-805.

Skinner, R. I., Robinson, W. H., and McVerry, G. H. 1993. *An introduction to seismic isolation*. England: John Wiley & Sons.

Takaoka, E., Takenaka, Y., Kondo, A., Hikita, M., and Kitamura, H. 2008. "Heat-mechanics interaction behavior of laminated rubber bearings under large and cyclic lateral deformation." In *Proc., 14th Conference on Earthquake Engineering*.

Tan, Y. 2022. *"Investigation of seismic performance of elastomeric isolation bearings using low-temperature hybrid simulation technique."* Doctoral dissertation, Kyoto University, Kyoto.

Tan, Y., Dang, J., Igarashi, A., Himeno, T., and Hamada, Y. 2023a. "Hysteretic restoring force model of high damping rubber bearings including thermo-mechanical coupled effect." *Engineering Structures*, 277, 115449.

Tan, Y., Dang, J., Igarashi, A., Himeno, T., and Hamada, Y. 2023b. "Hybrid simulation tests evaluating the seismic performance of lead high-damping rubber bearings at low temperatures." *Structure and Infrastructure Engineering*, 1-16.

Tan, Y., Liu, Y., Dang, J., Igarashi, A., Himeno, T., and Hamada, Y. 2024. "Stress-softening behavior of high-damping rubber bearings at low temperatures." *Journal of Structural Engineering*, 150(6), 04024050.

Wang, H., Zheng, W.-Z., Li, J., and Gao, Y.-Q. 2019. "Effects of temperature and lead core heating on response of seismically isolated bridges under near-fault excitations." *Advances in Structural Engineering*, 22(14), 2966-2981.

Wen, Y. K. 1976. "Method for random vibration of hysteretic systems." *Journal of Engineering Mechanics*, 102(2), 249-263.

Yakut, A., and Yura, J. A. 2002. "Parameters influencing performance of elastomeric bearings at low temperatures." *Journal of Structural Engineering*, 128(8), 986-994.

Yamamoto, M., Minewaki, S., Yoneda, H., and Higashino, M. 2012. "Nonlinear behavior of high-damping rubber bearings under horizontal bidirectional loading: full-scale tests and analytical modeling." *Earthquake Engineering and Structural Dynamics*, 41(13), 1845-1860.

Yamamoto, S., Kikuchi, M., Ueda, M., and Aiken, I. D. 2009. "A mechanical model for elastomeric seismic isolation bearings including the influence of axial load." *Earthquake Engineering and Structural Dynamics*, 38(2), 157-180.

Yaşar, C., Karuk, V., Cavdar, E., and Ozdemir, G. 2023. "Variation in mechanical properties of a lead–rubber bearing exposed to low temperature." *Journal of Cold Regions*

Engineering, 37(3), 04023012.

Yuan, Y., Wei, W., Tan, P., Igarashi, A., Zhu, H., Iemura, H., and Aoki, T. 2016. "A rate-dependent constitutive model of high damping rubber bearings: modeling and experimental verification." *Earthquake Engineering and Structural Dynamics*, 45(11), 1875-1892.

Zhang, R., and Li, A. 2020. "Experimental study on temperature dependence of mechanical properties of scaled high-performance rubber bearings." *Composites Part B: Engineering*, 190, 107932.

APPENDIX A

DESIGN PARAMETER OF HDR BEARING

A.1 Design Parameter of HDR Bearing

Table A.1 Parameter of design equivalent shear modulus for HDR bearing.

Type		c_0	c_1	c_2	c_3	c_4	c_5
HDR	G8	2.3686	-2.7376	1.7359	-0.47343	0.048822	-
	G10	2.9607	-3.4220	2.1699	-0.59179	0.061028	-
	G12	3.5528	-4.1064	2.6039	-0.71015	0.073234	-
HDR-S	G8	3.477	-5.200	3.993	-1.493	0.2686	-0.01804
	G10	3.961	-5.980	4.740	-1.813	0.3320	-0.02267
	G12	5.128	-7.971	6.227	-2.331	0.4162	-0.02762

Table A.2 Parameter of design equivalent damping ratio for HDR bearing.

Type		d_0	d_1	d_2	d_3
HDR	G8	0.21615	-0.047991	0.0045171	-
	G10	0.20844	-0.041555	0.0020510	-
	G12	0.20220	-3.035411	-0.0004006	-
HDR-S	G8	0.2120	0.01670	-0.02740	0.003700
	G10	0.2091	0.01611	-0.02704	0.003519
	G12	0.2086	0.01067	-0.02430	0.003025

LIST OF PUBLICATIONS

Journal Papers

1. **Shen J***, Igarashi A, Dang J, Hamada Y, Himeno T. A multi-layer thermo-mechanical coupling hysteretic model for high damping rubber bearings at low temperature. *Earthquake Engineering & Structural Dynamics*. 2024;53:1028-1047.

2. (Under revision) **Shen J***, Igarashi A, Dang J, Hamada Y, Himeno T. A rate-dependent thermo-mechanical coupling hysteretic model for lead high damping rubber bearings at low temperature. *Journal of Structural Engineering*.

3. (Under review) **Shen J***, Igarashi A, Dang J, Hamada Y, Himeno T. Seismic performance of lead high damping rubber bearings tested by real-time and pseudo-dynamic hybrid simulations at low temperatures. *Earthquake Engineering & Structural Dynamics*.

Conference Paper (Peer Review)

1. **Shen J**, Igarashi A, Dang J, Hamada Y, Himeno T, Shinmyo H. Heating and Thermal Conductivity Effect Inside High Damping Rubber Bearing at Low Temperature. *IABSE Symposium Manchester 2024: Construction's Role for a World in Emergency*. Manchester, United Kingdom. April 2024. pp. 904-912.

2. **Shen J**, Igarashi A, Dang J, Hamada Y, Himeno T, Shinmyo H. A multi-layer thermal coupling hysteric model for high damping rubber bearings at low temperature. *18th World Conference on Earthquake Engineering (WCEE)*. Milan, Italy. July 2024.

Proceedings

1. **Shen J**, Tan Y, Igarashi A. Numerical investigation on high damping rubber (HDR) bearing at low temperature with hybrid simulation. *33rd KKHTCNN Symposium on Civil Engineering*. Singapore. December 2022. S-3-5. (Oral presentation)

2. **Shen J**, Igarashi A, Dang J, Hamada Y, Himeno T, Shinmyo H, Nabeshima N. A multi-layer thermal coupled hysteretic model for high damping rubber bearings at low temperature. *78th Japan Society of Civil Engineering (JSCE) Annual Meeting.* Hiroshima, Japan. September 2023. CS2-12. (Oral presentation)

3. **Shen J**, Igarashi A, Dang J, Hamada Y, Himeno T, Shinmyo H. A multi-layer thermo-mechanical coupling model for high damping rubber bearings at low temperature. *16th Japanese Earthquake Engineering Symposium (JEES)*. Yokohama, Japan. December 2023. B-7-6. (Oral presentation)